

**HIGH-PERFORMANCE COMPUTING MODEL FOR A BIO-FUEL  
COMBUSTION PREDICTION WITH ARTIFICIAL INTELLIGENCE**

by

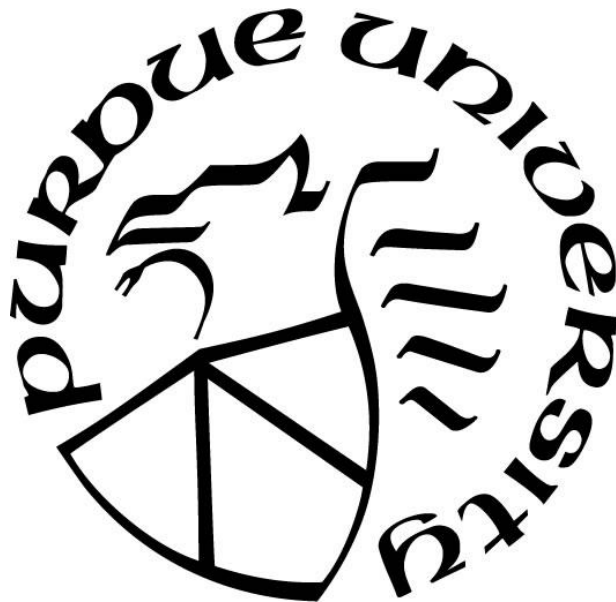
**Veeraraghava Raju Hasti**

**A Dissertation**

*Submitted to the Faculty of Purdue University*

*In Partial Fulfillment of the Requirements for the degree of*

**Doctor of Philosophy**



School of Mechanical Engineering

West Lafayette, Indiana

December 2019

**THE PURDUE UNIVERSITY GRADUATE SCHOOL  
STATEMENT OF COMMITTEE APPROVAL**

Dr. Jay P. Gore, Chair

School of Mechanical Engineering

Dr. Robert P. Lucht

School of Mechanical Engineering

Dr. Gregory Blaisdell

School of Aeronautics and Astronautics

Dr. Li Qiao

School of Aeronautics and Astronautics

**Approved by:**

Dr. Nicole L. Key

Head of the Graduate Program

*Dedicated to*

*Grandmother: Venkatamma Dommaraju*

*Mother: Jayamma Hasti*

*Father: Ramachandra Raju Hasti*

*Sister: Jagadeeswari Hasti*

*Sister: Rama Hasti*

*Niece: Abhishri*

*Niece: Yashmita*

*Nephew: Gopi Dommaraju*

## ACKNOWLEDGMENTS

I have immense pleasure in acknowledging the constant support, guidance, inspiration, and encouragement provided by my advisor Prof. Jay P. Gore. Prof. Jay is very generous and kind to share his deep insights in the field of combustion and I learned a lot from his teachings and discussions. I am fortunate to have Prof. Jay as my teacher, guide, philosopher, and most importantly as my friend. I am grateful to my mentors Prof. Roddam Narasimha, Dr. Hukam Mongia and Mr. Kuhn Terrel for constant support and guidance. My sincere thanks to Prof. Robert P. Lucht for the constant support, guidance, and encouragement on various stages of this work. I would like to sincerely thank Prof. Blaisdell for several useful discussions on turbulence modeling and statistical analysis. I would like to thank Prof. Li Qiao for serving on my advisory committee.

I would like to thank all my teachers, friends, research group members, collaborators at Argonne National Laboratory and Convergent Science Inc., for their guidance, encouragement, and support. I am thankful to Dr. Jeff Moder for providing computing resources on NASA Pleiades Supercomputer and all NJFCP members for many technical discussions and sharing experimental data.

I am deeply indebted to my parents, sisters, nieces and all my family members for their unconditional love, encouragement, and support. Without them none of this would have been possible. They have been my constant source of inspiration, energy, and wisdom. I truly owe everything to my parents and family. I dedicate this work to my beloved parents, sisters, nieces and all my family members.

I sincerely acknowledge the financial support from the School of Mechanical Engineering, Graduate School, Purdue University, Department of Energy (DOE), National Aeronautics and Space Administration (NASA) and Federal Aviation Administration (FAA).

# TABLE OF CONTENTS

LIST OF TABLES .....	8
LIST OF FIGURES .....	9
ABSTRACT .....	14
1. INTRODUCTION .....	16
1.1 Motivation.....	16
1.2 Selected fuels for the present study .....	17
1.3 Spray combustion in gas turbine engines.....	17
1.4 Artificial intelligence for online monitoring, diagnostics, and control.....	19
1.5 Literature review .....	19
1.5.1 Experimental studies.....	19
1.5.2 Computational modeling studies .....	20
1.5.3 Artificial intelligence for combustion applications .....	22
1.6 Research objectives.....	23
1.7 Structure of the report .....	24
2. COMPUTATIONAL METHODOLOGY.....	25
2.1 Governing equations .....	25
2.2 Lagrangian description for the spray .....	26
2.3 Droplet evaporation model .....	27
2.4 Secondary breakup model.....	28
2.5 Dynamic drag model.....	29
2.6 Droplet dispersion model.....	29
2.7 Chemical kinetic models.....	29
2.8 Computational domain, boundary conditions, and meshing strategy .....	30
2.9 Spray boundary conditions .....	33
2.10 Numerics.....	34
3. VALIDATION WITH EXPERIMENTS .....	36
3.1 Test case 1: PARAT pilot stabilized flame.....	36
3.1.1 Non-reacting simulation .....	38
3.1.2 Reacting simulation .....	42

3.2	Test Case 2: Volvo bluff-body stabilized flame .....	56
4.	NONREACTING SIMULATION.....	79
4.1	Determination of the number of cells across cooling holes .....	79
4.2	Flow rate calculations through swirler passages (component-wise).....	82
4.3	Flow rate calculations through all passages on the combustor liners .....	84
5.	LEAN BLOWOUT COMPUTATION AND ANALYSIS .....	89
5.1	Lean blowout (LBO) simulation methodology.....	89
5.2	Mesh sensitivity study.....	90
5.3	Reacting spray comparison at near LBO stable flame condition.....	92
5.4	Flame shape comparison at near LBO stable flame condition .....	94
5.5	The heat release rate from stable flame to lean blowout .....	95
5.6	Global lean blowout (LBO) equivalence ratio.....	96
5.7	Combustion model sensitivity.....	97
5.8	Flame structure analysis during LBO .....	98
6.	APPLICATION OF ARTIFICIAL INTELLIGENCE .....	106
6.1	Machine learning approach based on a probe data .....	106
6.1.1	Machine learning model .....	107
6.1.1.1	Dimensionality reduction .....	108
6.1.1.2	Training support vector machine (SVM) models .....	108
6.1.1.3	Finding optimal sensor locations .....	109
6.1.1.4	Evaluation of machine learning model and metric for LBO detection.....	109
6.2	Machine learning approach based on spatiotemporal features .....	114
6.2.1	Machine learning model .....	114
6.2.1.1	Data preprocessing .....	114
6.2.1.2	Feature extraction – Convolutional autoencoder.....	115
6.2.1.3	Classification – Support Vector Machine.....	118
6.2.1.4	Evaluation of machine learning model for LBO detection.....	119
7.	CONCLUSIONS AND RECOMMENDATIONS .....	124
7.1	Conclusions.....	124
7.2	Recommendations for future work .....	126
	REFERENCES .....	128

VITA.....	140
PUBLICATIONS.....	141

## LIST OF TABLES

Table 1.1. Comparison of properties for A-2 and C-1 fuels [2] .....	17
Table 2.1. Number of Species in the Kinetic Models for A-2 and C-1 Fuels.....	30
Table 3.1. Operating conditions for Volvo test rig validation case[45].....	58
Table 3.2. Boundary conditions for Volvo test rig validation case[45].....	58
Table 4.1. Flow splits comparison for an experimental total flow rate of 31.8 g/s for swirlers (all passages open) with RANS for a maximum cell size of 3 mm and different mesh resolution [1]. .....	83
Table 4.2. Comparison of component-wise swirler flow rates with experimental data for 10 million cells [1]. .....	83
Table 5.1. Details of the minimum mesh resolution for establishing a mesh independent solution with a base size of 3 mm [2-4].....	90
Table 6.1. Convolutional autoencoder parameters .....	116

## LIST OF FIGURES

Figure 1.1 (a) Spray (b) Iso-surface of Temperature = 1800 K in the Referee gas turbine combustor.....	18
Figure 1.2. Complex flow field resulting from the multiple flow interactions with a spray inside referee combustor. (streamlines plotted on Z=0 plane). HCHO (or CH <sub>2</sub> O) iso-contours are also shown with thick black lines.....	18
Figure 2.1. The computational domain of referee combustor (left), magnified view of the hybrid airblast swirler (right), and 2D cross-section at Z=0 (bottom) [3, 4].....	31
Figure 2.2. Computational grid for a reacting case with AMR at t= 5 ms (top) and t= 10 ms (bottom). Contours are colored with axial velocity (m/s) [3, 4]. .....	32
Figure 2.3. Spray boundary conditions .....	33
Figure 3.1. Computational domain for Non-Reacting simulations[47] .....	39
Figure 3.2. The mesh and three magnified x-y plane sections of it at z=0 for non-reacting flow simulations with adaptation based on the instantaneous velocity gradients[47] .....	40
Figure 3.3. Contours of Axial velocity profile on the center plane of the burner[47] .....	41
Figure 3.4. Radial profiles of axial velocity [47].....	41
Figure 3.5. The mesh in the x-y plane at z=0 for reacting simulations of PARAT with adaptation based on instantaneous temperature gradients[47] .....	43
Figure 3.6. Reacting flow mean axial velocity contour and mean, rms axial velocity and turbulence intensity comparison at y/d=0.2[47] .....	44
Figure 3.7. Mesh Sensitivity Study – Comparison of Mean temperature [K] profiles along the centerline. Contour plot corresponds to 0.25 mm case[47] .....	44
Figure 3.8. Instantaneous axial velocity (m/s) (left) and instantaneous radial velocity (m/s) (right) .....	45
Figure 3.9. Instantaneous vorticity magnitude (1/s) .....	45
Figure 3.10. Iso-surface of second invariant of velocity gradient tensor (Q-criterion) for visualization of vortex tubes Left: Q = 100000 s – 2 Middle: Q = 10000 s – 2 Right: Q = 1000 s – 2. Colored by instantaneous temperature[47] .....	46
Figure 3.11. Divergence of instantaneous velocity (1/s) [47].....	47
Figure 3.12. Mean temperature profile along the centerline of the jet for all 3 flame conditions [49].....	50
Figure 3.13. RMS temperature profile along the centerline of the jet for all 3 flame conditions[49] .....	51

Figure 3.14. Radial profiles of mean and RMS temperatures at different x/ds for flame 1 (0% CO <sub>2</sub> ) and flame 3 (10% CO <sub>2</sub> ) [49].....	51
Figure 3.15. Progress variable .....	52
Figure 3.16. Mean temperature versus RMS temperature[49] .....	52
Figure 3.17. Mean mass fraction of OH showing thinner and longer reaction zone with CO <sub>2</sub> dilution .....	53
Figure 3.18. Instantaneous temperature comparison for three flames .....	53
Figure 3.19. Mole fraction of H <sub>2</sub> O, CO <sub>2</sub> , CO and H <sub>2</sub> for 0% CO <sub>2</sub> case[49].....	54
Figure 3.20. Mole fraction of H <sub>2</sub> O, CO <sub>2</sub> , CO and H <sub>2</sub> for 5% CO <sub>2</sub> case[49].....	54
Figure 3.21. Mole fraction of H <sub>2</sub> O, CO <sub>2</sub> , CO and H <sub>2</sub> for 10% CO <sub>2</sub> case[49].....	55
Figure 3.22. Equilibrium Constant for the instantaneous temperature obtained from JANAF tables for CO <sub>2</sub> + H <sub>2</sub> ↔ CO + H <sub>2</sub> O reaction[49] .....	55
Figure 3.23. Comparison of Ratio = XCOXH <sub>2</sub> O/XCO <sub>2</sub> XH <sub>2</sub> for three flames[49].....	56
Figure 3.24. Volvo Bluff Body for LES simulations[48]. .....	57
Figure 3.25. Boundaries for the Volvo bluff body test case[48]. .....	57
Figure 3.26. Mesh at the centreline plane in FGM (a-c) and TFM (d-f) simulations for base mesh sizes of 3mm, 2.5mm, and 1mm. Each case has 3 levels of maximum AMR refinement [48]....	59
Figure 3.27. Adaptive mesh refinement in action in the wake region behind the Volvo bluff body [48].....	60
Figure 3.28. Centerline mean axial velocity Profile at z/d=0, y/d=0 [48]. .....	63
Figure 3.29. Centerline turbulence intensity profile at z/d=0, y/d=0 [48]. .....	63
Figure 3.30. Transverse Mean U <sub>x</sub> Velocity Profile on z=0 plane at x/D=0.375 [48].....	64
Figure 3.31. Transverse Mean U <sub>x</sub> Velocity Profile on z=0 plane at x/D=0.95 [48]. .....	64
Figure 3.32. Transverse Mean U <sub>x</sub> Velocity Profile on z=0 plane at x/D=1.53 [48]. .....	64
Figure 3.33. Transverse Mean U <sub>x</sub> Velocity Profile on z=0 plane at x/D=3.75 [48]. .....	65
Figure 3.34. Transverse Mean U <sub>x</sub> Velocity Profile on z=0 plane at x/D=9.4 [48]. .....	65
Figure 3.35. Transverse Mean U <sub>y</sub> Velocity Profile on z=0 plane at x/D=0.375 [48]. .....	65
Figure 3.36. Transverse Mean U <sub>y</sub> Velocity Profile on z=0 plane at x/D=0.95 [48]. .....	66
Figure 3.37. Transverse Mean U <sub>y</sub> Velocity Profile on z=0 plane at x/D=1.53 [48]. .....	66
Figure 3.38. Transverse Mean U <sub>y</sub> Velocity Profile on z=0 plane at x/D=3.75 [48]. .....	66
Figure 3.39. Mean U <sub>y</sub> Velocity Profile on z=0 plane at x/D=9.4 [48].....	67

Figure 3.40. Transverse $U_x$ RMS Velocity Profile on $z=0$ plane at $x/D=0.375$ [48].	67
Figure 3.41. Transverse $U_x$ RMS Velocity Profile on $z=0$ plane at $x/D=0.95$ [48].	67
Figure 3.42. Transverse $U_x$ RMS Velocity Profile on $z=0$ plane at $x/D=1.53$ [48].	68
Figure 3.43. Transverse $U_x$ RMS Velocity Profile on $z=0$ plane at $x/D=3.75$ [48].	68
Figure 3.44. Transverse $U_x$ RMS Velocity Profile on $z=0$ plane at $x/D=9.4$ [48].	68
Figure 3.45. Transverse $U_y$ RMS Velocity Profile on $z/d=0$ plane at $x/D=0.375$ [48].	69
Figure 3.46. Transverse $U_y$ RMS Velocity Profile on $z/d=0$ plane at $x/D=0.95$ [48].	69
Figure 3.47. Transverse $U_y$ RMS Velocity Profile on $z/d=0$ plane at $x/D=1.53$ [48].	69
Figure 3.48. Transverse $U_y$ RMS Velocity Profile on $z/d=0$ plane at $x/D=3.75$ [48].	70
Figure 3.49. Transverse $U_y$ RMS Velocity Profile on $z/d=0$ plane at $x/D=9.4$ [48].	70
Figure 3.50. Transverse Mean Temperature Profile on $z/d=0$ plane at $x/D=3.75$ [48].	70
Figure 3.51. Transverse Mean Temperature Profile on $z/d=0$ plane at $x/D=8.75$ [48].	71
Figure 3.52. Transverse Mean Temperature Profile on $z/d=0$ plane at $x/D=13.75$ [48].	71
Figure 3.53. Transverse Mean CO mass fraction Profile on $z/d=0$ plane with FGM [48].	71
Figure 3.54. Temperature distribution in FGM (a-c) and TFM (d-g). TFM simulations have FTF =7.0 for (e-f) and FTF= 3.0 for (d) [48].	72
Figure 3.55. Time averaged temperature contours in FGM (a-c) and TFM (d-g). TFM simulations have FTF=7.0 for (e-f) and FTF=3.0 for (d) [48].	73
Figure 3.56. Time-averaged axial velocity distribution in FGM (a-c) and TFM (d-g) simulations. TFM simulations have FTF=7.0 for (e-f) and FTF=3.0 for (d) [48].	74
Figure 3.57. Instantaneous velocity magnitude in FGM (a-c) and TFM (d-g) simulations. TFM simulations have FTF=7.0 for (e-f) and FTF=3.0 for (d) [48].	75
Figure 3.58. Instantaneous vorticity magnitude in FGM (a-c) and TFM (d-g) simulations. TFM simulations have FTF=7.0 for (e-f) and FTF=3.0 for (d) [48].	76
Figure 3.59. Instantaneous distribution of OH mass fraction in FGM simulations [48].	77
Figure 4.1. Computational domain and boundary conditions for a single hole study [1].	80
Figure 4.2. Computational grid for $C_d$ sensitivity study. FE stands for Fixed Embedding [1].	80
Figure 4.3. Mesh sensitivity results for the coefficient of discharge for a single hole study with RANS model [1].	82
Figure 4.4. Comparison of component-wise flow splits for swirler passages for 10M cells [1, 4].	84
Figure 4.5. Mean velocity (m/s) contours for swirler flow paths: RANS (left) and LES (right) for 10 million cells [1].	85

Figure 4.6. Comparison of combustor flow splits [1].	85
Figure 4.7. LES time-averaged velocity (m/s) components on mid-plane for 10 million case (all passages open) [1, 4].	86
Figure 4.8. LES time-averaged velocity magnitude (m/s) on mid-plane with velocity vectors for 10 million cells (all passages open) [1, 4].	87
Figure 5.1. Staged fuel ramp down approach for LBO prediction. The red dot represents the measured lean blow-out global equivalence ratio [2-4].	90
Figure 5.2. The fraction of resolved turbulent kinetic energy (TKE) with a minimum cell size of 0.375 mm and maximum cell size (base size) of 3 mm (total cell count is 10 million cells) [4].	91
Figure 5.3. Effect of mesh resolution on the global LBO equivalence ratio for C-1 fuel [4].	91
Figure 5.4. Effect of mesh resolution on the heat release rate for C1 fuel [4].	92
Figure 5.5. Spray statistics comparison with PDPA data [12] for a stable flame at $\phi = 0.096$ [2-4].	93
Figure 5.6. Line of Sight averaged mass fraction of OH from LES compared with experimental OH* from chemiluminescence [2-4].	94
Figure 5.7. Heat release rate with detailed chemistry simulations using FRC combustion model [2-4].	95
Figure 5.8. Heat release rate with FGM combustion model and compact mechanism [4].	96
Figure 5.9. Global LBO equivalence ratio comparison between experiments [6] and LES [2-4].	96
Figure 5.10. LBO Equivalence ratio comparison between LES (detailed chemistry solver) and experiments [2-4].	97
Figure 5.11. Effect of combustion model on the fuel sensitivity to the computed LBO global equivalence ratio [4].	97
Figure 5.12. Comparison of temperature (filled contours), velocity (vectors), and iso-contour of mean mass fraction of OH = 5e-04 (black line) for C-1 fuel.	98
Figure 5.13. Instantaneous temperature [K] contour plots (left) at the combustor mid-plane and formaldehyde mass fractions (right) for A-2 and C-1 fuel during LBO [2-4].	99
Figure 5.14. Temperature versus mixture fraction scatterplots for A-2 fuel (top) and C-1 fuel (bottom) sampled from the primary zone. Colored with CH <sub>2</sub> O mass fraction [3, 4].	101
Figure 5.15. Temperature versus mixture fraction scatterplots for A-2 fuel sampled from the primary zone. Colored with OH mass fraction [3, 4].	101
Figure 5.16. Mean temperature [K] contours for A-2 (left) and C-1 (right) with streamlines in the flame stabilizing primary zone at a stable flame condition with $\phi = 0.096$ near the lean blow-out point [3, 4].	102

Figure 5.17. The probability density function of the temperatures of the recirculating gases in the primary zone for A-2 fuel (left) and C-1 fuel (right) [3, 4]. .....	103
Figure 5.18. Primary zone sampling region for combustion process investigation during LBO. ....	104
Figure 5.19. Evolution of the Volume averaged scalars in the primary zone of the combustor from stable flame to complete lean blowout (LBO) process. ....	105
Figure 6.1. The machine learning model for determining optimal sensor location.....	107
Figure 6.2. The optimal location for T and YOH sensor .....	110
Figure 6.3. The probability density function of T, YOH, and YCH <sub>2</sub> O at location 1 .....	111
Figure 6.4. Variation of Kurtosis (a) and skewness (b) of T, YOH, and YCH <sub>2</sub> O at location 1. ....	111
Figure 6.5. Moving average of T, YOH, and YCH <sub>2</sub> O at location 1 .....	112
Figure 6.6. Time-series of T, YOH, YCH <sub>2</sub> O and f at location 1 and LBO Indicator (p) .....	113
Figure 6.7. The proposed methodology for LBO detection.....	114
Figure 6.8. The architecture of the convolutional autoencoder .....	117
Figure 6.9. Mean square error vs epochs .....	119
Figure 6.10. (a) Autoencoder input (b) Autoencoder output with 64 nodes in the dense layer (c) Autoencoder output with 128 layers in the dense layer .....	120
Figure 6.11. YOH distribution at different time instants (top) and its autoencoder reconstruction for an equivalence ratio of 0.096 (bottom) .....	120
Figure 6.12. YOH distribution at different time instants (top) and its autoencoder reconstruction for equivalence ratio of 0.090 (bottom) .....	121
Figure 6.13. YOH distribution at different time instants (top) and its autoencoder reconstruction for an equivalence ratio of 0.085 (bottom) .....	121
Figure 6.14. YOH distribution at different time instants (top) and its autoencoder reconstruction for an equivalence ratio of 0.082 (bottom) .....	121
Figure 6.15. (a) Input to the autoencoder and (b-e) 4 out of the 32 feature-maps in the first convolutional layer.....	122
Figure 6.16. LBO indicator for the entire dataset (all time-steps and all equivalence ratios) ...	123

## ABSTRACT

Author: Hasti, Veeraraghava Raju. PhD

Institution: Purdue University

Degree Received: December 2019

Title: High-Performance Computing Model for a Bio-Fuel Combustion Prediction with Artificial Intelligence.

Committee Chair: Jay Gore

The main accomplishments of this research are

- (1) developed a high fidelity computational methodology based on large eddy simulation to capture lean blowout (LBO) behaviors of different fuels;
- (2) developed fundamental insights into the combustion processes leading to the flame blowout and fuel composition effects on the lean blowout limits;
- (3) developed artificial intelligence-based models for early detection of the onset of the lean blowout in a realistic complex combustor.

The methodologies are demonstrated by performing the lean blowout (LBO) calculations and statistical analysis for a conventional (A-2) and an alternative bio-jet fuel (C-1).

High-performance computing methodology is developed based on the large eddy simulation (LES) turbulence models, detailed chemistry and flamelet based combustion models. This methodology is employed for predicting the combustion characteristics of the conventional fuels and bio-derived alternative jet fuels in a realistic gas turbine engine. The uniqueness of this methodology is the inclusion of as-it-is combustor hardware details such as complex hybrid-airblast fuel injector, thousands of tiny effusion holes, primary and secondary dilution holes on the liners, and the use of highly automated on the fly meshing with adaptive mesh refinement. The flow split and mesh sensitivity study are performed under non-reacting conditions. The reacting LES simulations are performed with two combustion models (finite rate chemistry and flamelet generated manifold models) and four different chemical kinetic mechanisms. The reacting spray characteristics and flame shape are compared with the experiment at the near lean blowout stable condition for both the combustion models. The LES simulations are performed by a gradual reduction in the fuel flow rate in a stepwise manner until a lean blowout is reached. The computational methodology has predicted the fuel sensitivity to lean blowout accurately with correct trends between the conventional and alternative bio-jet fuels. The flamelet generated

manifold (FGM) model showed 60% reduction in the computational time compared to the finite rate chemistry model.

The statistical analyses of the results from the high fidelity LES simulations are performed to gain fundamental insights into the LBO process and identify the key markers to predict the incipient LBO condition in swirl-stabilized spray combustion. The bio-jet fuel (C-1) exhibits significantly larger  $\text{CH}_2\text{O}$  concentrations in the fuel-rich regions compared to the conventional petroleum fuel (A-2) at the same equivalence ratio. It is observed from the analysis that the concentration of formaldehyde ( $\text{CH}_2\text{O}$ ) increases significantly in the primary zone indicating partial oxidation as we approach the LBO limit. The analysis also showed that the temperature of the recirculating hot gases is also an important parameter for maintaining a stable flame. If this temperature falls below a certain threshold value for a given fuel, the evaporation rates and heat release rate decreases significantly and consequently leading to the global extinction phenomena called lean blowout. The present study established the minimum recirculating gas temperature needed to maintain a stable flame for the A-2 and C-1 fuels.

The artificial intelligence (AI) models are developed based on high fidelity LES data for early identification of the incipient LBO condition in a realistic gas turbine combustor under engine relevant conditions. The first approach is based on the sensor-based monitoring at the optimal probe locations within a realistic gas turbine engine combustor for quantities of interest using the Support Vector Machine (SVM). Optimal sensor locations are found to be in the flame root region and were effective in detecting the onset of LBO ~20ms ahead of the event. The second approach is based on the spatiotemporal features in the primary zone of the combustor. A convolutional autoencoder is trained for feature extraction from the mass fraction of the OH ( $Y_{OH}$ ) data for all time-steps resulting in significant dimensionality reduction. The extracted features along with the ground truth labels are used to train the support vector machine (SVM) model for binary classification. The LBO indicator is defined as the output of the SVM model, 1 for unstable and 0 for stable. The LBO indicator stabilized to the value of 1 approximately 30 ms before complete blowout.

# 1. INTRODUCTION

The material presented in this chapter is obtained from the author's published papers [1-3] and the project progress report [4].

## 1.1 Motivation

Almost 84% of the total energy used today is coming from burning oil, gas and coal. Burning these fuels produce pollutants like CO<sub>2</sub>, NO<sub>x</sub>, soot, and particulate matter, etc. To limit global temperature just to 2°C rise would demand a 75% reduction in carbon emissions by 2050. The global population is expected to increase from today's 7.7 billion to 11.2 billion in 2100. On the other hand, the consumption of global fossil fuels is increasing and new reserves are difficult to find. What are our future energy options for a sustainable planet and economy? These questions motivated research on bio-fuels for future energy needs.

The material discussed in this section is obtained from the author's AIAA conference papers [1, 2]. Biofuels are offering promising solutions with an alternative to depleting fossil fuels. Biofuel can be obtained from various sources like bio-waste (forest waste, food waste, etc.), agricultural crops, marine algae, etc., After we convert these sources into fuel, it is very important for us to know how safe they are to handle, store and burn. Air-breathing combustion for energy and propulsion applications must remain viable for the foreseeable future [1]. It is important to understand the characteristics and combustion performance of biofuels (or alternative jet fuels) as well as petroleum-derived jet fuels to better understand how fundamental fuel properties impact applications, fuel efficiencies, and emissions [2]. While recognizing that the entire flight envelope is of interest in certifying fuels (which for the near term are likely to be blends of alternative and petroleum-derived stocks), lean blowout (LBO), high altitude relight (HAR), and cold start effects related to fuel properties have been identified as most important considerations i.e. as certification figures of merit [5]. Fit for purpose fuels (or drop-in) must meet these figures of merit as presently characterized for the ranges of petroleum-derived jet fuels presently in the field [2].

Laboratory experiments are time-consuming and very expensive. For example, the fuel qualification process currently takes about 5 years and costs \$4 million dollars. Therefore, developing a high fidelity high-performance computing methods for computer simulations for

virtual fuel experiments helps to reduce time and cost. These calculations help us to know exactly how these fuels burn under any given condition and allow us to accurately estimate how much heat energy produced and emissions like CO<sub>2</sub>, NO<sub>x</sub>, etc., Computer simulations also help to optimize the fuel performance and offer new avenues in lowering pollutants and developmental costs.

## 1.2 Selected fuels for the present study

The material presented in this section is obtained from the author’s AIAA conference papers [2, 3]. A-2 jet fuel represents the global norm found in the field for petroleum-derived jet fuels, while C-1 is a bio-derived alternative jet fuel composed almost entirely of only two specific iso-paraffins, 2,2,4,6,6-pentamethylheptane (iso dodecane) and iso-cetane [2]. The properties of A-2 and C-1 fuels are shown in Table 1.1 [2, 6-9].

Table 1.1. Comparison of properties for A-2 and C-1 fuels [2]

	Mol. Formula	Mol. Weight (kg/kmol)	Composition (% by mass)						H/C
			Cyclo-Paraffins	Iso-Paraffins	n-Paraffins	Aromatics	Alkenes	H	
A-2	C <sub>11.4</sub> H <sub>22.1</sub>	159	31.86	29.45	20.03	18.66	<0.001	13.84	1.91
C-1	C <sub>12.6</sub> H <sub>27.2</sub>	178	0.05	99.63	<0.001	<0.01	0.32	15.28	2.17

	DCN	$\left(\frac{F}{A}\right)_{\text{stoich}}$	Viscosity (mPa s)	Density kg/m <sup>3</sup>	$\Delta h_c \left(\frac{\text{MJ}}{\text{kg}}\right)$	10% Distillation Temp, K	90% Distillation Temp, K	Flash Point K	Freeze Point K
A-2	48.3	0.06803	1.17	803	43.1	449	517	321	222
C-1	17.1	0.06665	0.98	760	43.9	451	501	323	212

## 1.3 Spray combustion in gas turbine engines

The material presented in this section is obtained from the author’s AIAA conference paper [1]. A single cup combustor (“referee combustor”) shown in Figure 1.1 was designed at AFRL and used for experimental characterization of lean blow out (LBO) and ignition for a wide range of

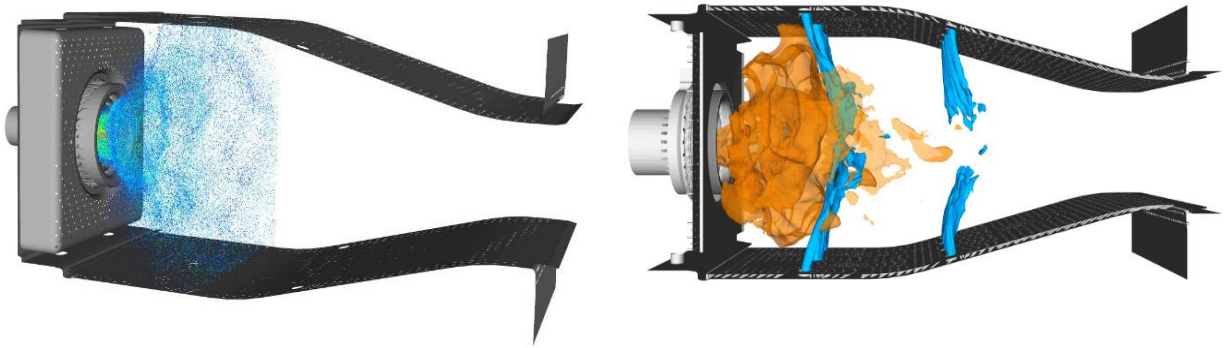


Figure 1.1 (a) Spray (b) Iso-surface of Temperature = 1800 K in the Referee gas turbine combustor

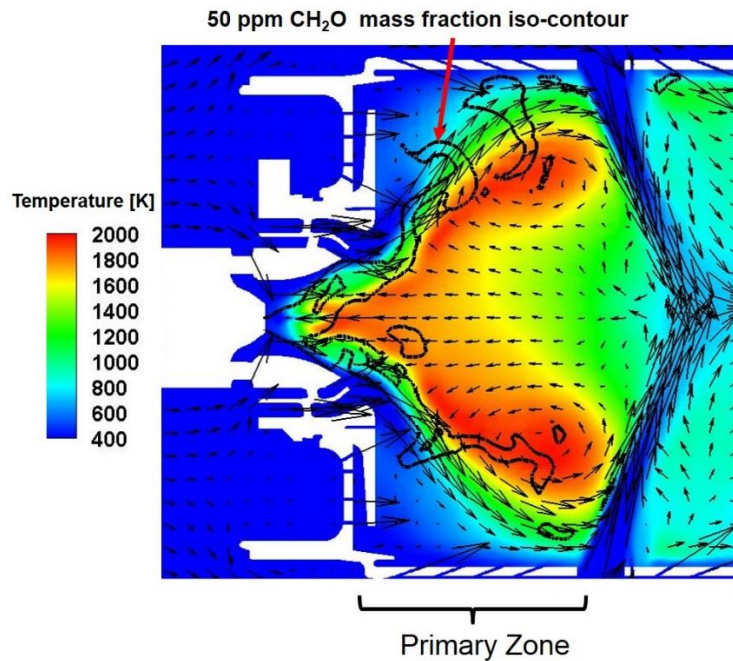


Figure 1.2. Complex flow field resulting from the multiple flow interactions with a spray inside referee combustor. (streamlines plotted on  $Z=0$  plane). HCHO (or  $\text{CH}_2\text{O}$ ) iso-contours are also shown with thick black lines.

fuels and operating conditions [1, 9-13]. These experiments are aimed at mimicking the geometry and operating conditions of a real gas turbine combustor. Air from the compressor outlet entering the combustor is split among multiple passages within and around the combustor as shown in Figure 1.2 [1]. The split flow consists of air going through different swirler passages for assisting atomization and mixing of the fuel and for stabilization of the flame. Air that bypasses the swirlers

is directed into the combustor through primary and secondary crossflow dilution holes. The remainder of the flow enters the main combustion chamber through numerous liner effusion and dome cooling holes. The effusion cooling holes play an important role in reducing thermal loads on the combustor liner. The resulting turbulent flow field evolves over a very complex geometry with flow passages that have a wide range of length scales. Moreover, the flow distribution through all of these flow passages affects the combustion process [1]. The details on the fuel injection, spray processes, evaporation, mixing, ignition, combustion, flame holding and fuel effects on the combustion stability can be found in the literature[14, 15].

#### **1.4 Artificial intelligence for online monitoring, diagnostics, and control**

The modern gas turbine engines are operated towards lean combustion to meet the stringent emission regulations. However, lean combustion can introduce instabilities to the flame which can eventually lead to the blowout. Lean blowout (LBO) can also have very severe consequences for aircraft engines and poses a major safety hazard. The lean blowout is one of the most important figures of merit for certification of a gas turbine engine combustor and aviation fuels [5] to ensure flight safety to avoid accidents like TACA Flight 110 in May 1988, Pinnacle Airlines Flight 3701 in October 2004, and British Airways Flight 38 in January 2008. The lean blowout limits prediction for a given fuel in a realistic combustor is a major challenge in the engine combustor design phase. This is due to the lack of a reliable model that accounts for complex physicochemical processes involved in the combustion phenomena [16]. Lean blowout is dominated by fuel kinetic effects. Hence, serious efforts are needed for online engine health monitoring, diagnostics, and prevention utilizing the state of the art artificial intelligence techniques for real-time control for prevention of catastrophic failures.

#### **1.5 Literature review**

##### **1.5.1 Experimental studies**

The literature review presented in this section is obtained from the author's AIAA conference paper [1-3]. The National Jet Fuel Combustion Program (NJFCP) utilizes a single cup combustor ("referee combustor") for experimental characterization of lean blow out (LBO) and ignition for a wide range of fuels and operating conditions [1, 3, 6, 10, 11, 13]. A suite of non-

reacting flow split experiments characterizes the airflow inside the combustor [1]. The flow rate measurements in the referee combustor and their computations for non-reacting conditions are available in references [1, 17-20]. Detailed spray and LBO measurements have been carried in the referee combustor for a wide range of fuels [2, 6, 7, 10, 13, 21, 22]. These datasets are used to benchmark and validate CFD models for realistic gas turbine combustors operating on a wide range of fuel properties. Three petroleum-derived jet fuels (A1-A3) and nine test fuels including several bio-derived jet fuels are considered to study the effects of physical and chemical properties.

The literature review presented in this section is obtained from the author's AIAA conference paper [1-3]. Stouffer et.al[6] examined the ignition and LBO characteristics with physical and chemical properties for 8 different fuels in the referee combustor and reported that fuels with low derived cetane number (DCN) blow-out more readily, i.e. at a more rich fueling limit than fuels with higher DCN [2]. Lieuwen et.al[23] reported experimental results on the impact of fuel composition on auto-ignition, flashback and blow-out processes in a syngas operated gas turbine combustor [2]. These studies revealed that fuel composition with higher hydrogen content led to LBO characteristics with blowout occurring at a leaner equivalence ratio. Stohr et. al [24] performed chemiluminescence imaging, OH-PLIF, and stereo PIV to understand the dynamics of the blowout process in partially premixed, swirl-stabilized methane combustion in a gas turbine combustor configuration at atmospheric pressure. Experimental results showed that the blowout process initially develops as extinction/re-ignition events at the flame root near the nozzle exit due to high strain rates and sustained flame extinction processes over a critical period of time leads to full extinction and blowout.

### **1.5.2 Computational modeling studies**

The literature presented in this section is obtained from the author's AIAA conference papers [1-3]. Multidimensional CFD modeling of such complex flows is challenging because of the complexity and the computational times involved. Therefore, simplifying assumptions are often used in computations of the flows. The combustor liner geometry is often simplified by ignoring the effusion holes altogether or by modeling the holes using mass inflow and outflow boundary conditions. Briones et.al [17, 18] have reported results of RANS calculations for the referee combustor flow field without film and effusion cooling holes but retaining their imprints on the liners. The modeling approach in these studies involves one dimensional adiabatic and

calorically perfect gas calculations of flows through the imprinted cooling holes. The approach requires *a priori* inputs of jet angle, orientation, and the coefficient of discharge ( $C_D$ ). The estimated flow rate defines the boundary conditions or the source terms (depending on the specifics of the numerical method) for the momentum at the inflow and the outflow ends of the effusion holes. Briones et.al [17, 18, 20, 25] with the support of non-reacting RANS simulations concluded that the methodology to estimate mass flow rates through several regions in a combustor is afflicted by three inherent systematic errors. One of the errors results from the differences in the orientation of the flow areas of individual passages on the combustor versus on the flow bench. The second error results from the differences in the local plenum pressures over the complex liner geometry. The third error accumulates from relatively small errors in the evaluation of the flows through individual liner cooling holes to a significant value. Gritsch et al. [26] measured the discharge coefficient ( $C_d$ ) for flow-through cylindrical holes at different orientations and inclinations with the cross-flow for a wide range of conditions.

The material presented in this section is obtained from the author's AIAA conference paper [2]. Esclapez et. al [11] reported LES simulations for A-2, C-5 and C-1 fuels to capture the fuel effects on the lean blow-out in the referee combustor using a low Mach number incompressible flow solver (VIDA) code. The Eddy viscosity-based WALE model was used for modeling the sub-grid-scale stress term for turbulence and a flamelet/progress variable (FPV) approach was used to model combustion. Hybrid chemistry-based chemical kinetic models [27-30] were employed to represent fuel chemistry for all three fuels. The results from their study at near LBO stable condition show that spray characteristics (SMD, axial velocity and radial velocity) and flame shape qualitatively agree with experimental data. Their LBO calculations suggested a more stable flame for C-1 than for A-2, with A-2 fuel blow-out occurring at an equivalence ratio of 0.090 while C-1 blow-out at an equivalence ratio of 0.085. Joshua et.al[31] performed LES simulations for A-2 and C-1 fuels in the referee combustor with adaptive mesh refinement and finite rate chemistry solver using Hychem skeletal mechanism [32]. The spray is represented as a single hollow cone with a specified SMD and Rosin-Rammler distribution and cone angle. These LES simulations showed blow-out for A-2 fuel at an equivalence ratio of 0.074 and for C-1 fuel at an equivalence ratio of 0.082.

### 1.5.3 Artificial intelligence for combustion applications

Machine learning has been successfully used in many areas like computer vision, speech recognition, natural language processing, traffic predictions, and online fraud detection, etc., But the application of machine learning for physics-driven problems is at the early stages and need more investigations to benefit from the state of art developments in this subject. Machine learning techniques have been recently used by a few researchers for combustion problems [33-46]. The problem of LBO has also been analyzed in the literature for simple laboratory-scale combustors. Akintayo. et. al. [40] used a high-speed video of swirl-stabilized gas turbine combustor. They trained a convolutional selective autoencoder model to reconstruct the input image if the flame was stable and output a black image if the flame was unstable. The authors have defined the instability metric based on the similarity between the input image and the corresponding output of the convolutional autoencoder. To identify the instability signature in the time domain, Sarkar et. al. [41] trained a Deep Belief Network (DBN) with stable and unstable flame images for a combustor. The output of the DBN was then fed to Symbolic Time Series Analysis (STSA) model followed by a D-Markov model. Ghosal et. al. [42] applied the Dynamic Mode Decomposition (DMD) and its sparsity promoting variant (DMDSP) to define instability metrics. Prediction of combustion instability in a swirl-stabilized combustor has also been studied using the chemiluminescence and pressure sensor data [43] by applying STSA and xD-Markov model. Support Vector Machine (SVM), a machine learning algorithm, was then used to predict the state of the combustion – nominal, impending blowout or progressive blowout.

Janakiraman et. al. [44] developed an online learning model based on Extreme Learning Machines (ELM) for a Homogeneous Charge Compression (HCCI) engine. ELM is a neural network with a single hidden layer and the parameters connecting the input layer to the hidden layer are randomly assigned. This helps in reducing the time required for training the model which is a crucial component of online learning. Prediction of heat output based on the images of the flame has also been studied with the prediction of up to 28 minutes in the future [45]. Application of machine learning to classify flow features in computational fluid dynamics (CFD) simulation has also been studied [46] using the sliding window approach followed by Convolutional Neural Network (CNN) based classifier.

Previous attempts of using machine learning for LBO identification have involved high-speed images, chemiluminescence data or pressure sensor data in simple laboratory type gas

turbine combustors. However, data sets required for training and validation of the machine learning algorithms for realistic engine combustor configurations is limited due to difficulties with experimental diagnostic methods to obtain the comprehensive flame data. The high-fidelity reacting large eddy simulations of realistic gas turbine engine combustors under engine relevant conditions can provide greater insights into events leading to LBO. The machine learning algorithms trained based on the high fidelity simulation data has several advantages over the existing simplistic data sets (1) accounts for the geometry induced flow complexity in the combustor, (2) accounts for the amount of fuel/air participation in the combustion resulting from complex multiple jets interactions and with spray in the primary zone (3) accounts for different time scales involved in the liquid-fueled combustion etc., Machine learning algorithms can also be used for identifying the undesirable events during the combustor operation in the flight envelope for early warning to prevent major accidents.

## **1.6 Research objectives**

The objective of the research is to develop a computational methodology with the LES turbulence model, automatic meshing, and adaptive mesh refinement for predicting the fuel sensitivity to combustion characteristics in a realistic gas turbine combustor under engine relevant conditions [1-3]. The specific objectives of the present work are summarized below:

- (1) application of automatic mesh generation with adaptive mesh refinement (AMR), all effusion holes resolved and gridded
- (2) model the spray from hybrid airblast injector as a multi-ring injection for spray representation in CFD with boundary conditions derived from PDPA measurements
- (3) evaluate the sensitivity of HyChem and compact kinetic models on LBO
- (4) evaluate the sensitivity of different combustion models on LBO
- (5) identify the global markers for LBO
- (6) establish fundamental insights into the combustion process during LBO for different fuels
- (7) understand the fuel composition effects on the lean blowout limits
- (8) develop robust machine learning models for early identification of the onset of the lean blowout.

## **1.7 Structure of the report**

The structure of the remaining thesis document is as follows: computational methodology is discussed in Chapter 2 followed by the validation in Chapter 3. Non-reacting simulations of referee combustor for flow splits estimation and comparison with experiments is presented in chapter 4. The lean blowout computation with different kinetic models and flame structure analysis is reported in chapter 5. The proposed machine learning model for the early detection of LBO onset is discussed in chapter 6. The important conclusions of this work are summarized in chapter 7 with recommendations for future research work.

## 2. COMPUTATIONAL METHODOLOGY

The details of the computational methodology for simulating the spray combustion in a realistic gas turbine combustor are discussed in this chapter. The part of the material presented in this chapter is obtained from the author's papers [1-3, 47-49].

### 2.1 Governing equations

The material discussed in this section is obtained from the author's AIAA conference paper [3]. The compressible form of the Favre filtered Navier-Stokes equations after LES decomposition is solved on a non-staggered, collocated computational grid along with the species transport equations, energy equation and the equation of state [1-3, 50].

Continuity:

$$\frac{\partial \bar{\rho}}{\partial t} + \frac{\partial \bar{\rho} \tilde{u}_j}{\partial x_j} = S \quad (1)$$

Conservation of Momentum:

$$\frac{\partial \bar{\rho} \tilde{u}_i}{\partial t} + \frac{\partial \bar{\rho} \tilde{u}_i \tilde{u}_j}{\partial x_j} = -\frac{\partial \bar{P}}{\partial x_i} + \frac{\partial \bar{\sigma}_{ij}}{\partial x_j} - \frac{\partial \tau_{ij}}{\partial x_j} \quad (2)$$

Species Continuity:

$$\frac{\partial \bar{\rho} \tilde{Y}_m}{\partial t} + \frac{\partial \bar{\rho} \tilde{u}_j \tilde{Y}_m}{\partial x_j} = \frac{\partial}{\partial x_j} \left( \bar{\rho} (D + D_t) \frac{\partial \tilde{Y}_m}{\partial x_j} \right) + \bar{\omega}_m, \quad m = 1, 2, 3, \dots, n \quad (3)$$

Conservation of Energy:

$$\begin{aligned} \frac{\partial \bar{\rho} \tilde{e}}{\partial t} + \frac{\partial \bar{\rho} \tilde{u}_j \tilde{e}}{\partial x_j} &= -\bar{P} \frac{\partial \tilde{u}_j}{\partial x_j} + \bar{\sigma}_{ij} \frac{\partial \tilde{u}_i}{\partial x_j} + \frac{\partial}{\partial x_j} \left( K \frac{\partial \tilde{T}}{\partial x_j} \right) + \frac{\partial}{\partial x_j} \left( \bar{\rho} (D + D_t) \sum_m \tilde{h}_m \frac{\partial \tilde{Y}_m}{\partial x_j} \right) + S^e, \\ &= 1, \dots, n \end{aligned} \quad (4)$$

The material discussed in this section is obtained from the author's AIAA conference paper [3]. The Redlich-Kwong equation of state is used to couple density, pressure, and temperature in the present compressible flow solver [3, 50]. The sub-grid stress tensor term,  $\tau_{ij} = \bar{\rho} (\tilde{u}_i \tilde{u}_j - \tilde{u}_i \tilde{u}_j)$  in the momentum equation is modeled using a non-viscosity based one equation sub-grid scale model to obtain the closure [3, 50-52]. The sub-grid stress tensor is related to the Leonard stress

tensor [53] and sub-grid kinetic energy as  $\tau_{ij} = 2k\bar{\rho} \frac{L_{ij}}{L_{kk}}$ , where,  $k = \frac{1}{2}(\widetilde{u_i u_i} - \widetilde{u_i} \widetilde{u_i})$ , is the sub-grid kinetic energy and is estimated by solving the following transport equation,

$$\frac{\partial \bar{\rho} k}{\partial t} + \frac{\partial \bar{\rho} \widetilde{u_j k}}{\partial x_j} = \frac{\partial}{\partial x_j} \left( \frac{\mu}{Pr_{sgs}} \frac{\partial k}{\partial x_j} \right) + \tau_{ij} \overline{S_{ij}} - \rho \varepsilon \quad (5)$$

and, the sub-grid dissipation rate is calculated as ,  $\varepsilon = C_\varepsilon \frac{k^{\frac{3}{2}}}{\Delta}$ , where  $C_\varepsilon = 1.0$  and  $\Delta$  is the grid size.

The material discussed in this section is obtained from the author's AIAA conference paper [3]. The Leonard stress tensor,  $L_{ij} = \widetilde{\widetilde{u_i u_j}} - \widetilde{u_i} \widetilde{u_j}$  here  $\widehat{\cdot}$  is called the test filter and it is calculated from the center cell and neighboring cells [3]. The test filter is larger than the first level filter i.e., grid size. This sub-grid scale modeling procedure is less dissipative on coarser grids compared to the viscosity based sub-grid scale models. The filtered reaction rate  $\overline{\omega_m}$  in Eq.3 is estimated using the Arrhenius law and the sub-grid level reaction rates are treated using a well-stirred reactor (WSR) model. The use of WSR with appropriate grid resolution for modeling the sub-grid turbulence chemistry interactions (TCI) in laboratory burners, jet flames, and engines under relevant conditions has been successfully reported in the literature [2, 3, 48, 54-65].

The flamelet generated manifold (FGM) combustion model also investigated in the present study with adaptive mesh refinement for computing the fuel sensitivity to lean blowout. The FGM model has been successfully employed in the literature for predicting phenomena like flame extinction and re-ignition in spray flames [66-71]. A compact kinetic mechanism based on fuel surrogates is used for representing chemical reactions [2]. The FGM model accounts for the effects of turbulence on the reaction rates via a joint PDF of mixture fraction, mixture fraction variance, and reaction progress variable. The more details on the FGM model formulation and implementation can be found in the CONVERGE documentation [50].

## 2.2 Lagrangian description for the spray

The equations of the droplet position ( $x_p$ ), velocity ( $u_p$ ), and temperature ( $T_p$ ) are given by the following equations. The particles are assumed to be spherical.

$$\begin{aligned} \frac{dx_p}{dt} &= u_p \\ m_p \frac{du_p}{dt} &= F \end{aligned}$$

$$m_p C_p \frac{dT_p}{dt} = Q$$

$$\frac{dm_p}{dt} = -\dot{m}_{\text{evap}}$$

where

t = time (s)

$m_p$  = mass of the parcel (kg)

F = summation of all the forces acting on the parcel (N)

$C_p$  = specific heat at constant pressure (J/kg-K)

Q = net rate of heat transfer to the parcel (W)

$\dot{m}_{\text{evap}}$  = parcel evaporation rate (kg/s)

### 2.3 Droplet evaporation model

The Frossling correlation is employed to calculate the drop evaporation rates [4, 72, 73]. The time rate of change of droplet radius is given by the following expression as a function of the laminar mass diffusivity of the fuel vapor, a mass transfer number, and a Sherwood number [50].

$$\frac{dr_0}{dt} = -\frac{\alpha_{\text{spray}} \rho_{\text{gas}} D}{2\rho_1 r_0} B_d \text{Sh}_d$$

where,

$$B_d = \frac{Y_1^* - Y_1}{1 - Y_1^*}$$

$$Y_1^* = \frac{M_{\text{C}_n\text{H}_{2m}}}{M_{\text{C}_n\text{H}_{2m}} + M_{\text{Mix}} \left( \frac{P_{\text{gas}}}{p_v} - 1 \right)}$$

$\text{Sh}_d$  = Sherwood number, and is calculated using the following expression

$$\text{Sh}_d = \left( 2.0 + 0.6 \text{Re}_d^{\frac{1}{2}} \text{Sc}^{\frac{1}{3}} \right) \frac{\ln(1+B_d)}{B_d}$$

$\text{Re}_d$  = Reynolds number based on the relative velocity

Sc = Schmidt number of air and is calculated as

$$\text{Sc} = \frac{\mu_{\text{air}}}{\rho_{\text{gas}} D}$$

$$\rho_{\text{gas}} D = 1.293 D_0 \left( \frac{\hat{T}}{273} \right)^{n_0-1}$$

$\alpha_{\text{spray}}$  = scaling factor for the mass transfer coefficient

$D$  = mass diffusivity of liquid vapor in the air

$Y_1^*$  = vapor mass fraction at the drop's surface

$Y_1$  = vapor mass fraction

$M_{\text{Mix}}$  = molecular weight of the mixture

$d$  = drop diameter

$p_{\text{gas}}$  = gas pressure

$p_v$  = vapor pressure at the droplet temperature

$\rho_{\text{gas}}$  = gas density

$\rho_l$  = liquid density

$T_{\text{gas}}$  = gas temperature

$T_d$  = drop temperature

$\mu_{\text{air}}$  = air viscosity and is calculated at the temperature  $\hat{T}$

$$\hat{T} = \frac{T_{\text{gas}} + 2T_d}{3}$$

$D_0, n_0$  = Model constants derived from experiments

In the present work,  $D_0=4.16\text{e-}06$  kg/m-s and  $n_0=1.6$  is used for the single droplet evaporation study and referee combustor lean blow-out simulations.

## 2.4 Secondary breakup model

The secondary droplet atomization is modeled following the work of O'Rourke and Amsden[73]. This model is based on Taylor's analogy between the spring-mass system and distorting-oscillating droplet [50]. The breakup of the radius is calculated as per the following expression,

$$r = \frac{r_0}{1 + \frac{8K}{20} y^2 + \frac{\rho_l r_0^3}{\sigma} \dot{y}^2 \left( \frac{6K-5}{120} \right)}$$

More details on the mathematical description of this model can be found in [50].

## 2.5 Dynamic drag model

The drag coefficient is calculated as

$$C_D = C_{D,\text{sphere}}(1 + 2.632y)$$
$$C_{D,\text{sphere}} = \begin{cases} 0.424 & \text{Re} > 1000 \\ \frac{24}{\text{Re}} \left(1 + \frac{1}{6} \text{Re}^{\frac{2}{3}}\right) & \text{Re} \leq 1000 \end{cases}$$

where  $y$  is the droplet distortion calculated with the TAB model [50]. More details on this model are given elsewhere [72-74].

## 2.6 Droplet dispersion model

The effect of turbulent flow on parcels is accounted for by introducing the fluctuating velocity to the gas velocity. This sub-grid fluctuating velocity is based on the first term in the Taylor series expansion given by the following expression.

$$u'_i = 2(1 - 2Y)C_{\text{les}} \frac{dx^2}{24} \frac{\partial^2 \tilde{u}_i}{\partial x_j \partial x_j}$$

A detailed description of this model is given in [50].

## 2.7 Chemical kinetic models

The material discussed in this section is obtained from the author's AIAA conference paper [3]. Detailed chemical kinetics is a pre-requisite for high fidelity combustion simulations in order to capture the complex reaction pathways like strong chain branching, weak chain branching and chain termination at different operating pressures and temperatures [3]. Mechanisms with high-temperature chemistry are important for simulating stable flames and their propagation while those with low-temperature chemistry are crucial for simulating auto-ignition. The computational cost depends on the number of species in the mechanism and this makes detailed mechanism having hundreds of species prohibitively expensive for high fidelity simulations on fine mesh resolutions. The numerical computations employing hundreds of species may cause chemical stiffness due to the non-linearly coupled chemical reactions with a wide range of timescales [3]. Hence, reduced mechanisms are developed with varying levels of kinetic details to reduce the computational cost, stiffness and storage memory requirements with adequate accuracy in the calculations. The hybrid chemistry approach [27-30] developed for a real, multi-component fuel based on several lumped

reaction steps obtained from shock tube experiments for modeling fuel pyrolysis and the foundational fuel chemistry from USC Mech II for the oxidation of the pyrolysis products. This approach is employed for developing detailed mechanisms for both conventional (A-category) and alternative fuels (C-category) tested in the NJFCP program. The detailed HyChem model for conventional Jet-A fuel (A-2) and an alternative fuel (C-1) chosen for the present study contains 119 species with 843 reactions. Yang et al [32] employed a two-stage mechanism reduction technique using a directed relation graph (DRG), sensitivity analysis and timescale reduction using the linearized quasi-steady-state approximations and obtained skeletal and reduced versions of HyChem mechanisms for A-2 and C-1 fuels. The skeletal mechanism contains 41 species with 202 reactions for A-2 fuel and 34 species with 182 reactions for C-1 fuel. The reduced mechanism contains 31 species for A-2 fuel and 28 species for C-1 fuel. The compact chemical kinetic models [2] are developed based upon combustion property target surrogate mixture emulation [75-78] for A-2 and C-1 fuels [78, 79].

Table 2.1. The number of species in the kinetic models for A-2 and C-1 fuels.

	<b>A-2</b>	<b>C-1</b>
HyChem Detailed	119	119
HyChem Skeletal	41	34
HyChem Reduced	31	28
Dryer's Compact	41	35

## **2.8 Computational domain, boundary conditions, and meshing strategy**

The material discussed in this section is obtained from the author's AIAA conference paper [3] and more details on the computational domain, boundary conditions, and meshing strategy are given in [1-4]. The computational domain of the referee combustor is shown in Figure 2.1. A full-scale combustor is housed in a rectangular box of size 353.07 mm x 101.6 mm is chosen for the present study. The flow-through swirler passages, primary and secondary dilution holes, effusion

and film cooling holes are resolved in the present study. The airflow through window effusion and aft slot cooling holes located near the exit of the combustor does not participate in the combustion process and hence this flow is excluded in the present work. The total air mass flow rate of 338.7 g/s at temperature 394 K is specified at the inlet with a static pressure outlet boundary condition. The adiabatic condition is imposed on all the combustor walls. Spray boundary conditions are discussed in the next section.

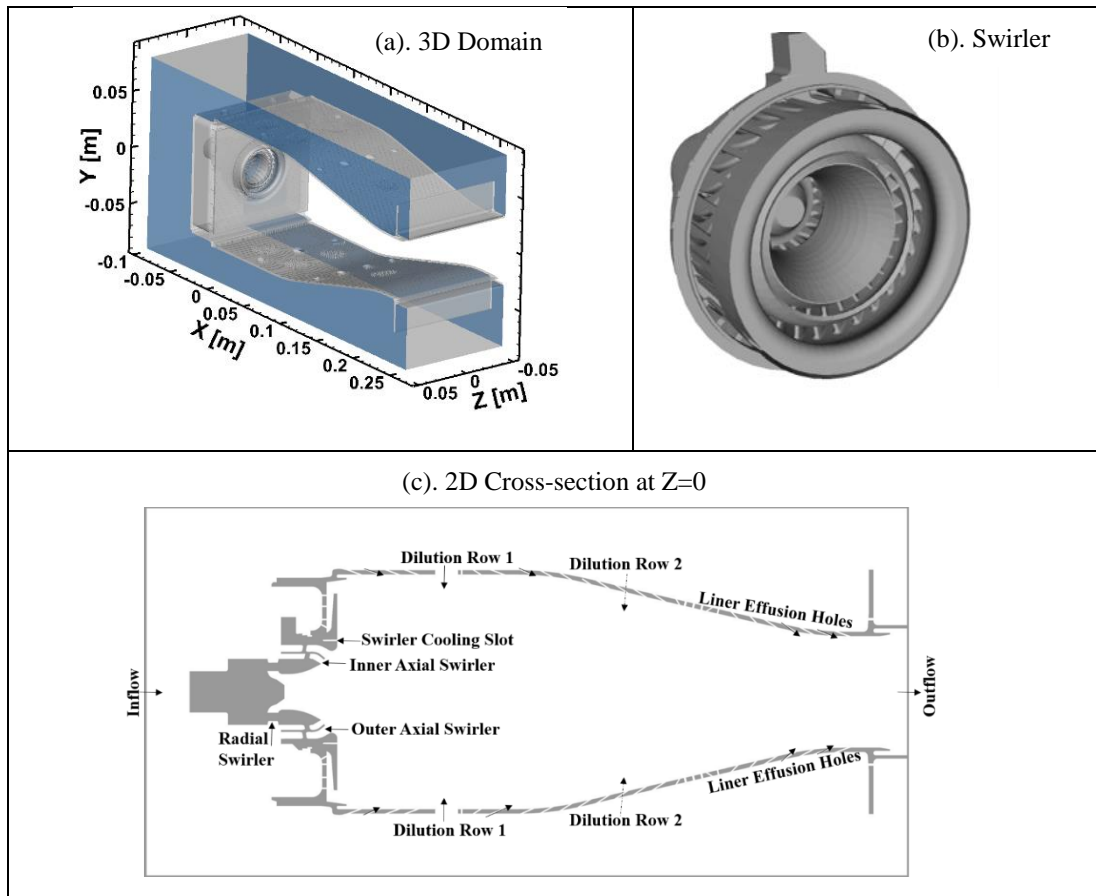


Figure 2.1. The computational domain of referee combustor (left), magnified view of the hybrid airblast swirler (right), and 2D cross-section at  $Z=0$  (bottom) [3, 4].

The material discussed in this section is obtained from the author's AIAA conference paper [1, 3]. A modified Cartesian cut cell method is employed in the present work that allows the use of orthogonal grids by eliminating the need for the grid to be morphed with the geometry while precisely capturing the boundary shapes [50, 80-83]. The computational mesh is generated and optimized on the fly with the Cartesian cut cell method and adaptive mesh refinement (AMR)

techniques for this complex realistic gas turbine combustor with the swirler, dilution holes, film cooling holes and thousands of effusion-cooling holes [1-4]. The AMR algorithm refines the mesh during the runtime based on the second gradients of velocity and temperature. Mesh refinement is added in regions of steep gradients while keeping the mesh coarser in regions of weaker gradients [1-3, 47-49, 80, 84]. The adaptive mesh refinement helps in optimal use of cells and in minimization of the cell count for a given accuracy in capturing the essential features of the flow. Mesh generation is completely automated with the flexibility of having mesh distribution as a function of maximum cell size (base size). The relative mesh size in different regions can be set a priori in this method to create fine mesh in the regions of importance, for example, near the injector and primary zones, effusion and film cooling holes, etc., The fine mesh embedded in those regions is kept through the entire flow simulations. To save computational time, extra mesh resolution can be added during the run time based on local temperature and velocity gradients using adaptive mesh refinement techniques. The maximum number of cells is specified to limit the number of embedded cells with adaptive mesh refinement.

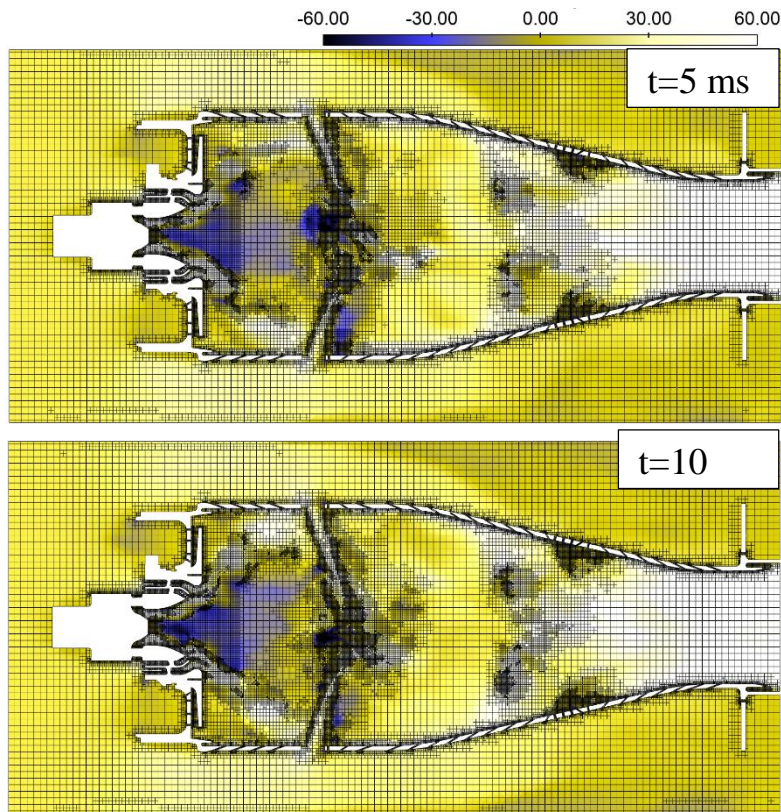


Figure 2.2. Computational grid for a reacting case with AMR at  $t= 5$  ms (top) and  $t= 10$  ms (bottom). Contours are colored with axial velocity (m/s) [3, 4].

The material discussed in this section is obtained from the author's AIAA conference paper [3]. The mesh resolution required to compute the mass flow rates under non-reacting conditions through the multi-passage air-blast swirler (while all other flow passages are closed) is determined using the comparison of RANS and LES computational results with experimental data from Refs. [7-10]. The present work is based on the meshing approach discussed in [1] for the treatment of effusion cooling flows through tiny inclined holes. For the gas turbine combustor simulations, the mesh is refined in shear layers, flame front, recirculation regions and near the jets as shown for a reacting case in Figure 2.2. A maximum cell size of 3 mm and a minimum cell size of 0.375 mm near the injector region and in the effusion and film cooling holes resulting in a total count of 10 million cells are used for the present LBO calculations[1-3]. The mesh sensitivity and resolved kinetic energy distribution on the chosen mesh resolution is discussed in the Chapter 5.

## 2.9 Spray boundary conditions

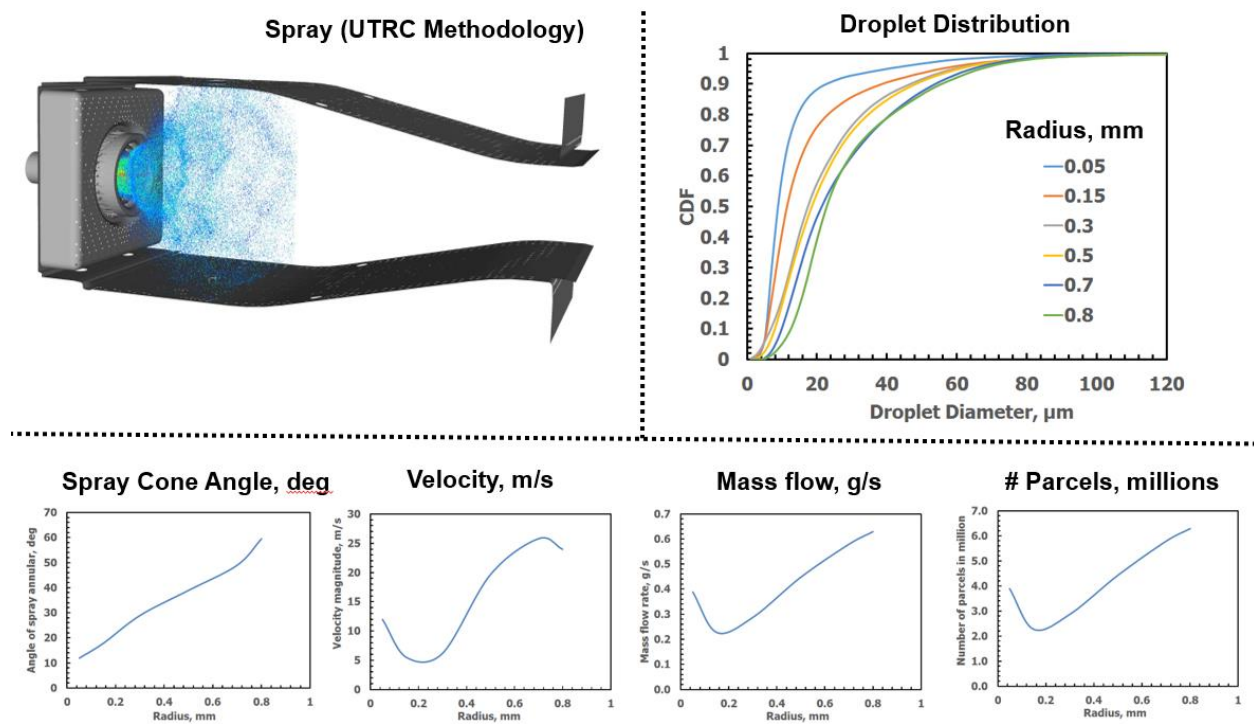


Figure 2.3. Spray boundary conditions

The material discussed in this section is obtained from the author's AIAA conference paper [3]. The spray boundary conditions (droplet diameter, average velocity, and cone angle) specified

at 2 mm from the nozzle exit in the present work are based on the UTRC approach using non-reacting PDPA measurements [2, 3, 21, 85, 86] at 25.4 mm from the deflector plate. The nozzle inlet is represented by six ring nozzles, each having a different CDF distribution for droplet diameter as shown in Figure 2.3.

## 2.10 Numerics

The material discussed in this section is obtained from the author's AIAA conference paper [3]. The details on the CFD numerics are given in [1-3]. The pressure-velocity coupling is obtained by using modified Pressure Implicit with Splitting of Operator (PISO) algorithm [87] based on the Predictor-Corrector method. A Rhie-Chow interpolation scheme [88] is used to avoid the spurious oscillations in the pressure-velocity solution resulting from the use of collocated quantities (cell-centered values). The governing conservation equations are discretized using a second-order accurate central differencing scheme for spatial discretization and a fully implicit first-order accurate time integration scheme in order to maintain numerical stability. The global time step size is calculated during each computational cycle based on the maximum convection CFL number, the speed of sound CFL number, and the diffusive CFL number, maximum time step for the spray and the chemical time scale. A multi-zone model along with AMR, a fast iterative ODE solver CVODES accelerate the detailed chemistry calculations. The multi-zone approach in the present work groups computational cells with similar temperatures ( $T$ ) and equivalence ratios ( $\phi$ ) into separate bins, with specified limits on these two variables. This multi-zone binning concept was first introduced by Aceves et al. [89] and improved by others [90]. After clustering into bins of similar temperature and equivalence ratio, the zone-average values of species concentrations and temperature are used to compute the reaction rates for each zone (rather than for every individual cell). The zonal temperature and mass fractions are then remapped onto the cells, such that the temperature and composition non-uniformities are preserved. Detailed descriptions of chemistry acceleration for combustion calculations with and without the multi-zone model can be found in Raju et al [90]. The calculations are run in parallel on distributed memory machines using the Message Passing Interface (MPI). Automatic domain decomposition allows for efficient load balancing as the adaptive mesh refinement changes the distribution of the cells significantly. The LES simulations are performed using the Broadwell nodes on the NASA Pleiades supercomputer.

Each Broadwell node contains two 14 core E5-2680v4 (2.4 GHz) processors and 128 GB of memory.

The material discussed in this section is obtained from the author's AIAA conference paper [3]. Reacting flow simulations are carried out for referee combustor with liquid fuels using the Eulerian-Lagrangian approach with the large eddy simulation turbulence model using the CONVERGE code [1-3, 50, 80]. Combustion is treated using finite rate chemistry with Compact and HyChem kinetic models and laminar closure for turbulence-chemistry interactions (well-stirred reactor assumption). Flamelet generated manifold combustion model is also utilized for evaluating the flamelet approach on capturing the fuel sensitivity to lean blowout.

### 3. VALIDATION WITH EXPERIMENTS

The adaptive mesh refinement based computational methodology and grid sensitivity for combustion calculations are validated with laboratory flames for which detailed measurements are available in the literature. The velocity and temperature measurements are not available in the realistic gas turbine combustor employed in this research for detailed validation of the combustor flow field. The material presented in this chapter is obtained from the author's published papers [47-49].

#### 3.1 Test case 1: PARAT pilot stabilized flame

The material discussed in this section is obtained from the author's paper [49]. The details on the test case 1 are also given in [47, 49, 91]. Emissions regulations and depletion of fossil fuels have motivated research on developing fuel flexible, efficient, reliable and low emission engines for energy and propulsion applications [47, 49]. Lean premixed combustion with Exhaust Gas Recirculation (EGR) is a promising technique to reduce the NO<sub>x</sub> emissions and the CO<sub>2</sub> capture cost in power plants [92-94]. Mitsubishi Heavy Industries (MHI) demonstrated up to 40% NO<sub>x</sub> reduction using EGR for a lean premixed combustor at a fixed combustor outlet temperature of 1700°C [95]. The main challenges associated with EGR are flame instability and lean blowout [96]. Understanding the effects of EGR on premixed flame structure, operability and emissions is an important topic of research. Among many species in the exhaust, CO<sub>2</sub> is known to have a significant impact on the flame structure, stability and emissions [97-101]. According to the literature on laminar premixed flame studies [100, 101], CO<sub>2</sub> dilution can influence the flame structure through thermal, kinetic and transport effects. The kinetic effects are predominant in determining the flame stability limits for a gas turbine combustor.

The material discussed in this section is obtained from the author's paper [49]. Extensive experimental studies on premixed methane/air flames with CO<sub>2</sub> dilution have been reported in the literature because of an increased interest in combined power plants with EGR and CO<sub>2</sub> capture [47, 49]. Han *et.al* [102] reported temperature measurements using dual pump vibrational coherent anti-Stokes Raman scattering (CARS) and velocity profiles measurements near the nozzle exit using particle image velocimetry (PIV) in methane/air turbulent premixed flames with CO<sub>2</sub>

dilution. These experiments were carried out at atmospheric pressure and temperature. The thermal and transport effects were minimized by operating the flames nearly at constant Reynolds numbers, Lewis numbers, and adiabatic flame temperatures. Reynolds number is defined based on the nozzle exit diameter ( $d$ ), bulk velocity ( $U$ ), and mixture density ( $\rho$ ), and viscosity ( $\mu$ ). Lewis number is the ratio of thermal diffusivity to mass diffusivity of the mixture at the nozzle exit. One of the objectives of their study was to understand the kinetic effects associated with CO<sub>2</sub> dilution on the turbulent premixed flame structure. They observed that with increasing CO<sub>2</sub> dilution: (a) mean flame length increased, (b) turbulent burning velocity decreased while combustion intensity increased, (c) departure from the universal flame brush structure and (d) collapse of RMS vs mean temperature onto a single curve for all three conditions (0%, 5% and 10% CO<sub>2</sub> dilution). Han *et.al* [103] also investigated the turbulent flame structure and burning velocity through 9 kHz OH planar laser-induced fluorescence (PLIF) for identical test conditions as in Ref. [102]. The reduction in laminar flame speed with increasing CO<sub>2</sub> dilution resulted in a wider distribution of unburned reactant pockets in the flame. The authors observed that the consumption speed of the fine-scale unburned reactant pockets is higher than the unstretched laminar flame speed. The CO<sub>2</sub> dilution affected the flame surface density and the mean progress variable distribution in a consistent manner. Reuter *et.al* [97] performed OH planar laser-induced fluorescence measurements in methane/air flames with CO<sub>2</sub> dilution to study the kinetic, thermal and transport effects. Reuter *et al* also analyzed the relative importance between these effects on the turbulent burning velocity, flame surface density, flame wrinkling, and progress variable. Kobayashi *et.al* [104] investigated the effect of CO<sub>2</sub> dilution at elevated pressure (1 MPa) and temperature (573 K) in CH<sub>4</sub>/Air turbulent premixed flames using OH-PLIF measurements. Reported OH PLIF data were consistent with those shown in the literature. CO<sub>2</sub> dilution resulted in a decrease in turbulent burning velocity and an increase in the flame length. The mean volume of the turbulent flame region increased with CO<sub>2</sub> dilution because of the reduced scales of wrinkling and reduced local burning velocities. Kobayashi and coworkers [104, 105] also observed that CO<sub>2</sub> dilution can suppress combustion instabilities possibly because of the enlarged turbulent flame brush.

The material discussed in this section is obtained from the author's paper [49]. The literature review on CFD studies for premixed flames is also given in [47, 49, 91]. There is extensive literature on large eddy simulations of turbulent premixed jet flames with a co-flow and hot gas as a pilot [106-112]. Large eddy simulations (LES) of lean premixed combustion with EGR

are needed to gain an improved fundamental understanding of the physicochemical processes affecting the flame structure, the combustion stability, and the pollutant formation. Comparisons of the results of the LES models of lean premixed combustion vis à vis the structure, stability, and emissions with experimental data are important for assessing their predictive capabilities. Duwig *et.al* [54] reported LES simulations of premixed jet flames stabilized by a pilot using finite rate chemistry and LES turbulence model. The authors found that a skeletal mechanism of 20 species showed good agreement with experimental data for velocity, temperature, and species mass fractions. LES has the potential to be used for designing low emission gas turbine engine combustors with EGR to reduce cost and time during the industrial development cycles. Validation of LES results using detailed experimental data aimed at gaining a fundamental understanding of chemical kinetics effects in a turbulent environment consisting of non-premixed regions, changes in fuel hydrogen content, and changes in dry EGR based CO<sub>2</sub> concentrations is a logical next step. The experiments by Han *et.al* [102] utilized for LES simulations in the present study are unique because these were designed to study the kinetic effects of CO<sub>2</sub> on the flame structure by matching the Reynolds numbers, Lewis numbers and adiabatic flame temperatures.

The material discussed in this section is obtained from the author's paper [49]. The overall objective of this study is to conduct LES simulations of H<sub>2</sub> piloted methane/air lean premixed turbulent flames stabilized on the PARAT burner with CO<sub>2</sub> dilution [47, 49]. The specific objectives are:

- (1) compare LES results with measurements of mean and RMS profiles of temperature and velocity;
- (2) utilize the species and temperature distributions to identify the flame structure; and
- (3) study the effects of non-equilibrium chemistry on the species distributions.

### **3.1.1 Non-reacting simulation**

The material discussed in this section is obtained from the author's AIAA conference paper [47]. The computational domain for the non-reacting flow simulations is shown in Figure 3.1. This model consists of all components of the burner as it is in the test hardware. The bluff body, the turbulence generation plates and the annular gap for pilot hydrogen flow are all simulated [47]. The domain for the free jet region is 60D in the axial direction and 32D in the radial direction. Mass flow boundary conditions with a specified mass flow rate normal to the boundaries are used

at the air inlet, fuel inlet, and pilot inlet boundaries. No-slip and adiabatic boundary conditions are used for all walls. Pressure boundary conditions with atmospheric pressure are specified along all open boundaries surrounding the free jet. An outflow boundary condition with atmospheric pressure is used for the outlet at the top. A computational grid consisting of 8 million cells is used for non-reacting simulations and the mesh on  $z = 0$  plane is shown in Figure 3.2.

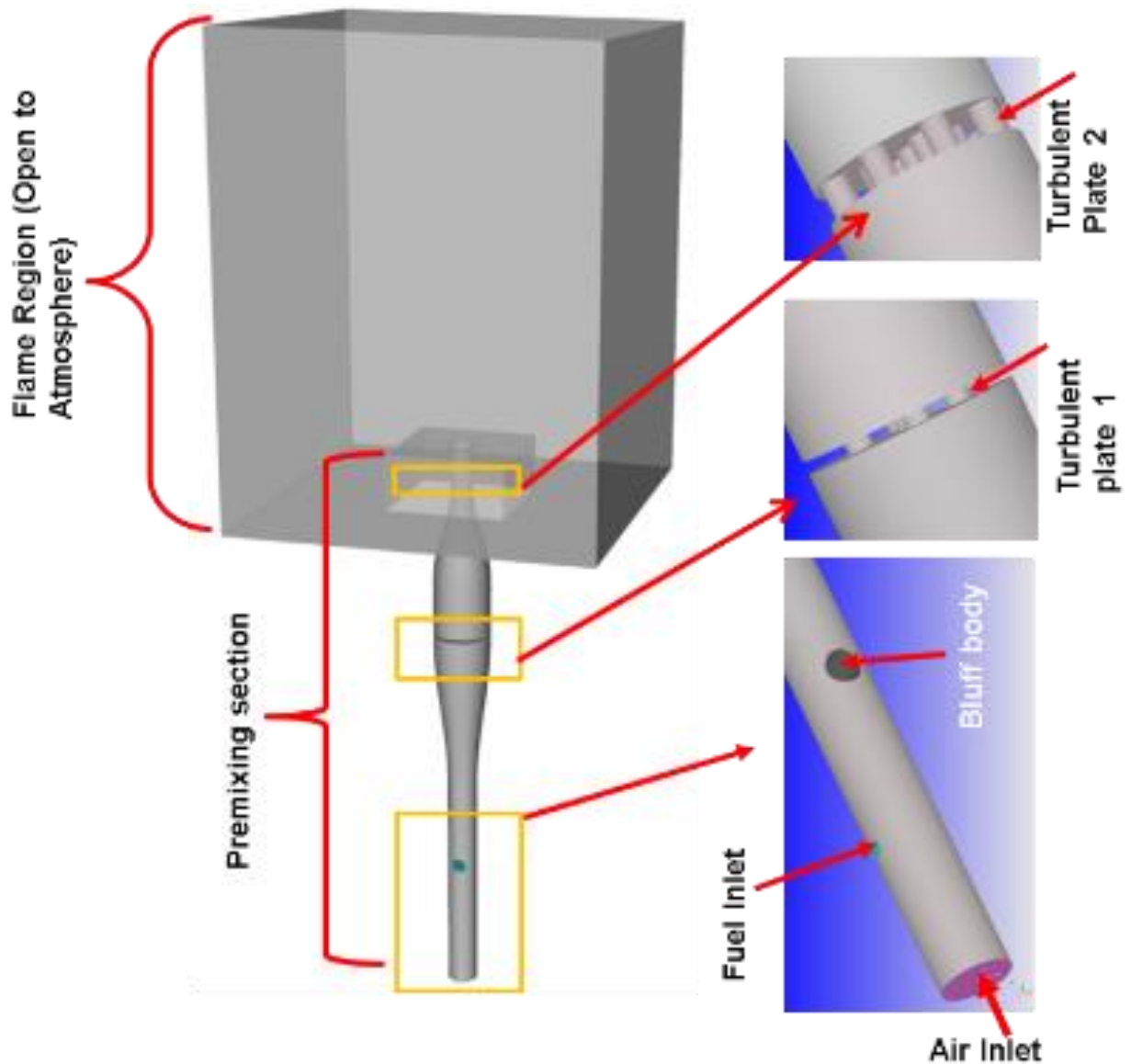


Figure 3.1. Computational domain for Non-Reacting simulations[47]

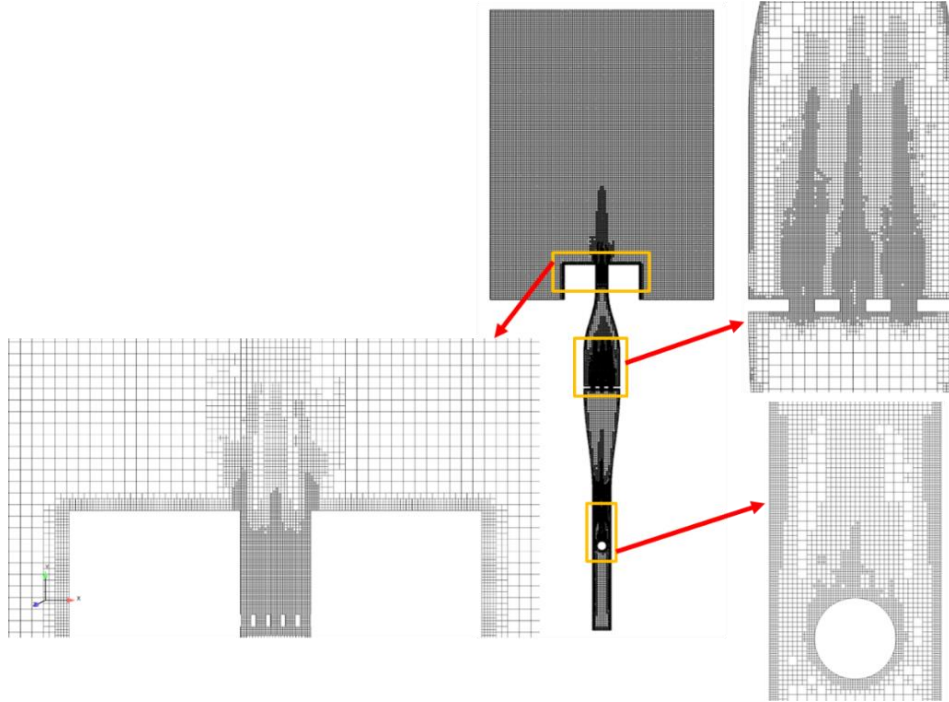


Figure 3.2. The mesh and three magnified x-y plane sections of it at  $z=0$  for non-reacting flow simulations with adaptation based on the instantaneous velocity gradients[47]

The material discussed in this section is obtained from the author's AIAA conference paper [47]. The contours of axial velocity on  $z=0$  (burner center plane) from non-reacting RANS simulations are shown in Figure 3.3[47]. These contours show the wake region behind the cylindrical bluff body, deceleration of the flow in the divergent section, flow acceleration through small holes in both the turbulence generation plates and in the converging section. A quantitative comparison of axial velocity with hot wire anemometer measurements is shown in Figure 3.4 at  $y/d=1, 2, 3, 4$  and  $5$ . The current results with the RNG  $k-\epsilon$  model match reasonably well with the experimental data at all five locations. The presence of a second turbulence generation plate at 30 mm upstream the nozzle exit induces a central peak in the velocity profile at the nozzle exit as observed from both the measurements and the computations. The reduced mass flow through holes near the wall due to the displacement boundary layer effects leading to more mass flow and momentum through the center holes results in a unique profile captured by the present computations. The velocity and turbulence kinetic energy profile at the nozzle exit are extracted from the non-reacting simulation and used as inlet boundary condition for the reacting LES simulations.

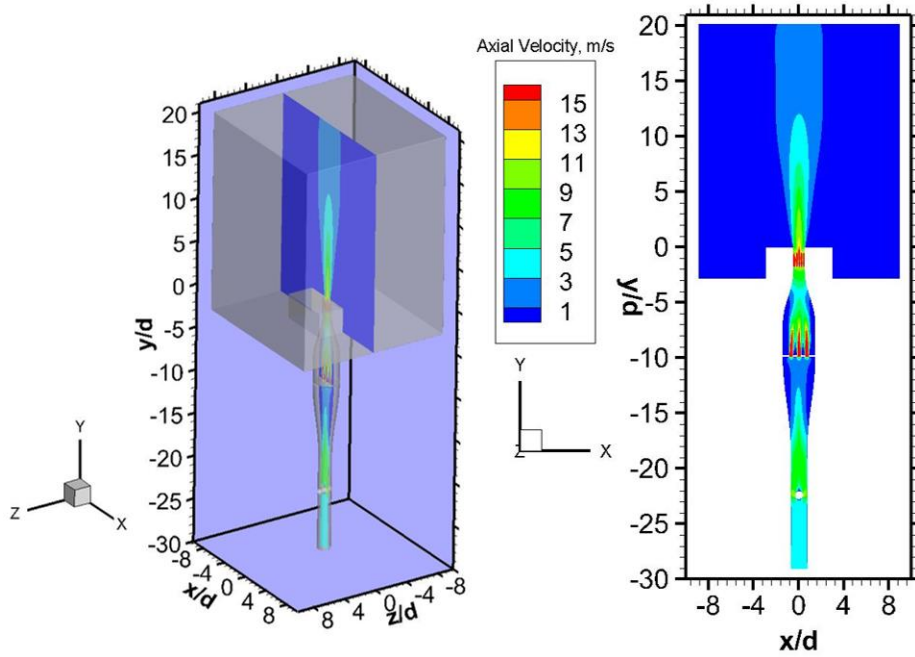


Figure 3.3. Contours of Axial velocity profile on the center plane of the burner[47]

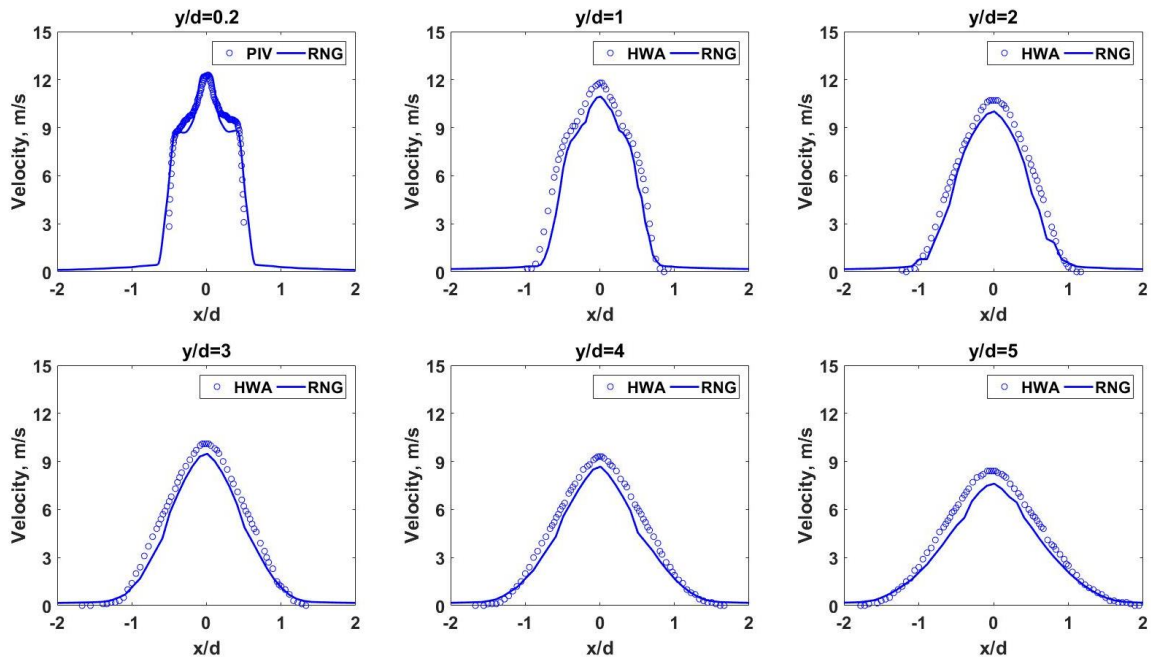


Figure 3.4. Radial profiles of axial velocity [47]

### 3.1.2 Reacting simulation

The material discussed in this section is obtained from the author's AIAA conference paper [47]. The premixing section is excluded in the reacting LES simulations to enable using very fine mesh in the jet flame regions and to save computational time [47, 49]. A computational domain of size 60D in the axial direction and 32D in the cross-stream direction is considered for reacting flow and included a small portion of the burner and pilot hydrogen inlet. The mesh is adapted with 5 levels of refinement based on local instantaneous temperature and velocity gradients to resolve the flame structure in the present LES simulations. Two different meshes with total cell count of 10 million (minimum cell size 0.3125 mm) and 15 million (minimum cell size 0.25 mm) were evaluated to study the sensitivity of prediction to the mesh resolution. A sample of mesh refinement added by AMR is shown in Figure 3.5. It is clearly seen that grid resolution is automatically added to resolve the complex flow behavior in regions near shear layer and flame front while leaving the remaining grid coarse to minimize simulation time.

The material discussed in this section is obtained from the author's AIAA conference paper [47]. The mean velocity contours from reacting LES simulations are shown in Figure 3.6 [47, 49]. The burner and the pilot flame profiles are marked with a white rectangle at the bottom and the mean velocity contours with the maximum represented by the burner exit velocity (red) and the minimum represented by the surrounding quiescent flow (blue) are depicted with a color pallet separated by  $\sim 2$  m/s. The present Cartesian coordinate system did not involve an assumption of axial symmetry and the excellent symmetry observed in Figure 3.6 resulted from the calculation themselves. The figure shows a symmetric potential core around the computationally inferred axis and an axisymmetric shear layer within which the velocity decays to the surrounding value. Subtle changes in the axial velocity decay are observed by the emergence of a region of approximately 20% lower axial velocity which recovers back to the exit value probably because of the heat release leading to lower density. The decrement in the peak axial velocity continues because of the radial spreading of the jet countered by the decrease in density caused by the heat release. This continues until the flame tip is reached beyond which the velocity decreases more rapidly because of the annular spread. The reacting flow measurements of the mean and RMS axial velocity and the turbulence intensity at the burner exit are shown in the panels on the right and agree with the computations not surprisingly so because of the proximity of the measurement station to the jet exit.

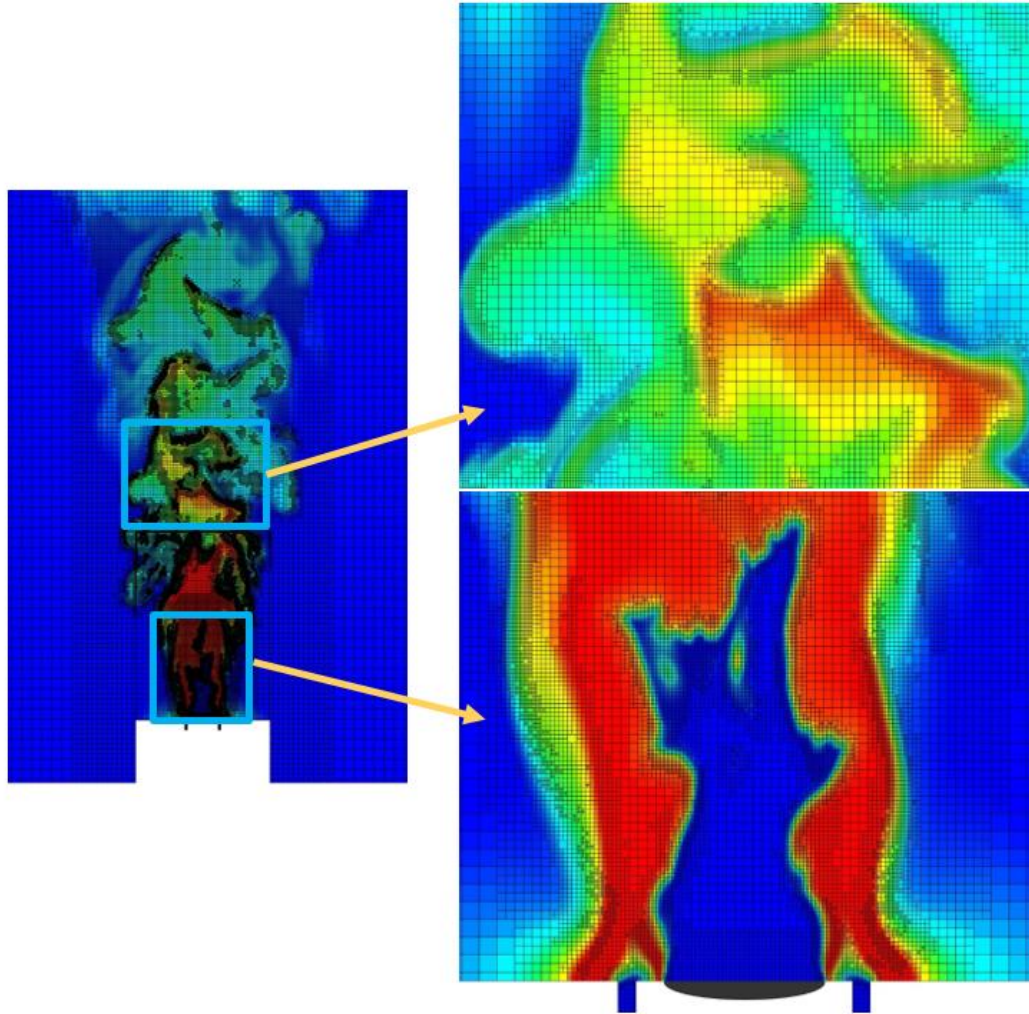


Figure 3.5. The mesh in the x-y plane at  $z=0$  for reacting simulations of PARAT with adaptation based on instantaneous temperature gradients[47]

The material discussed in this section is obtained from the author's AIAA conference paper [47]. Mean temperature profiles along the centerline are compared for two different meshes in Figure 3.7 [47, 49]. This plot shows that the computed mean temperatures are independent of the mesh size and hence the results for the 0.25 mm grid spacing are chosen for further analysis.

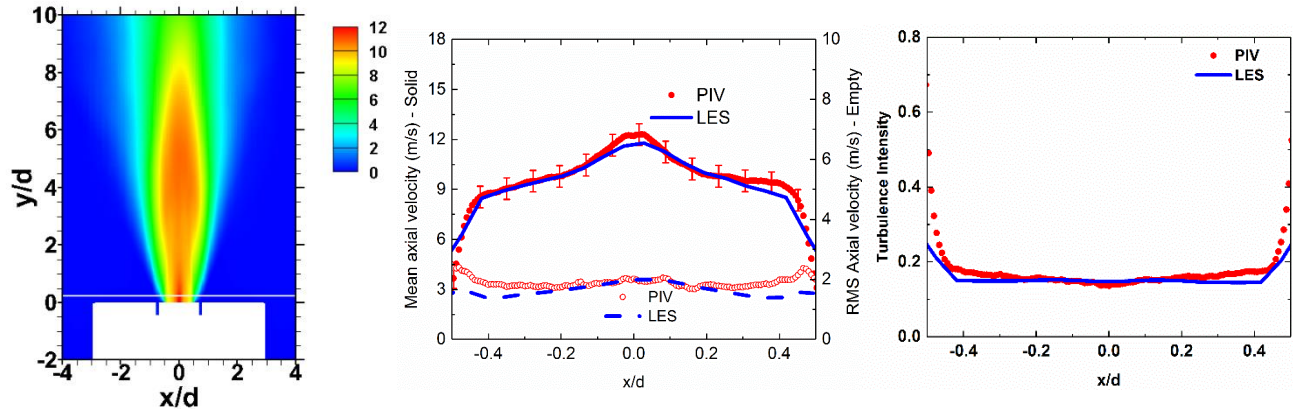


Figure 3.6. Reacting flow mean axial velocity contour and mean, rms axial velocity and turbulence intensity comparison at  $y/d=0.2$ [47]

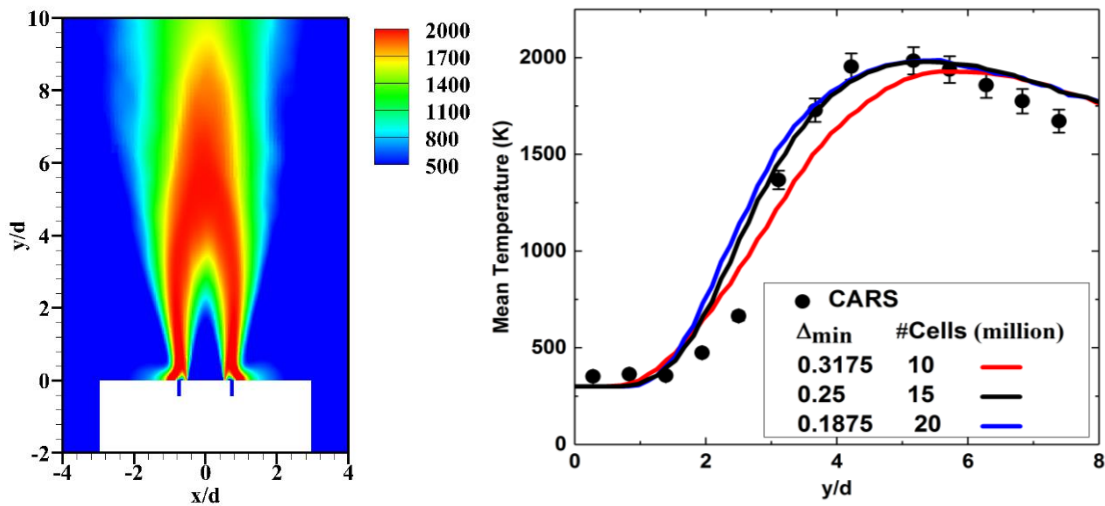


Figure 3.7. Mesh Sensitivity Study – Comparison of Mean temperature [K] profiles along the centerline. Contour plot corresponds to 0.25 mm case[47]

The material discussed in this section is obtained from the author's AIAA conference paper [47]. The instantaneous axial velocity (y-component) and radial velocity (x-component) on  $z=0$  plane are shown in Figure 3.8 [47, 49]. Similar to the mean axial velocity, the instantaneous velocity depicts a decay from the peak value of 12 m/s. However, the direction of decay in case of the instantaneous velocity is not necessarily axial but also radial and azimuthal depending on the time and location. The jet also shows multiple scales of departure from axisymmetric including an overall swag and multiple scales that appear to be multiples of the largest fluctuation scale. The existence of a semi-organized structure of the flow field is confirmed by the radial velocity component which also shows remarkable overall symmetry but significant local departures from

an axisymmetric flow field. The two velocity profiles clearly show the presence of streamwise and cross-stream vorticity that is a characteristic of turbulence. The instantaneous distribution of vorticity magnitude shown in Figure 3.9 depicts a wide range of vortex structures. Plotted to a scale limited to a relatively small maximum value of vorticity magnitude the flow shows a rich content as seen in the left-most panel. This richness declines rapidly if the scale is expanded by a factor of 10 and only an order of magnitude fewer structures remains visible. Finally, at a factor of 10 larger magnitudes a few structures with strong vorticity magnitudes remain and these are the structures supporting rapid mixing of products and reactants and heat release.

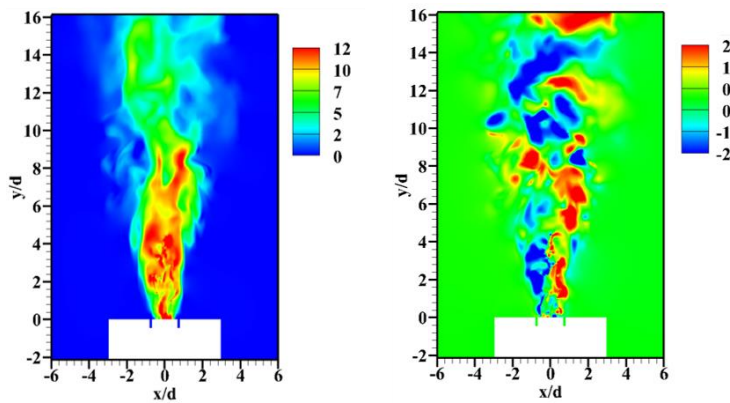


Figure 3.8. Instantaneous axial velocity (m/s) (left) and instantaneous radial velocity (m/s) (right)

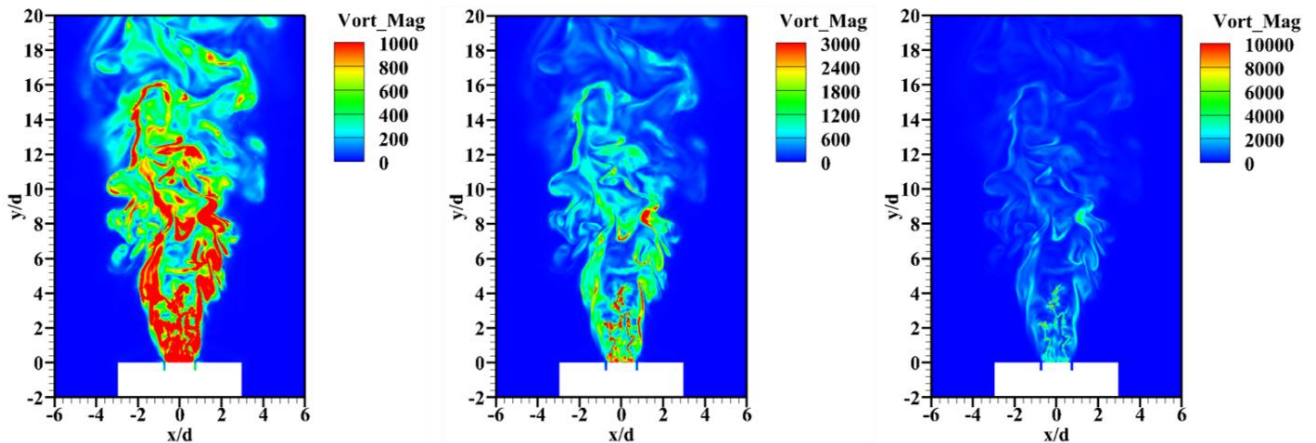


Figure 3.9. Instantaneous vorticity magnitude (1/s)

The material discussed in this section is obtained from the author’s AIAA conference paper [47]. The isosurface of the second invariant of the velocity gradient tensor (also called Q-criterion)

is used to visualize the vortex structures [47, 49, 113-115]. These structures are shown in Figure 3.10 with the color pallet linked to the local temperature value. Clearly, the highest values of the second invariant of vorticity occur within the shear layer near the jet exit and near the flame tip region. A longer and wider flow region now are included in the description of the vortical flow and many larger size structures with lower energy per unit volume appear in the flow field. Any flow field can be separated into a potential and a vortical component. The divergence of the potential component is zero in nonreactive flows and represents a quantity proportionate to the heat release rate per unit volume in the reacting flows. The divergence is plotted to two different scales in Figure 3.11. The left panel magnifies the value of the heat release rate in specific regions and the right panel focuses on the region of intense heat release by increasing the maximum value of the scale by a factor of 30. Now the thin flamelet regions become quite clear but do not rule out the importance of many regions with smaller heat release rate per unit volume but a larger volume of such a release.

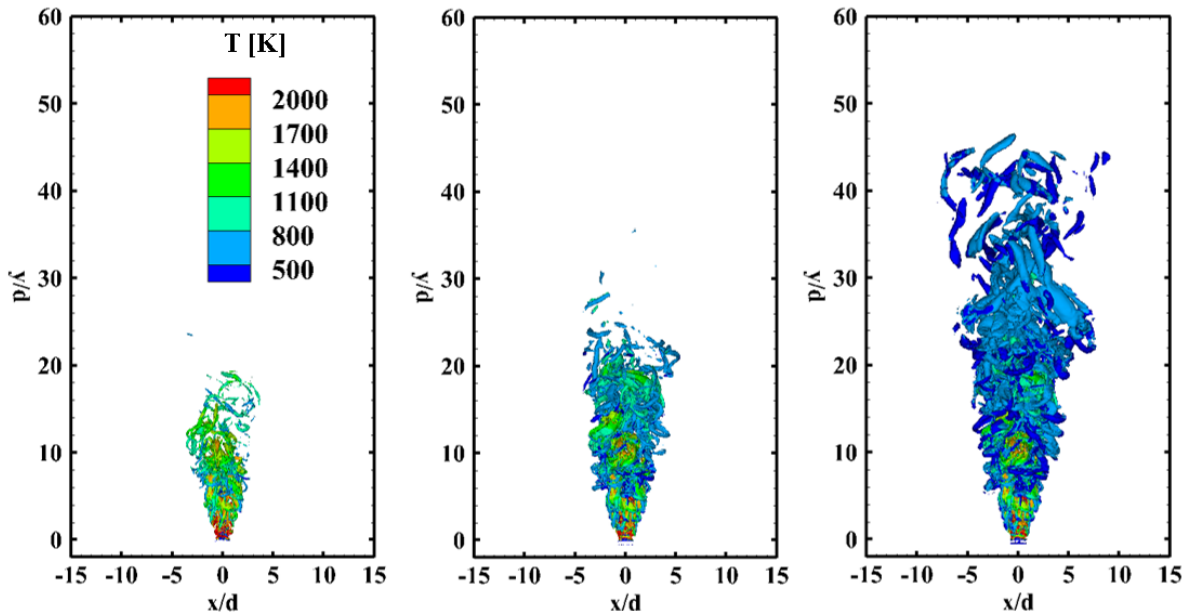


Figure 3.10. Iso-surface of second invariant of velocity gradient tensor ( $Q$ -criterion) for visualization of vortex tubes Left:  $Q = 100000 \text{ s}^{-2}$  Middle:  $Q = 10000 \text{ s}^{-2}$  Right:  $Q = 1000 \text{ s}^{-2}$ . Colored by instantaneous temperature[47]

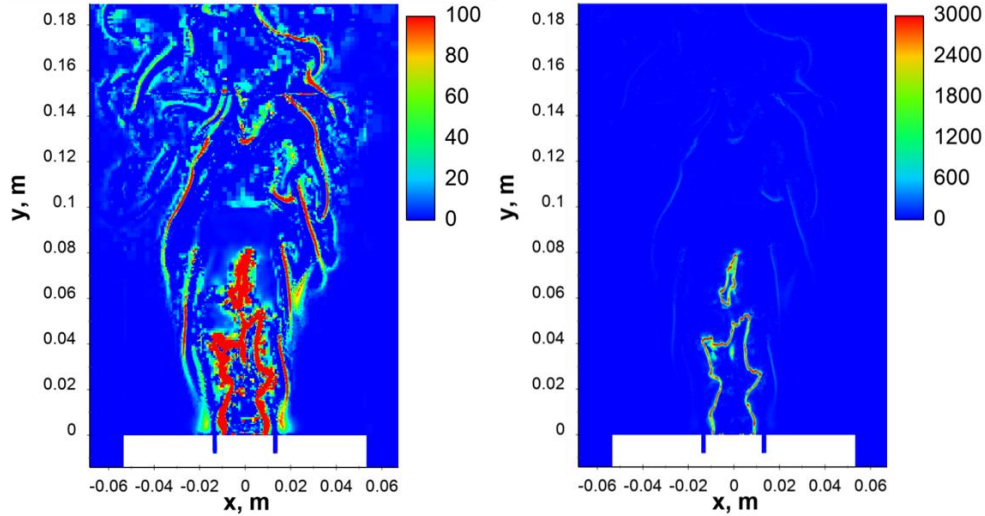


Figure 3.11. Divergence of instantaneous velocity (1/s) [47]

The material discussed in this section is obtained from the author's published paper [47, 49]. Mean temperature profiles along the centerline are compared with the experimental data for the flames in Figure 3.12[47, 49]. The LES results and the CARS data show an agreement of the mean temperatures for the three flames within a range of 6 K for the best and 26 K for the worst. The increase in the mean temperature along the axis is captured within similar error bars until the peak flame temperature is reached. The experimentally observed locations of the peak temperature for the three flames are 93, 113, and 133 mm respectively. The computed locations of peak temperatures for the three flames are 95, 111, and 120 mm respectively. The agreement for the first two flames is outstanding while the agreement for the third flame is not as good within experimental uncertainty. The decay in the mean temperature beyond the peak temperature points is somewhat over predicted for the flame with 0% CO<sub>2</sub> but captured satisfactorily for the flames with CO<sub>2</sub> addition. The computed and measured RMS of temperature along the centerline is shown in Figure 3.13. The differences until one diameter from the exit may be attributed to the widely discussed limitations of CARS data at low temperatures [6]. The computations consistently show shorter distances of rapid increases in the RMS temperatures for all three flames. The peak values of RMS temperatures are captured well for the 0% and 10% CO<sub>2</sub> flames while the peak value is higher than the measurements for the 5% CO<sub>2</sub> flame.

The material discussed in this section is obtained from the author's paper [49]. Radial profiles of mean and rms temperature profiles at  $y/d = 1.94$  and 5 are compared for 0% and 10%

CO<sub>2</sub> cases in Figure 3.14 [47, 49]. Similar results are expected for the 5% CO<sub>2</sub> case. While neither the measurements nor the computations assume axisymmetric profiles in an a priori manner, both capture the expected symmetry in a remarkable manner. However, significant quantitative differences between measurements and computations exist in the width of the temperature profiles, with the measurements showing remarkably narrower profiles than the computations. At  $y/d = 1.94$ , the differences could be attributed to the limited number of experimental data points. However, the differences in the width of the profiles at  $y/d = 5$  may need further attention. The mean progress variable computed from LES is compared with PLIF and CARS data in Figure 3.15. The mean progress variable is computed based on temperature definition for the progress variable in CARS and LES. The one reason for the initial mismatch seen in Figure 3.15 could be attributed to the difference in the different minimum temperatures in both methods. The minimum temperature is measured as around 350K in the unburnt reactant zone which is at 300 K whereas in LES the minimum temperature is 300 K.

The material discussed in this section is obtained from the author's paper [49]. Taken together, the agreement between measured and computed mean temperatures and temperature profiles is strong enough to proceed with further analysis of flame structure [47, 49]. The turbulent premixed flame structure is analyzed following the pioneering work of Bray, Moss, and Libby [116-118]. One of the remarkable results of this theory is that in the thin flame limit, the  $T_{RMS}$  is related to  $T_{mean}$  as:  $T_{RMS} = \sqrt{(T_{Max} - T_{mean})(T_{mean} - T_{min})}$ . The relationships between the present measurements of RMS temperatures and mean temperatures along the axis and along a radius at two axial locations are shown in Figure 3.16 as symbols. The results of the computations at the corresponding locations and for the corresponding flames are shown as lines labeled as LES. The collapse between the experimental data from the three flames and the computations results from the three flames is remarkable. The departures of both, for all three flames, by almost equal magnitudes from the thin flame limit is also noted and suggest that the computations capture the combustion process and the effects of CO<sub>2</sub> addition on the process remarkably well.

The material discussed in this section is obtained from the author's paper [49]. The encouraging agreement of the computed and experimental values of a parameter tied to the flame structure justifies a further examination of the details of the computational results particularly starting with important reaction steps involving the compounds of practical interest such as CO<sub>2</sub>, H<sub>2</sub>O and the corresponding minor species CO and H<sub>2</sub> [47, 49]. The OH concentration is a good

indicator of heat release rates in flames and the effect of CO<sub>2</sub> dilution on the heat release rates is compared in terms of mean mass fraction of OH contours for three flames in Figure 3.17. Given the importance of instantaneous temperatures to detailed reaction steps, instantaneous temperature distributions are shown in Figure 3.18. The false-color plots present instantaneous temperature contours separated by 300 K in the range 500 K to 2000 K. Details of the annular pilot flame and the flame attachment region, the cold potential core, the annular premixed flame are observed in the near burner region. As the jets progress further the effects of turbulent fluctuations are clearly observed in all three cases. Pocket formations and releases into the surrounding in the radial and the axial direction are notable. The emergence of thin hot regions far from the nominal flame height defined by the peak mean temperature is obvious.

The material discussed in this section is obtained from the author's paper [49]. Figure 3.19 to Figure 3.21 shows the contour plots of species mole fractions involved in the water gas shift reaction [47, 49]. For the species concentrations without CO<sub>2</sub> addition, as expected there is similarity between the mole fractions of the major product species and the temperature. In the top left panel, mole fraction profiles of H<sub>2</sub>O show the expected effect of the hydrogen pilot flame. Beyond the pilot flame, the H<sub>2</sub>O mole fractions range from 0 to 0.18. The CO<sub>2</sub> mole fraction varies from 0 to maximum of 0.122 while the CO and H<sub>2</sub> mole fractions vary from 0 to  $5(10^{-3})$  consistent with their minor species status in lean premixed flames. How the ratio of these mole fractions compares with the equilibrium constant of the water gas shift reaction at the local temperature is one of the interesting questions. This is taken up following a brief discussion of the changes in the profiles of CO<sub>2</sub>, H<sub>2</sub>O, CO and H<sub>2</sub> observed with CO<sub>2</sub> addition to the fuel stream. As expected, the addition of CO<sub>2</sub> and subsequent increase in temperature leads to its dissociation and increase in the mole fraction of CO and corresponding increase in the mole fraction of H<sub>2</sub>O. The conversion of H<sub>2</sub> to H<sub>2</sub>O leads to a decrease in the availability of H<sub>2</sub> is expected to lead to a decrease in the reaction rates of all reactions because of the decrement of concentration of H atom from the system. Thus an indirect effect of CO<sub>2</sub> addition involves increase in the potential for emission of CO as observed in the bottom panels of Figure 3.20 and Figure 3.21. Clearly, there is a danger of increased emissions of CO with increasing EGR as is widely known in the community. Using high hydrogen content fuels is one of the mitigating factors utilized in the industry. Future experimental and computational work along the lines of the present study should include a fuel mixture with high levels of hydrogen and CO<sub>2</sub>.

The material discussed in this section is obtained from the author's paper [49]. Figure 3.22 shows a contour plot of the equilibrium constant for the water gas shift reaction  $\text{CO}_2 + \text{H}_2 \leftrightarrow \text{CO} + \text{H}_2\text{O}$  [47, 49]. As expected the equilibrium constant contour plots are very similar to the temperature contour plots, the former being a unique function of the later and independent of the individual equilibrium mole fractions of the species but only a function of a ratio of their products:  $K_p(T) = \frac{X_{\text{CO}|eq}X_{\text{H}_2\text{O}|eq}}{X_{\text{CO}_2|eq}X_{\text{H}_2|eq}}$ . The departure of the actual mole fractions of the species from equilibrium can be depicted by plotting the ratio:  $\frac{X_{\text{CO}}X_{\text{H}_2\text{O}}}{X_{\text{CO}_2}X_{\text{H}_2}}$ . for comparison. Figure 3.23 shows such a ratio. Clearly, there are significant differences between the equilibrium constant and the ratio of mole fractions. In fact, significant increases in mole fractions of CO higher than the equilibrium value are observed at most high-temperature locations. A decrease in temperature promotes recombination but not to equilibrium values. Insufficient time for completion of CO oxidation reactions provided by the rapid turbulent mixing and further slowing down of the reverse reaction because of external addition of CO<sub>2</sub> for the EGR emulating flames leads to approximately 15% to 30% super equilibrium CO concentrations.

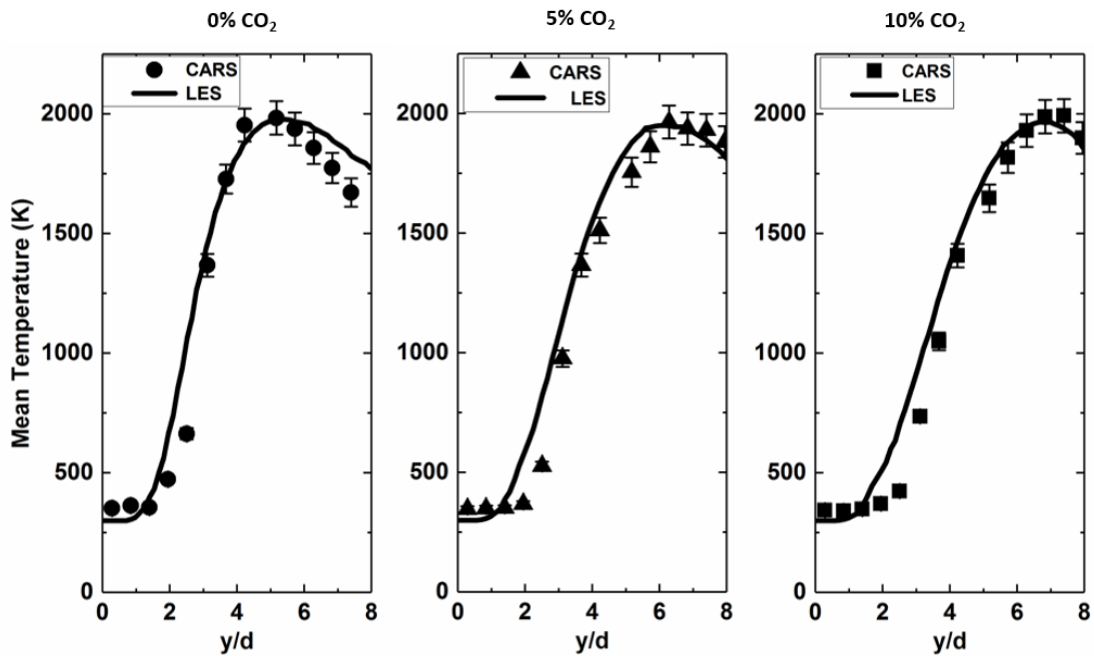


Figure 3.12. Mean temperature profile along the centerline of the jet for all 3 flame conditions [49]

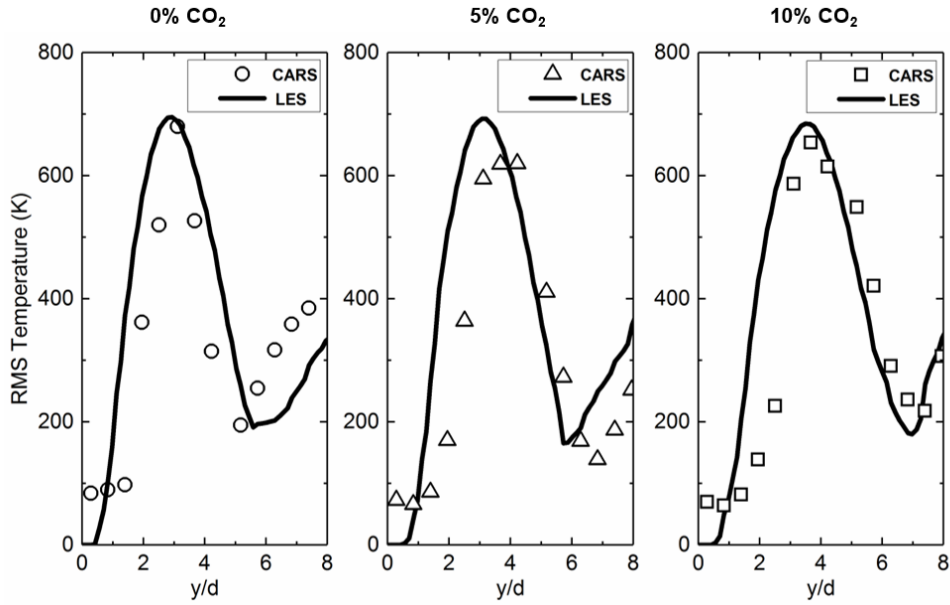


Figure 3.13. RMS temperature profile along the centerline of the jet for all 3 flame conditions[49]

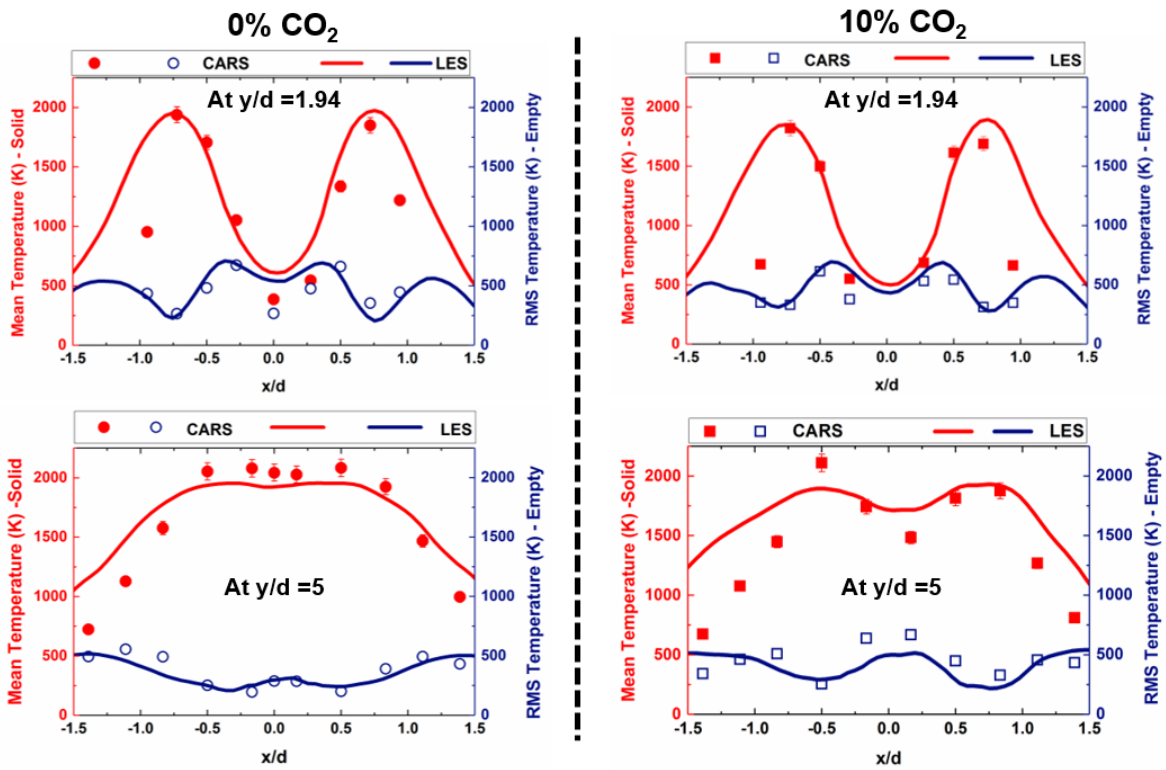


Figure 3.14. Radial profiles of mean and RMS temperatures at different x/ds for flame 1 (0% CO<sub>2</sub>) and flame 3 (10% CO<sub>2</sub>) [49].

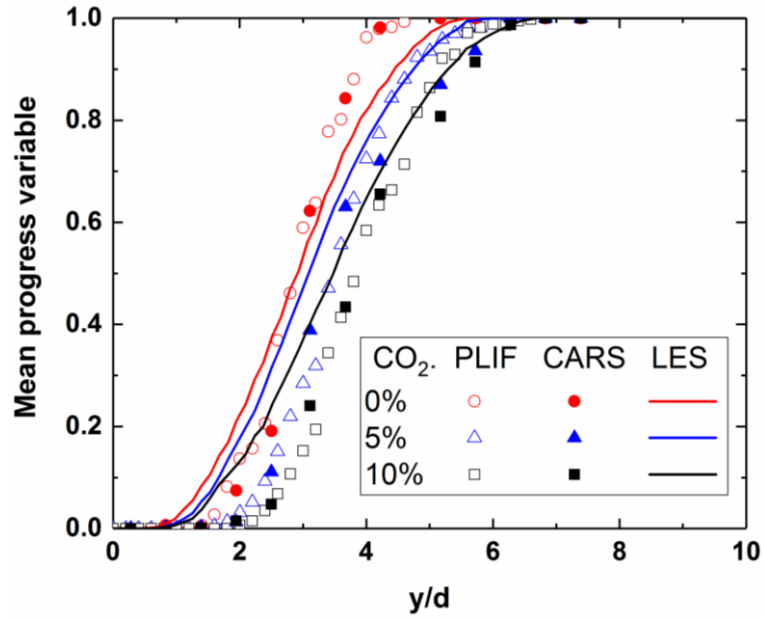


Figure 3.15. Progress variable

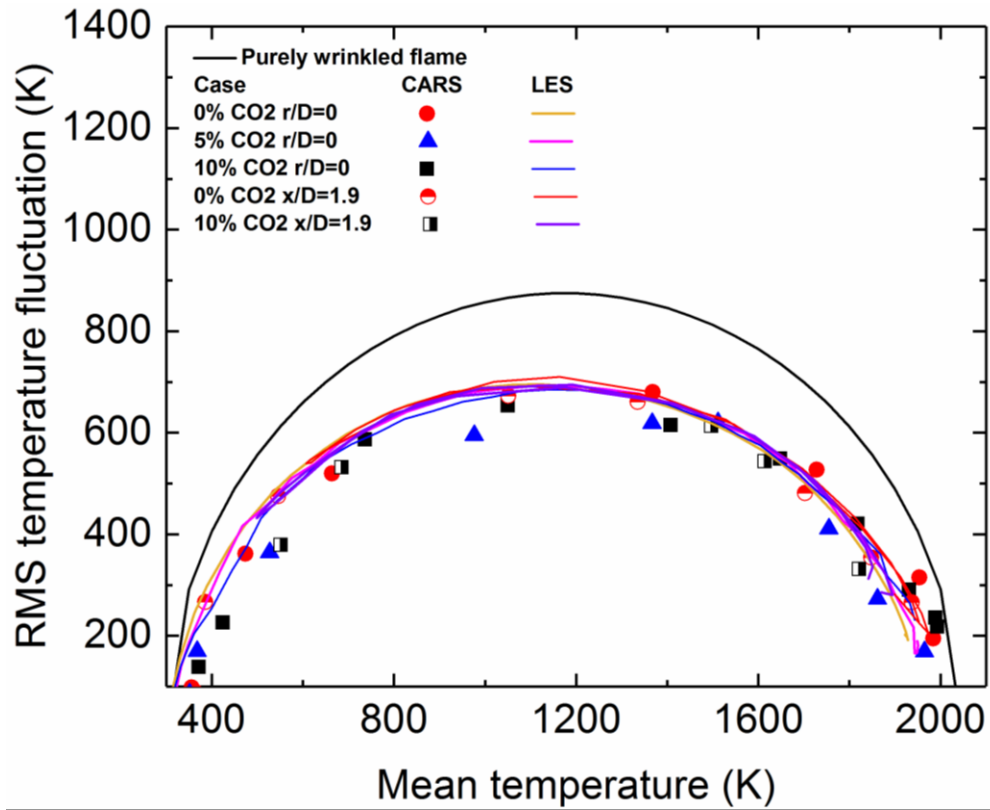


Figure 3.16. Mean temperature versus RMS temperature[49]

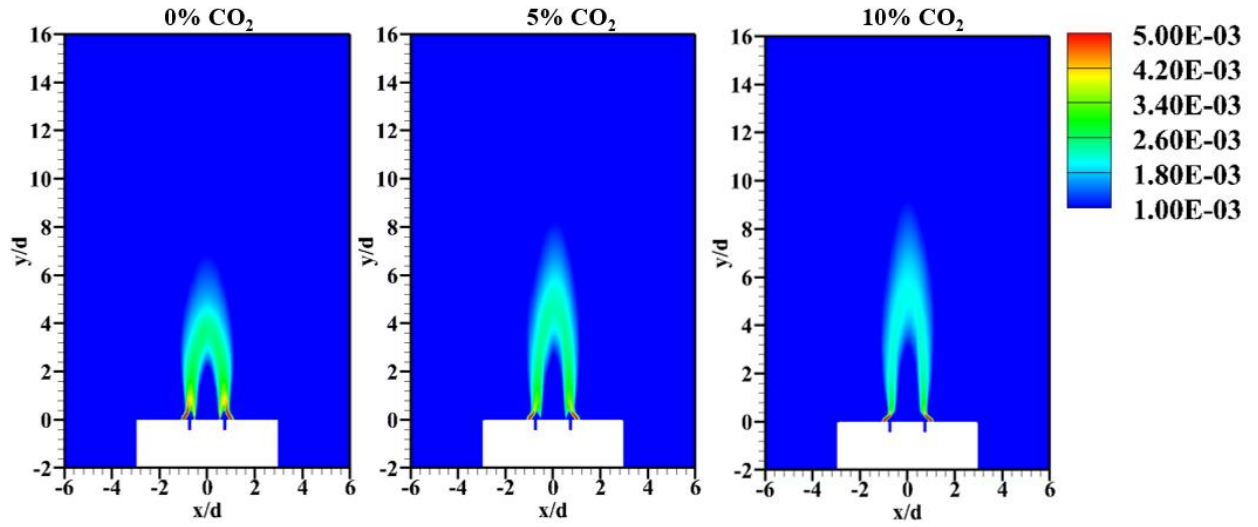


Figure 3.17. Mean mass fraction of OH showing thinner and longer reaction zone with CO<sub>2</sub> dilution

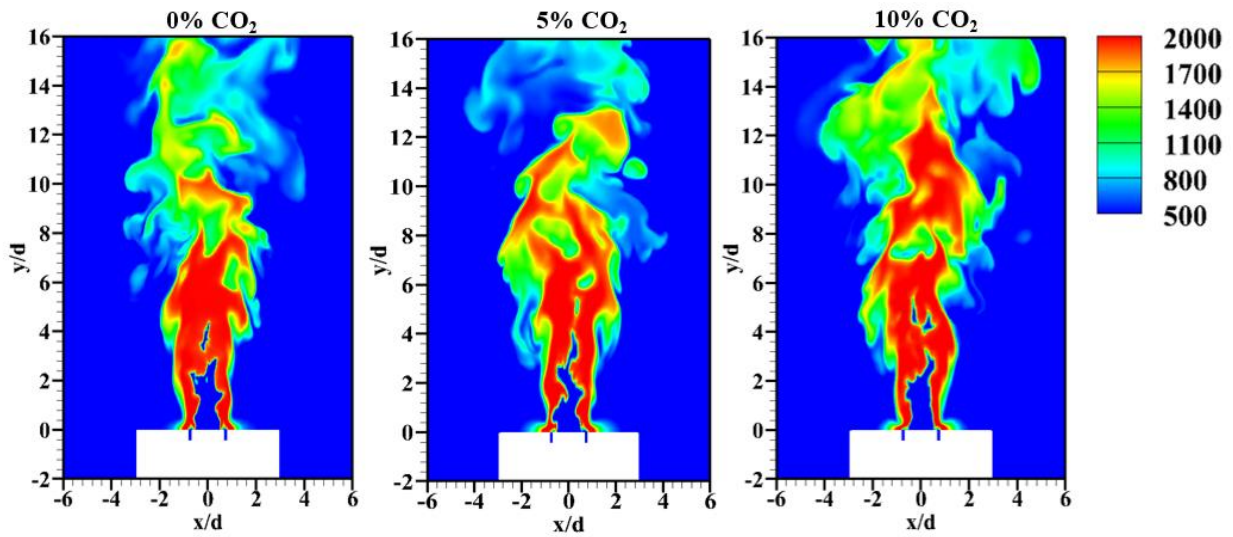


Figure 3.18. Instantaneous temperature comparison for three flames

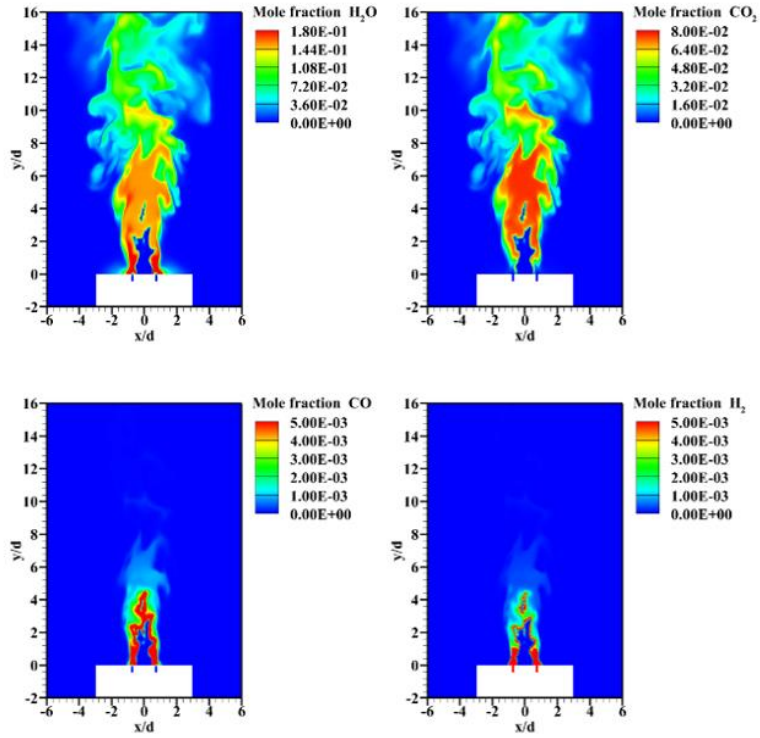


Figure 3.19. Mole fraction of H<sub>2</sub>O, CO<sub>2</sub>, CO and H<sub>2</sub> for 0% CO<sub>2</sub> case[49]

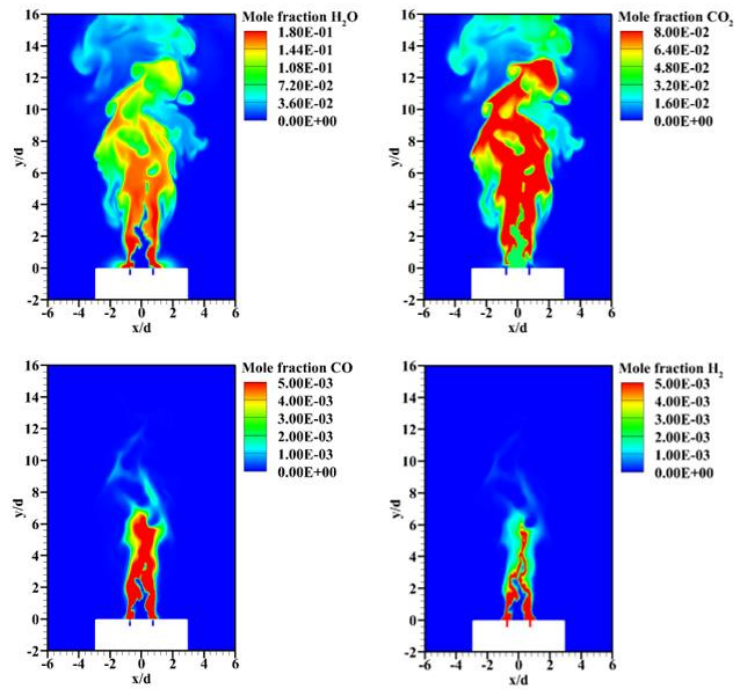


Figure 3.20. Mole fraction of H<sub>2</sub>O, CO<sub>2</sub>, CO and H<sub>2</sub> for 5% CO<sub>2</sub> case[49]

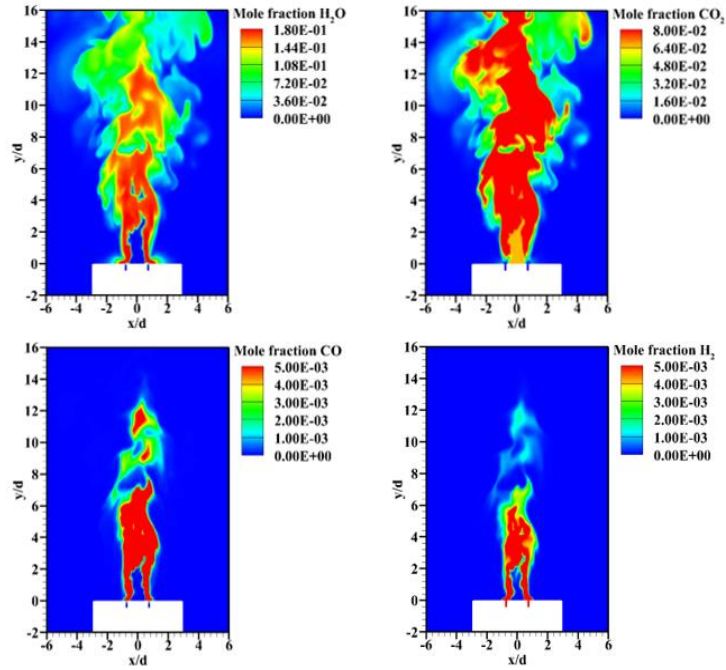


Figure 3.21. Mole fraction of H<sub>2</sub>O, CO<sub>2</sub>, CO and H<sub>2</sub> for 10% CO<sub>2</sub> case[49]

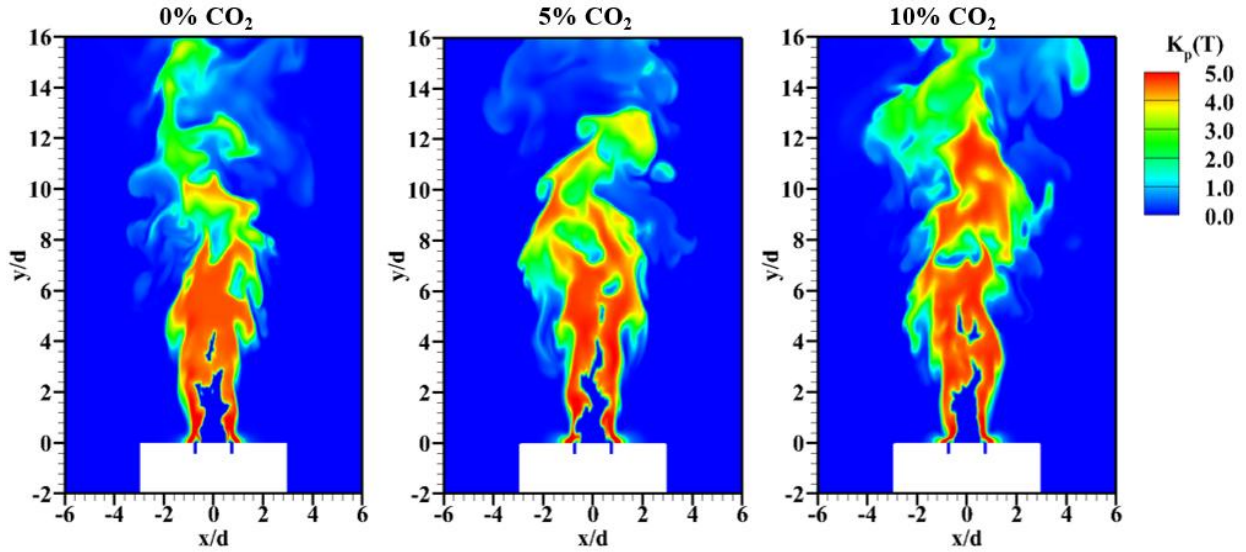


Figure 3.22. Equilibrium Constant for the instantaneous temperature obtained from JANAF tables for CO<sub>2</sub> + H<sub>2</sub> ↔ CO + H<sub>2</sub>O reaction[49]

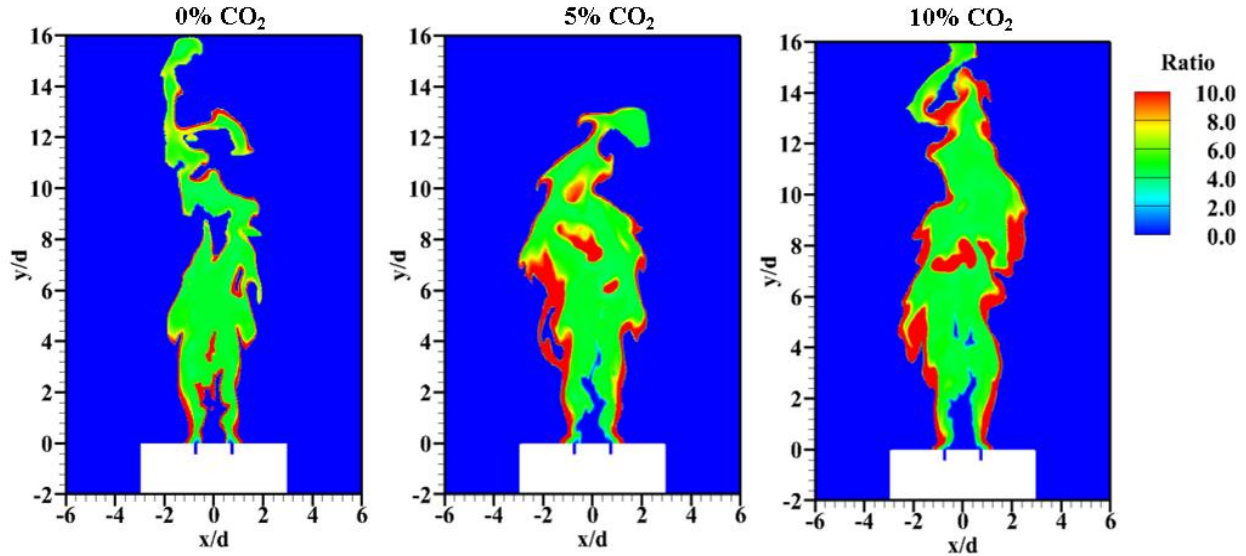


Figure 3.23. Comparison of Ratio =  $X_{CO}X_{H_2O}/X_{CO_2}X_{H_2}$  for three flames[49]

The material discussed in this section is from the author's published paper [47, 49]. The computational results show excellent agreement with available experimental data for mean axial velocity, r.m.s axial velocity, mean temperature, and r.m.s temperature. The computational results captured the equality of the peak temperatures within uncertainty limits. The computations correctly captured the experimentally observed increases in mean flame length. In summary, the CFD methodology based on a high fidelity LES turbulence model and detailed chemistry is able to capture the kinetic effects of CO<sub>2</sub> dilution in turbulent premixed hydrogen stabilized methane/air jet flames.

### 3.2 Test Case 2: Volvo bluff-body stabilized flame

The material discussed in this section is from the author's AIAA conference paper [48]. The Volvo combustion system consists of a rectangular channel with an equilateral triangular bluff body-mounted spanwise to the flow. Air at a specified temperature is supplied as the oxidizer and gaseous propane is used as the fuel. The simulation domain of the Volvo test case is shown in Figure 3.24. The V-shaped triangular cylinder used as the flame holder has a height of  $D=4\text{cm}$ . The size of the computational domain is  $22D$ ,  $3D$  and  $2D$  in the streamwise, wall-normal and spanwise directions, respectively. The upstream length with respect to the back-face of the flame

holder is  $5D$ . At the inlet, a premixed mixture of fuel-air is introduced at a constant mass flow rate of  $0.2079 \text{ kg/s}$  with a uniform velocity of  $17.6 \text{ m/s}$ . The fuel/air mixture is composed of premixed propane-air at a constant temperature of  $288 \text{ K}$  at an equivalence ratio of  $0.62$ . The boundary zones for Volvo bluff body test case are shown in Figure 3.25. The operating conditions are shown in Table 3.1 and boundary conditions in Table 3.2. The computational grids for Volvo bluff body are shown in Figure 3.26 and Figure 3.27.

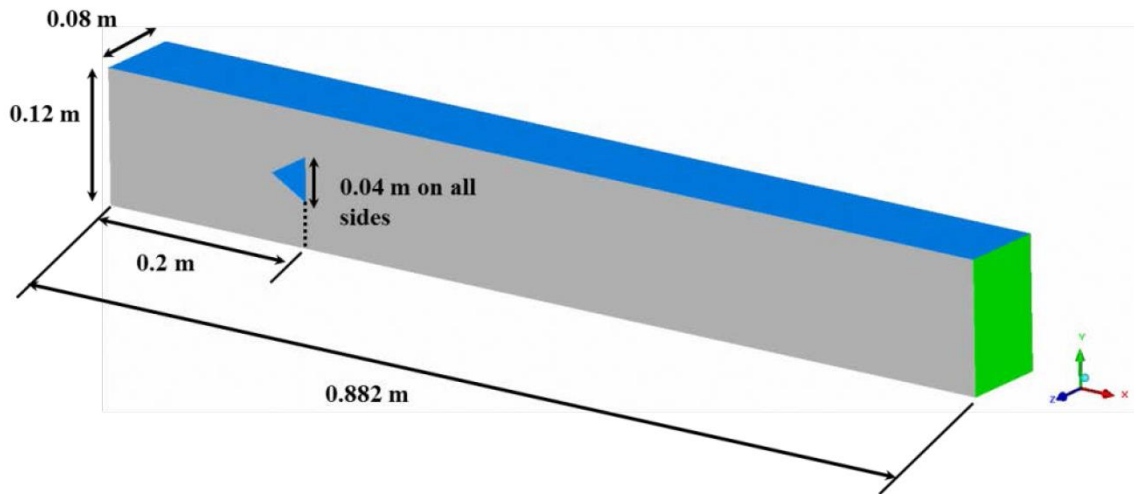


Figure 3.24. Volvo Bluff Body for LES simulations[48].

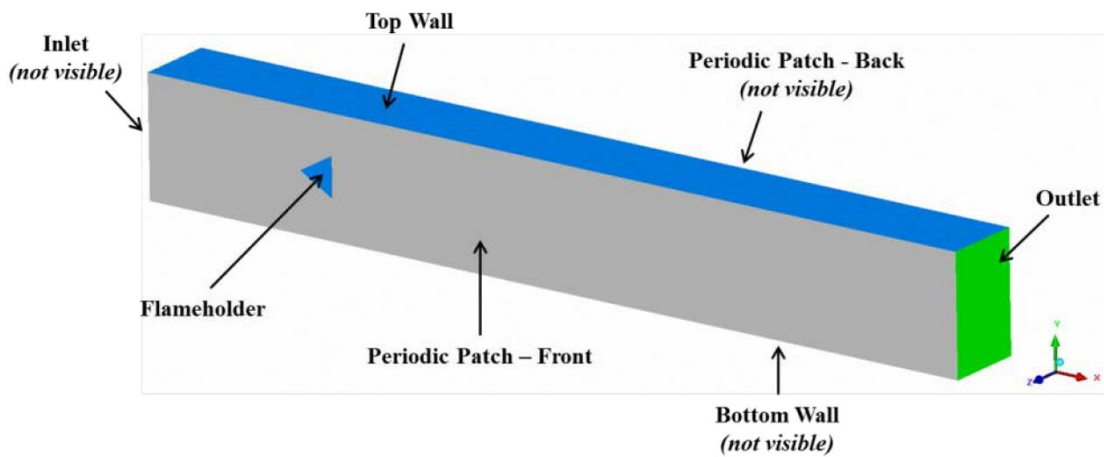


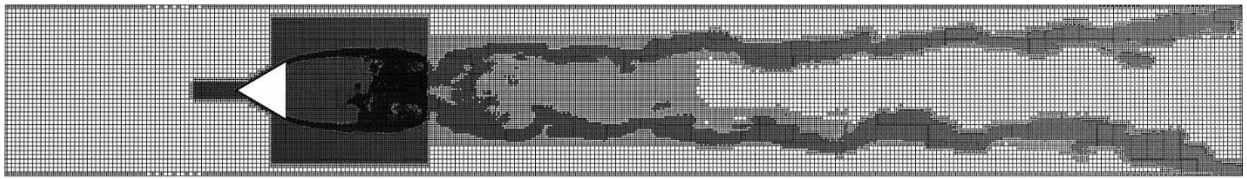
Figure 3.25. Boundaries for the Volvo bluff body test case[48].

Table 3.1. Operating conditions for Volvo test rig validation case[48].

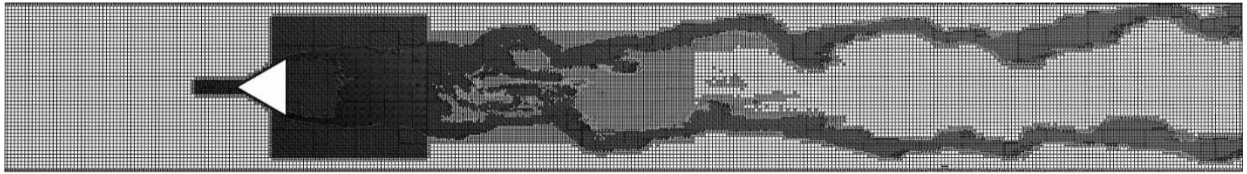
Operating Conditions	Required Case	Optional Case
Premixed Fuel/Oxidizer	Propane / Air	Propane / Air
Equivalence Ratio	0.62	0.62
Pressure, kPa	100	100
Inlet Temperature, K	288	600
Mass Flow Rate, kg/s	0.2079	0.2079
Bulk Velocity, m/s	17.6	36.6
Bulk Mach Number	0.053	0.077
Bulk Reynolds Number	47,000	28,000
Unburned / Burned Density Ratio	5.9	3.1

Table 3.2. Boundary conditions for the Volvo test rig validation case[48].

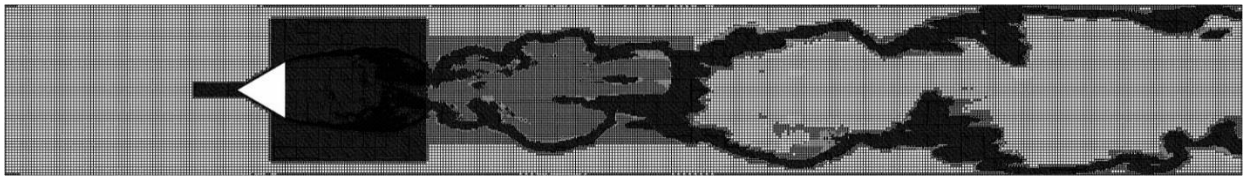
Operating Conditions	Required Case	Optional Case
Inlet Premixed Fuel/Oxidizer	Propane / Air	Propane / Air
Inlet Equivalence Ratio	0.62	0.62
Inlet Stagnation Temperature	288	600
Inlet Mass Flow Rate, kg/s	0.2079	0.2079
Inlet Velocity Profile	Uniform Steady Flow	Uniform Steady Flow
Inlet Bulk Velocity, m/s	17.6	36.6
Inlet Turbulence Intensity	0	0
Flame Holder Thermal BC, K	Adiabatic	Adiabatic
Flame Holder Surface Velocity	No Slip	No Slip
Top and Bottom Wall Temperature	Adiabatic	Adiabatic
Top and Bottom Wall Velocity	No Slip	No Slip
Front and Back Patches	Periodic	Periodic
Outlet	Static Pressure (P= 100 kPa)	Static Pressure (P=100 kPa)



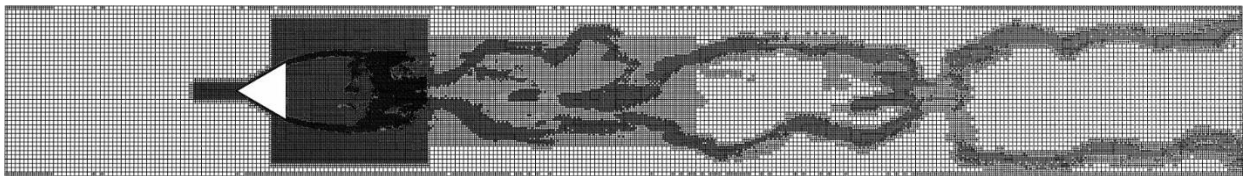
a. FGM (3mm)



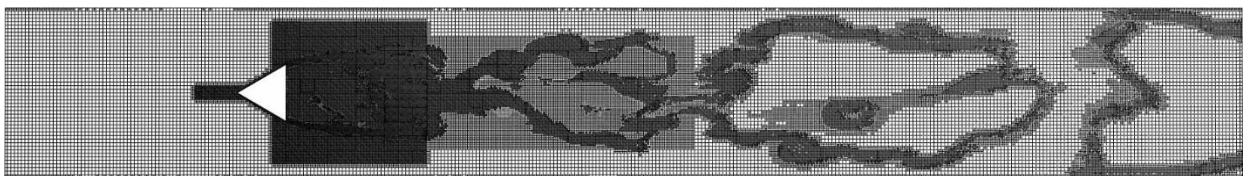
b. FGM (2.5mm)



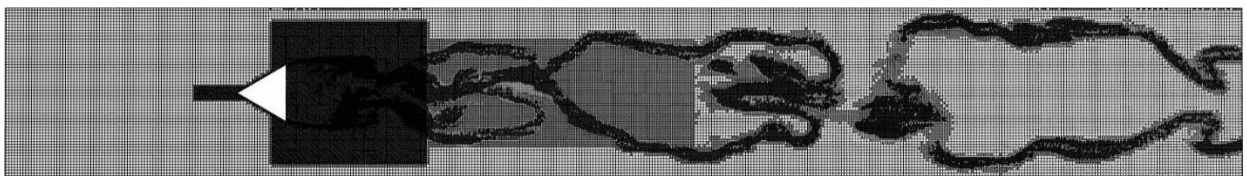
c. FGM (2mm)



d. TFM (3mm)



e. TFM (2.5mm)



f. TFM (2mm)

Figure 3.26. Mesh at the centreline plane in FGM (a-c) and TFM (d-f) simulations for base mesh sizes of 3mm, 2.5mm, and 1mm. Each case has 3 levels of maximum AMR refinement [48].

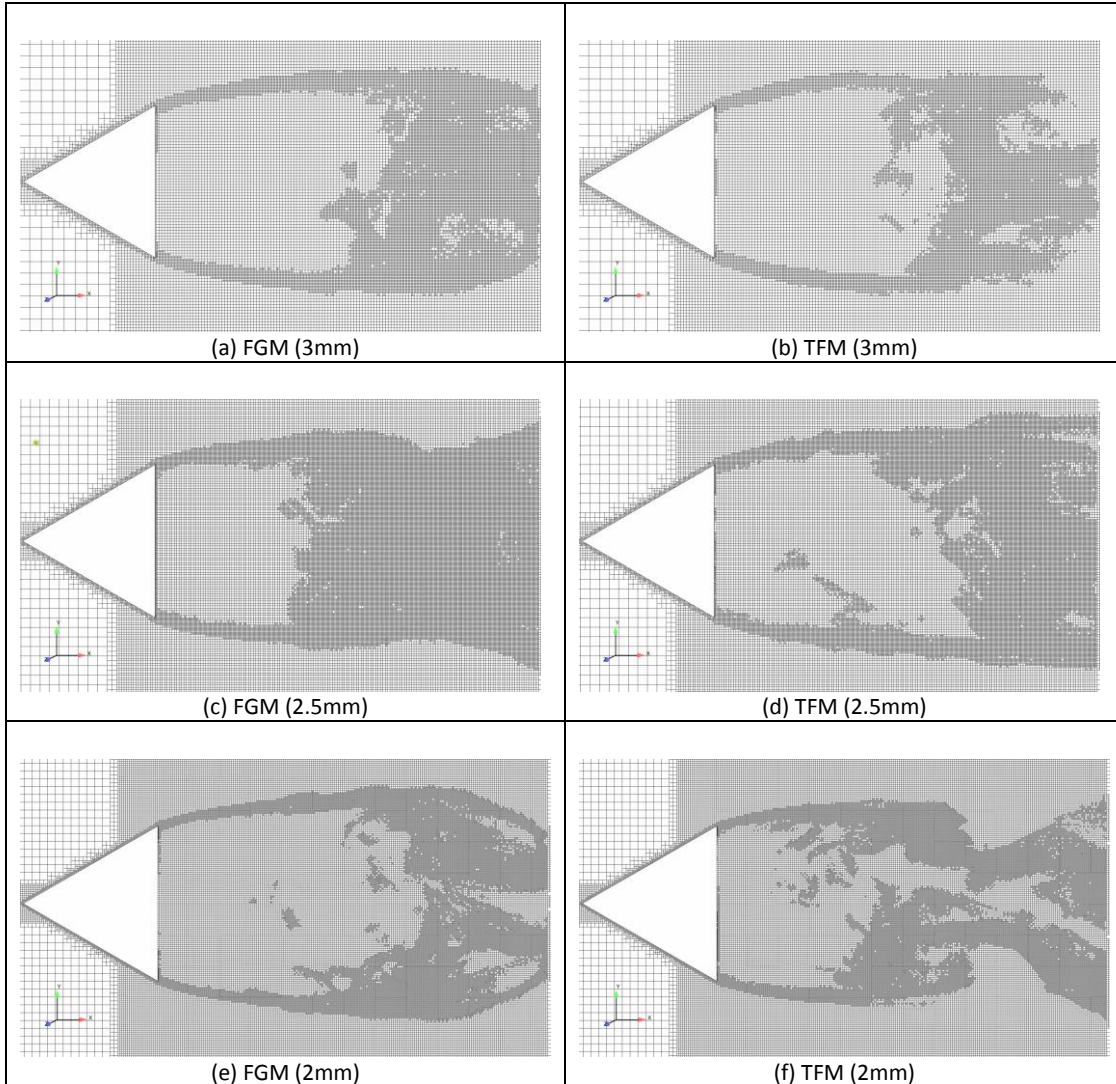


Figure 3.27. Adaptive mesh refinement in action in the wake region behind the Volvo bluff body [48]

In this section, we discuss the grid-convergence study conducted with FGM and TFM combustion models in the LES framework [48]. The numerical results are compared to the experimental data. We also discuss the effect of numerical wall boundary conditions, namely adiabatic and iso-thermal walls, for an identical mesh setting. We present results for four different cases

- (a) FGM: FGM simulation with the adiabatic wall for 3mm, 2.5mm and 2mm mesh
- (b) FGM-Wall BC: FGM simulations with adiabatic and fixed temperature wall (free-stream temperature) at 3mm base mesh.

- (c) TFM FTF=7: TFM simulation with the adiabatic wall for 3mm, 2.5mm and 2mm mesh using a value of 7 for the flame thickening function.
- (d) TFM FTF=3(wake) TFM simulation with the adiabatic wall for 3mm and 2mm mesh using a value of 3 and 7 for the flame thickening function in the re-circulation zone and further downstream, respectively.

Normalized mean axial velocity profile along the center-line is compared against the experimental data for the three mesh levels and for the two combustion models in Figure 3.28 [48]. FGM over predicts the value of centerline velocity further downstream. The centreline velocity predicted by TFM, with a value of the flame thickening function as 3.0, matches quite well with the experimental data as shown in Figure 3.28 (d). The effect of thermal boundary conditions on the top and bottom walls is simulated in this study and we find that the two numerical thermal boundary conditions have no significant impact on the results as shown in Figure 3.28 (b). This is easily explained from Figure 3.54 and Figure 3.55 which shows the presence of a layer of cold gases at almost freestream temperature close to the walls. TFM with thickening factor 7 predicted longer reattachment distance for the wake region. Reducing this factor to 3, a TFM simulation using a 3mm base mesh predicts similar results as \_ne meshes (2mm) and results are almost grid convergent. The grid convergence is evident from sub-figures (d) in Figures Figure 3.28-Figure 3.52. Turbulence intensity profiles along the centerline are shown in Figure 3.29. The turbulence intensity profile is over-predicted for all grid resolution with both FGM and TFM models. FGM and TFM models also tend to over-predict the anisotropy along the centerline.

Radial profiles of mean axial velocity at different axial locations ( $x/D=0.375, 0.95, 1.53, 3.75$  and  $9.4$ ) are shown in Figure 3.30 to Figure 3.34 [48]. Although, the mean axial velocity is under-predicted at  $x/D=0.375$  the results are nearly grid-independent. TFM model with a thickening factor of 3 in the wake region shows grid converged results at all locations. Radial profiles of mean  $U_y$  are shown in Figure 3.35 to Figure 3.39. These plots show nearly grid converged results for both combustion models except at  $x/D=0.95$  and  $1.53$ . Radial profiles of RMS values for  $U_x$  are shown in Figure 3.40 to Figure 3.44. Predictions show sensitivity to the grid up to  $y/D=\pm 0.5$  for both combustion models and after that the results are grid converged. Radial profiles for RMS values of  $U_y$  at different axial locations are shown in Figure 3.45. Similar to RMS predictions of  $U_x$ , results are sensitive to grid in the region up to  $y/D=\pm 0.5$  and beyond that, the results are grid-independent. TFM model predictions in-general look better compared to

FGM model. At  $x/D=9.4$ , both models show similar results for all grid resolutions and results are grid-independent. The mean temperature profiles at  $x/D=3.75$ ,  $8.75$  and  $13.75$  are shown in Figure 3.50 to Figure 3.52 respectively. Both combustion models show grid converged results for mean temperature. The radial profiles for mean CO mass fraction are shown only for FGM model with detailed mechanism in Figure 3.53. The FGM model predictions agree with experimentally predicted trends in the CO profiles and results are sensitive to the grid resolution. Because the chemical time scale of CO is much larger than that of  $C_3H_8$ , using models that include non-equilibrium states would likely improve the prediction of CO level, i.e., unsteady flamelet model or detailed finite rate chemistry model. Since the current TFM simulations use two-step chemistry, the CO level is one order lower than the FGM results (didn't show). CO prediction would be improved if UCSD mechanism is used with TFM. Figure 3.54, Figure 3.56 and Figure 3.58 show the distribution of instantaneous temperature, mean streamwise velocity, and instantaneous vorticity from FGM and TFM simulations with different grid resolutions. Generally, the maxima of the mean streamwise velocity at the outflow boundary from FGM simulation is about 50% greater than that in the TFM simulation. A higher outflow velocity in the FGM simulations indicates a much higher overall heat release in the computational domain. From the plot instantaneous temperature in Figure 3.54, FGM case shows a "finer" (smaller scale) wrinkling of the flame downstream. This "fine" wrinkling of the flame front is likely due to the small vortices generated in the flame front as indicated by the large vorticity value in the flame front downstream. This could be due to a relatively large dispersion error generated at the flame front since the flame is under-resolved for the FGM case. Close to the bluff body, there is no fine wrinkling of the flame front which could be attributed to a higher grid resolution. For TFM cases, the flame front is well resolved which reduces the effect of numerical error. Moreover, as the flame front is thickened, its response to small-scale vortices is much smaller compared to an un-thickened flame.

Since the grid resolution just downstream of the bluff body is higher compared to the mesh resolution further downstream, tested another set of TFM simulations with the thickening factor of 3 right after the wake while keeping thickening factor as 7 in the further downstream regions [48]. In this set of simulations, the results didn't show much difference between 3mm and 2mm base mesh, which further indicates the grid size for converged results is around 0.375mm (3mm base mesh with 3 levels of refinement). For TFM simulations with a thickening factor of 7 in all regions, the length of the recirculation zone predicted with a 3mm base mesh (Figure 3.28(d)) is

larger compared to the experimental data and the corresponding 2mm base mesh simulation. One should note that thickening the flame will recover the correct laminar flame speed, but the flame response to flow strain or vortices is changed. The larger is the thickening of the flame, the slower is the response to the flow. Even though the efficiency factor can make some corrections to the flame response, its accuracy will decrease with a large thickening factor. With adaptive mesh refinement in different regions, one could keep the thickening factor to be relatively small in regions with the high-velocity gradient or turbulent fluctuations, i.e., near the bluff body for this case. This helps the correct prediction of flame response to the flow field and at the same time keep the total cell count small.

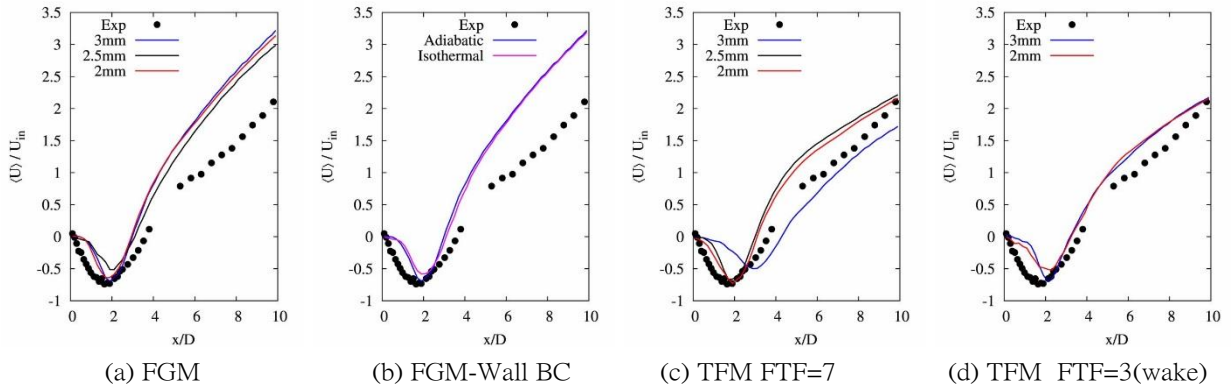


Figure 3.28. Centerline mean axial velocity Profile at  $z/d=0$ ,  $y/d=0$  [48].

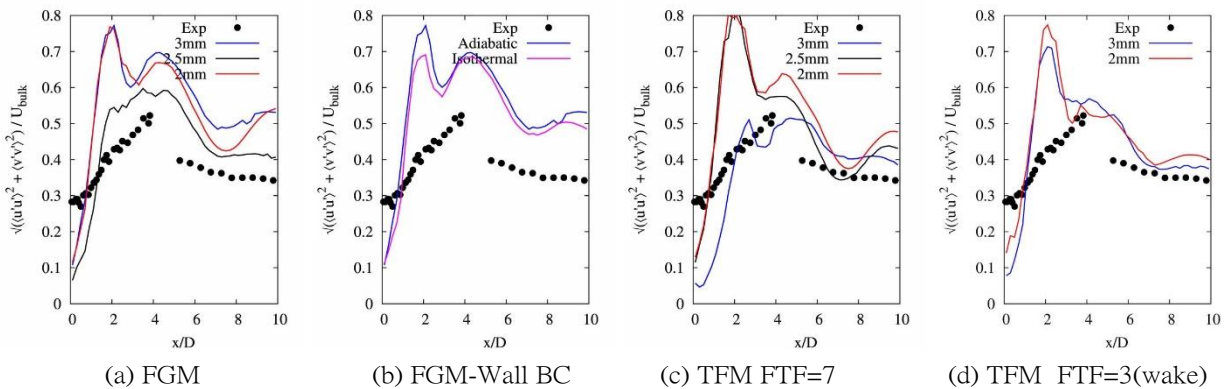


Figure 3.29. Centerline turbulence intensity profile at  $z/d=0$ ,  $y/d=0$  [48].

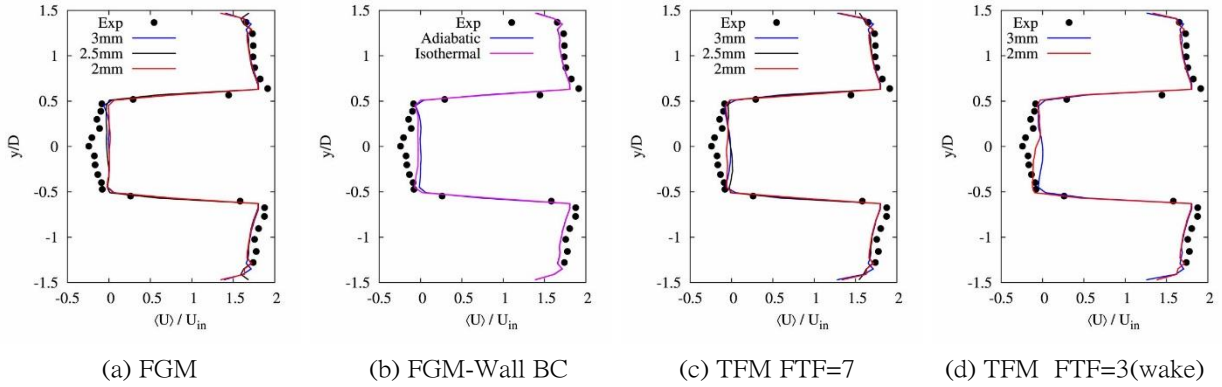


Figure 3.30. Transverse Mean  $U_x$  Velocity Profile on  $z=0$  plane at  $x/D=0.375$  [48].

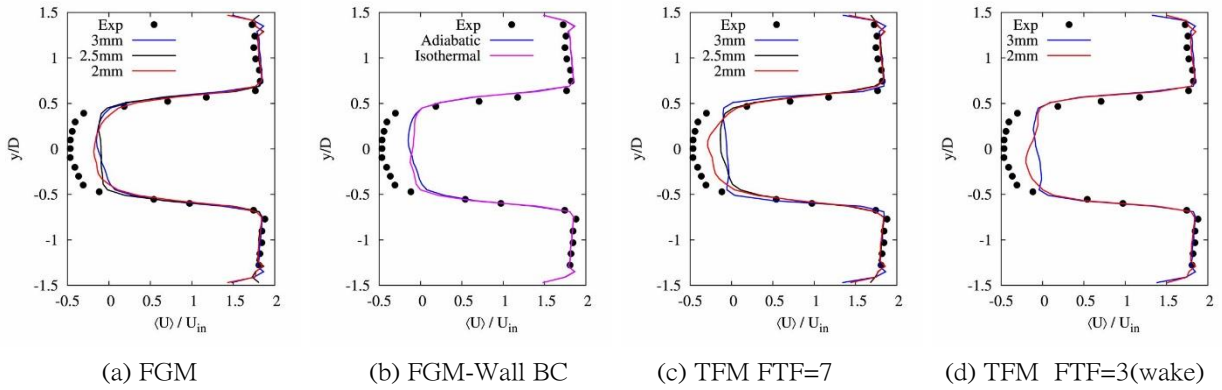


Figure 3.31. Transverse Mean  $U_x$  Velocity Profile on  $z=0$  plane at  $x/D=0.95$  [48].

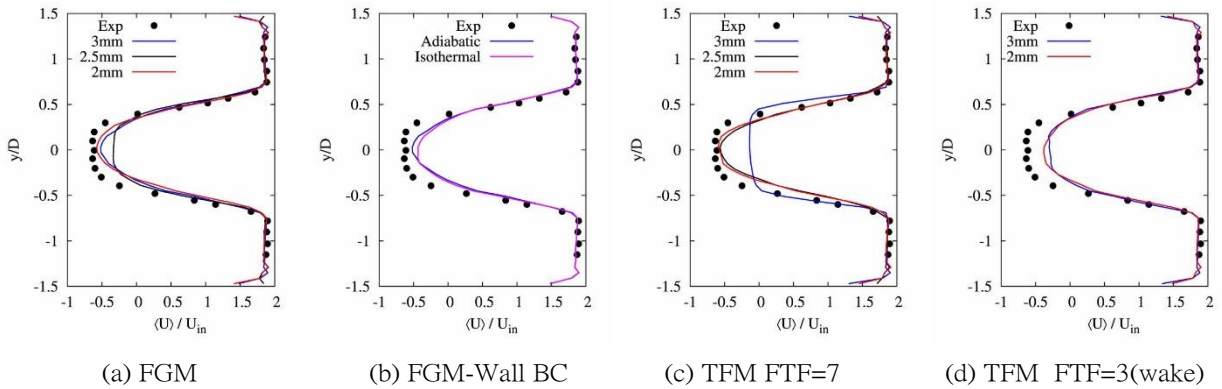


Figure 3.32. Transverse Mean  $U_x$  Velocity Profile on  $z=0$  plane at  $x/D=1.53$  [48].

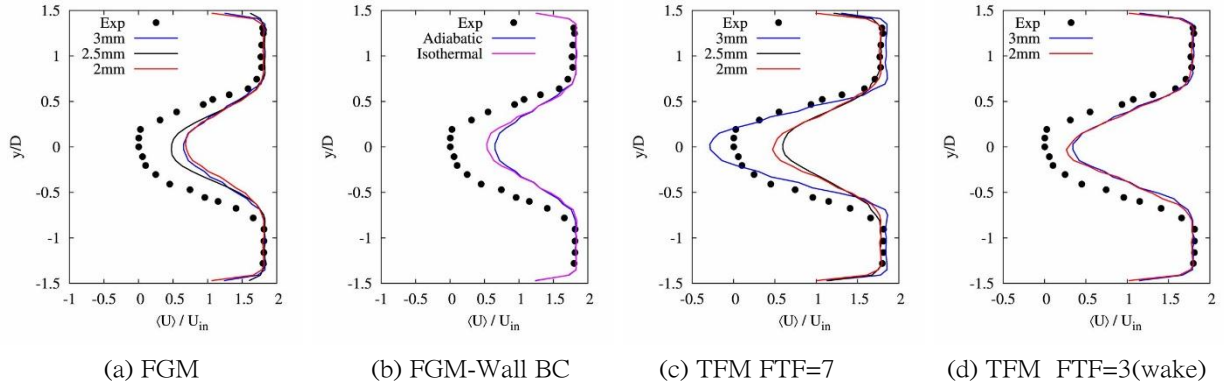


Figure 3.33. Transverse Mean  $U_x$  Velocity Profile on  $z=0$  plane at  $x/D=3.75$  [48].

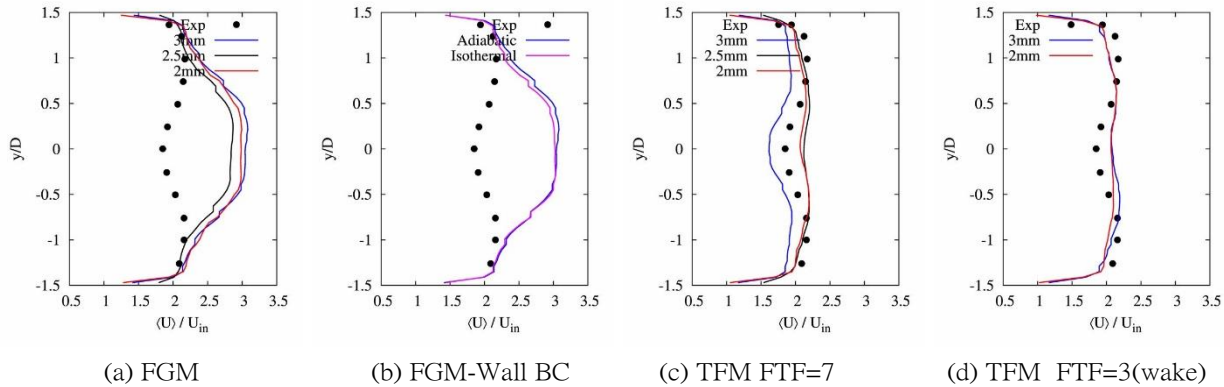


Figure 3.34. Transverse Mean  $U_x$  Velocity Profile on  $z=0$  plane at  $x/D=9.4$  [48].

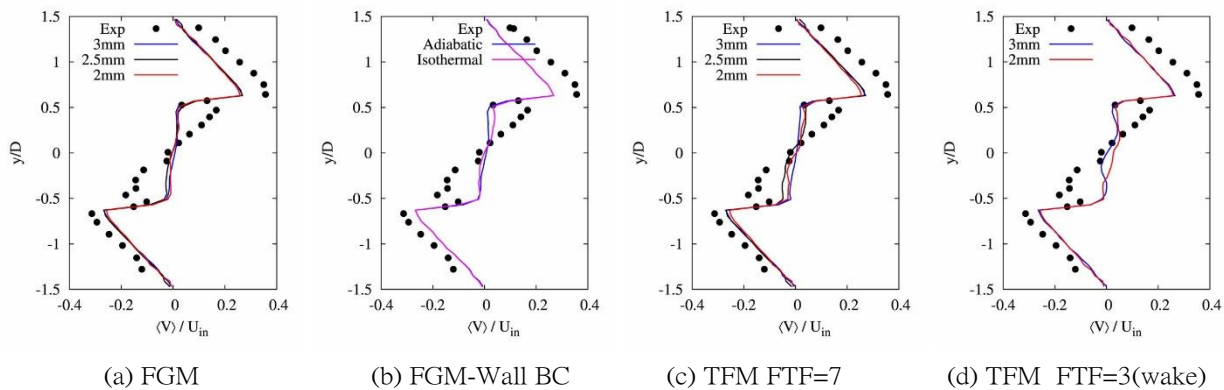


Figure 3.35. Transverse Mean  $U_y$  Velocity Profile on  $z=0$  plane at  $x/D=0.375$  [48].

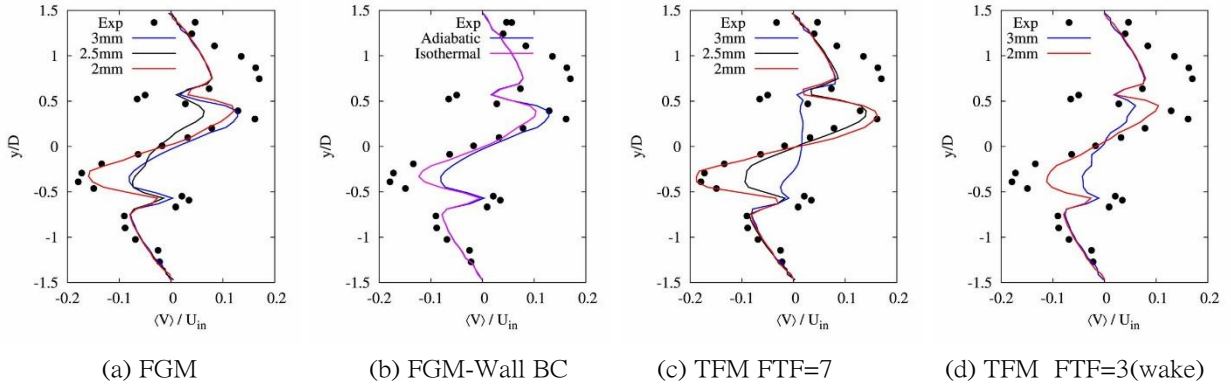


Figure 3.36. Transverse Mean  $U_y$  Velocity Profile on  $z=0$  plane at  $x/D=0.95$  [48].

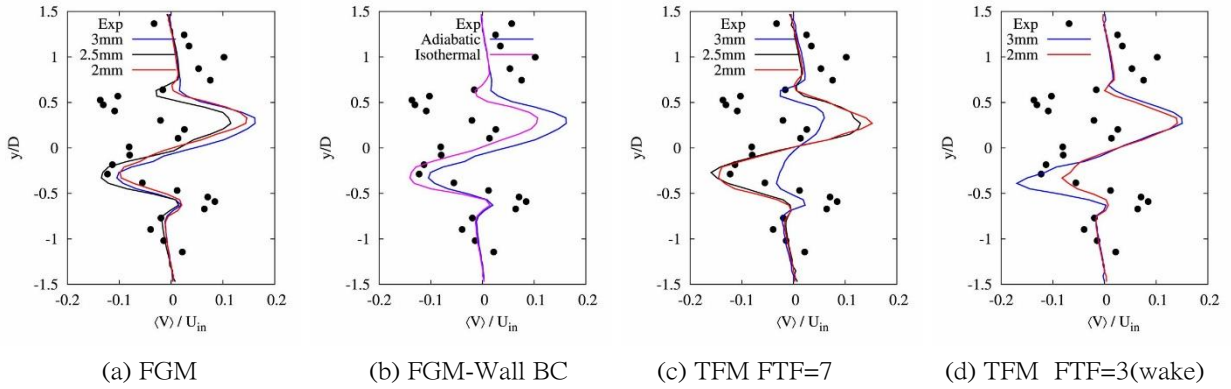


Figure 3.37. Transverse Mean  $U_y$  Velocity Profile on  $z=0$  plane at  $x/D=1.53$  [48].

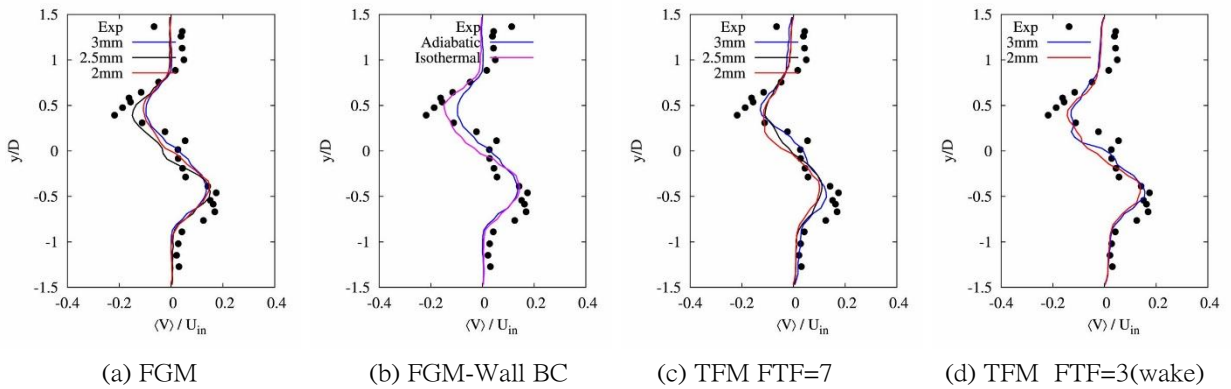


Figure 3.38. Transverse Mean  $U_y$  Velocity Profile on  $z=0$  plane at  $x/D=3.75$  [48].

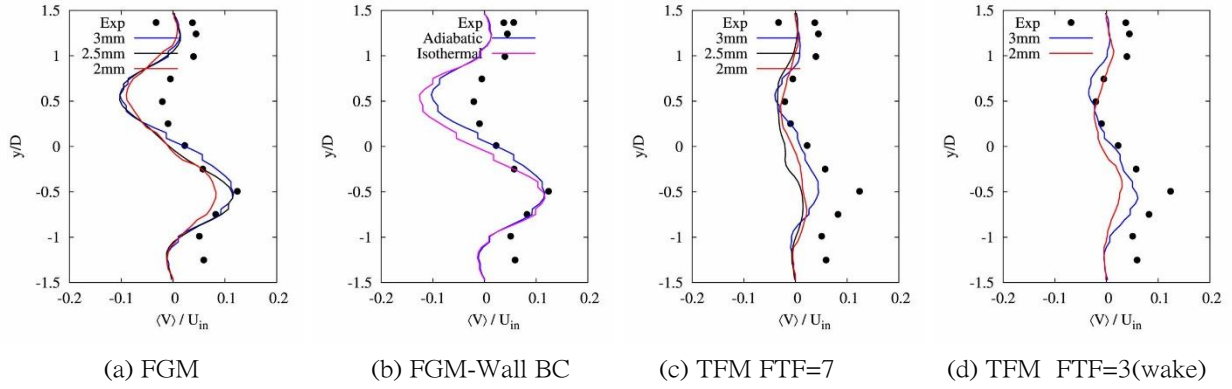


Figure 3.39. Mean  $U_y$  Velocity Profile on  $z=0$  plane at  $x/D=9.4$  [48].

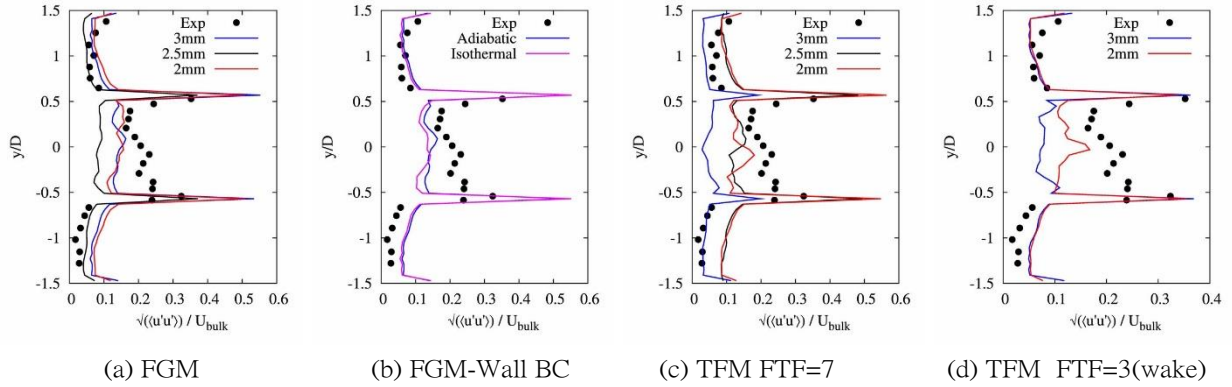


Figure 3.40. Transverse  $U_x$  RMS Velocity Profile on  $z=0$  plane at  $x/D=0.375$  [48].

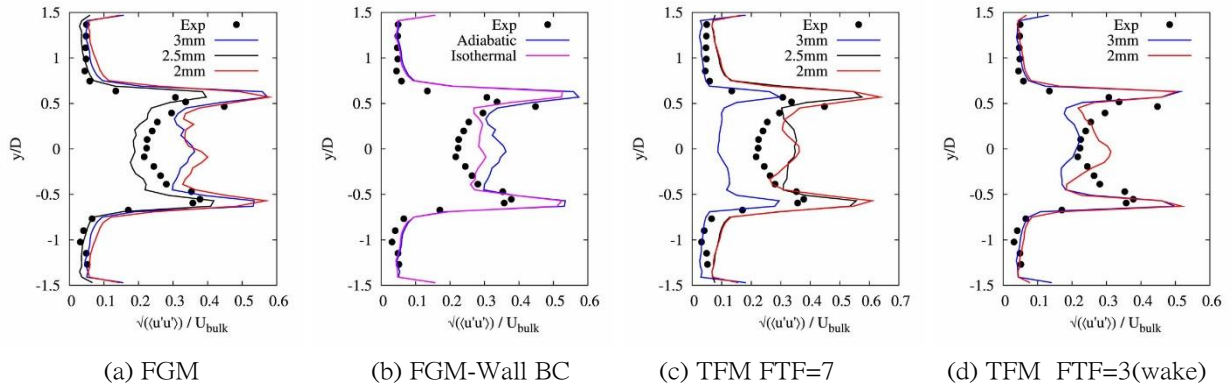


Figure 3.41. Transverse  $U_x$  RMS Velocity Profile on  $z=0$  plane at  $x/D=0.95$  [48].

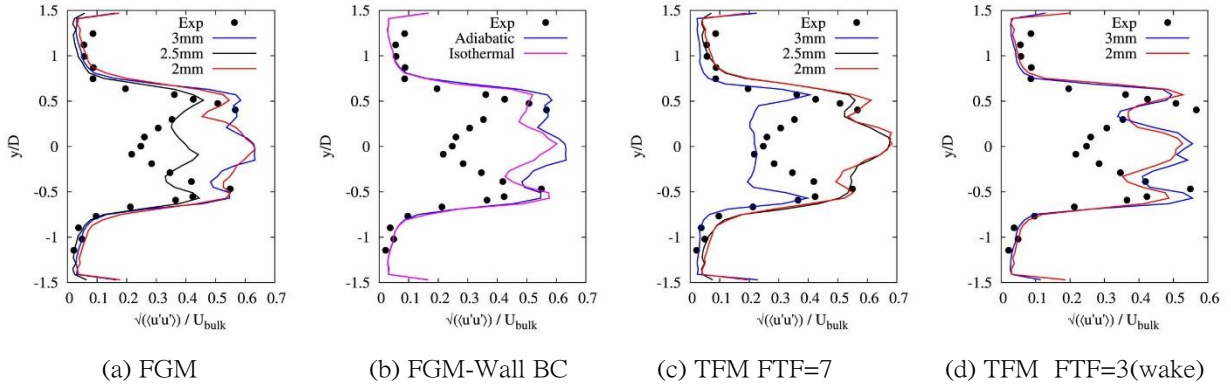


Figure 3.42. Transverse  $U_x$  RMS Velocity Profile on  $z=0$  plane at  $x/D=1.53$  [48].

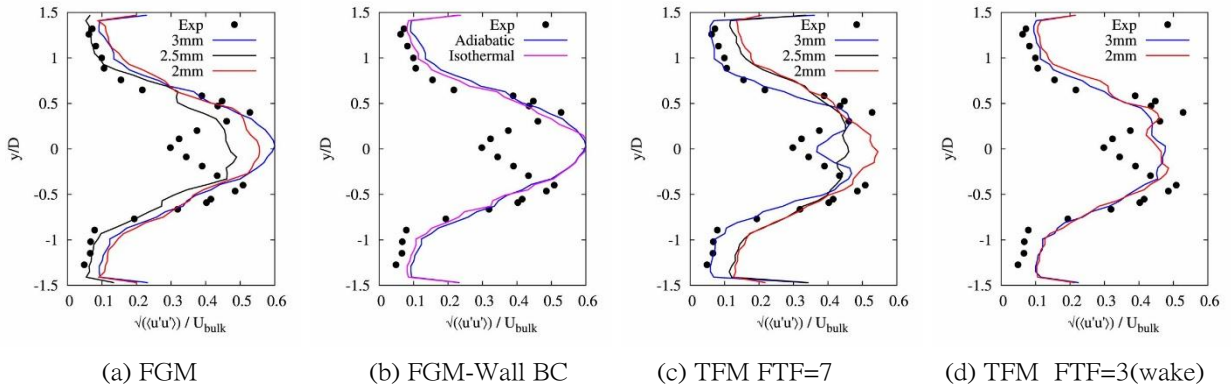


Figure 3.43. Transverse  $U_x$  RMS Velocity Profile on  $z=0$  plane at  $x/D=3.75$  [48].

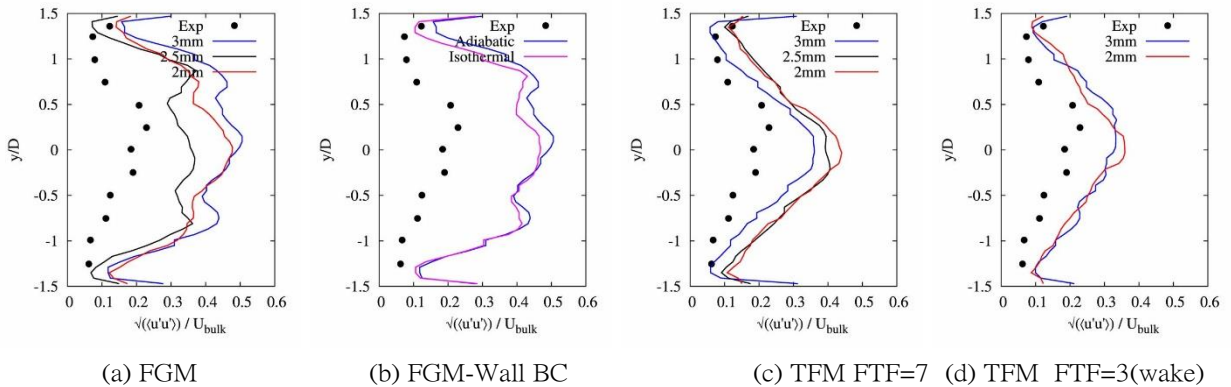


Figure 3.44. Transverse  $U_x$  RMS Velocity Profile on  $z=0$  plane at  $x/D=9.4$  [48].

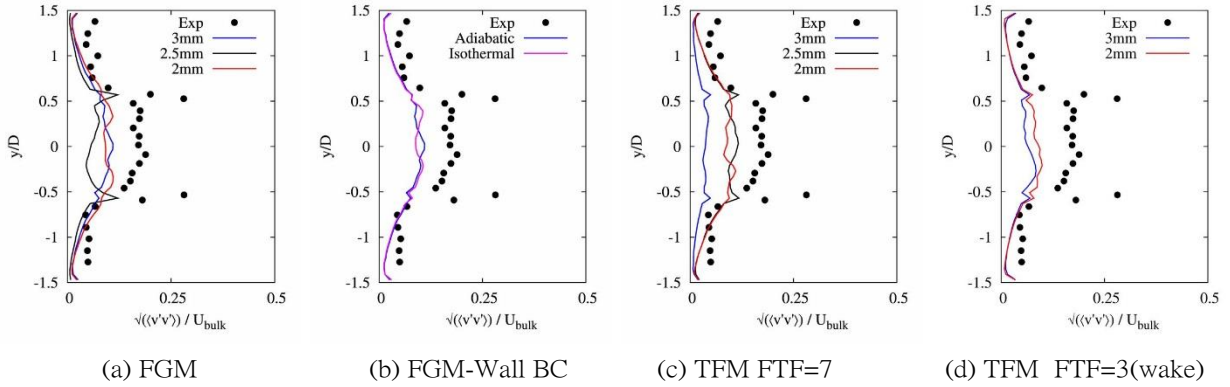


Figure 3.45. Transverse  $U_y$  RMS Velocity Profile on  $z/d=0$  plane at  $x/D=0.375$  [48].

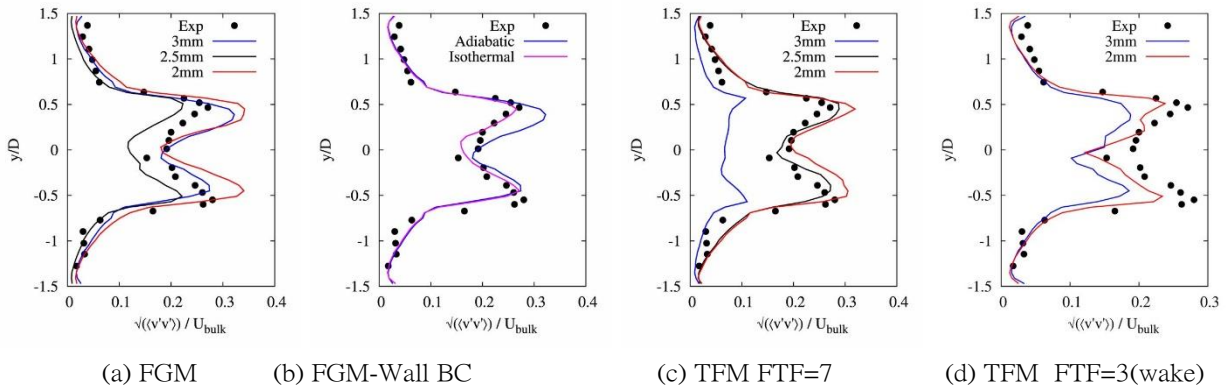


Figure 3.46. Transverse  $U_y$  RMS Velocity Profile on  $z/d=0$  plane at  $x/D=0.95$  [48].

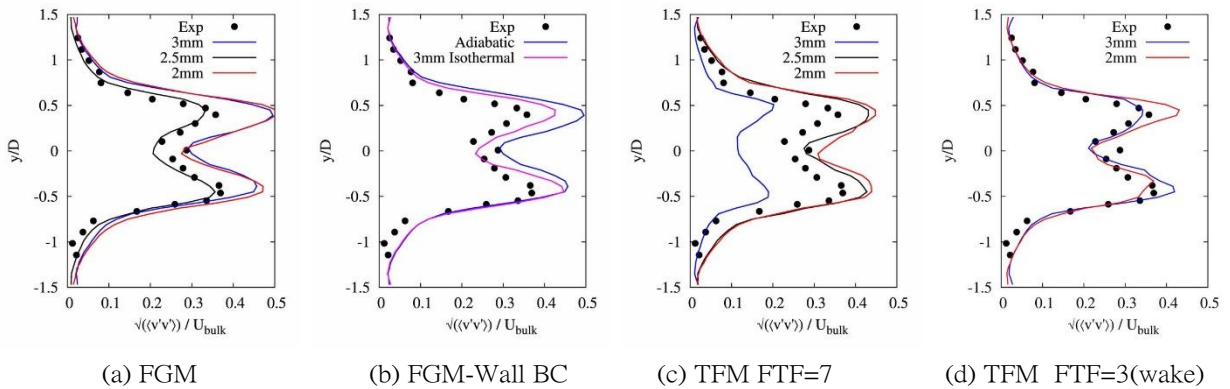


Figure 3.47. Transverse  $U_y$  RMS Velocity Profile on  $z/d=0$  plane at  $x/D=1.53$  [48].

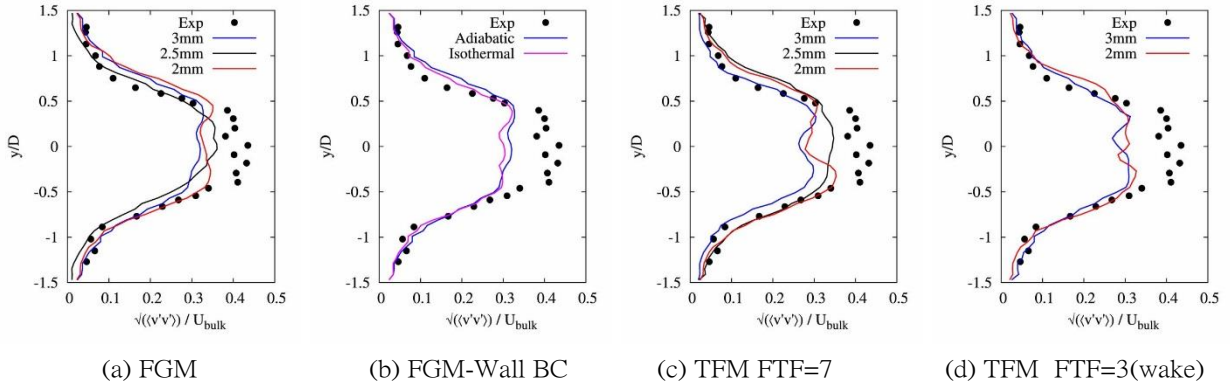


Figure 3.48. Transverse  $U_y$  RMS Velocity Profile on  $z/d=0$  plane at  $x/D=3.75$  [48].

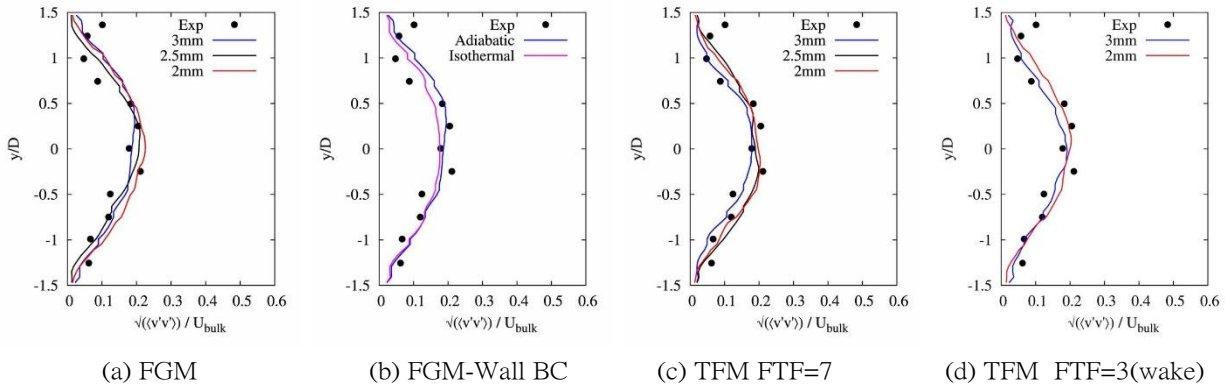


Figure 3.49. Transverse  $U_y$  RMS Velocity Profile on  $z/d=0$  plane at  $x/D=9.4$  [48].

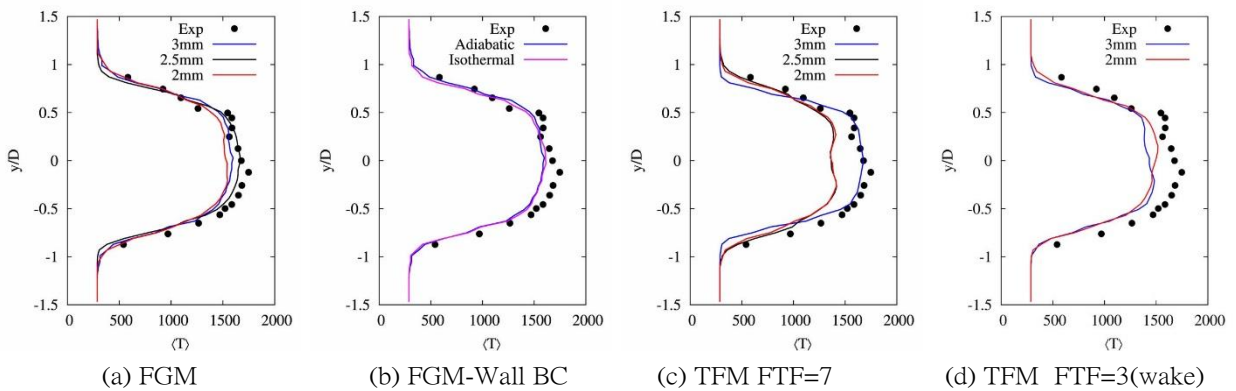


Figure 3.50. Transverse Mean Temperature Profile on  $z/d=0$  plane at  $x/D=3.75$  [48].

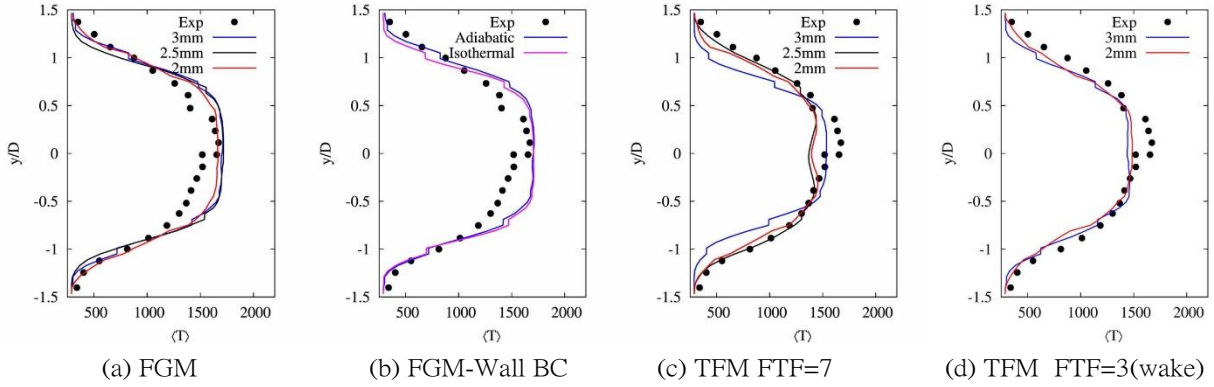


Figure 3.51. Transverse Mean Temperature Profile on  $z/d=0$  plane at  $x/D=8.75$  [48].

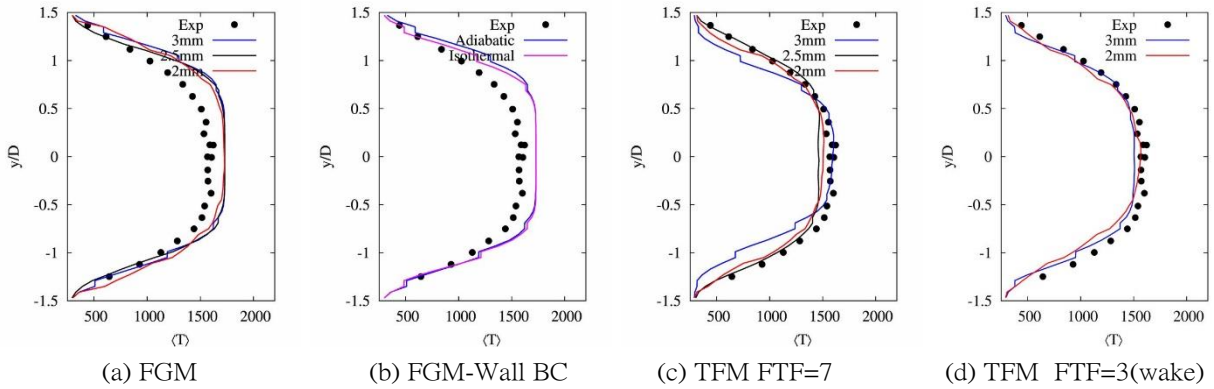


Figure 3.52. Transverse Mean Temperature Profile on  $z/d=0$  plane at  $x/D=13.75$  [48].

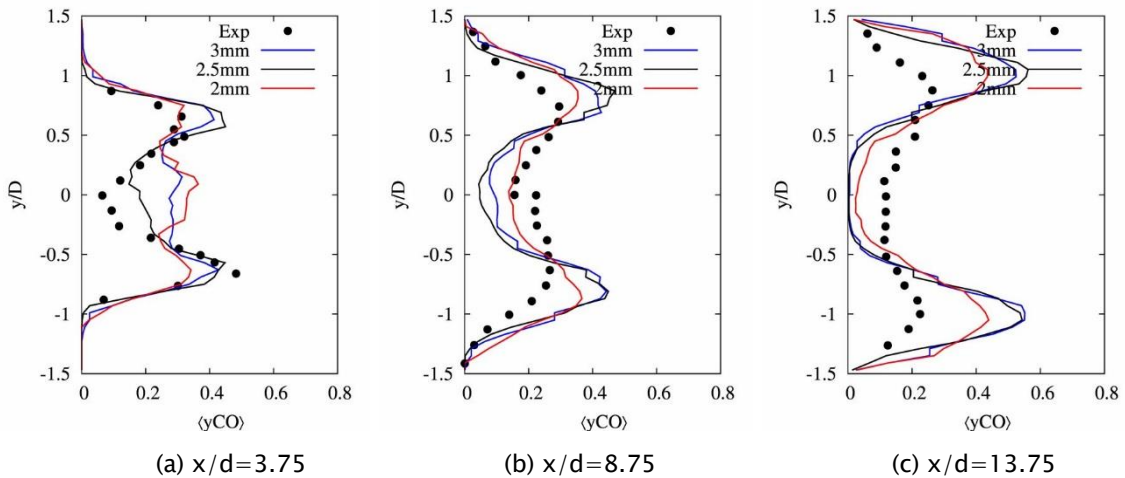
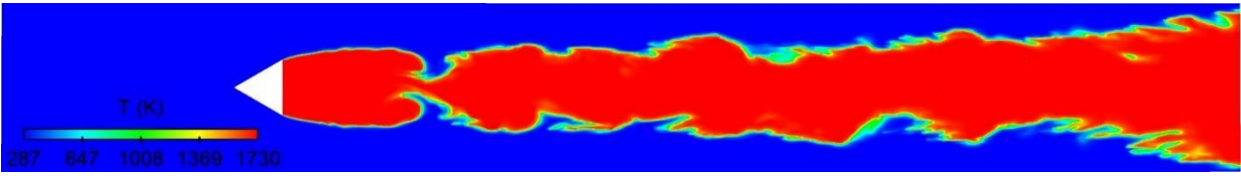
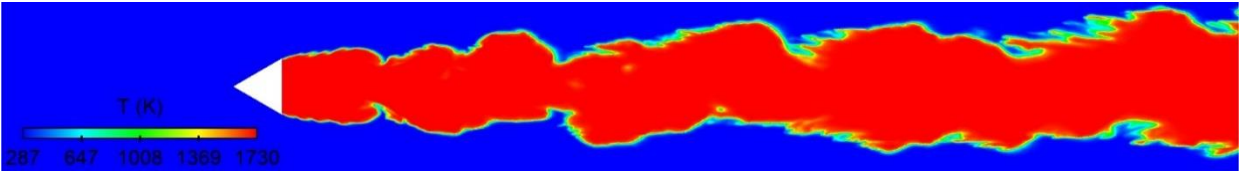


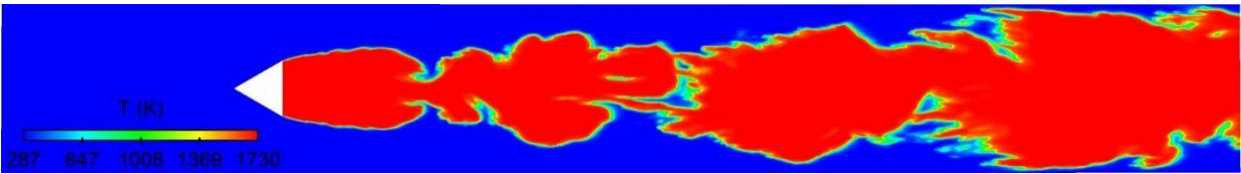
Figure 3.53. Transverse Mean CO mass fraction Profile on  $z/d=0$  plane with FGM [48].



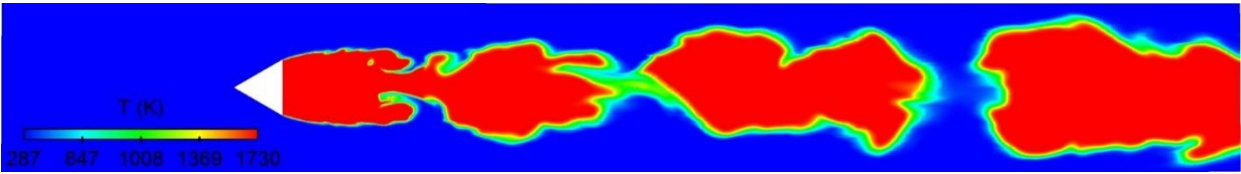
a. FGM (3mm)



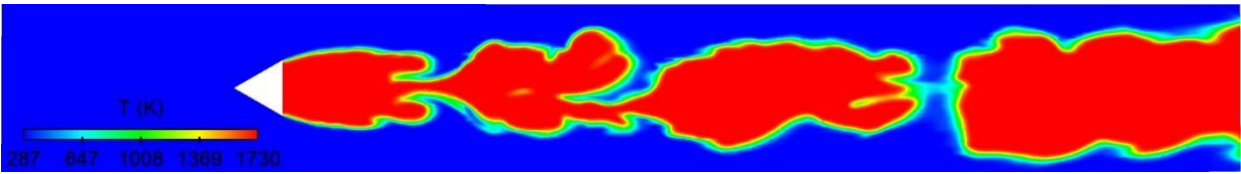
b. FGM (2.5mm)



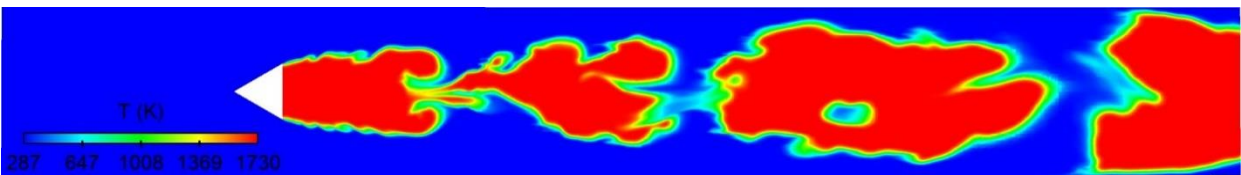
c. FGM (2mm)



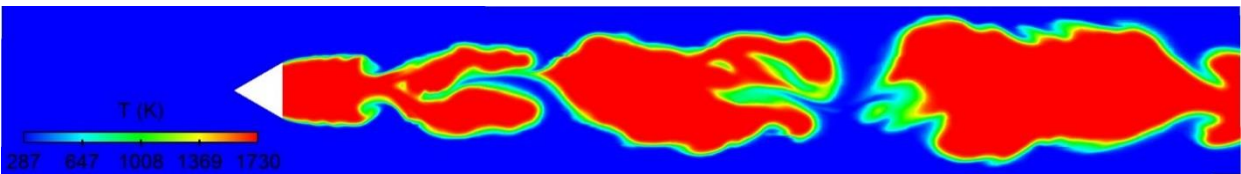
d. TFM, FTF=3 (3mm)



e. TFM (3mm)

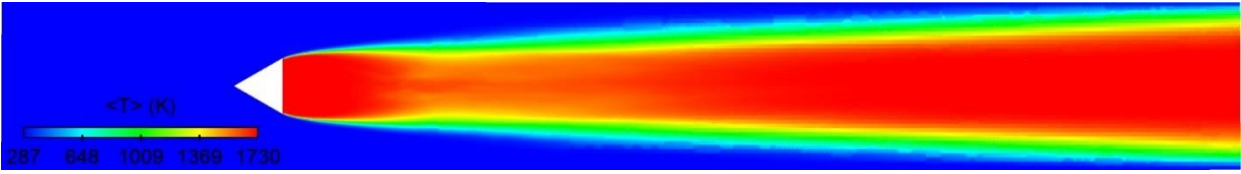


f. TFM (2.5mm)

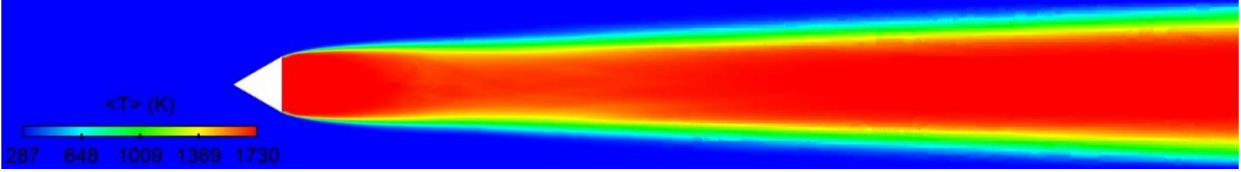


g. TFM (2mm)

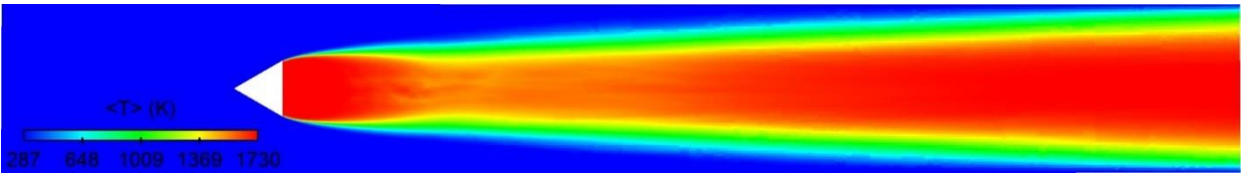
Figure 3.54. Temperature distribution in FGM (a-c) and TFM (d-g). TFM simulations have  $FTF = 7.0$  for (e-f) and  $FTF = 3.0$  for (d) [48].



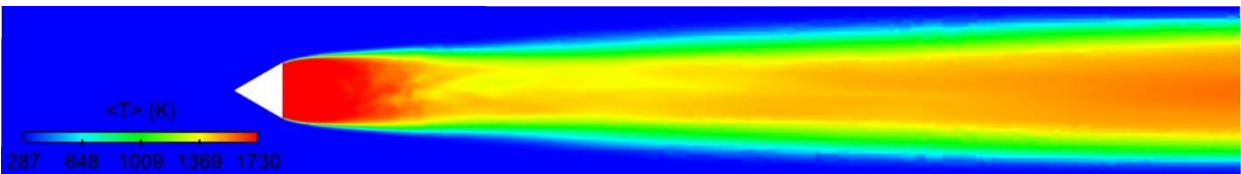
a. FGM (3mm)



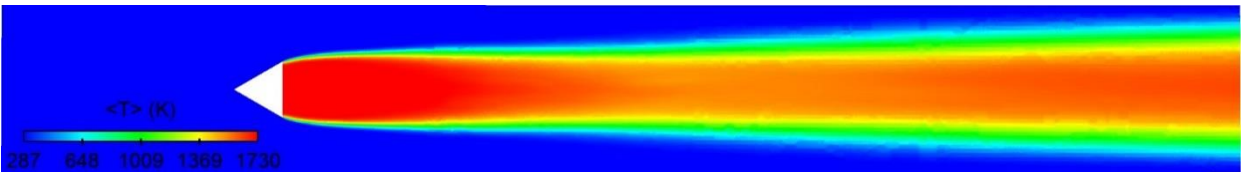
b. FGM (2.5mm)



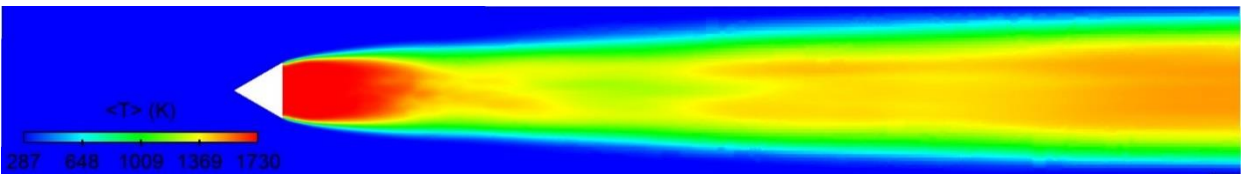
c. FGM (2mm)



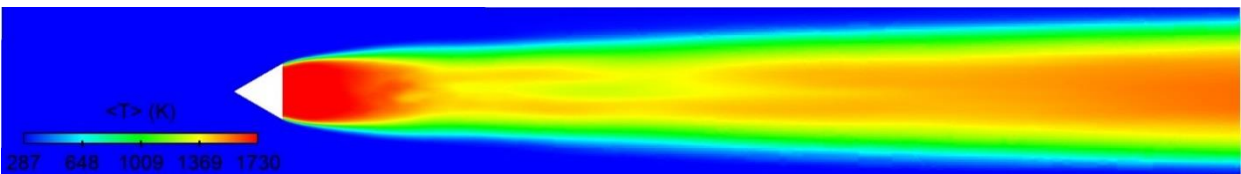
d. TFM, FTF=3 (3mm)



e. TFM (3mm)

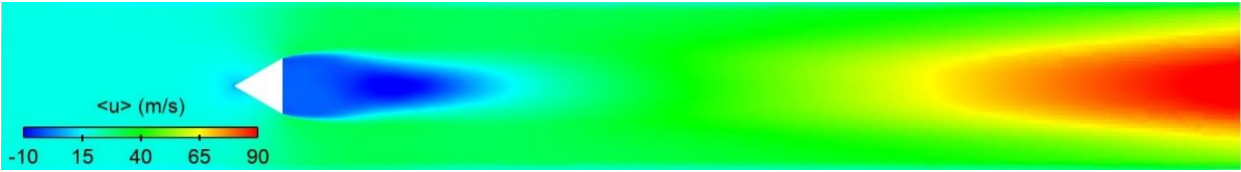


f. TFM (2.5mm)

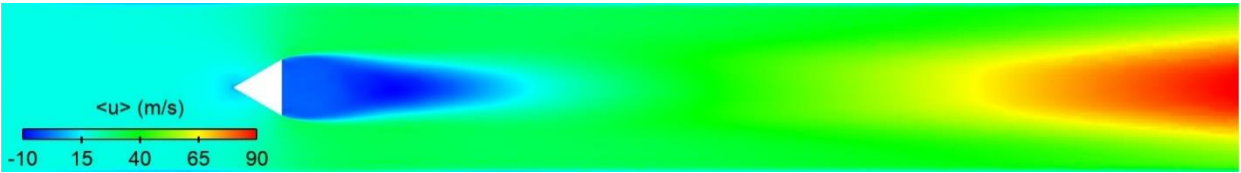


g. TFM (2mm)

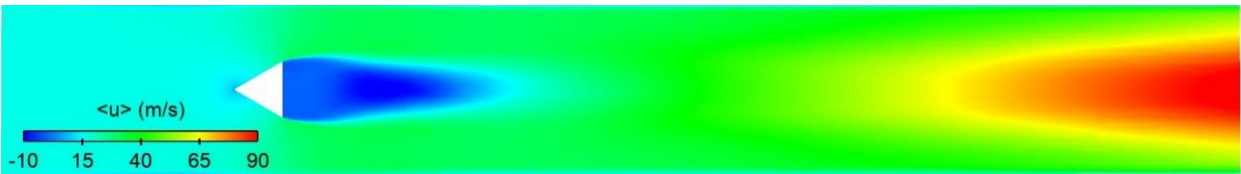
Figure 3.55. Time averaged temperature contours in FGM (a-c) and TFM (d-g). TFM simulations have  $FTF=7.0$  for (e-f) and  $FTF=3.0$  for (d) [48].



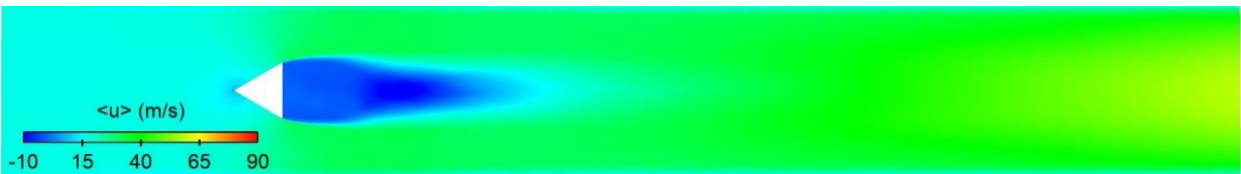
a FGM (3mm)



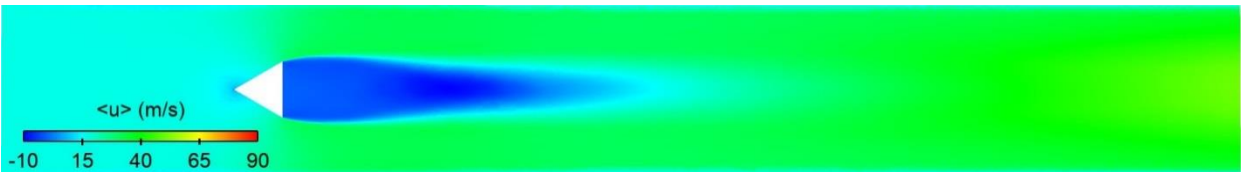
b FGM (2.5mm)



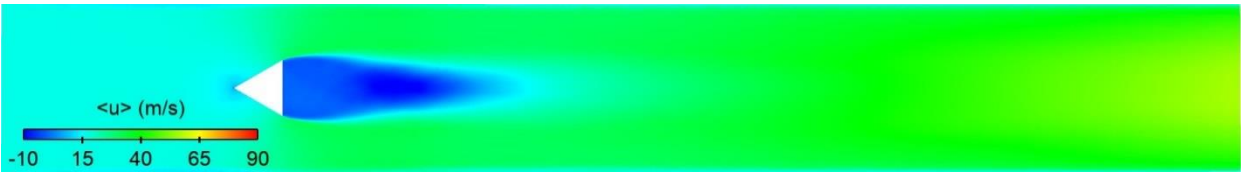
c FGM (2mm)



d TFM, FTF=3 (3mm)



e TFM (3mm)

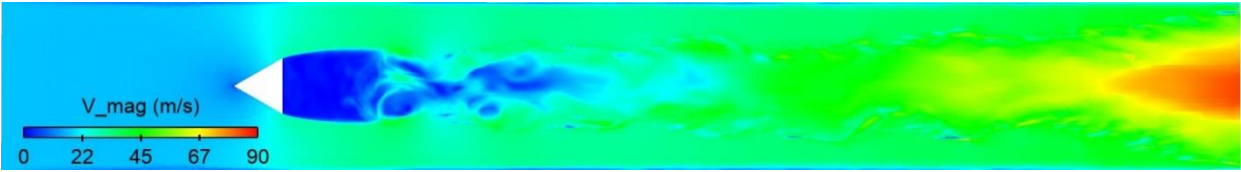


f TFM (2.5mm)

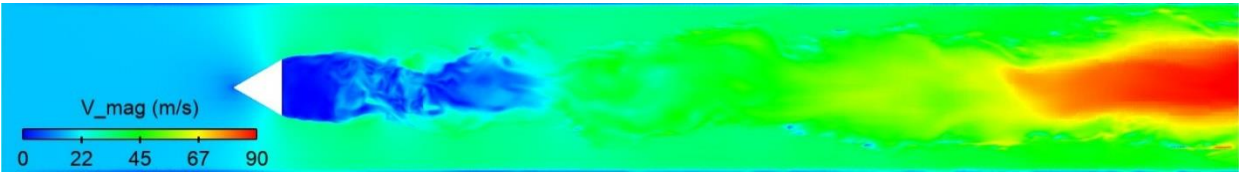


g TFM (2mm)

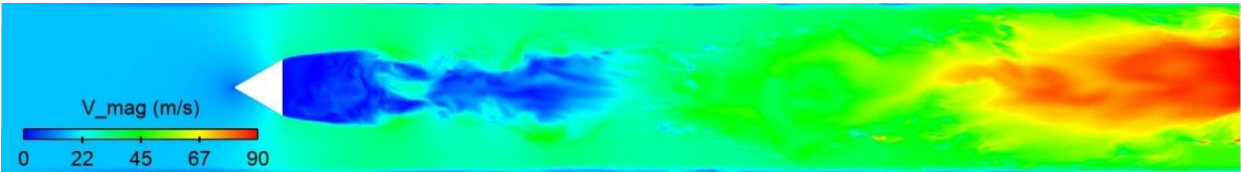
Figure 3.56. Time-averaged axial velocity distribution in FGM (a-c) and TFM (d-g) simulations. TFM simulations have FTF=7.0 for (e-f) and FTF=3.0 for (d) [48].



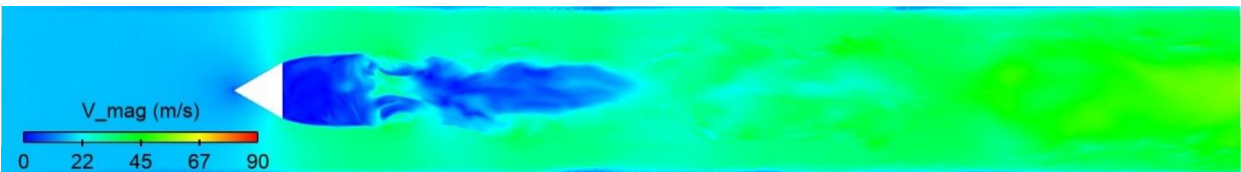
a FGM (3mm)



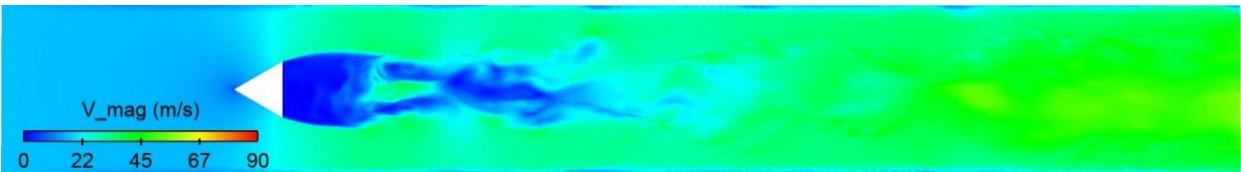
b FGM (2.5mm)



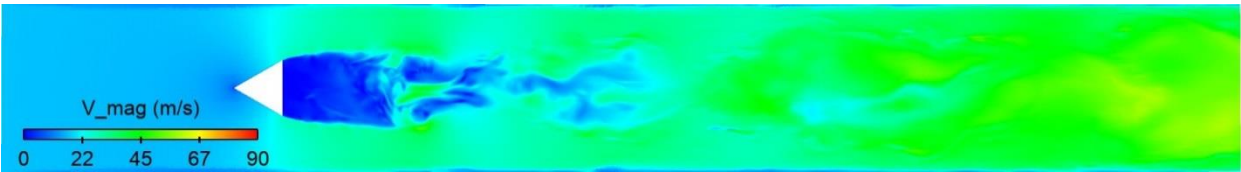
c FGM (2mm)



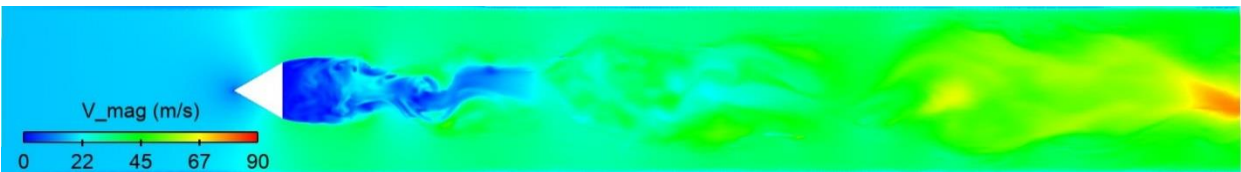
d TFM, FTF=3 (3mm)



e TFM (3mm)



f TFM (2.5mm)



g TFM (2mm)

Figure 3.57. Instantaneous velocity magnitude in FGM (a-c) and TFM (d-g) simulations. TFM simulations have  $FTF=7.0$  for (e-f) and  $FTF=3.0$  for (d) [48].

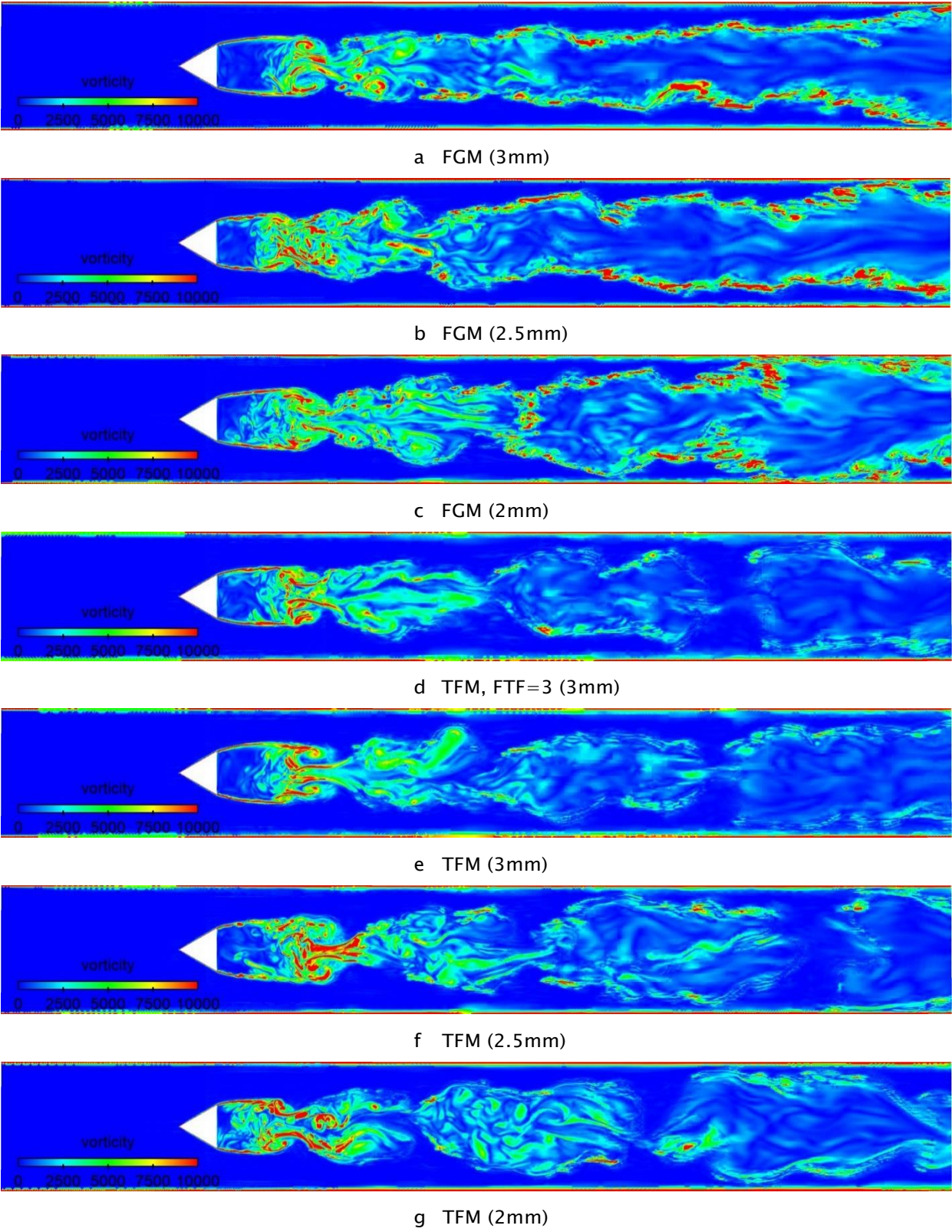


Figure 3.58. Instantaneous vorticity magnitude in FGM (a-c) and TFM (d-g) simulations. TFM simulations have FTF=7.0 for (e-f) and FTF=3.0 for (d) [48].

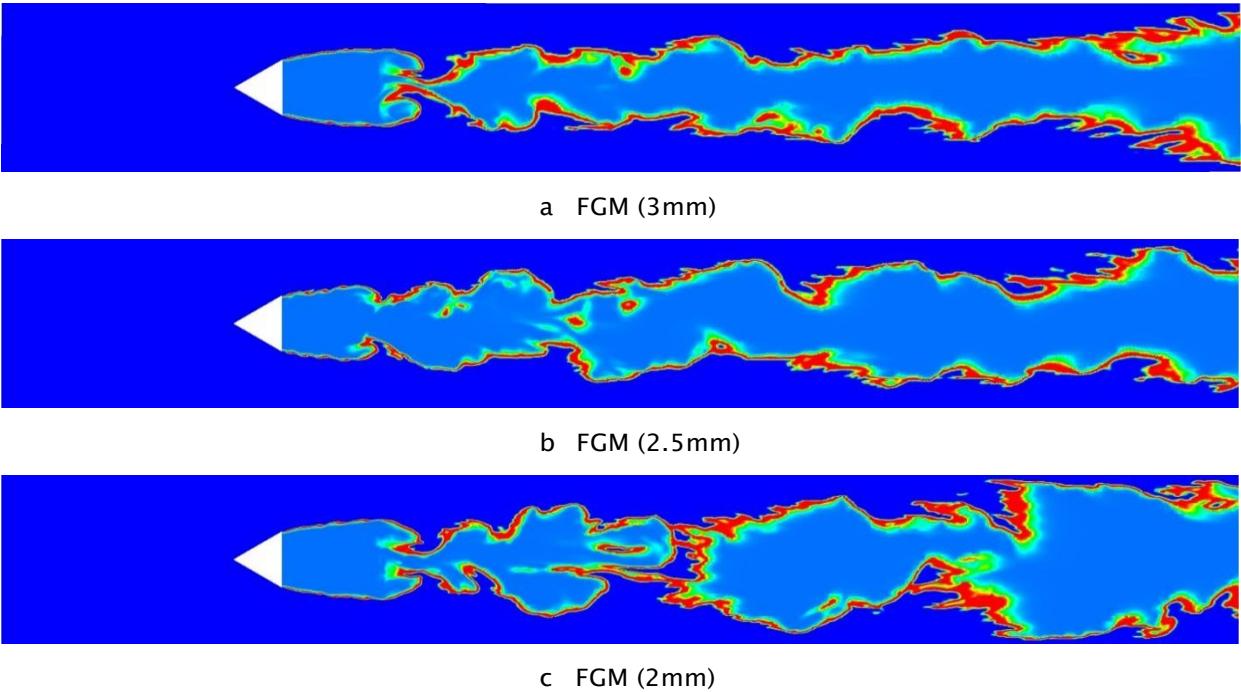


Figure 3.59. Instantaneous distribution of OH mass fraction in FGM simulations [48].

The grid convergence is studied for the premixed turbulent flame in a bluff body stabilized Volvo combustor using Flamelet Generated Manifold (FGM) and Thickened Flame (TFM) models in the LES framework on three grid resolutions of 3mm, 2.5mm and 2mm [48]. For all cases Adaptive Mesh Refinement adds further refinement, as needed, up to a maximum of 3 refinement levels, giving the smallest cell sizes of 0.375mm, 0.3125mm and 0.25mm for the three cases. The effect of the numerical wall boundary condition is also studied. The numerical results are compared against the experimental data and the major findings are outlined below:

1. We show that the mean temperature profiles are grid converged for both combustion models, FGM and TFM, at a 0.3125mm smallest cell size (2.5mm base mesh and 3 levels of refinement).
2. TFM shows a better match for axial velocity further downstream of the combustor ( $x=D > 4$ ). This is attributed to a better resolution of the flame front in TFM cases due to flame thickening. The FGM model over-predicts the burn-rate/overall heat-release, leading to a higher velocity downstream.
3. TFM with thickening factor 7 predicts a longer reattachment distance in the wake region for 3mm base mesh. Reducing the thickening factor to 3 in the region surrounding the re-

circulation bubble for the 3mm case, the results match 2mm base mesh and show grid-convergence.

4. Mean quantities for temperature, axial velocity, transverse velocity show grid-independent whereas the RMS profiles are sensitive to the grid resolutions near the center-line up-to  $y=D = \pm 0.5$ .
5. Trend-wise variations in CO profiles are predicted correctly with the FGM model but results show dependency on the grid resolution.
6. The effect of numerical boundary condition for the wall, namely adiabatic and prescribed temperature, was found to be minimal. This is not surprising as the flame stays mostly away from the wall and the gas close to the wall is mostly at free-stream temperature. It is clear that the wall heating would be mostly dominated by radiation, which is not considered as part of this study.

## 4. NONREACTING SIMULATION

The material presented in this chapter is obtained from the author's AIAA conference paper [1]. Numerical simulations are first performed under the non-reacting conditions to calculate the flow-split through various parts of a realistic gas turbine combustor inclusive of swirler passages, dilution jets, and all effusion/slot cooling holes [1, 4, 119]. Numerical simulations including hardware details such as liners with effusion holes are challenging due to: (a) highly complex meshing of a large number of tiny effusion holes, and (b) requirement for an optimized robust mesh for a faster turnaround time to support engineering design calculations. With the goal to optimize turnaround time and accuracy, flow-split studies are carried out using steady-state Reynolds Averaged Navier-Stokes (RANS) and Large Eddy Simulation (LES) approaches. The results help establish the efficacy of numerical simulations in the determination of combustor flow splits. The method used in the numerical calculation of component-wise flow splits involves closing all other passages except the one of interest while maintaining the pressure drop and is similar to the method used in the experiments. The total flow split, in turn, is estimated with all flow passages open, allowing for interaction with different flows. This study is aimed at establishing a computational method for capturing the flow-splits and the velocity fields which in turn are essential for predictive gas turbine simulations.

### 4.1 Determination of the number of cells across cooling holes

The material presented in this chapter is obtained from the author's AIAA conference paper [1]. Computing flow through tiny effusion holes requires knowledge of the mesh resolution needed for engineering calculations [1]. A fine mesh with a resolved boundary layer may be desirable but it also makes the CFD model computationally very expensive. A single sector of a combustor can have 1000-2000 effusion holes which would not only need a huge number of boundary layer cells (10-20 million) but the meshing itself is very challenging. The sharp corners at the inlet and outlet of each hole pose a big challenge for the meshing tools and a compromised mesh also affects the robustness of the solver. Hence, it is imperative to find the balance between computational time and accuracy which can offer a fast and robust engineering solution to serve the gas turbine industry. To address this problem, a separate validation exercise is undertaken for flow through a

single hole with law-of-the-wall boundary condition instead of a no-slip wall. The single hole with crossflow on both ends is representative of an effusion hole. The study will help validate the efficacy of the law-of-the-wall boundary condition and also help understand the minimum mesh resolution needed for accuracy. The methodology is validated against an independent experiment that mimics the flow through an effusion hole of a combustor. Experimental data are available for the discharge coefficient ( $C_d$ ) for a cylindrical film hole at different inclination and orientation angles with respect to crossflow, over a wide range of internal and external flow conditions[26].

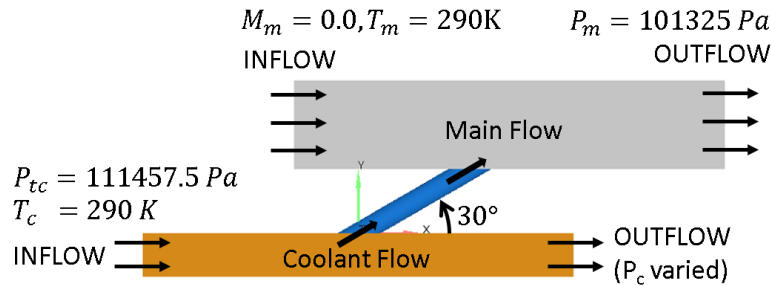


Figure 4.1. Computational domain and boundary conditions for a single hole study [1].

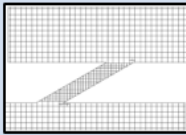
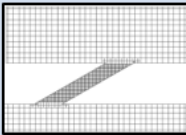
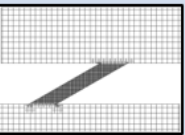
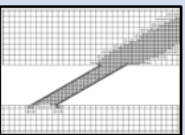
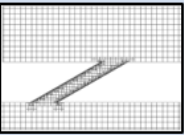
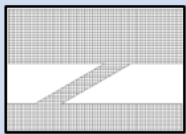
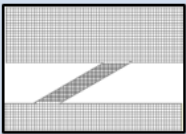
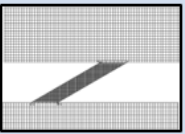
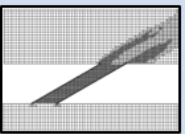
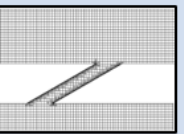
# of Cells across tube	FE 4 cells	FE 8 cells	FE 16 cells	Velocity AMR 7-14 cells	$Y^+$ AMR 8-10 cells
4mm base mesh					
Cell count	19K	24K	61K	67K	41K
2mm base mesh					
Cell count	131K	136K	173K	344K	231K

Figure 4.2. Computational grid for  $C_d$  sensitivity study. FE stands for Fixed Embedding [1].

The material presented in this chapter is obtained from the author's AIAA conference paper [1]. The test case chosen for this study is a 10 mm hole with a 30° inclination angle and 0° orientation angle and is shown in Figure 4.1. Inflow total pressure is 111.45 kPa and temperature

290K. The outflow static pressure is varied to get different crossflow Mach numbers at the inlet of the hole. The cross-flow Mach number on the exit side of the hole is zero with temperature set to 290 K and outlet static pressure 1 atm. The two base cell sizes considered in this study are 4 mm and 2 mm [1]. For a fixed base cell size, the mesh in the hole region is varied by adding a fixed embedding (FE), using AMR based on second gradients of velocity and  $Y^+$  to get different mesh resolutions to understand the sensitivity on computed discharge coefficient. Figure 4.2 shows the mesh at each refinement level for both base mesh sizes and the corresponding total cell count. All single hole studies are carried out using the RANS and  $k - \epsilon$  turbulence model.

The material presented in this chapter is obtained from the author's AIAA conference paper [1]. Steady-state RANS results are compared against the experimental data for a single hole discharge coefficient ( $C_d$ ) with different mesh resolutions as shown in Figure 4.2 [1]. These results correspond to a pressure drop of 10% across the hole. The computed  $C_d$  results are plotted as a function of hole inlet cross-flow Mach number ( $M_c$ ). RANS models underpredict the value of  $C_d$  up to an inlet crossflow Mach number of  $M_c < 0.25$  and then it over predicts. The sharp decrease in  $C_d$  is observed in the experiments after  $M_c > 0.3$  which is not captured with the RANS model. A similar conclusion is reached in [120] where the authors use 50 cells across the holes and try to resolve the boundary layer. As the inlet cross-flow Mach number increases, the size of the separation bubble at the hole inlet also increases causing deviation in the  $C_d$  prediction. The RANS  $k - \epsilon$  realizable model is over predicting the separation bubble size with Mach number, resulting in a slightly lower  $C_d$  values. The results show grid independence with cell size of around 2 mm for a 10 mm hole. This corresponds to 5 cells across the 10 mm cylindrical hole. Refining the mesh further by decreasing smallest cell size does not have much impact on the prediction of  $C_d$ . On the other hand, additional refinement increases the total cell count and therefore, total computational time. The observation from this study is that it may be difficult to capture the detailed flow physics inside individual cooling holes with "law of the wall" approach near wall and fewer computational cells but the approach is reasonably sufficient for computing nearly accurate mass flux and direction for engineering calculations in complex industrial geometries with an added advantage of faster run-times and robust meshing.

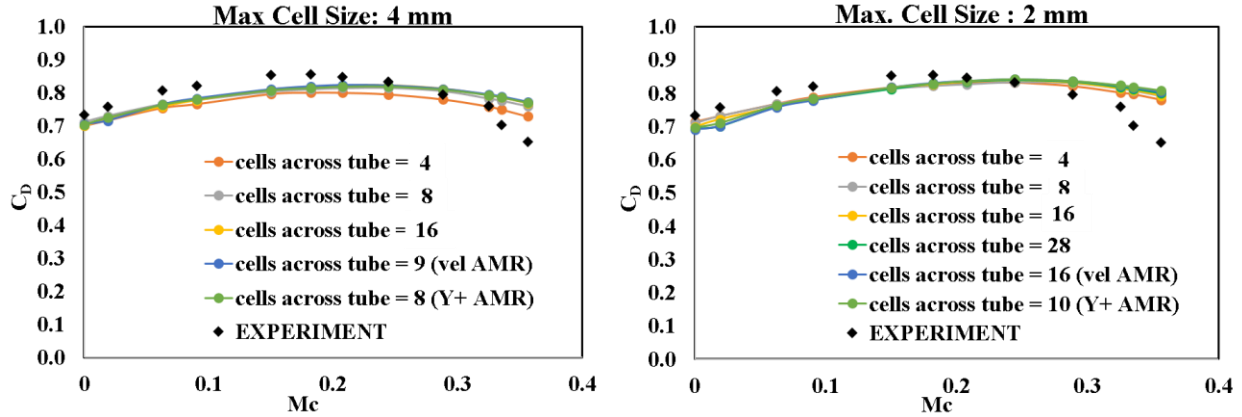


Figure 4.3. Mesh sensitivity results for the coefficient of discharge for a single hole study with RANS model [1].

#### 4.2 Flow rate calculations through swirler passages (component-wise)

The material presented in this chapter is obtained from the author's AIAA conference paper [1]. Mesh sensitivity study is carried out using steady-state RANS with all swirler passages open while dilution, effusion, and film cooling holes are sealed off [1, 4]. For this arrangement, only the total flow rate is available from the experimental data for comparison. The computed total flow rates are compared for different mesh resolutions in Table 4.1 and it is observed that the total flow rate is matching well with experimental data with a maximum deviation of 1.62% for the coarse mesh case. All passages show grid convergence for flow rate calculations. Based on this study, a maximum cell size of 3 mm and a minimum cell size of 0.375 mm are chosen for component-wise flow split calculations. For the component-wise flow split study, a comparison between the experimental and computed results is presented in Table 4.2 [4]. Figure 4.4 shows a bar chart comparing the swirler flow splits with the experimental data. Computed results are in excellent agreement with experimental data for outer axial, inner axial and radial swirlers [4]. Both RANS and LES underestimate (by about 22%) the order of magnitude smaller swirler cooling flow [4]. However, the flow splits contributing to over 95% of the total flow are captured accurately by both computational models [4].

Table 4.1. Flow splits comparison for an experimental total flow rate of 31.8 g/s for swirlers (all passages open) with RANS for a maximum cell size of 3 mm and different mesh resolution [1].

Flow passage	Flow rates (g/s)		
Total Cells (Millions)	10	21	35
Outer Axial Swirler	14.1	14.0	14.01
Inner Axial Swirler	10.4	10.2	10.2
Radial Swirler	6.8	6.7	6.7
Cooling Holes	1.1	1.1	1.0
Total	32.31	32.0	32.0

The material presented in this chapter is obtained from the author’s AIAA conference paper [1]. The mean velocity magnitude contours are plotted for swirler passages in Figure 4.5 [1]. Flow from the outer axial swirler turns 90° just after exiting the swirler and flows along with the deflector plate and then turns axially near the liner and flow along the liner walls. Airflow through inner axial swirler flows inward close to the exit and it expands radially outwards as it exits the swirl cup and enters the combustor. Air from radial swirler flows along the walls of the swirler cup and exits radially outwards into the combustor. Swirler flow behavior changes when there is flow through all the passages as it is seen in the velocity contours at the bottom panel of Figure 4.5. The interactions between the airflow from each passage make the overall flow exit the swirl cup radially outwards and not along the deflector plate.

Table 4.2. Comparison of component-wise swirler flow rates with experimental data for 10 million cells [1].

	Measured		Present Work				Erdmann et.al[19]	
			RANS)		Computed (LES)		RANS	
	g/s	%	g/s	%	g/sec	%	g/s	%
Outer Axial Swirler	13.35	41	13.36	41	13.25	41	13.61	42
Inner Axial Swirler	10.08	31	10.30	32	10.36	32	10.36	32
Radial Swirler	7.60	23	7.58	23	7.61	23.5	7.16	22
Swirler Cooling Holes	1.51	4.7	1.16	3.6	1.18	3.6	1.23	3.8

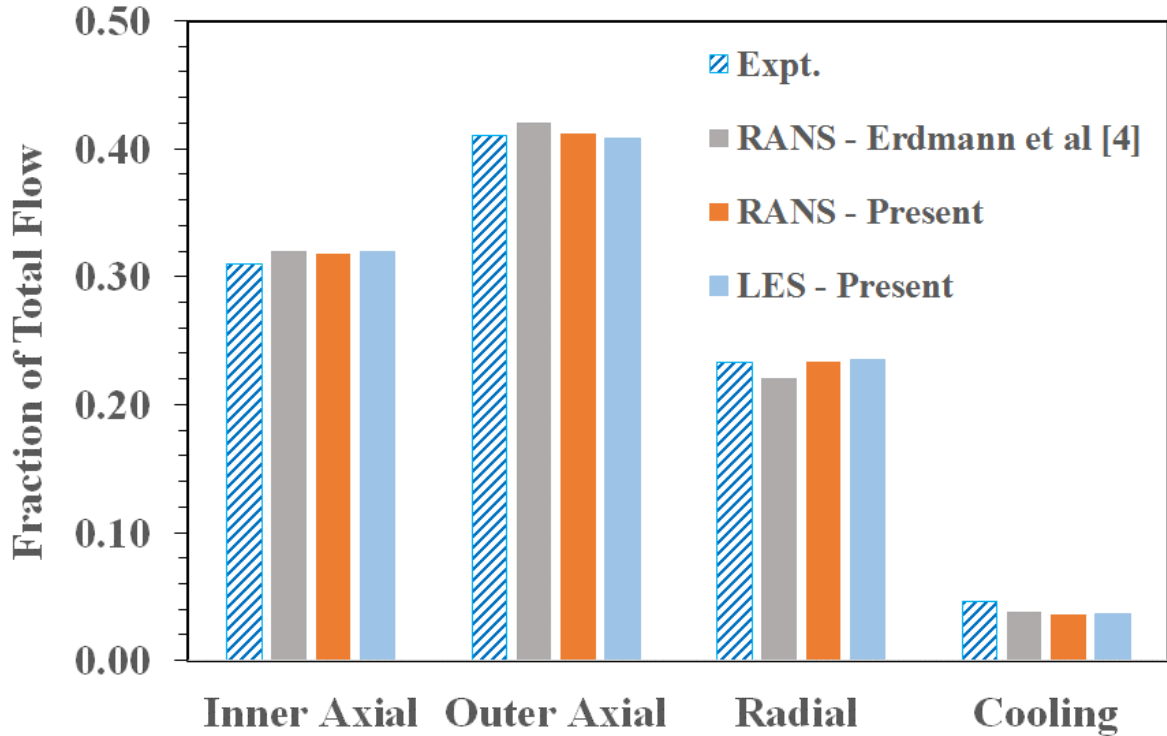


Figure 4.4. Comparison of component-wise flow splits for swirler passages for 10M cells [1, 4].

### 4.3 Flow rate calculations through all passages on the combustor liners

The material presented in this chapter is obtained from the author’s AIAA conference paper [1]. RANS model is evaluated for a total cell count of 10 million with a maximum cell size of 3 mm and a minimum cell size of 0.375 mm [1, 4]. The LES model is evaluated for a total cell count of 10 million and a total cell count of 21 million. The LES results for the two different meshes show grid convergence for flow splits. Both RANS and LES estimate similar flow split for total swirler, total dilution, and total effusion flow and comparison with experimental data and previous literature in Figure 4.6. Total swirler flow is overestimated by 19% with the coarse mesh and by 17.6% with the fine mesh; total dilution flow is overestimated by 14% with the coarse mesh and 9% with the fine mesh, and total effusion flow underestimated by 11.7% with coarse mesh and 10.6% with fine mesh [1, 4]. The differences between experiments and computations can be attributed to the interactions between the flows from multiple passages, numerical errors associated with model limitations and also three systematic errors associated with the experimental procedure [20] in arriving at the experimental flow rates at the near LBO stable condition [1, 4].

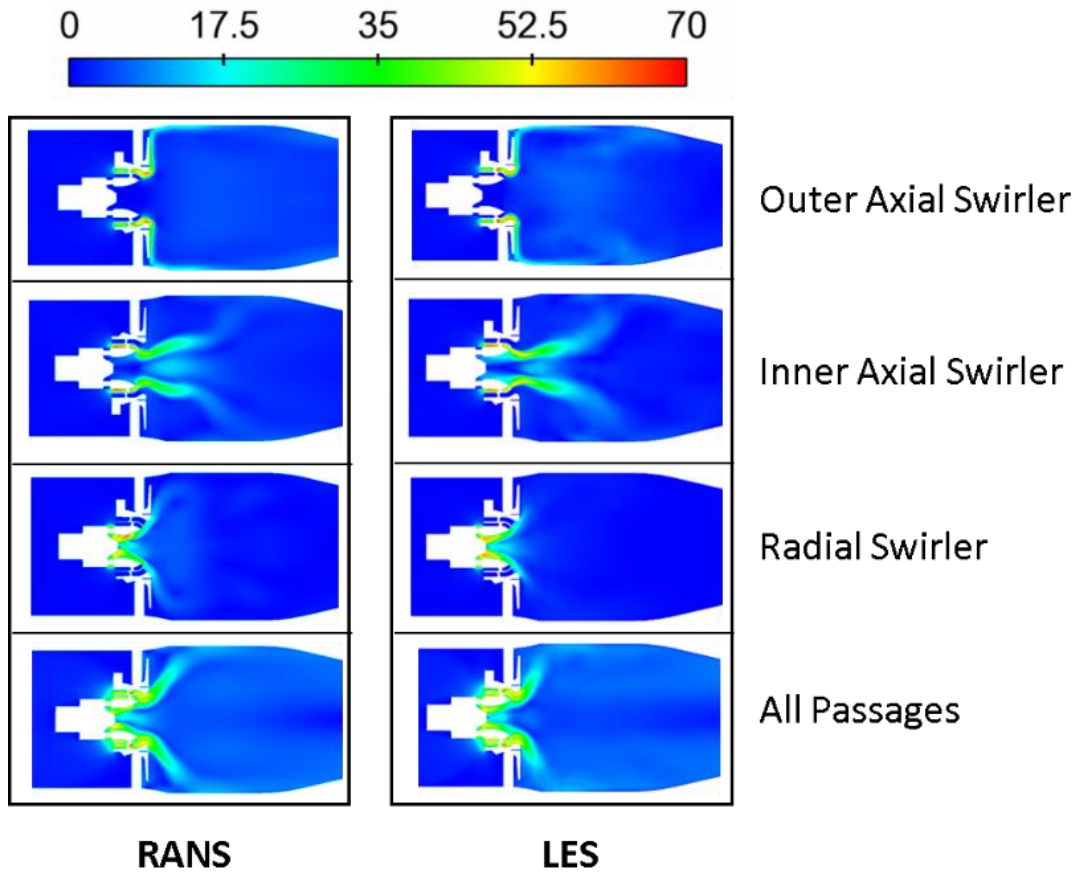


Figure 4.5. Mean velocity (m/s) contours for swirler flow paths: RANS (left) and LES (right) for 10 million cells [1].

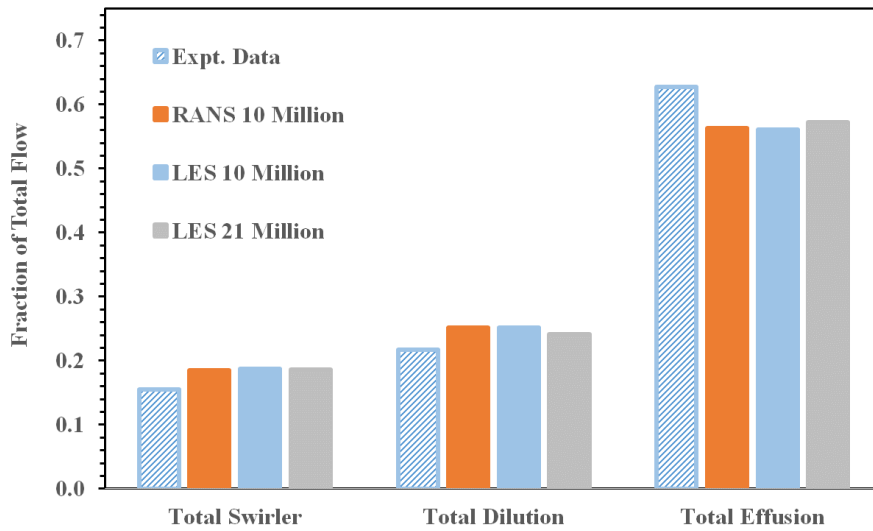


Figure 4.6. Comparison of combustor flow splits [1].

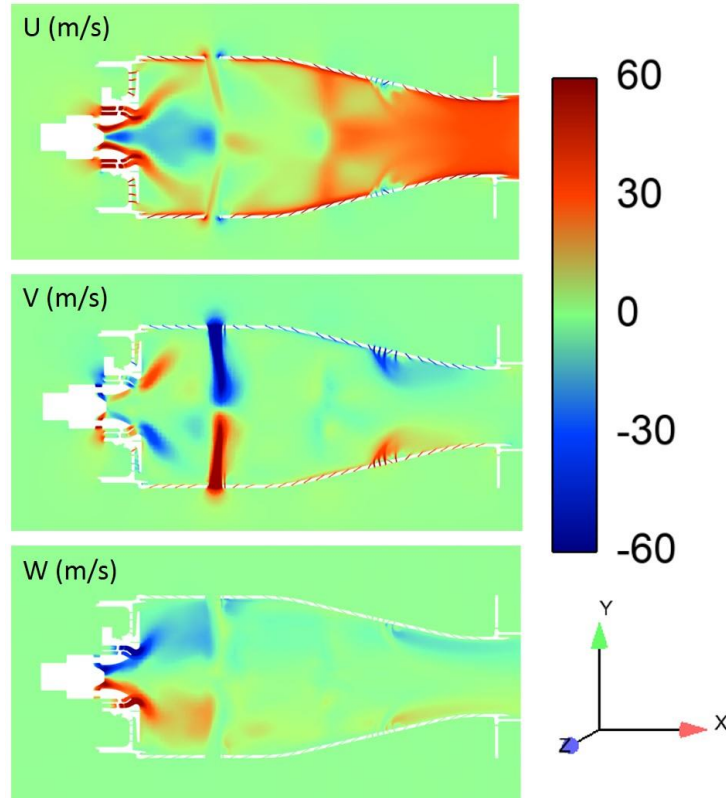


Figure 4.7. LES time-averaged velocity (m/s) components on mid-plane for 10 million case (all passages open) [1, 4].

The material presented in this chapter is obtained from the author's AIAA conference paper [1]. The mean velocity components on  $XY$ -plane at  $Z=0$  (center) plane are shown in Figure 4.7 [1] [1, 4]. The axial velocity contours on the top panel clearly show the flow recirculation region at the center of the primary zone, higher velocity in the shear layers and flow acceleration in the convergent section. The middle panel for  $Y$ -velocity contours shows positive velocity for flows aligned in the positive  $Y$ -direction and negative for flows aligned in the negative  $Y$ -direction. The bottom panel for  $Z$ -velocity clearly shows the clockwise (looking from the exit) rotation of the swirling flow in the primary zone. The mean velocity magnitudes on the  $XY$ -plane at  $Z=0$  are shown in Figure 4.8 [1, 4]. Air flows through all swirler passages interact resulting in a radially outward airflow entering the combustor. The primary dilution holes result in the highest velocities and their impingement leads to local flow reversals in this cross-section. The bending of the cross jets in the streamwise direction is observed. However, the dilution jets have a high enough momentum to impinge upon each other. A relatively low-velocity region exists beyond the cross-

flow jets and the primary zone. Flow is accelerated as it passes through the convergent section. The flows from the effusion holes form a film on the liner walls and pass along the wall. While the overall flow field seen in Figure 4.8 is highly symmetric around the X-axis, small dissymmetries observed in the experiments are also captured in the results of the simulations. For example, the measured angles of the cross-jets are 13 and 14 degrees while the computed angles of the cross-jets are 12 and 13 degrees respectively. While these comparisons are encouraging, more quantitative measurements of velocities and other detailed flow features are proposed for comparison with the LES results [1, 4].

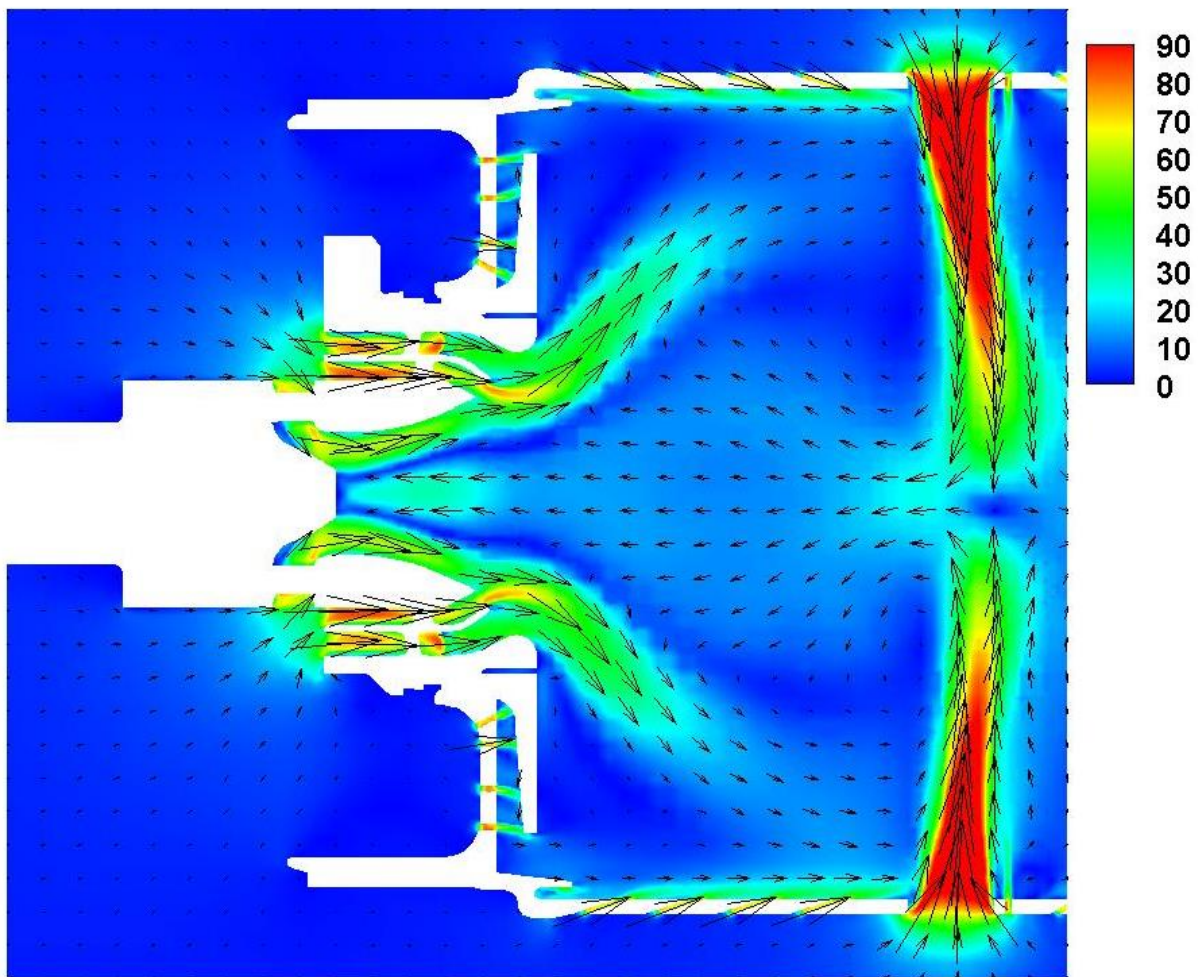


Figure 4.8. LES time-averaged velocity magnitude (m/s) on mid-plane with velocity vectors for 10 million cells (all passages open) [1, 4].

The material presented in this chapter is obtained from the author's AIAA conference paper [1]. The primary zone aerodynamics and the air-fuel ratio play a major role in achieving the desired combustion characteristics and flame stability over a wide range of operating conditions [1, 4]. The two counter-rotating large scale recirculation zones observed in the primary zone are created by a combination of the swirler airflow and the opposed primary dilution jets as shown in Figure 4.8. When the flow is reacting, a portion of the hot products is entrained back into the unburnt mixture. These entrained products lead to the ignition of the incoming mixture. The swirl components imparted to the air by the hybrid swirler produce high turbulence, strong shear regions with rapid mixing rates [1]. The combustor aerodynamics in the primary zone and the first set of cross jets control the size and shape of the flame stabilizing counter-rotating vortices. The flow downstream of the primary zone is affected by the secondary cross jets, cooling holes, and their interactions. The computed flow features with the present methodology agree qualitatively with the established literature [1, 14].

The material presented in this chapter is obtained from the author's AIAA conference paper [1]. Detailed flow rate calculations are presented for component-wise as well as total flow splits for a complex combustor [1, 4]. RANS and LES models are employed with different mesh resolutions. A highly automated, on the fly meshing strategy, along with adaptive mesh refinement was used to demonstrate the feasibility of CFD modeling. The computational results are compared with non-reacting flow splits data from a complex combustor. It is observed that with the present meshing strategy of capturing the flow through effusion holes, a minimum of 5-8 cells per effusion hole is sufficient. The computed flow rates for individual passages at the actual test conditions are in good agreement with the experimental data. Grid sensitivity studies are reported for the combustor swirler configuration. The results for combustor total flow splits show under-prediction for the effusion flow and over prediction for dilution and swirler flows. Overall, the RANS, as well as LES calculations, capture similar flow splits compared to the experiments. Flow interaction effects between swirler and primary jets are observed to be significant in creating strong vortex structures with toroidal flow recirculation in the primary zone [1, 4].

## 5. LEAN BLOWOUT COMPUTATION AND ANALYSIS

Lean Blow-Out (LBO) calculations for an alternative bio-jet fuel (C-1) and conventional fuel (A-2) are performed using Large Eddy Simulations (LES) methodology discussed in Chapter 2 for a realistic gas turbine combustor [1-4, 47-49, 119]. The liquid spray is modeled with a Lagrangian approach, and finite rate chemistry is implemented using compact and HyChem reaction mechanisms developed for the A-2 and C-1 fuels [1-3]. The flamelet generated manifold model with a compact kinetic mechanism also implemented to demonstrate the fuel sensitivity to lean blowout with reduced computational time. Lean Blow-Out (LBO) conditions are reached by decreasing the fuel flow rate gradually in a stepwise manner. Four different kinetic mechanisms and two combustion models are evaluated in this study. The LES results are analyzed in detail to understand the mechanism of LBO and key markers for identification of the incipient LBO condition in a realistic gas turbine combustor. The material presented in this chapter is obtained from the author's AIAA conference papers [2, 3] and project progress report [4].

### 5.1 Lean blowout (LBO) simulation methodology

The material presented in this chapter is obtained from the author's AIAA conference papers [2, 3] and the project progress report [4]. LES simulations are carried out at a global equivalence ratio of 0.096, which was experimentally found to produce stable combustion [2-4]. From this condition, the fuel flow rate is reduced in a gradual stepwise manner with larger time steps first and progressively reduced flow rate reduction steps as evidence of impending blowout behavior is approached as shown in Figure 5.1. The simulations are run with a fixed global equivalence ratio for at least two flow-through times, estimated to be approximately 30 ms. The fixed equivalence ratio is maintained beyond 30 ms if a quasi-steady heat release rate is not reached during either of those limits. The heat release rate is used as a criterion for identifying the lean blowout. The global equivalence ratio steps resulting from this process are plotted as a function of time in Figure 5.1 for fuel A-2 on the left-hand side and fuel C-1 on the right-hand side. Experimental data shown as red filled circles indicate that the C-1 fuel shown on the right-hand frame blows out at higher equivalence ratio than for the A-2 fuel (left-hand frame).

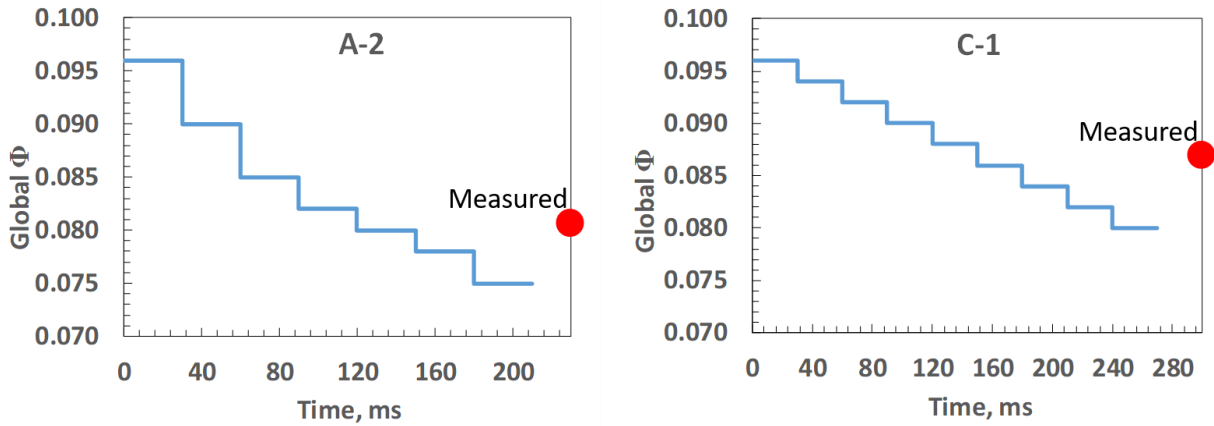


Figure 5.1. Staged fuel ramp down approach for LBO prediction. The red dot represents the measured lean blow-out global equivalence ratio [2-4].

## 5.2 Mesh sensitivity study

The material discussed in this chapter is obtained from the author’s project progress report [4] and the author’s AIAA conference papers [2, 3]. The mesh sensitivity study is carried to understand the effect of mesh resolution on the computed LBO equivalence ratio for C-1 fuel with Won-Dryer compact mechanism [2-4]. The mesh details are shown in Table 5.1 and corresponding computed lean blowout global equivalence ratio is shown in Figure 5.3. The 10M mesh evaluation under the reacting flow conditions showed that more than 95% of the turbulent kinetic energy is resolved in the combustor as shown in Figure 5.2. The volume integrated heat release rate is compared for different mesh resolutions in Figure 5.4. The stable heat release rate is noticed for both mesh resolutions at the near LBO condition showing stable flame corresponding to global equivalence ratio of 0.094 and then a decrease in heat release rate due to flame extinction at 0.092 for both mesh resolutions. It is noted from this study that minimum mesh resolution of 0.375 mm and 0.1875 mm considered in this study yielded the same LBO global equivalence ratio.

Table 5.1. Details of the minimum mesh resolution for establishing a mesh independent solution with a base size of 3 mm [2-4]

Total Cells (Millions)	10	25
Adaptive Mesh Refinement Level	3	4
Min.Cell Size, mm	0.375	0.1875

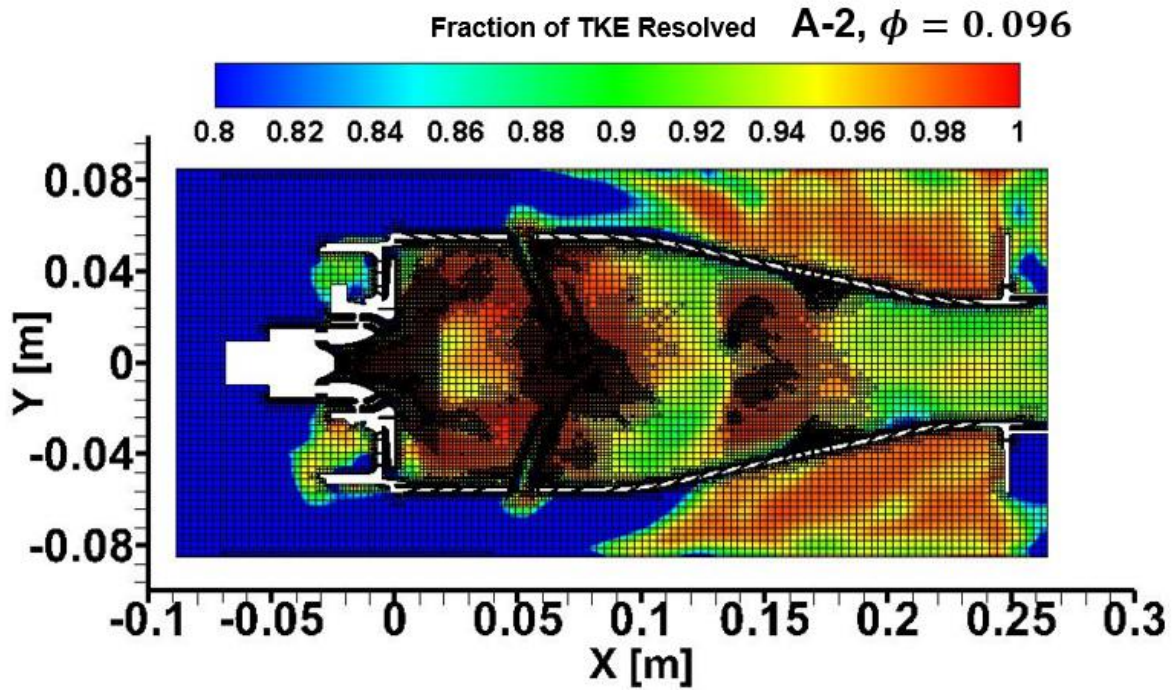


Figure 5.2. The fraction of resolved turbulent kinetic energy (TKE) with a minimum cell size of 0.375 mm and maximum cell size (base size) of 3 mm (total cell count is 10 million cells) [4].

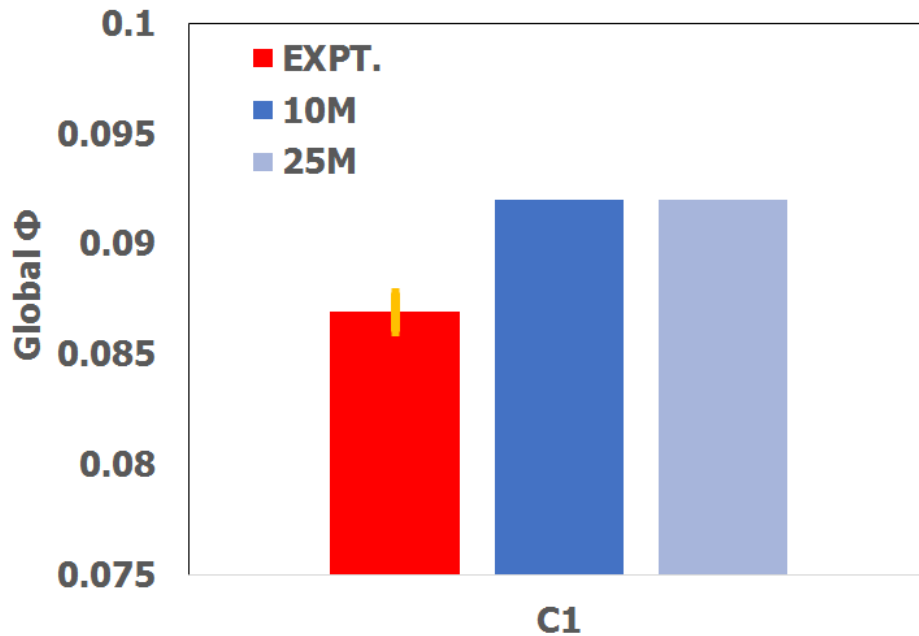


Figure 5.3. Effect of mesh resolution on the global LBO equivalence ratio for C-1 fuel [4].

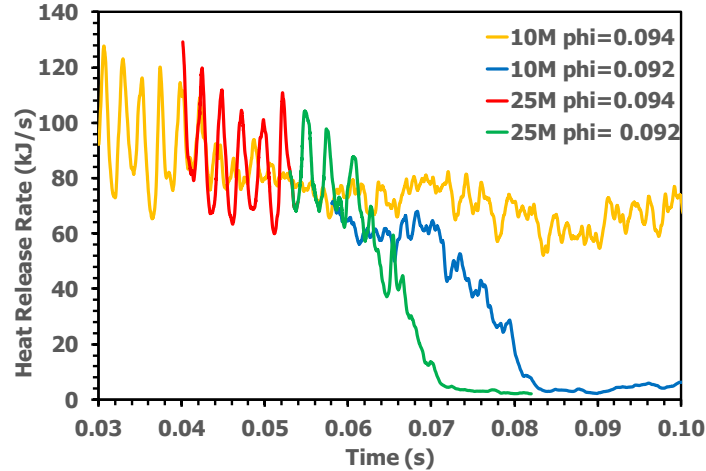


Figure 5.4. Effect of mesh resolution on the heat release rate for C1 fuel [4].

### 5.3 Reacting spray comparison at near LBO stable flame condition

The material discussed in this chapter is obtained from the author's project progress report [4] and the author's AIAA conference papers [2, 3]. Spray statistics are calculated from LES simulations at a stable operating point over a period of two flow-through times [2-4]. The averaging process over two flow-through times is started after the flame and heat release rate reached a quasi-steady state. Figure 5.5 shows the experimental [12] and predicted statistics of droplets with finite rate chemistry (FRC) and flamelet generated manifold (FGM) combustion models at four axial stations as a function of radial distance. The fuel spray exhibits a pattern with smaller diameter droplets near the hollow cone surface 10mm downstream of the nozzle exit. This distribution widens in the radial direction as we go towards the downstream locations with larger droplets towards the center and vice-versa. Both combustion models with LES are able to satisfactorily capture this trend for both the fuels. Better agreement with experiments is observed for the downstream locations. Axial and radial velocities increase away from the center and then decrease again with increasing spray cone angle. These trends are accurately captured for the near-nozzle regions as well as in downstream regions for both fuels. Overall, the Lagrangian spray setup is able to accurately capture the spray breakup and evaporation.

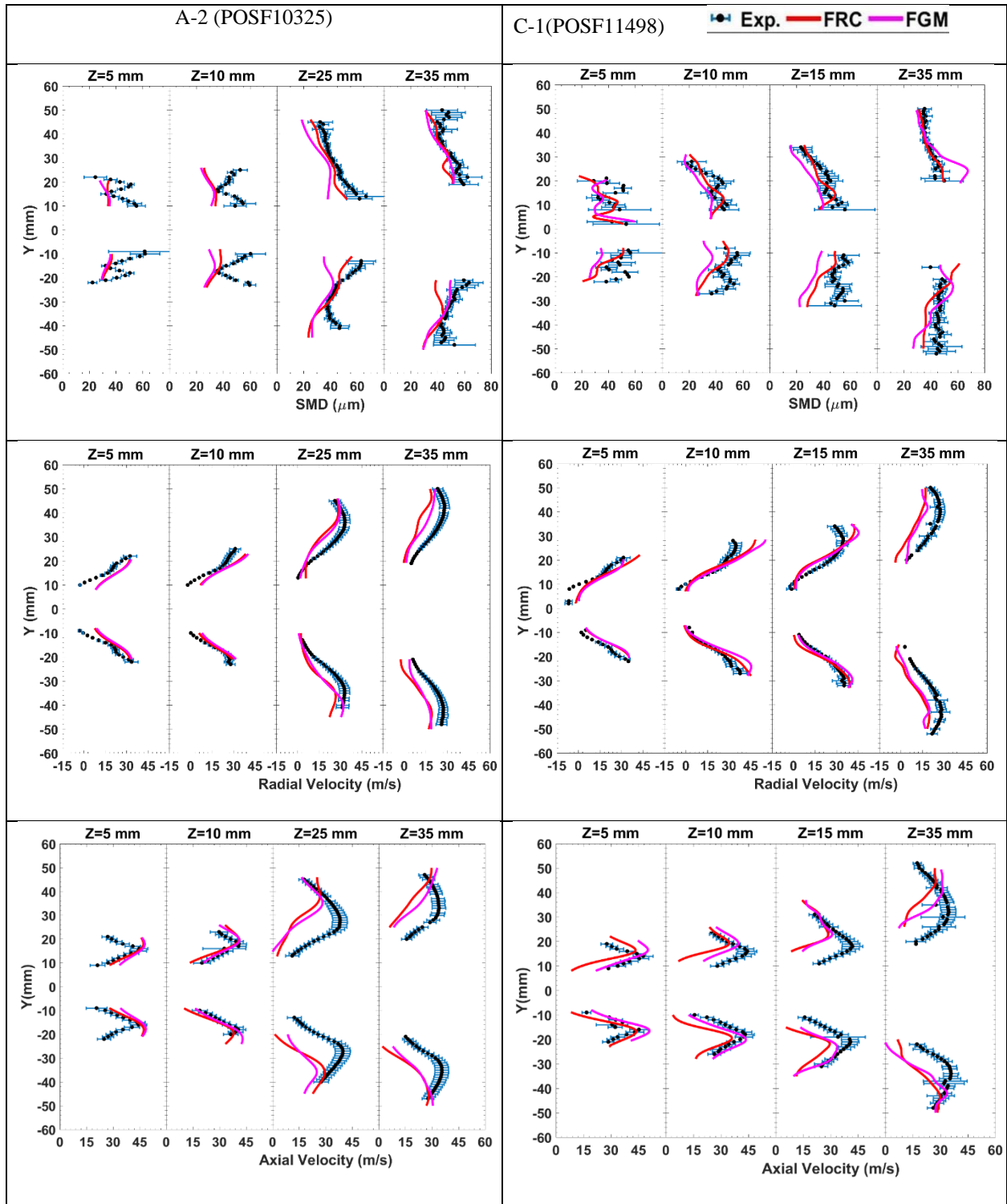


Figure 5.5. Spray statistics comparison with PDPA data [12] for a stable flame at  $\phi = 0.096$  [2-4].

## 5.4 Flame shape comparison at near LBO stable flame condition

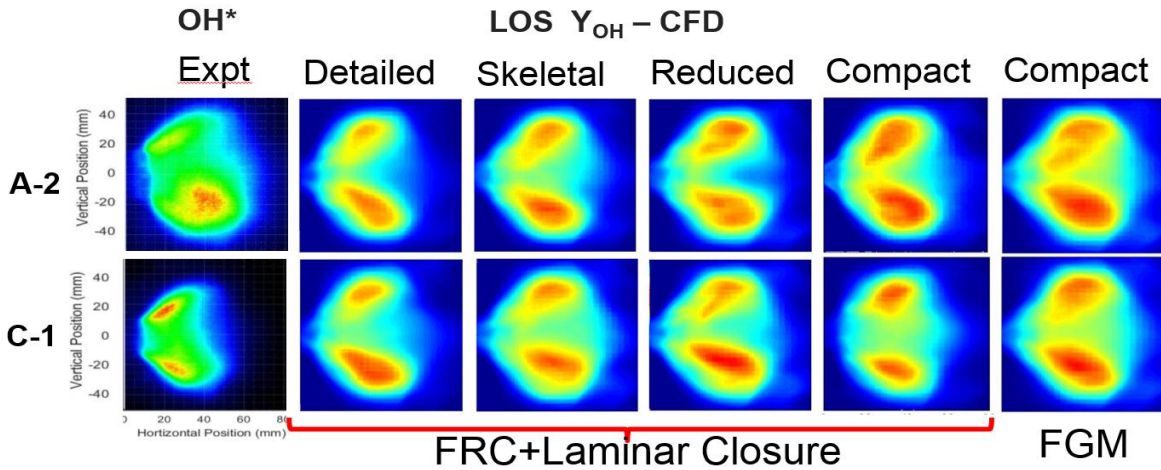


Figure 5.6. Line of Sight averaged mass fraction of OH from LES compared with experimental OH\* from chemiluminescence [2-4].

The material discussed in this chapter is obtained from the author's project progress report [4] and the author's AIAA conference papers [2, 3]. The OH\* chemiluminescence data from UIUC experiments [12] is utilized to compare the line of sight averaged OH mass fraction from LES simulations with two combustion models [2-4]. They are reported for detailed, skeletal, reduced and compact mechanisms in Figure 5.6 alongside experimentally observed OH\* chemiluminescence. The results from the compact, detailed, the skeletal and the reduced mechanisms are qualitatively similar. The experimental data (OH\* chemiluminescence) and the results of the detailed mechanism calculations (OH) show a similar spread in radial and axial directions. It must be noted these comparisons are qualitative in nature. The experimental images are based on false color and do not indicate a quantitative measurement of the OH field. The horizontal position of 0 mm corresponds to the deflector plate. OH formation marks the high-temperature heat release regions which extend 50 mm downstream of the deflector plate and also correspond to the downstream location of first row of dilution holes. This is the flame stabilization region of the swirl-stabilized flame. It exhibits a truncated cone shape with high regions of OH/heat release corresponding to the cone angle of the hollow spray cone. This indicates strong burning and heat release near the spray cone surface downstream of the swirl cup. The A-2 fuel exhibits a higher degree of asymmetry in OH\* for this configuration and measurements. These regions of intense heat release are captured qualitatively by all the four chemistry mechanisms. The computed

flame shape with FGM combustion model shows stronger and larger reaction zone compared to FRC model.

### 5.5 The heat release rate from stable flame to lean blowout

The material discussed in this chapter is obtained from the author’s project progress report [4] and the author’s AIAA conference papers [2, 3]. The evolution of heat release rates for each equivalence ratio and the two different fuels with finite rate chemistry combustion model and compact and HyChem skeletal mechanism are shown in Figure 5.7 [2-4]. The flame is observed to be stable for the first couple of milliseconds, this is followed by a steady decrease and eventually by a sharp drop in heat release rate for both A-2 and C-1 fuels. The heat release rates are allowed to reach a steady-state before the next step down. The evolution of heat release rates with FGM combustion model with mean heat release rate (dotted black line ) and ideal heat release rate (ideal heat release rate) are shown in Figure 5.8.

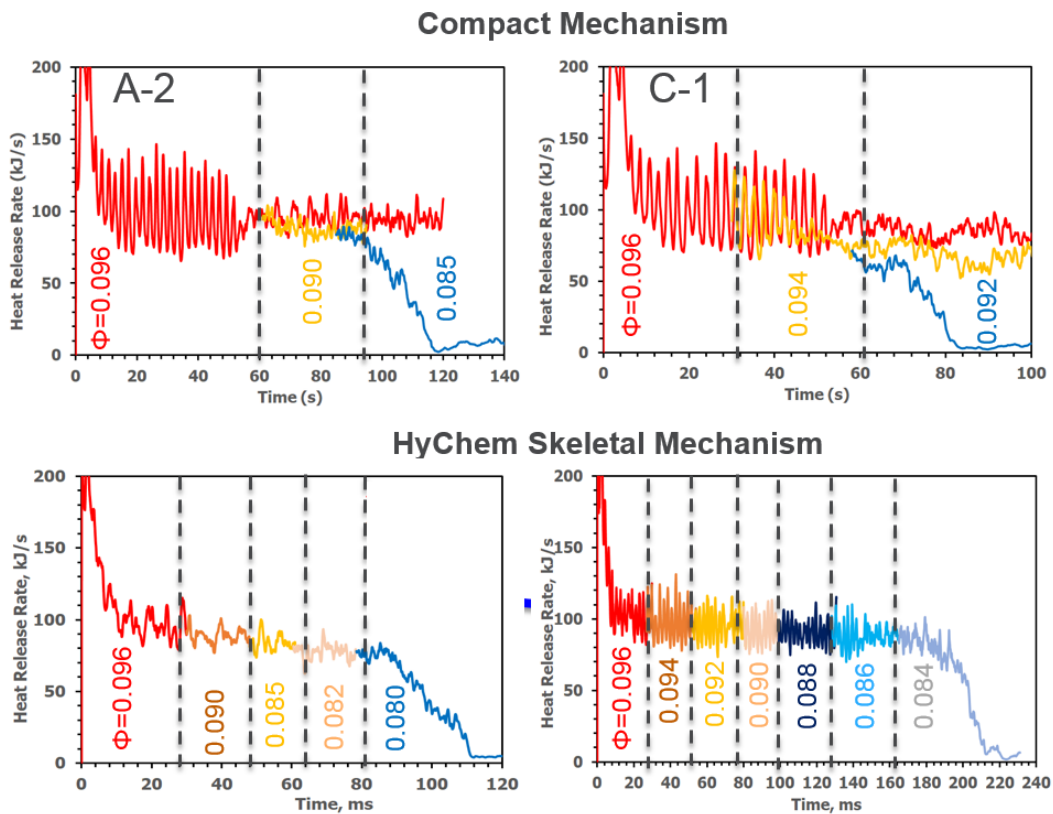


Figure 5.7. Heat release rate with detailed chemistry simulations using FRC combustion model [2-4].

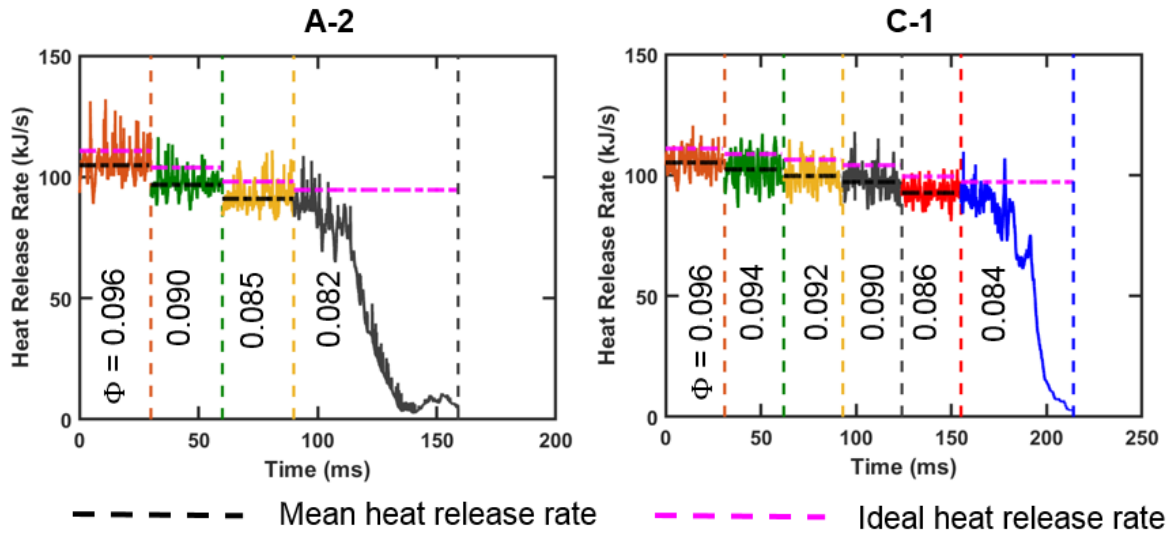


Figure 5.8. Heat release rate with FGM combustion model and compact mechanism [4]

### 5.6 Global lean blowout (LBO) equivalence ratio

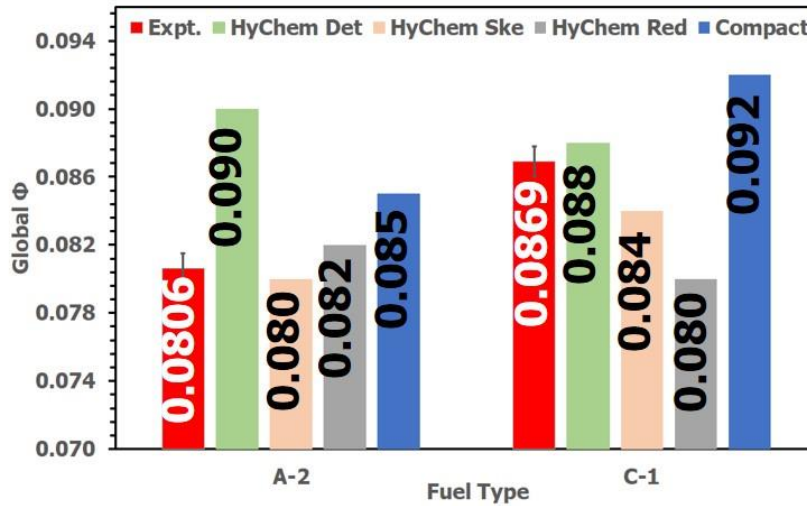


Figure 5.9. Global LBO equivalence ratio comparison between experiments [6] and LES [2-4].

The material discussed in this chapter is obtained from the author’s project progress report [4] and the author’s AIAA conference papers [2, 3]. The LBO trends computed with finite rate chemistry (FRC) model for both fuels are summarized and compared against experiments in Figure 5.9 and Figure 5.10 [2-4]. C-1 blows-out at a significantly higher equivalence ratio compared to

A-2 in the experiments. This LBO dependence on the fuel physical and chemical properties is very complex. The simulations are able to capture qualitatively the trend in LBO for each fuel as well as their relative behaviors with compact and HyChem skeletal mechanisms.

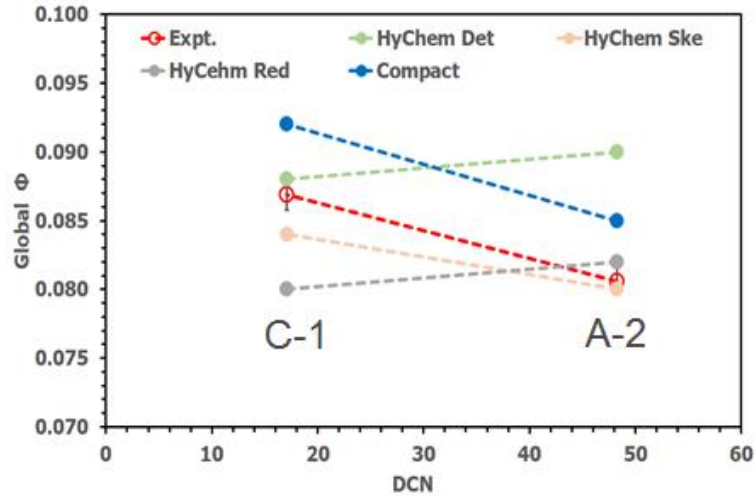


Figure 5.10. LBO Equivalence ratio comparison between LES (detailed chemistry solver) and experiments [2-4].

### 5.7 Combustion model sensitivity

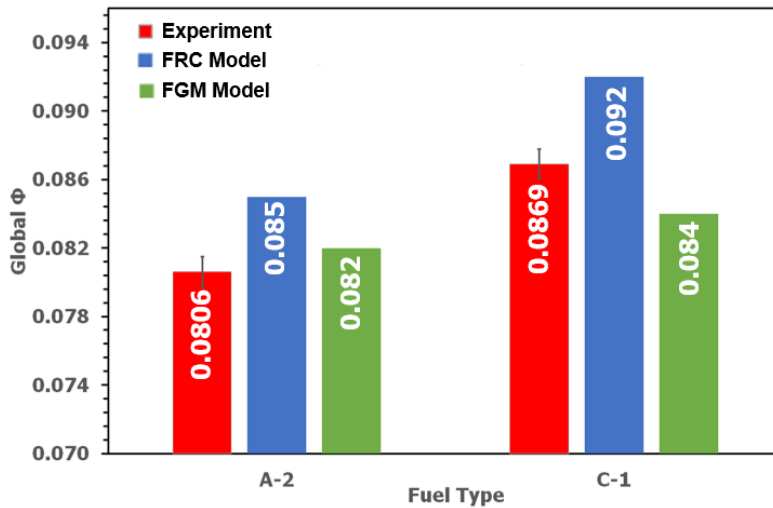


Figure 5.11. Effect of combustion model on the fuel sensitivity to the computed LBO global equivalence ratio [4].

The Flamelet Generated Manifold (FGM) approach under the adaptive mesh refinement framework is assessed for fuel sensitivity to LBO predictions [4]. The Won-Dryer compact mechanism is chosen for this study. The FGM model successfully captured the fuel sensitivity to lean blowout with a 60% reduction in the computational time compared to the finite rate chemistry model. The computed velocity, temperature, and mean OH mass fraction contours are compared for FRC and FGM combustion models in Figure 5.12. The results with FRC model show pointed flame root and smaller reaction zone whereas FGM model results show stronger flame root and much larger reaction zone. However, validation data from experiments would truly help for verification of the computational modal results and further enhancements.

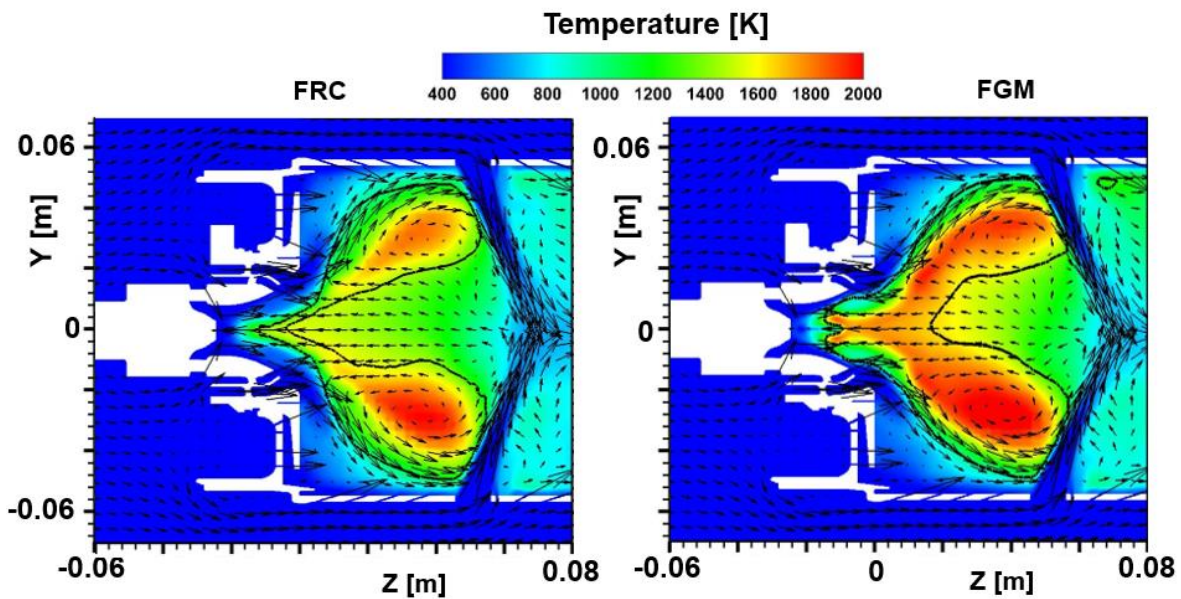


Figure 5.12. Comparison of temperature (filled contours), velocity (vectors), and iso-contour of mean mass fraction of OH = 5e-04 (black line) for C-1 fuel.

## 5.8 Flame structure analysis during LBO

The material discussed in this chapter is obtained from the author's project progress report [4] and the author's AIAA conference papers [2, 3]. The swirl stabilized spray flame in gas turbine combustors are a result of highly coupled and unsteady processes that are difficult to quantify and measure [1-4]. Even though high fidelity experimental data is available, validated models can be used to gain further insights into such processes. These insights can further improve understanding of flame stabilization and key factors governing LBO limits. LES results from the HyChem skeletal mechanism are chosen for understanding the flame extinction process during the LBO for

both A-2 and C-1 fuels [2-4]. A qualitative analysis of the flame during LBO is presented in Figure 5.13. Instantaneous temperature contour plots at the combustor mid-plane are shown on the left for both fuels and corresponding formaldehyde mass fractions are shown on the right. The primary recirculation zone corresponds to the region of intense heat release rate. These regions correspond to the high OH formation regions described in the previous section. For A-2 fuel, after the final step-down, at an equivalence ratio of 0.080, a lifted flame is observed to stabilize inside the swirler cup region between the 0 to 5 ms window. The formaldehyde is observed to form in the regions very near to the nozzle tip and follows the spray. It gets oxidized to form the high-temperature regions. As time progresses, the flame stabilization point starts to move in the axial direction and a remarkable shift in the CH<sub>2</sub>O regions is observed away from the nozzle tip. The heat release in the primary recirculation region decreases considerably by 15 ms with a considerable shift of CH<sub>2</sub>O formation in the downstream regions. Finally, the flame is observed to blowout by 25 ms. A similar trend is observed for the C-1 fuel, however, at a much higher global equivalence ratio of 0.084. The C-1 fuel has significantly higher CH<sub>2</sub>O formation even at 0 ms and this will be analyzed further in the next section. From these plots, it can be summarized that overall the flame is observed to shift downstream as we approach LBO along with a downstream movement of intermediate species. The reduction of heat release rates and overall temperatures lead to partial oxidation of these intermediate species which shows up as a corresponding downstream shift in the contour plots.

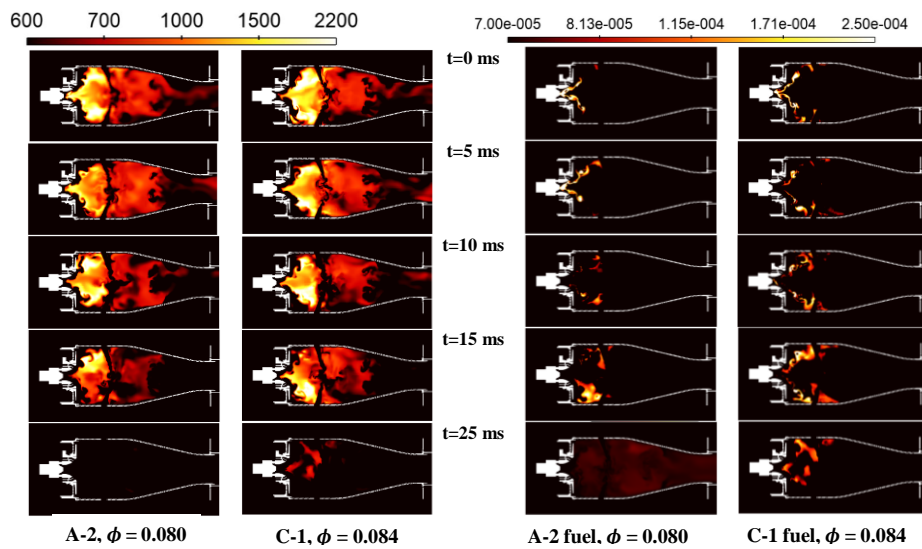


Figure 5.13. Instantaneous temperature [K] contour plots (left) at the combustor mid-plane and formaldehyde mass fractions (right) for A-2 and C-1 fuel during LBO [2-4].

The material discussed in this chapter is obtained from the author's project progress report [4] and the author's AIAA conference papers [2, 3]. To understand the flame stabilization and key factors governing LBO limits, species formation in the mixture fraction space can be analyzed during the LBO process [2-4]. For this analysis, only the primary flame stabilization region upstream of the first-row dilution holes, up to the nozzle tip is analyzed in the mixture fraction space. These are reported in Figure 5.14. The aim is to identify key markers or events that are universal in nature, with respect to different fuels, and these can be used to identify the onset of LBO. Each point in the T-Z space is colored by  $\text{CH}_2\text{O}$  mass fraction. The red dotted line corresponds to the stoichiometric mixture fraction. These data points are also reported for the stable configuration at 0.096. We first consider the stable operating point for A-2.  $\text{CH}_2\text{O}$  is observed to form in the rich regions in the temperature range of 1000-1600 K. This is similar to previous observations in high-pressure diffusion flames [121, 122]. These regions are subsequently oxidized in the high-temperature regions. After a series of step-downs in equivalence ratio to 0.080, we see that  $\text{CH}_2\text{O}$  formation shifts towards the richer regions highlighted by the dotted lines. This shift indicates partial oxidation of the HC fuel due to a global reduction in heat release and corresponding temperatures.

The material discussed in this chapter is obtained from the author's AIAA conference papers [2, 3] and the author's project progress report [4]. The C-1 fuel, on the other hand, indicates relatively higher  $\text{CH}_2\text{O}$  concentrations in the rich regions even for the stable operating point [3, 4]. This is an early indication of partial oxidation and the likelihood of the flame blowing out at relatively higher equivalence ratios. As expected, as we reduce the equivalence ratios, formaldehyde formation shifts to the richer regions indicating partial oxidation and the flame subsequently blow out by 15 ms. The higher concentration of intermediates in the rich regions can be attributed to the lowered temperatures and a corresponding decrease in the oxidation rates of intermediate species. The reduction in HRR and overall temperatures further leads to a reduction in the overall evaporation efficiency and this finally leads to a blowout. The oxidation of the intermediate species to high-temperature radicals and saturated combustion products is the step that has a huge impact on the LBO limits. The high-temperature species formation, on the other hand, does not show such trends. Most of the OH formation occurs near the stoichiometric mixtures at high temperatures and continues to exhibit this pattern up to the blowout.

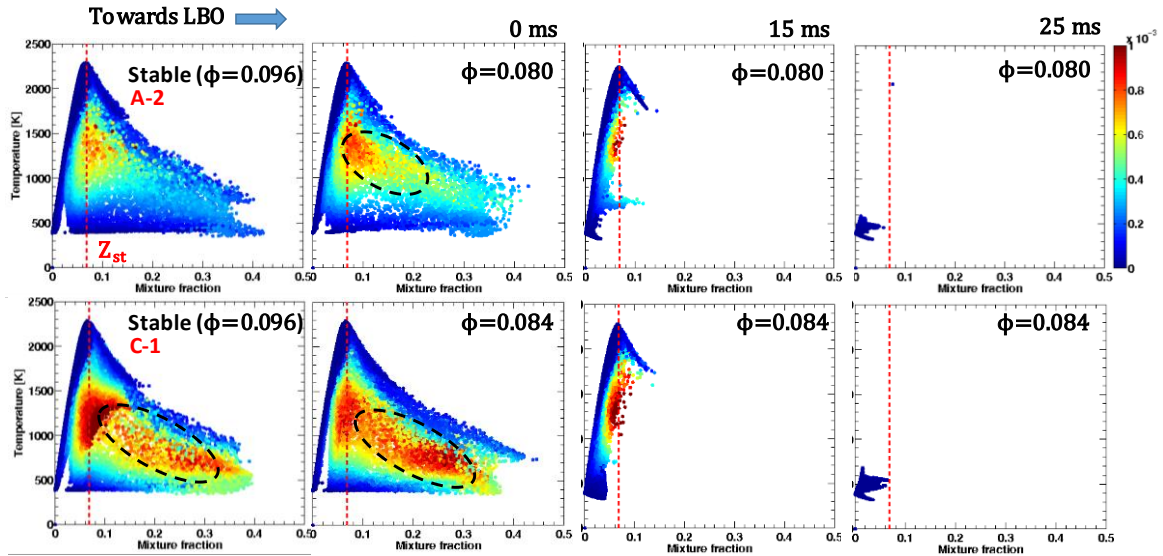


Figure 5.14. Temperature versus mixture fraction scatterplots for A-2 fuel (top) and C-1 fuel (bottom) sampled from the primary zone. Colored with CH<sub>2</sub>O mass fraction [3, 4].

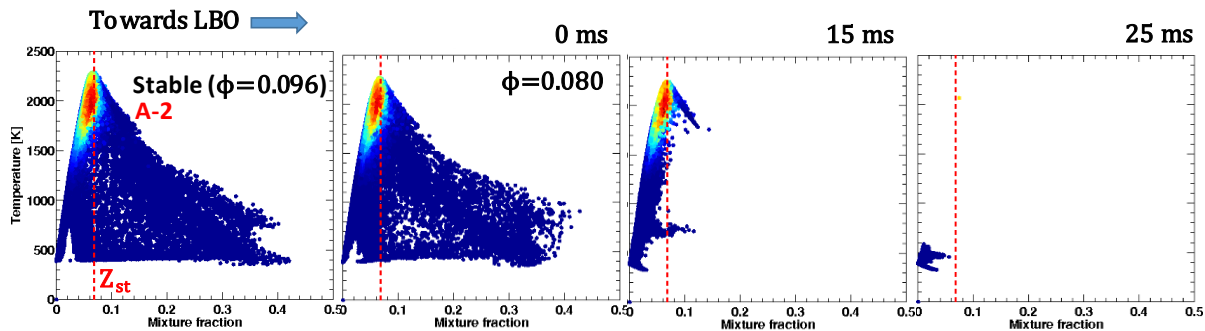


Figure 5.15. Temperature versus mixture fraction scatterplots for A-2 fuel sampled from the primary zone. Colored with OH mass fraction [3, 4].

The material discussed in this chapter is obtained from the author's AIAA conference papers [2, 3] and the author's project progress report [4]. The intermediate radical OH is formed in the high-temperature stoichiometric regions and does not shift with lower global equivalence ratios as shown in Figure 5.15 [3, 4]. This study showed that the trend of increasing concentrations of intermediate species in rich regions is an important marker during the LBO process. In this geometry, the swirler vanes are used to generate a swirling flow, and a subsequent breakdown of the vortex leads to the formation of a strong recirculation zone [3, 4]. This central recirculation zone (CRZ) facilitates the mixing and plays a key role in stabilizing the root of the flame. It

recirculates high-temperature products and radicals into the base of the flame and mixes them with the fresh reactants. Hence, this recirculation zone and the transience is studied to understand their impact on the LBO process. A central clip plane with mean temperature contours and streamlines are shown for both fuels in Figure 5.16. Temperatures from the primary zone (shown by the dotted red box) are isolated from the 3-D CFD domain and further filtered based on their axial velocities. The computational cells that have axial velocities in the negative direction are selected for analysis. As this is a non-uniform grid, these points are weighted with their respective cell volumes. These sets of points represent the recirculating fluid that flows from the high-temperature regions towards the base of the flame. Statistical analysis is carried out by generating a probability density function of the temperature distribution of these points and shown in Figure 5.17.

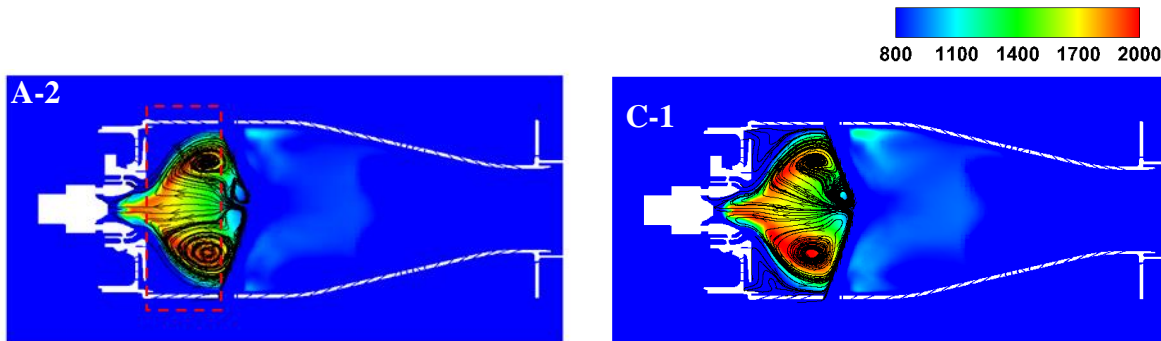


Figure 5.16. Mean temperature [K] contours for A-2 (left) and C-1 (right) with streamlines in the flame stabilizing primary zone at a stable flame condition with  $\phi = 0.096$  near the lean blow-out point [3, 4].

The material discussed in this chapter is obtained from the author's AIAA conference papers [2, 3] and the author's project progress report [4]. The PDF of temperatures of the primary zone, recirculating fluid for A-2 and C-1 fuel at the stable flame configuration of 0.096 global equivalence ratio is shown as a solid red line in Figure 5.17 [3, 4]. At this condition, the temperature distribution of the recirculation zone shows a non-uniform, multi-modal distribution with a peak in the 500 K zone and major part of the distribution spread in the range of 1500 K – 2300 K. This indicates that high temperatures are a major part of the recirculation zone and these play a significant role in stabilizing the flame. As we gradually reduce the global equivalence ratios, 0.090, as well as 0.085 global equivalence ratios, represent a stable flame configuration with reduced heat release rates. These reduced fuel flow rates also exhibit a similar distribution; however, the distributions show more bias towards the low temperatures. In these simulations, the

flame finally blows out at the global equivalence ratio of 0.080. At this final step down, the distribution is observed to have shifted significantly. The second peak of the bimodal distribution corresponding to the high-temperature region is now at a significantly lower temperature compared to the previous equivalence ratios. As the flame finally approaches LBO, we observe that this distribution shifts towards the low-temperature region and merges into a delta PDF type of distribution. Thus, it is observed that, as the flame blows out, the recirculation zone cools down due to the decrease in overall heat release rates. This causes lower evaporation rates and further triggers a reduction in heat release leading to a cyclic process. This weakening of the recirculation zone is a key marker of flame stability. A significant shift in the PDF distribution of temperatures of the recirculating fluid can be marker for the start of LBO. In order to further test this hypothesis, the same analysis is carried out for the C-2 fuel which is observed to blow out at 0.084 in the simulations. At the stable flame configuration, the PDF distribution is similar to A-2 with significant distribution in the 1500 K – 2300 K range. The other stable configuration of 0.090 also shows a similar distribution where the high-temperature points are in similar range. As the fuel flow is stepped down to 0.084 global equivalence ratio; the second mode shows a significant shift towards the low temperatures compared to previous equivalence ratios. As the flame blows out, the distribution becomes unimodal followed by a delta distribution after blowout. Overall, analysis of these CFD results indicates that if the recirculation zone temperature shifts beyond a certain value, the flame reaches an unstable configuration and blows out [3, 4].

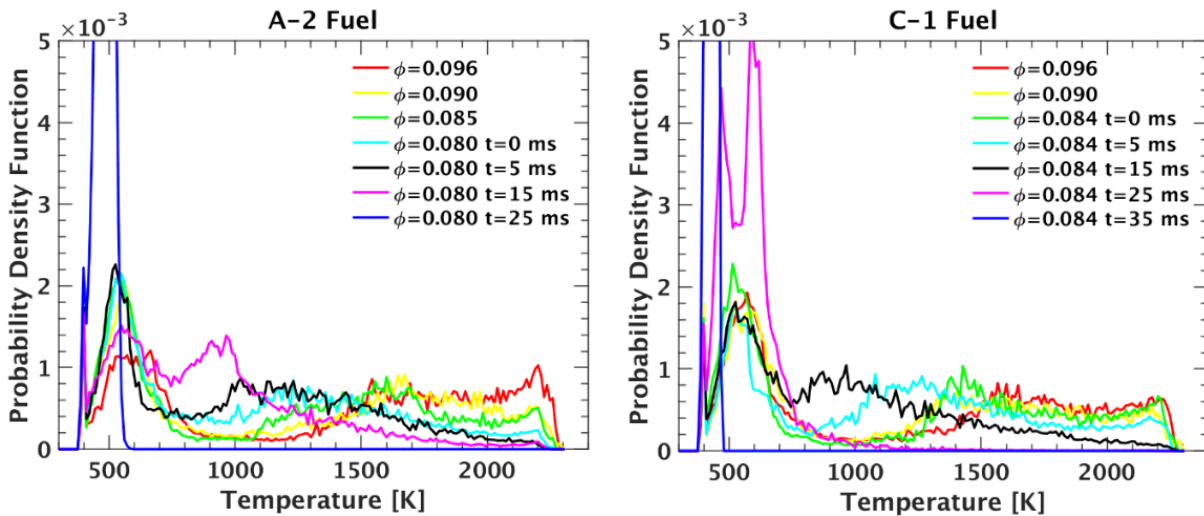


Figure 5.17. The probability density function of the temperatures of the recirculating gases in the primary zone for A-2 fuel (left) and C-1 fuel (right) [3, 4].

The volume-averaged temperature ( $T$ ), equivalence ratio ( $\Phi$ ),  $Y_{OH}$  and  $Y_{CH_2O}$  from the FGM simulations within the primary zone (shown in Figure 5.18) are plotted in Figure 5.19. For the near stable flame conditions, all the variables are decreased with time. The equivalence ratio decreases, the temperature and OH shift to lower values but the  $CH_2O$  concentration increases due to partial oxidation during the LBO. A similar trend towards onset of LBO is observed in the experiments at Cambridge for a swirl stabilized laboratory combustor [123].

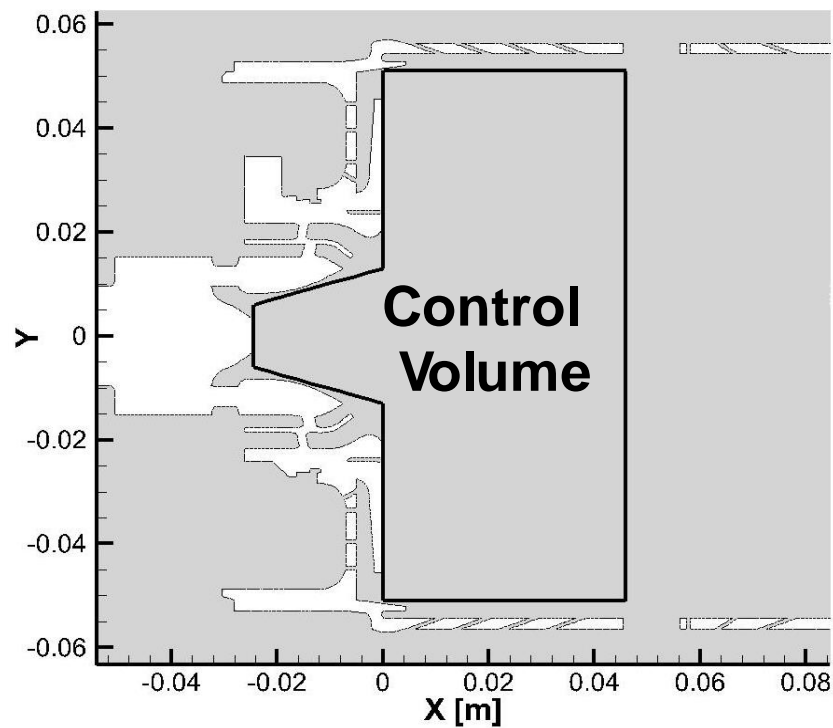


Figure 5.18. Primary zone sampling region for combustion process investigation during LBO.

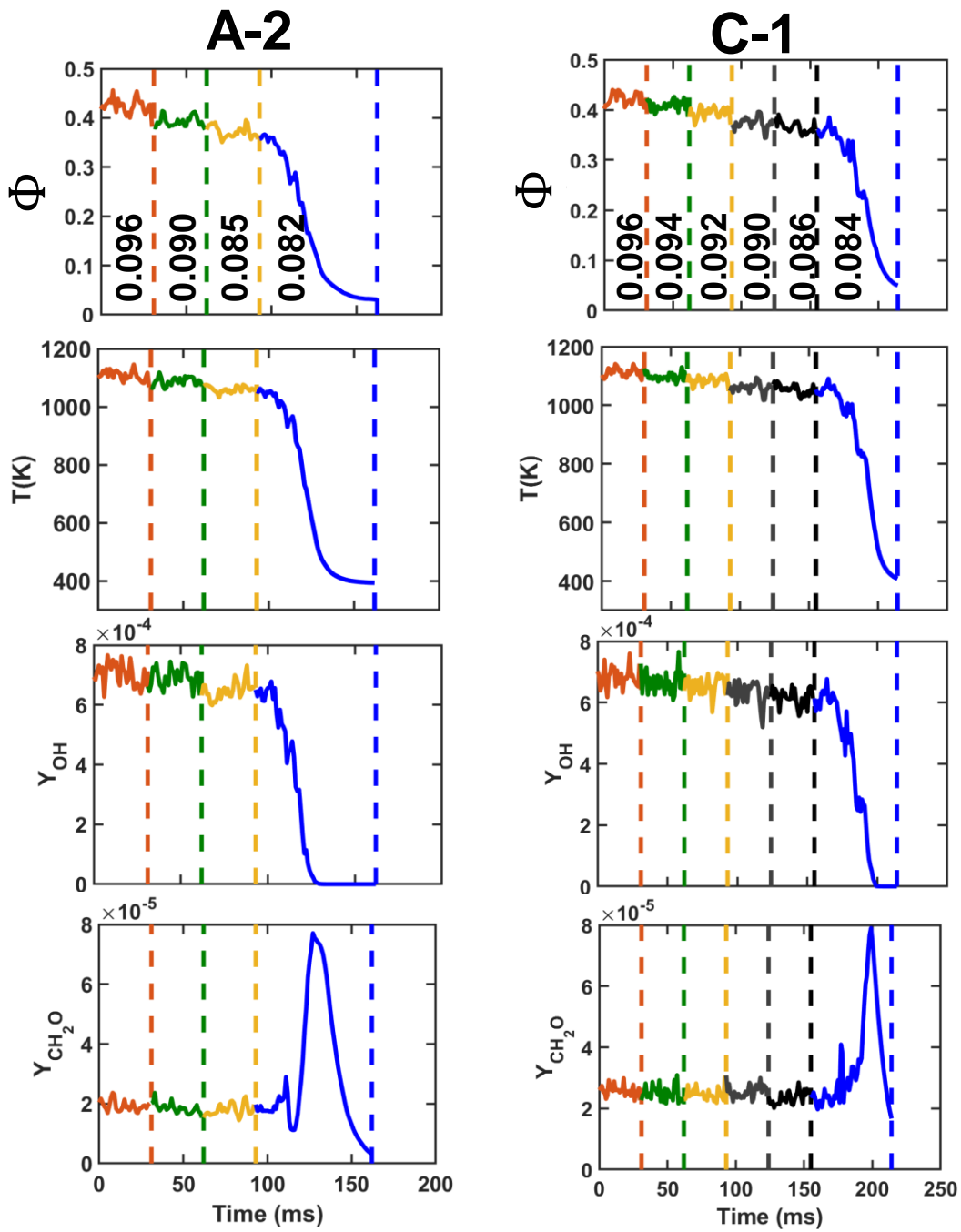


Figure 5.19. Evolution of the Volume averaged scalars in the primary zone of the combustor from stable flame to complete lean blowout (LBO) process.

## 6. APPLICATION OF ARTIFICIAL INTELLIGENCE

Modern gas turbine engines for propulsion and power applications are operated under lean combustion conditions to meet stringent emission regulations. However, lean combustion may introduce flame instabilities which may lead to a blowout defined as Lean blowout (LBO). LBO poses a major safety hazard in aviation engines. LBO is one of the most important figures of merit for certification of a gas turbine engine combustor and aviation fuels [5]. LBO prediction in a realistic combustor is a major challenge in the engine combustor design phase. This is due to a lack of reliable models that accounts for complex physicochemical processes involved in the combustion phenomena [124]. Potential solutions may include online engine health monitoring and diagnostics utilizing artificial intelligence (AI) techniques for real-time control to prevent catastrophic failures. The artificial intelligence-based data-driven model is investigated in this chapter for the identification of the incipient LBO condition for early warning to prevent engine failure. Two machine learning models are developed based on the following approaches for early warning of the LBO incipient condition:

- (1) Machine learning model based on a single point probe data: Optimal sensor location and identification of metric for scalars at these optimal locations for early identification of LBO.
- (2) Machine learning model based on spatiotemporal features: Identification of LBO incipient condition based on the spatiotemporal features within the primary zone.

### 6.1 Machine learning approach based on a probe data

The various sensing approaches for LBO detection utilizing the acoustic, optical and pressure sensors have been investigated [125-128]. The sensor locations play a key role in the identification of the onset of LBO [125]. The sensor placement strategy currently is based on physical intuition and trial and error basis [125-129]. However, the LBO mechanism in the practical combustor is poorly understood due to the complex nonlinear interactions between chemistry, flow turbulence, spray evaporation and mixing, and radiation [24, 130, 131]. The limitations associated with measurements in practical combustors at high pressure and temperature pose further challenges in acquiring data for understanding the LBO mechanism [6, 7, 10, 20].

Hence, there is limited literature on finding the optimal sensor locations and robust LBO detection criterion utilizing data-driven methods.

Machine learning has found many applications in the field of combustion. The problem of LBO detection is discussed for simple laboratory-scale combustors using data-driven methods and machine learning techniques [40, 43, 132, 133]. These studies have utilized high-speed images, OH\* chemiluminescence and pressure sensor data. High-fidelity numerical simulations of realistic gas turbine engine combustors under relevant conditions [1-3, 11] can provide insights and the training datasets for machine learning models. The specific objectives of this section are:

- (1) development of a machine learning model for finding optimal sensor location;
- (2) analysis of conventional statistical measures for LBO detection;
- (3) identification of a robust and practical metric based on machine learning for LBO detection

### 6.1.1 Machine learning model

The proposed machine learning model for arriving at the optimal sensor location is shown in Figure 6.1. The overall pipeline is divided into three main parts: (1) dimensionality reduction, (2) training Support Vector Machine (SVM) models, and (3) finding optimal sensor location. This method is tested for temperature and OH mass fraction ( $Y_{OH}$ ) as the indicator scalars for which optimal sensor locations are to be found. For brevity, temperature only is used for elaborating the process.

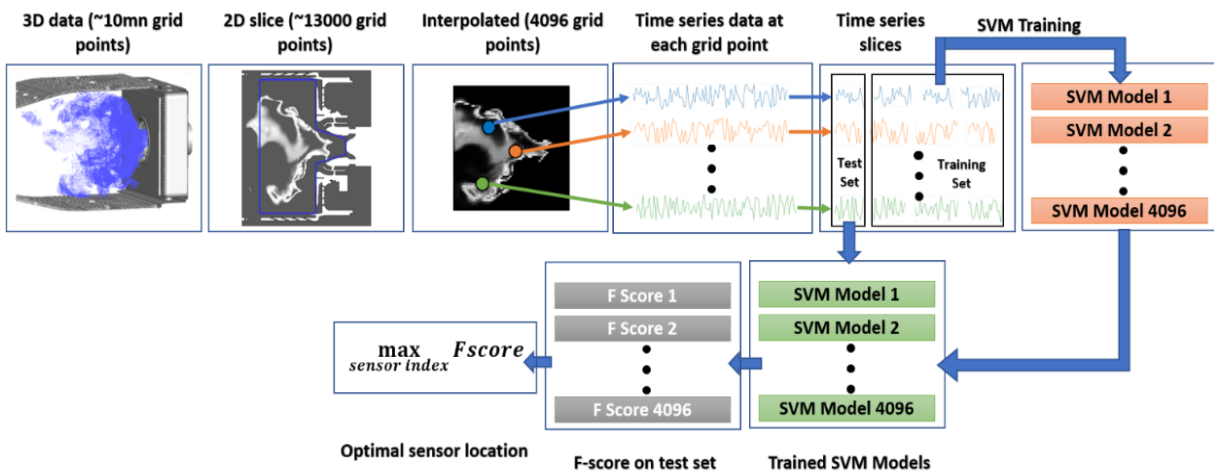


Figure 6.1. The machine learning model for determining optimal sensor location

### 6.1.1.1 Dimensionality reduction

The LES simulations provide very rich spatial data at each time-step at more than 10 million non-identical grid points. To limit the number of possible sensor locations, only the center plane of the combustor is considered. Heuristically, this plane contains the main features of flame dynamics. The section of the combustor close to the flame root has the most effect on flame stability [24]. For this work, the data in the primary zone containing approximately 13000 unstructured grid points, are locally mapped by interpolation onto a  $64 \times 64$  structured grid.

### 6.1.1.2 Training support vector machine (SVM) models

The time-series data for the temperature at each of the  $64 \times 64$  structured grid locations are extracted. These time-series contain 2646 time-steps out which 1946 represents stable conditions and 700 represent unstable conditions. The time-series for each grid location is sliced with a window of size of 1ms (10 samples). This window is shifted by 0.2ms to create all the slices. The present choices result in 1300 time slices, out which 344 represent equivalence ratios with unstable combustion and are labeled 1 and 956 represent equivalence ratios with stable combustion and are labeled as 0. These samples with the label 0 and 1 are randomly divided into a training set (90%) and a test set (10%). This ensures that the training and testing sets contain equal proportions of data samples representing stable and unstable combustor conditions.

For each grid location, the training dataset is used to train a Support Vector Machine (SVM) model. The SVM is a classifier aimed at maximizing the distance of the training samples from the separating hyperplane [134]. Given a training dataset  $(x_1, x_2, \dots, x_m)$  and their corresponding labels  $(y_1, y_2, \dots, y_m)$ , a discriminant function is defined as  $g(x) = w^T x + w_0$  and the resulting separating hyperplane is  $w^T x + b = 0$  where  $g$  is a discriminant function,  $w$  is the weight vector and  $w_0$  is the bias. To find  $w$  and  $w_0$ , the distance of the training data from the separating hyperplane is maximized while minimizing the number of misclassifications. The objective function for this optimization problem is  $\min_{w, w_0, \zeta} \frac{1}{2} w^T w + C \sum_{j=1}^m \zeta_j$  subject to the constraints  $y_j (w^T \psi(x_j) + w_0) \geq 1 - \zeta_j$  and  $\zeta_j \geq 0$ , for  $j = 1, 2, \dots, m$ , where  $\psi(x_j)$  is a transformation applied to the input  $x$ ,  $C$  is a penalty parameter and  $\zeta_j$  is a slack variable. The SVM is a linear classifier and requires a non-linear transformation for representation of the inherent non-linear decision boundary established by turbulent combustion. For this purpose, a kernel function is

defined as  $K(x_i, x_j) = \psi^T(x_i)\psi(x_j)$ , and a new input  $x$  is classified using the function  $h(x) = \text{sign}(\sum_{j=1}^m \lambda_j^* y_j K(x_j, x) + w_0^*)$ , where  $\sum_{j=1}^m \lambda_j^* y_j x_j = w^*$  and  $w_0^*$  are the optimal values of  $w$  and  $w_0$ .  $\lambda_j^*$  are introduced when the dual of the SVM optimization is solved. In the present work, the SVM classifier was implemented in Python 3.6 using scikit-learn [135] library. The radial basis function (rbf) was selected as the kernel function  $K(x_i, x_j)$  and the penalty parameter ( $C$ ) was set to unity.

### 6.1.1.3 Finding optimal sensor locations

A metric is defined to quantify the quality of a sensor at each of the grid locations. A sensor at a location with optimal quality can differentiate between a normal condition and an LBO precursor condition. Hence, false negatives (not detecting LBO when it occurs) and false positives (detecting LBO when the conditions are normal) have to be minimized. A recall function is defined as  $\text{Recall} = \text{TP}/(\text{TP} + \text{FN})$  where TP is the number of true positives and FN is the number of false negatives. The recall function is deceptively clever in reaching a unity value for all values of true positives if 0% false negatives can be achieved. Another metric of performance is defined by  $\text{Precision} = \text{TP}/(\text{TP} + \text{FP})$ . Precision emphasizes the effects of false positives. A large value of FP leads to a low value of precision for all values of TP. The F-score =  $2/(\text{Precision}^{-1} + \text{Recall}^{-1})$  captures the trade-off between precision and recall. At all the grid locations, the trained SVM models were tested using the test set and the F-score was used as a metric of performance. Each SVM model was trained using a subset of the time-series data at a particular location. Hence, the performance of the SVM model on the test set, which is a subset of the time-series data at the same location, was used as a metric of optimality for placing a sensor at that grid point. The definition of the F-score establishes an intuitive range of 0 to 1 for its values. Within this range, the higher the F-score, the better the location of the point sensor.

### 6.1.1.4 Evaluation of machine learning model and metric for LBO detection

The proposed machine learning model is successful in establishing the optimal probe locations for multiple scalar variables extracted from the LES simulations based on the F-score metric discussed in the previous section. In Figure 6.2, the optimal sensor location for temperature is designated as location 1 and the optimal sensor location for  $Y_{\text{OH}}$  is designated as location 2. Location 1 and location 2 both lie in the proximity of each other and of the flame root. F-scores

for both the temperature and the  $Y_{OH}$  probes at these locations were found to be  $\sim 0.94$ . The SVM models at other locations had a high recall value but a low precision. This generally resulted from the misclassification of many non-LBO events making the locations non-optimal.

Conventional statistical properties of turbulent combustion at the optimal sensor locations such as probability density functions (pdfs), kurtosis, skewness, and moving averages are studied next. Figure 6.3 shows the pdf for  $T$ ,  $Y_{OH}$ ,  $f$  (mixture fraction) and  $Y_{CH_2O}$  (mass fraction of  $CH_2O$ ) at location 1 for different equivalence ratios. As the equivalence ratio decreases, the three pdfs ( $T$ ,  $Y_{OH}$ , and  $f$ ) shift to lower values (the left) and the pdf for  $Y_{CH_2O}$  shifts to higher values (the right).

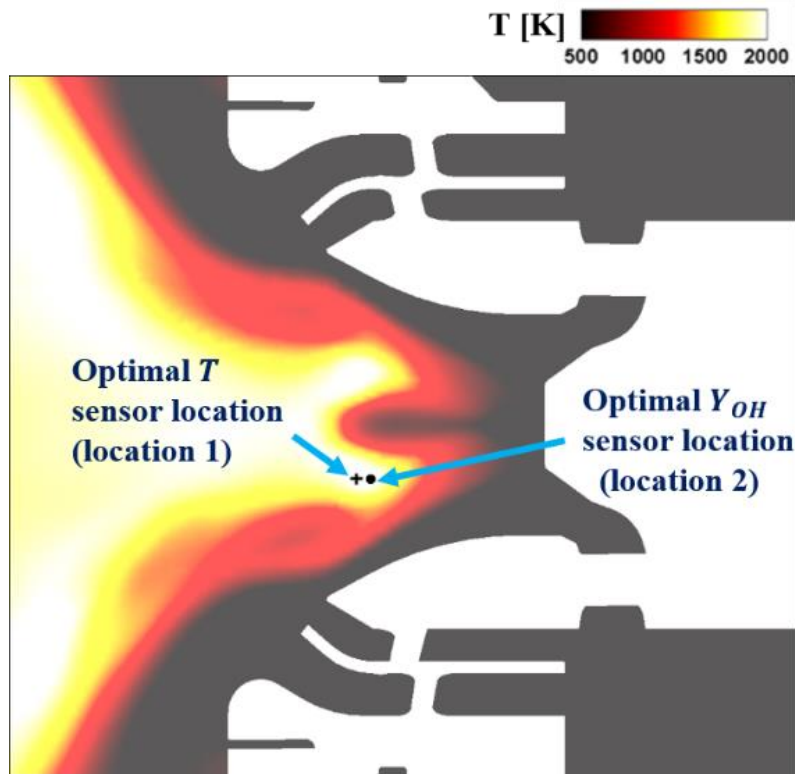


Figure 6.2. The optimal location for  $T$  and  $Y_{OH}$  sensor

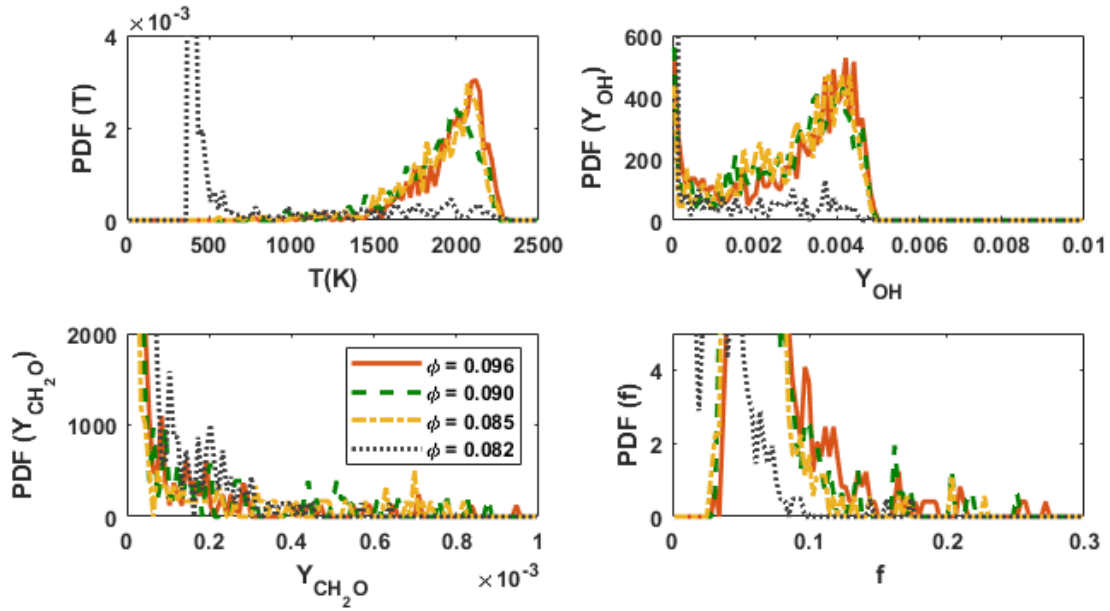


Figure 6.3. The probability density function of  $T$ ,  $Y_{OH}$ , and  $Y_{CH_2O}$  at location 1.

Kurtosis is widely used for anomaly detection. Figure 6.4(a) shows kurtosis of  $T$ ,  $Y_{OH}$ ,  $f$  and  $Y_{CH_2O}$  at location 1 for different equivalence ratios. Kurtosis of  $T$  and  $Y_{OH}$  remain almost constant for  $\phi = 0.096, 0.090$  and  $0.085$  which do not lead to LBO. Kurtosis for  $T$  decreases for  $\phi = 0.082$  whereas the kurtosis of  $Y_{OH}$  increases. Hence, threshold values for kurtosis of  $T$  and  $Y_{OH}$  can be estimated for detecting the LBO. These trends reinforce location 1 as an optimal sensor location for  $T$  and location 2, as an optimal sensor location for  $Y_{OH}$ . Threshold values for kurtosis cannot be estimated for  $f$  and  $Y_{CH_2O}$  at location 1 as the kurtosis value vary for stable conditions.

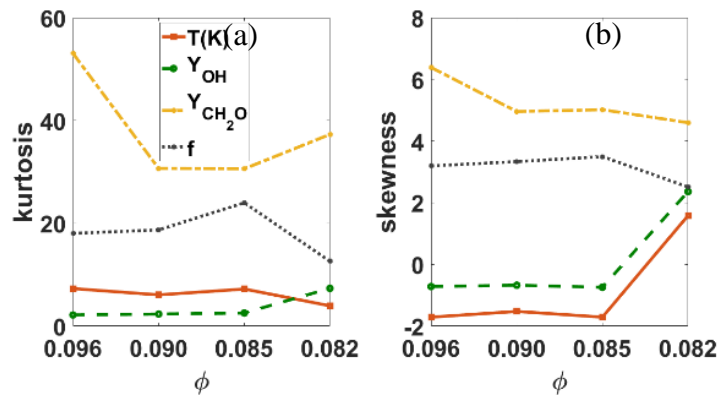


Figure 6.4. Variation of Kurtosis (a) and skewness (b) of  $T$ ,  $Y_{OH}$ , and  $Y_{CH_2O}$  at location 1.

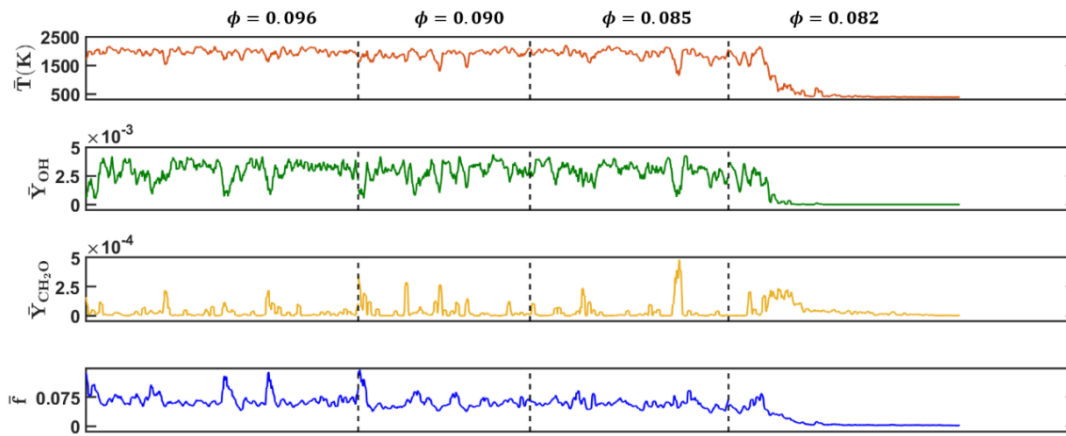


Figure 6.5. Moving average of  $T$ ,  $Y_{OH}$ , and  $Y_{CH_2O}$  at location 1.

The changes in the skewness are plotted in Figure 6.4(b) and are consistent with the changes observed in Figure 6.3. The skewness of  $T$  and  $Y_{OH}$  remain almost constant for  $\phi = 0.096, 0.090$  and  $0.085$  and shows a significant increase as the  $\phi$  is decreased to  $0.082$ . Hence, threshold values for the skewness of  $T$  and  $Y_{OH}$  can be estimated for detecting the LBO. The skewness for mixture fraction ( $f$ ) also remain constant for  $\phi$  not leading LBO and decreases for  $\phi = 0.082$ . This implies that a threshold-based indicator for LBO can be defined using skewness of  $T$ ,  $Y_{OH}$  and  $f$ . The skewness for  $Y_{CH_2O}$  is approximately constant for  $\phi = 0.085$  and  $0.082$  suggesting that  $Y_{CH_2O}$  is not a good indicator for LBO at location 1. The moving averages of  $T$ ,  $Y_{OH}$ , and  $Y_{CH_2O}$  at location 1 using a window of 10 time-steps (1ms) are also evaluated for LBO indication as shown in Figure 6.5.

The LBO indicators based on threshold values of skewness and kurtosis of  $T$  and  $Y_{OH}$  require a significant amount of data from sensors at prescribed locations and at relatively high sampling frequencies. The collection of a large amount of data in real-time may lead to significant delays in LBO detection. Hence, pdf, skewness, and kurtosis of  $T$  and  $Y_{OH}$  are not practical indicators of early warning of LBO. The moving average of  $T$  over 1ms (10 time-steps) as shown in Figure 6.5 is relatively constant as compared to the other variables. However, it shows sudden dips even for  $\phi = 0.096, 0.090$  and  $0.085$ . A control scheme based on a threshold value for change in the moving average of temperature may lead to excessive false positives rendering it to be unsuitable as an early warning indicator.

Figure 6.6 shows the results of classification by the SVM model for T at sensor location 1. The input for the model is a vector of 10 consecutive temperature values (time-series slices of 1ms). These slices are created from the time-series data for all the equivalence ratios at every 0.2ms. This input data set contains both the training and the testing data as described in Section 6.1.1.2. The LBO indicator ( $p$ ) is 1 when the SVM model classifies the input as unstable and is 0 when the SVM model classifies the input to be stable. As seen in Figure 6.6, there are no false positives. When the equivalence ratio is reduced to 0.082, which leads to LBO and is hence marked as unstable, the LBO indicator shows 0 for about 11 ms. This region of false negatives occurs because the time-series resembles the stable region. The LBO indicator shows a spike and then stabilizes to the value of 1 indicating impending blowout. The LBO indicator based on the SVM model required only 1ms (10 data points) of data as compared to a large amount of data required for building PDFs, kurtosis-based and skewness-based indicators. The number of false positives, in this case, was 0. This is much better than applying a threshold on the moving average over the same 1ms time period. It can be observed from Figure 6.6 that the trained SVM model detects LBO approximately 20ms prior to blowout.

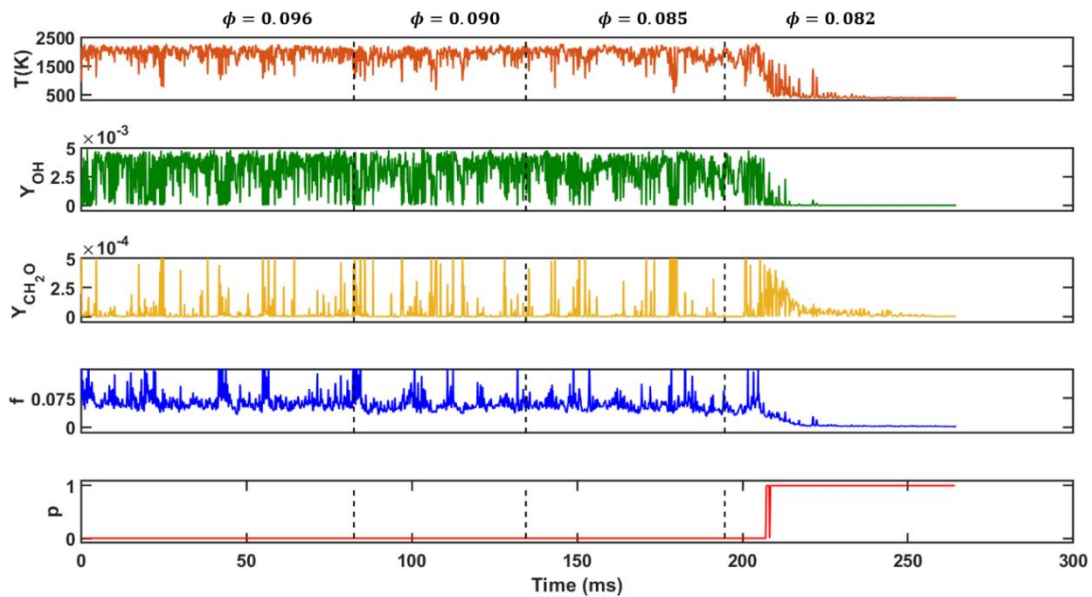


Figure 6.6. Time-series of  $T$ ,  $Y_{OH}$ ,  $Y_{CH_2O}$  and  $f$  at location 1 and LBO Indicator ( $p$ )

## 6.2 Machine learning approach based on spatiotemporal features

The point probe analysis proposed in the above section using sensors may not be the ideal approach for a robust prediction of the onset. It does not take into account the physicochemical processors at other key locations. Hence, a prediction approach utilizing the spatiotemporal data is proposed and evaluated in this section.

### 6.2.1 Machine learning model

The proposed architecture for a machine learning model is shown in Figure 6.7. The details of the data generated using high-performance computing (HPC) are discussed in the above section. The spatial distribution of the mass fraction of OH ( $Y_{OH}$ ) was extracted on a uniform  $64 \times 64$  two-dimensional mesh at the center plane of the combustor for dimensionality reduction of the data. A convolutional autoencoder (encoder-decoder) model was trained using this 2D dataset for further dimensionality reduction. The dense layer of the convolutional autoencoder (output of the encoder) is a compressed representation of the  $64 \times 64$  input. The encoder portion of the trained autoencoder model was used for feature extraction. These features with appropriate labels were then used to train a Support Vector Machine (SVM) model for classification of the  $Y_{OH}$  distribution as corresponding to a stable flame or an unstable flame. An LBO indicator is defined based on the output of the trained SVM model. The details of each of these steps are given in this section.

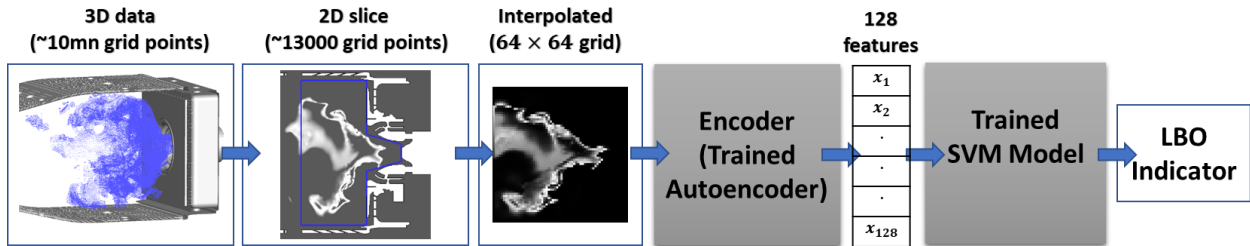


Figure 6.7. The proposed methodology for LBO detection

#### 6.2.1.1 Data preprocessing

Due to the adaptive nature of the mesh used for the CFD simulations, the spatial data available at each time-step is not on a uniform grid. Also, for each time-step, the simulation data contains approximately 10 million mesh points. If each of these mesh points is considered as a

feature of the combustor system, a very complex model will be required to capture the very high data complexity. This, in turn, requires a huge amount of data samples. In this case, the number of data samples is equal to the number of time steps for which the simulations are run. The number of data samples is limited by the computational costs. If all the equivalence ratios are considered, data is available for 2646 time steps out of which 700 belong to unstable category and the rest to stable category. Hence a significant dimensionality reduction of the available data is required.

The CFD simulations provide variables like temperature, pressure, velocity fields, the mass fraction of radicals, etc. at all the mesh points in the combustor. In the present study, only the mass fraction of OH ( $Y_{OH}$ ) is considered as it is a good representative of the flame in the combustor. Heuristically, the center plane is known to capture the main features of the flame dynamics. Also, the section of the combustor close to the flame root has the most effect on flame stability [24, 125]. Only the data in the primary zone is considered in the present analysis. The primary zone contains approximately 13000 unstructured mesh points which are interpolated on a  $64 \times 64$  structured mesh. For each equivalence ratio, the  $Y_{OH}$  data is normalized with the maximum value of the  $Y_{OH}$  at the first time-step of the time series data of that equivalence ratio. Applying this process, a set of 2621 matrices with dimension  $64 \times 64$  is obtained out of which 800, 520, 601 and 700 correspond to the equivalence ratio 0.096, 0.090, 0.085 and 0.082 respectively. Further dimensionality reduction is achieved using convolutional autoencoder.

### **6.2.1.2 Feature extraction – Convolutional autoencoder**

In order to extract higher-level features from the 2D  $Y_{OH}$  data, a convolutional autoencoder [136] model is used. The architecture of the convolutional autoencoder is shown in Figure 6.8. The convolutional autoencoder consists of two main components: an encoder and a decoder. The encoder transforms the input into a lower-dimensional representation and then the decoder reconstructs the input using this compressed representation. The autoencoder architecture is similar to one used by [40] but the number of filters and the number of dense layers units were tuned for the data used in this study.

Table 6.1. Convolutional autoencoder parameters

	Layer	Type	Output Shape	Number of trainable parameters
<b>ENCODER</b>	Input	Input	$64 \times 64$	-
	Conv1	Convolution layer	$62 \times 62 \times 32$	320
	Conv2	Convolution layer	$60 \times 60 \times 32$	9248
	MP1	Max-pooling	$30 \times 30 \times 32$	0
	Conv3	Convolution layer	$28 \times 28 \times 32$	9248
	MP2	Max-pooling	$14 \times 14 \times 32$	0
	Conv4	Convolution layer	$12 \times 12 \times 32$	9248
	R1	Reshape layer	$4608 \times 1$	0
	Dense	Fully-connected layer	$128 \times 1$	589952
<b>DECODER</b>	FC1	Fully-connected layer	$961 \times 1$	123969
	R2	Reshape layer	$31 \times 31 \times 1$	0
	UP1	Upsampling	$62 \times 62 \times 1$	0
	Deconv	Deconvolution layer	$64 \times 64 \times 1$	10

**Encoder:** As described in Table 6.1, the encoder consists of four convolutional, two max-pooling, one reshape and one fully-connected layer. When a mono-channel input image  $x$  of dimensions  $(m \times n)$  is convolved with  $N$  filters of size  $(f \times f)$ , the output is a convolutional layer,  $Y$ , of dimension  $((m - f + 1) \times (n - f + 1) \times N)$ . For the  $k^{\text{th}}$  filter, the corresponding layer in the convolutional layer is given by  $Y^k = \sigma_c(x * W^k + b^k)$  where  $Y^k$ ,  $W^k$  and  $b^k$  is the convolutional layer, the weight matrix and the bias corresponding to the  $k^{\text{th}}$  filter respectively,  $\sigma_c$  is an activation function and  $*$  denotes the 2D convolution. All the convolutional layers have 32  $3 \times 3$  filters and padding is not applied. Max-pooling is applied to obtain a translational-invariant representation. The max-pooling function applies a window to the input and finds the maximum over that window. After max-pooling, the dimension of the input is reduced by a constant factor. For all the max-pooling layers the window size is  $2 \times 2$ .

The encoder transforms the input as multiple convolutional and max-pooling layers are applied sequentially. This transformed input, a multi-dimensional array, is then reshaped into a vector. This reshape layer is connected to another fully-connected layer with a specified number

of nodes. This fully-connected layer is referred to as the dense layer. The transformation from the reshape layer to the dense layer is given by  $a_i = \sigma_e(\theta_i \tilde{x} + b_i)$  where  $a_i$ ,  $\theta_i$  and  $b_i$  represents the activation, weight matrix and the bias corresponding to the  $i^{\text{th}}$  node of the dense layer respectively,  $\sigma_e$  is an activation function and  $\tilde{x}$  vector of the reshape layer. The dense layer has 128 nodes and is the compressed representation of the  $64 \times 64$  input  $Y_{OH}$  distribution. Rectified Linear Unit (ReLU) is used as the activation function for the convolution layer and the fully-connected layers. Padding is not applied before the convolutional and max-pooling layers which are reflected in the output shape shown in Table 6.1.

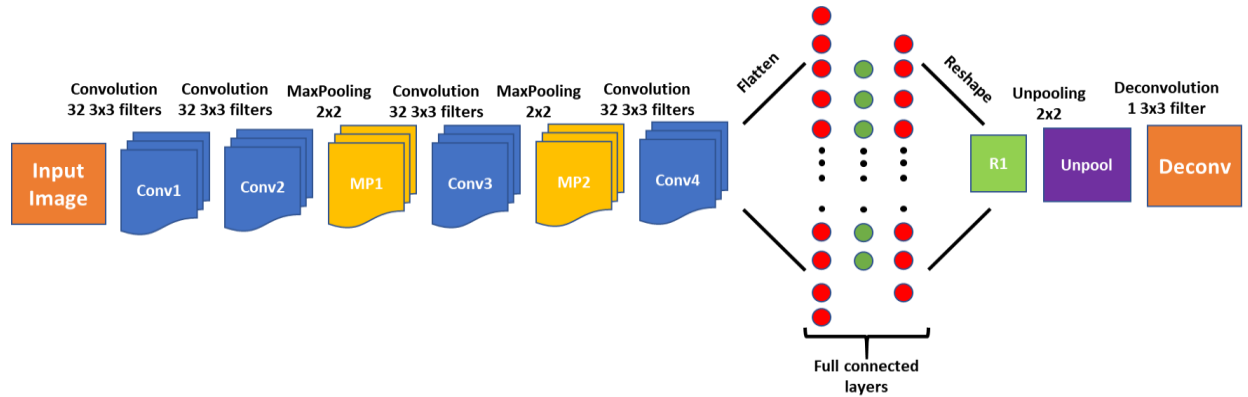


Figure 6.8. The architecture of the convolutional autoencoder.

**Decoder:** The decoder takes this compressed representation of the input, created by the encoder, and transforms it into a reconstruction of the autoencoder input. In the present analysis, the decoder has one fully-connected, reshape, unpooling and deconvolution layer. The fully-connected layer is obtained by transforming the dense layer of the encoder as  $a_i = \sigma_d(\theta_i \tilde{x}_d + b_i)$  where  $a_i$ ,  $\theta_i$  and  $b_i$  represents the activation, weight matrix and the bias corresponding to the  $i^{\text{th}}$  node respectively,  $\sigma_d$  is an activation function and  $\tilde{x}_d$  is dense layer. This fully-connected layer is reshaped into a matrix. The unpooling layer stretches the input by repeating each value in the matrix over a given window size. This operation is opposite to that of max-pooling. The window size for unpooling layer is chosen to be  $2 \times 2$ . The deconvolution layer applies transformation to the input which is like the convolution operation. The dimension of the output is, however, bigger than that of the input. Rectified Linear Unit (ReLU) is used as the activation function for the fully-connected and deconvolution layer.

The weight matrices and bias terms corresponding to all the filters and the fully connected layers are learned by minimizing a loss function. The loss function measures how well the autoencoder was able to recreate the input. A total of 741,995 trainable parameters are present in this model. The trainable parameters were optimized by minimizing the Mean Square Error (MSE) between the input and output (reconstructed input) given by  $L(\theta) = \frac{1}{mn} \sum_{i=1}^m \sum_{j=1}^n (Y_{ij} - X_{ij})^2$  where X and Y are input and output of the autoencoder model respectively and have a dimension of  $m \times n$ . In the present study, X and Y have a  $64 \times 64$  dimension.

Out of 2621, the 700 samples corresponding to the equivalence ratio of 0.082 lead to blowout while the rest 1921 do not lead to blowout. These sets of 700 and 1921 samples are divided into three groups: train (90%), validate (5%) and test (5%). This ensures that the equal proportion of stable and unstable flame samples are present in these three sets. The autoencoder is trained on the training set. The convolutional autoencoder was implemented in Python 3.6 using TensorFlow 2.0 [137]. The training was performed for 500 epochs in batches of 128 samples. Adam optimizer [138] was used with a constant learning rate of  $10^{-4}$ . Each of the 2621 samples in the  $Y_{OH}$  dataset is fed to the autoencoder model and encoder output or the activation value of the nodes in the dense layer are extracted as features representing the input. The samples corresponding the equivalence ratio of 0.082 are labeled as unstable (1) and the rest of the samples are labeled as stable (0).

### 6.2.1.3 Classification – Support Vector Machine

The 1921 samples with label 0 and the 700 samples with label 1 are randomly divided into three groups: train (80%), validate (10%) and test (10%). This ensures that the equal proportion of stable and unstable samples are present in these three sets. The Support Vector Machine (SVM) is used for classification of the reduced dimensional representation of the  $Y_{OH}$  distribution as corresponding to stable (0) flame or unstable (1) flame. SVM is a classifier aimed at maximizing the distance of the training samples from the separating hyperplane [134]. For a training dataset  $(x_1, x_2, \dots, x_m)$  with corresponding labels  $(y_1, y_2, \dots, y_m)$ , the separating hyperplane  $w^T x + w_0 = 0$  is found by maximizing the distance of the training data from this hyperplane while minimizing the number of misclassifications. Here,  $w$  is the weight vector and  $w_0$  is the bias. This is equivalent to solving  $\min_{w, w_0, \zeta} \frac{1}{2} w^T w + C \sum_{j=1}^m \zeta_j$  subject to the constraints  $y_j (w^T \phi(x_j) + w_0) \geq 1 - \zeta_j$  and  $\zeta_j \geq 0$ , for  $j = 1, 2, \dots, m$ , where,  $C$  is a penalty parameter and  $\zeta_j$  is a slack variable.

The transformation  $\phi(x_j)$  is applied to the input  $x$  to obtain non-linear decision boundary. This transformation is encompassed in a kernel function  $K(x_i, x_j) = \phi^T(x_i)\phi(x_j)$ . A new input  $x$  is classified using the following function  $h(x) = \text{sign}(\sum_{j=1}^m \lambda_j^* y_j K(x_j, x) + w_0^*)$  where  $\sum_{j=1}^m \lambda_j^* y_j x_j = w^*$  and  $w_0^*$  are the optimal value of  $w$  and  $w_0$ .  $\lambda_j^*$  are introduced in the setup when the dual of the SVM optimization is solved.

The SVM classifier was implemented in Python 3.6 using scikit-learn [135] library. To find the optimal kernel and regularization constant, the SVM classifier was trained with penalty parameter ranging from 0.0001 to 10 increased by a factor of 10 and with linear, polynomial, radial basis function (rbf) and sigmoid kernels. Based on the accuracy on the validation set, the regularization constant was set to 10 and a polynomial of degree four was selected as a kernel.

#### 6.2.1.4 Evaluation of machine learning model for LBO detection

The autoencoder model is validated using the validation set. Figure 6.9 shows the Mean Square Error (MSE) between the input and output of the autoencoders on the training set and the validation set. The problem of overfitting was not observed as the validation error did not increase with epochs. The model was trained with 64 and 128 nodes in the dense layer (encoder output). Figure 6.10 shows sample input and its reconstruction for these two variants of the model. Clearly, the model with 128 nodes in the dense layer was able to reconstruct the input in a much better way than the model with 64 nodes.

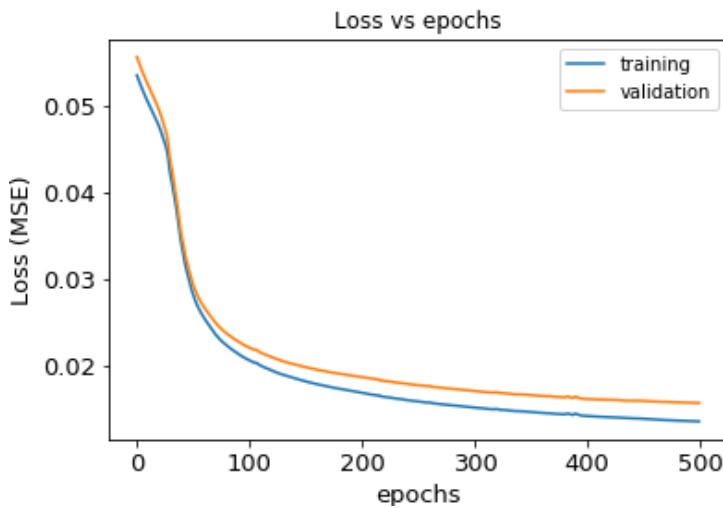


Figure 6.9. Mean square error vs epochs

Figure 6.11 to Figure 6.14 show the visualization of  $Y_{OH}$  and its autoencoder reconstruction at different time instances and for different equivalence ratios. A good reconstruction implies that the autoencoder model was able to learn and encode the higher-level features of the input. The autoencoder is able to reconstruct the general shape of the input. It is also able to capture fine features like pockets within the flame where  $Y_{OH}$  is absent (refer Figure 6.15(b) at  $t = 112\text{ms}$ ).

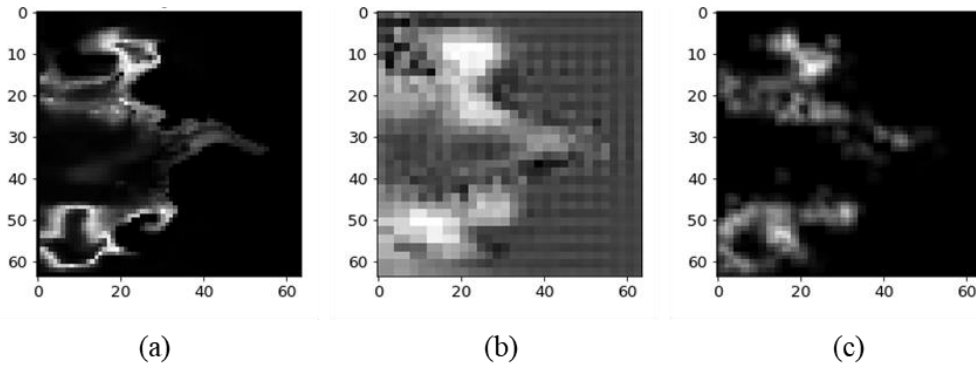


Figure 6.10. (a) Autoencoder input (b) Autoencoder output with 64 nodes in the dense layer (c) Autoencoder output with 128 layers in the dense layer

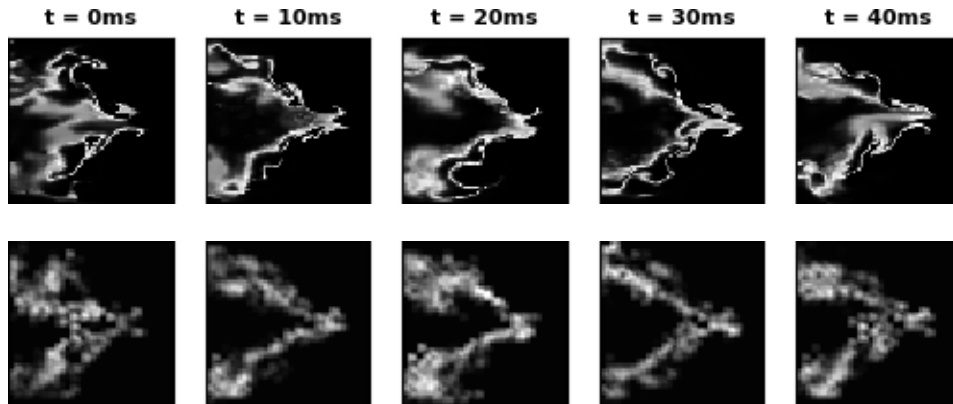


Figure 6.11.  $Y_{OH}$  distribution at different time instants (top) and its autoencoder reconstruction for an equivalence ratio of 0.096 (bottom)

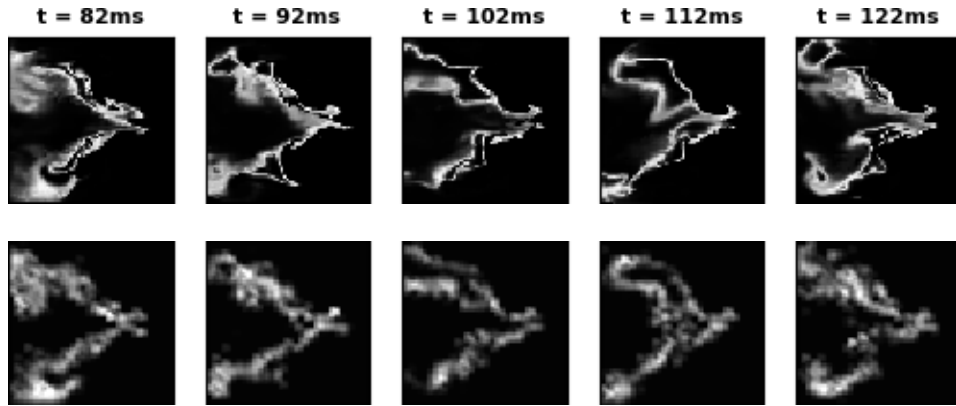


Figure 6.12.  $Y_{OH}$  distribution at different time instants (top) and its autoencoder reconstruction for equivalence ratio of 0.090 (bottom)

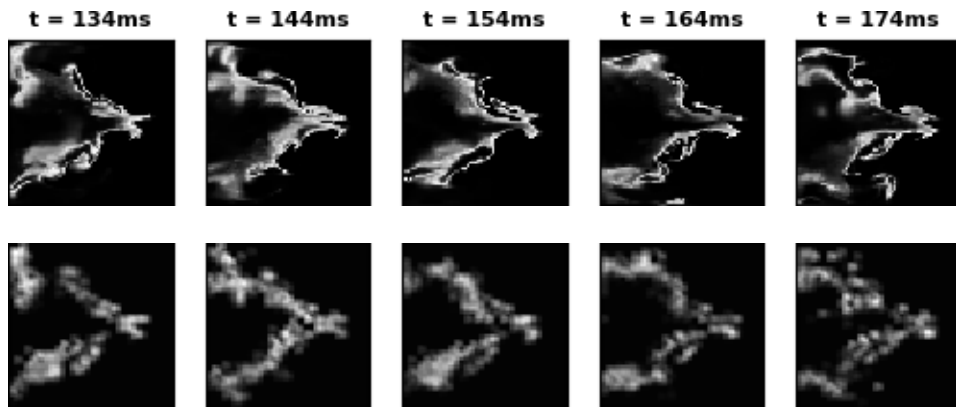


Figure 6.13.  $Y_{OH}$  distribution at different time instants (top) and its autoencoder reconstruction for an equivalence ratio of 0.085 (bottom)

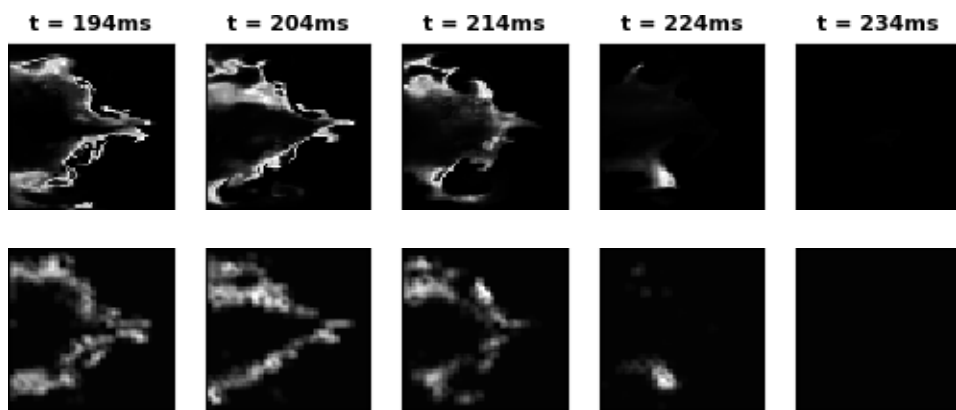


Figure 6.14.  $Y_{OH}$  distribution at different time instants (top) and its autoencoder reconstruction for an equivalence ratio of 0.082 (bottom)

In the autoencoder model, the input data undergoes several transformations before getting reconstructed as the output. Visualizing these intermediate transformations can help in understanding the features learned by the model. The first convolutional layer has size closer to the input dimension and hence is easy to interpret. This layer can be thought of as a set of 32 images. Figure 6.15 shows the visualization of the feature maps corresponding to 4 filters for the first convolution layer. The first image in Figure 6.15 is the input to the autoencoder encoder. Bottom edges can be seen in (b) and top edges in (c). Figure 6.15(d) shows that the autoencoder tries to capture the edge around the area where  $Y_{OH}$  is present while Figure 6.15(e) shows the areas which are devoid of  $Y_{OH}$ .

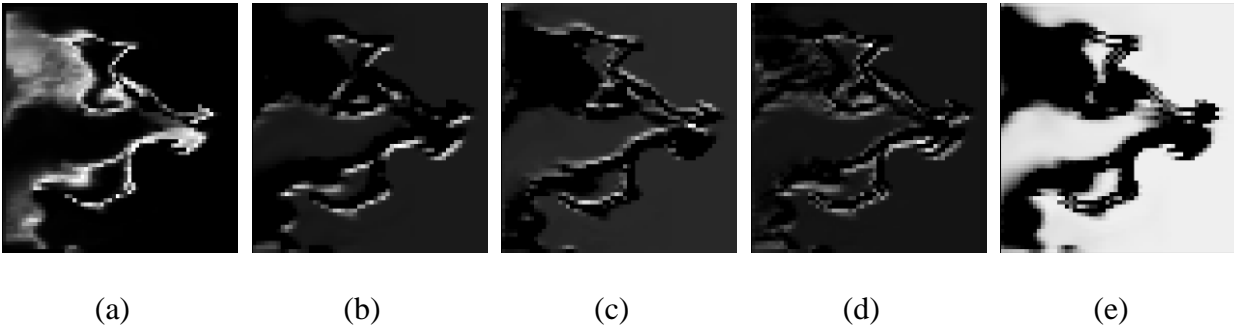


Figure 6.15. (a) Input to the autoencoder and (b-e) 4 out of the 32 feature-maps in the first convolutional layer

The features extracted using the autoencoder were used to train, validate and test the SVM model. The SVM model was tested on the test set which included 70 samples corresponding to unstable label and 192 samples corresponding to stable label. The accuracy on the test set was 96.6%. For lean blowout, the false negatives are critical as it can lead to severe safety concerns. Hence, it is important that false negatives are minimized. Recall =  $\frac{TP}{TP+FN}$  where TP is the number of true positives and FN is the number of false negatives. On the test set, the recall was 94.2%. A high recall value indicates that the number of false negatives is less. Ideally, recall should be close to 1. Precision considers the effect of false positives (FP) and is defined as Precision =  $\frac{TP}{TP+FP}$ . The effect of false positives is not catastrophic since the control system will adjust the inputs to make the flame more stable if it encounters signs of lean blowout. However, the purpose of running lean is to improve efficiency and keep emissions under control. It is important to minimize the

number of false positives as false positives can decrease the efficiency temporarily and exceed the emissions limit. Hence, the precision value needs to be maximized. The precision on the test set was 88.98%. The F-score considers the tradeoff between precision and recall. It is defined as F –

$$\text{score} = \frac{2}{\left(\frac{1}{\text{Precision}} + \frac{1}{\text{Recall}}\right)}. \text{ The F-score on the test set was 91.52\%.$$

The SVM model was then used to classify the  $Y_{OH}$  data at each time step in the entire dataset (train + validate + test) and the result is shown in Figure 6.16. The LBO indicator is 1 when the SVM model predicts the input to be unstable and is 0 when the SVM model predicts the input to be 0. Here, the input is compressed representation (128 features) of the  $64 \times 64$   $Y_{OH}$  data. A few false positives are observed for the equivalence ratio of 0.096 and 0.085. For the equivalence ratio of 0.082, initially, the LBO Indicator is 0 showing that the flame is stable. This is followed by intermittent changes in the LBO Indicator which then settles to the value of 1 approximately 30ms before the actual blowout (indicated by the red dashed line). These intermittent changes in the LBO indicator correspond to the intermittent nature of the stability of the flame before blowout.

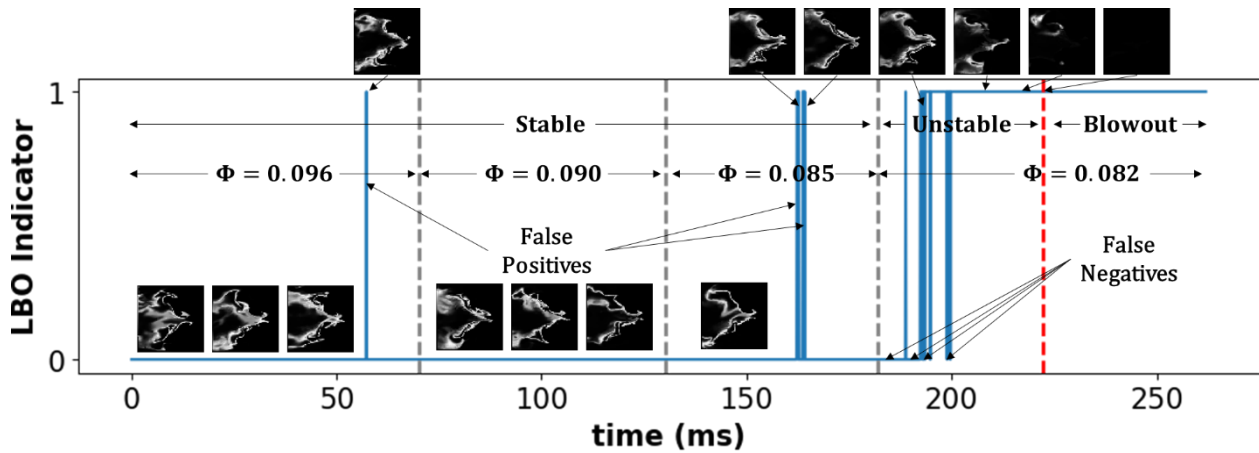


Figure 6.16. LBO indicator for the entire dataset (all time-steps and all equivalence ratios)

## 7. CONCLUSIONS AND RECOMMENDATIONS

The important findings of the research work and recommendations for further research are discussed in this chapter. The material presented in this chapter is obtained from the author's papers [1-3].

### 7.1 Conclusions

The material discussed in this section is obtained from the author's AIAA conference papers [1-3]. The high fidelity large eddy simulation methodology developed based on finite rate chemistry and flamelet generated manifold combustion models for a realistic gas turbine combustor [1-4]. Detailed flow rate calculations are presented for component-wise as well as total flow splits for a complex combustor. RANS and LES models are employed with different mesh resolutions. A highly automated, on the fly meshing strategy, along with adaptive mesh refinement was used to demonstrate the feasibility of CFD modeling. The computational results are compared with non-reacting flow splits data from a complex combustor. It is observed that with the present meshing strategy of capturing the flow through effusion holes, a minimum of 5-8 cells per effusion hole is sufficient for engineering calculations. The computed flow rates for individual passages at the actual test conditions are in good agreement with the experimental data. Grid sensitivity studies are reported for the combustor swirler configuration. The results for combustor total flow splits show under-prediction for the effusion flow and over prediction for dilution and swirler flows. Overall, the RANS, as well as LES calculations, capture similar flow splits compared to the experiments. Flow interaction effects between swirler and primary jets are observed to be significant in creating strong vortex structures with toroidal flow recirculation in the primary zone.

The material discussed in this section is obtained from the author's AIAA conference papers [1-3]. LES calculations with compact and HyChem skeletal mechanisms are able to capture the LBO limits and their sensitivities with respect to two different fuels accurately [1-4]. The model setup consists of a detailed spray injection along with well-defined flow boundary conditions. The modeling approach is initially validated against a stable operating point where the global equivalence ratio is 0.096. The Lagrangian spray setup is able to capture the trends in spray SMD and velocities for both the fuels. The flame shape and position at the stable condition is also

in tune with the experimentally observed OH\* chemiluminescence data. The LBO process is simulated by systematic step reduction in global equivalence ratios. The simulations correctly capture the trend of the C-1 fuel blowing off at higher equivalence ratios compared to A-2.

The material discussed in this section is obtained from the author's AIAA conference papers [1-3]. The blowout process is studied in detail by analyzing the heat release rate, the temperatures and intermediate species distributions in the primary zone of the referee combustor [1-4]. The present study identified the key markers for conventional and bio-jet fuel that can be used to define the stability limits. Two main observations are reported that mark the onset of an unstable flame. It has been observed in simulations that formation of intermediate species like formaldehyde, move towards the richer regions of the flame as we approach the LBO limit. These high concentrations indicate incomplete oxidation near the LBO limits. The C-2 fuel shows significantly higher CH<sub>2</sub>O formation in richer regions for the same equivalence ratio compared to A-2 and exhibits a higher LBO limit. In the second part of the analysis, it has been observed that the temperature in the recirculation zone is also an important indicator of the stability of the flame. The temperature distributions show a remarkable shift in distributions as we approach an unstable configuration. The observation is consistent over both the fuels with different LBO limits. Overall, the study points to the feasibility of using CFD models to evaluate different fuels and their figures of merit like LBO for a realistic gas turbine combustor in a predictive fashion [1-4].

The novel machine learning models are developed for early detection and warning of the incipient LBO condition based on a single point probe data and spatiotemporal features in the primary zone. A novel strategy using machine learning for optimal placement of sensors with specific examples of temperature (T) and OH mass fraction ( $Y_{OH}$ ) sensors are successfully demonstrated in this work. The performance of these SVM models on the test data was quantified using F-score and was used as a metric of sensor location optimality. The sensor location with highest F-score was demonstrated to be the optimal location. The optimal locations for T and  $Y_{OH}$  sensors were found to be in the proximity of the flame root. Statistical measures like probability density function, kurtosis, skewness and moving averages were computed at the optimal location for the T sensor. Thresholds on kurtosis and skewness of T and  $Y_{OH}$  were used as indicators but required significant number of data points which cause unacceptable delays in LBO detection. A threshold on the moving average of T captured the LBO but is susceptible to false positives. The trained SVM model for detecting LBO based on the time-series data was found to be practical and

robust as compared to the conventional statistical measures. This sensor-based model detected LBO approximately 20 ms prior to the complete lean blowout.

The machine learning model is developed based on the spatial distribution of the mass fraction of OH ( $Y_{OH}$ ) obtained in the primary zone of the combustor. An SVM model is trained for binary classification, and the features extracted by the trained convolutional autoencoder. A good agreement is observed between the autoencoder reconstruction of the  $Y_{OH}$  distribution and the original distribution showing that the features extracted by the autoencoder are a good compressed representation of the original data. The predictions on the test set have a 96.6% accuracy and 94.2% recall. The LBO indicator fluctuated between 0 and 1 for the equivalence ratio leading to LBO and stabilized to the value of 1 approximately 30ms before the actual blowout. The machine learning model based on the spatiotemporal features detected the incipient LBO condition 10ms ahead of the machine learning model based on the single probe data at the optimal sensor location.

## **7.2 Recommendations for future work**

The material discussed in this section is obtained from the author's AIAA conference papers [1-3]. The present work is focused on computing the fuel sensitivity to LBO and detailed investigation of the combustion process during LBO. Two different combustion models and four different kinetic models are evaluated in the present work. The detailed comparison for velocity, temperature, and species between these models and experiments will help for model evaluation and further enhancements to develop robust computational models. The detailed investigation of the HyChem detailed mechanism and reduced mechanism can be undertaken to develop a consistent and robust computational methodology for LBO prediction. The quantitative reaction pathway analysis can be performed to identify the key pathways leading to the LBO and compare these pathways between different kinetic models and for different fuels. The present simulations utilized the multi-ring injection to represent the complex spray from the hybrid airblast atomizer. Spray processes will have significant impact on the combustion calculations. Spray modeling including the primary and secondary atomization in a realistic complex combustor employed in the present study can be very beneficial to the community. The present LBO computational methodology employed the adiabatic condition for all combustor walls. Gas turbine combustors under engine relevant high-pressure conditions have high rate of heat transfer to the liner walls

through convection and radiation [4]. Combustor liner walls are heated through radiation and convection from the flame on the hot side and are cooled through convection to the cold air in the annulus and radiation to the outer casing. Thermal conduction along the liner wall also contributes to the distribution of heat flux and wall temperature. Transient three dimensional solid-fluid fully coupled numerical simulations can be undertaken in the future to account for the effects of turbulent combustion and flame radiation on the rate of heat transfer to the combustor liner [4]. The coupled simulations facilitate accurate estimation of liner temperature distribution and heat losses and the subsequent effect on the flame stabilization and lean blowout process [4]. The solution accuracy can be further improved by including the models for the gas phase radiation, soot and soot radiation, and NO<sub>x</sub> emissions.

## REFERENCES

- [1] Hasti, V. R., Kundu, P., Kumar, G., Drennan, S. A., Som, S., and Gore, J. P. "Numerical Simulation of Flow Distribution in a Realistic Gas Turbine Combustor," *2018 Joint Propulsion Conference*, No. AIAA 2018-4956, 2018.  
doi: doi:10.2514/6.2018-4956
- [2] Hasti, V. R., Kundu, P., Kumar, G., Drennan, S. A., Som, S., Won, S. H., Dryer, F. L., and Gore, J. P. "Lean blow-out (LBO) computations in a gas turbine combustor," *2018 Joint Propulsion Conference*, No. AIAA 2018-4958, 2018.  
doi: doi:10.2514/6.2018-4958
- [3] Hasti, V. R., Kundu, P., Kumar, G., Drennan, S. A., Som, S., and Gore, J. P. "A Numerical Study of Flame Characteristics during Lean Blow-Out in a Gas Turbine Combustor," *2018 Joint Propulsion Conference*, No. AIAA 2018-4955, 2018.  
doi: doi:10.2514/6.2018-4955
- [4] Lucht, R. P. "Project 029(A) National Jet Fuels Combustion Program – Area #5: Atomization Test and Models, Purdue University," *ASCENT National Jet Fuel Combustion Program (NJFCP)*, <https://ascent.aero/documents/2019/07/ascent-project-029a-2018-annual-report.pdf/>, 2018.
- [5] Colket, M., Heyne, J., Rumizen, M., Gupta, M., Edwards, T., Roquemore, W. M., Andac, G., Boehm, R., Lovett, J., Williams, R., Condevaux, J., Turner, D., Rizk, N., Tishkoff, J., Li, C., Moder, J., Friend, D., and Sankaran, V. "Overview of the National Jet Fuels Combustion Program," *AIAA Journal* Vol. 55, No. 4, 2017, pp. 1087-1104.  
doi: 10.2514/1.J055361
- [6] Stouffer, S., Hendershott, T., Monfort, J. R., Diemer, J., Corporan, E., Wrzesinski, P., and Caswell, A. W. "Lean Blowout and Ignition Characteristics of Conventional and Surrogate Fuels Measured in a Swirl Stabilized Combustor," *55th AIAA Aerospace Sciences Meeting*, No. January, 2017, pp. 1-14.  
doi: 10.2514/6.2017-1954
- [7] Corporan, E., Edwards, J. T., Stouffer, S., DeWitt, M., West, Z., Klingshirn, C., and Bruening, C. "Impacts of Fuel Properties on Combustor Performance, Operability and Emissions Characteristics," *55th AIAA Aerospace Sciences Meeting*, No. January, 2017, pp. 1-19.  
doi: 10.2514/6.2017-0380
- [8] Edwards, J. T. "Reference Jet Fuels for Combustion Testing," *55th AIAA Aerospace Sciences Meeting*, 2017, pp. 1-58.  
doi: 10.2514/6.2017-0146
- [9] Stachler, R. D., Heyne, J. S., Stouffer, S. D., Miller, J. D., and Roquemore, W. M. "Investigation of Combustion Emissions from Conventional and Alternative Aviation Fuels in a Well-Stirred Reactor," *Submitted to the 55th AIAA Aerospace Sciences Meeting*, No. January, 2017, pp. 1-28.  
doi: 10.2514/6.2017-0382
- [10] Monfort, J. R., Stouffer, S., Hendershott, T., Wrzesinski, P., Foley, W., and Rein, K. D. "Evaluating Combustion Instability in a Swirl-Stabilized Combustor Using Simultaneous Pressure, Temperature, and Chemiluminescence Measurements at High Repetition Rates," *55th AIAA Aerospace Sciences Meeting*, No. January, 2017, pp. 1-12.

- [11] Esclapez, L., Ma, P. C., Mayhew, E., Xu, R., Stouffer, S., Lee, T., Wang, H., and Ihme, M. "Fuel effects on lean blow-out in a realistic gas turbine combustor," *Combustion and Flame* Vol. 181, 2017, pp. 82-99.  
doi: <https://doi.org/10.1016/j.combustflame.2017.02.035>
- [12] Mayhew, E., Mitsingas, C. M., McGann, B., Hendershott, T., Stouffer, S., Wrzesinski, P., Caswell, A. W., and Lee, T. "Spray Characteristics and Flame Structure of Jet A and Alternative Jet Fuels," *55th AIAA Aerospace Sciences Meeting*, No. January, 2017.  
doi: 10.2514/6.2017-0148
- [13] Hendershott, T. H., Stouffer, S., Monfort, J. R., Diemer, J., Busby, K., Corporan, E., Wrzesinski, P., and Caswell, A. W. "Ignition of Conventional and Alternative Fuel at Low Temperatures in a Single-Cup Swirl-Stabilized Combustor," *2018 AIAA Aerospace Sciences Meeting*. American Institute of Aeronautics and Astronautics, 2018.
- [14] Arthur, H. L., and Dilip, R. B. *Gas Turbine Combustion: Alternative Fuels and Combustion*: CRC Press, 2010.
- [15] Lefebvre, A. H. "Fuel Effects on Gas Turbine Combustion—Ignition, Stability, and Combustion Efficiency," *Journal of Engineering for Gas Turbines and Power* Vol. 107, No. 1, 1985, pp. 24-37.
- [16] Mongia, H., Vermeersch, M., and Held, T. "A simple reactor-based approach for correlating lean blowout of turbopropulsion engine combustors," *37th Joint Propulsion Conference and Exhibit*.
- [17] Briones, A. M., Rankin, B. A., Stouffer, S. D., Erdmann, T. J., and Burrus, D. L. "Parallelized Automated, Predictive, Imprint Cooling Model for Combustor Liners," *ASME Turbo Expo* Vol. 139, No. March, 2016, pp. 1-15.  
doi: 10.1115/1.4034499
- [18] Briones, A. M., Stouffer, S., Vogiatzis, K., and Rankin, B. A. "Effects of Liner Cooling Momentum on Combustor Performance," *55th AIAA Aerospace Sciences Meeting*, No. January, 2017, pp. 1-17.  
doi: 10.2514/6.2017-0781
- [19] Erdmann, T. J., David, L., Briones, A. M., Stouffer, D., Rankin, B. A., and Andrew, W. "Experimental and Computational Characterization of Flow Rates in a Multiple-Passage Gas Turbine Combustor Swirler," 2017, pp. 1-11.
- [20] Briones, A. M., Stouffer, S. D., Vogiatzis, K., Rein, K., and Rankin, B. A. "Effects of Effusion and Film Cooling Jet Momenta on Combustor Flow Fields," *Journal of Engineering for Gas Turbines and Power* Vol. 140, No. 8, 2018, pp. 081503-081503-10.  
doi: 10.1115/1.4039178
- [21] Bokhart, A., Shin, D., Gejji, R. M., Sojka, P., Gore, J. P., Lucht, R. P., Naik, S. V., and Buschhagen, T. "Spray Measurements at Elevated Pressures and Temperatures Using Phase Doppler Anemometry," *55th AIAA Aerospace Sciences Meeting*. American Institute of Aeronautics and Astronautics, 2017.
- [22] Mayhew, E., Mitsingas, C. M., McGann, B., Hendershott, T., Stouffer, S., Wrzesinski, P., Caswell, A. W., and Lee, T. "Spray Characteristics and Flame Structure of Jet A and Alternative Jet Fuels," *55th AIAA Aerospace Sciences Meeting*, 2017.  
doi: 10.2514/6.2017-0148

- [23] Lieuwen, T., McDonell, V., Petersen, E., and Santavicca, D. "Fuel Flexibility Influences on Premixed Combustor Blowout, Flashback, Autoignition, and Stability," *Journal of Engineering for Gas Turbines and Power* Vol. 130, No. 1, 2008, pp. 11506-11510.
- [24] Stöhr, M., Boxx, I., Carter, C., and Meier, W. "Dynamics of lean blowout of a swirl-stabilized flame in a gas turbine model combustor," *Proceedings of the Combustion Institute* Vol. 33, No. 2, 2011, pp. 2953-2960.  
doi: <https://doi.org/10.1016/j.proci.2010.06.103>
- [25] Erdmann, T. J., Burrus, D. L., Briones, A. M., Stouffer, S. D., Rankin, B. A., and Caswell, A. W. "Experimental and Computational Characterization of Flow Rates in a Multiple-Passage Gas Turbine Combustor Swirler," No. 50855, 2017, p. V04BT04A076.  
doi: 10.1115/GT2017-65252
- [26] Gritsch, M., Schulz, A., and Wittig, S. "Effect of Crossflows on the Discharge Coefficient of Film Cooling Holes With Varying Angles of Inclination and Orientation," *Journal of Turbomachinery* Vol. 123, No. 4, 2001, pp. 781-787.
- [27] Wang, H., Xu, R., Wang, K., Bowman, C. T., Hanson, R. K., Davidson, D. F., Brezinsky, K., and Egolfopoulos, F. N. "A physics-based approach to modeling real-fuel combustion chemistry - I. Evidence from experiments, and thermodynamic, chemical kinetic and statistical considerations," *Combustion and Flame*, 2018.  
doi: <https://doi.org/10.1016/j.combustflame.2018.03.019>
- [28] Xu, R., Wang, K., Banerjee, S., Shao, J., Parise, T., Zhu, Y., Wang, S., Movaghar, A., Lee, D. J., Zhao, R., Han, X., Gao, Y., Lu, T., Brezinsky, K., Egolfopoulos, F. N., Davidson, D. F., Hanson, R. K., Bowman, C. T., and Wang, H. "A physics-based approach to modeling real-fuel combustion chemistry – II. Reaction kinetic models of jet and rocket fuels," *Combustion and Flame*, 2018.  
doi: <https://doi.org/10.1016/j.combustflame.2018.03.021>
- [29] Tao, Y., Xu, R., Wang, K., Shao, J., S Johnson, E., A, M., X, H., J, P., T, L., K, B., F Egolfopoulos, N., D Davidson, F., R Hanson, K., C Bowman, T., and Wang, H. "A Physics-based approach to modeling real-fuel combustion chemistry - III. Reaction kinetic model of JP10," *Combustion and Flame (Submitted)*, 2018.
- [30] Wang, K., Xu, R., Parise, T., Shao, J., Lee, D. J., Movaghar, A., Park, J., Gao, Y., Lu, T., Egolfopoulos, F. N., Davidson, D. F., Hanson, R. K., Bowman, C. T., and Wang, H. "A Physics-based approach to modeling real-fuel combustion chemistry - IV. HyChem Modeling of Combustion Kinetics of a Bio-derived Jet Fuel and Its Blends with a Conventional Jet A," *Combustion and Flame (Submitted)*, 2018.
- [31] Joshua, P., Luis, B., Waldo, A., Gaurav, K., Scott, D., and Omid, S.-A. "On Predictions of Fuel Effects on Lean Blow Off Limits in a Realistic Gas Turbine Combustor using Finite Rate Chemistry," *GT2018-77070, ASME 2018 Turbo Expo*, . Oslo, Norway, 2018.
- [32] Gao, Y., Xu, R., Wang, H., and Lu, T. "Reduced High-Temperature Combustion Chemistry Models of Jet Fuels," *10th U. S. National Combustion Meeting*. College Park, Maryland, USA, 2017.
- [33] Kalogirou, S. A. "Artificial intelligence for the modeling and control of combustion processes: a review," *Progress in Energy and Combustion Science* Vol. 29, No. 6, 2003, pp. 515-566.  
doi: [https://doi.org/10.1016/S0360-1285\(03\)00058-3](https://doi.org/10.1016/S0360-1285(03)00058-3)

- [34] Di Mauro, A., Chen, H., and Sick, V. "Neural network prediction of cycle-to-cycle power variability in a spark-ignited internal combustion engine," *Proceedings of the Combustion Institute* Vol. 37, No. 4, 2019, pp. 4937-4944.  
doi: <https://doi.org/10.1016/j.proci.2018.08.058>
- [35] Raman, V., and Hassanaly, M. "Emerging trends in numerical simulations of combustion systems," *Proceedings of the Combustion Institute* Vol. 37, No. 2, 2019, pp. 2073-2089.  
doi: <https://doi.org/10.1016/j.proci.2018.07.121>
- [36] T. Henry de Frahan, M., Yellapantula, S., King, R., S. Day, M., and W. Grout, R. "Deep learning for presumed probability density function models," *Combustion and Flame* Vol. 208, 2019, pp. 436-450.  
doi: <https://doi.org/10.1016/j.combustflame.2019.07.015>
- [37] Popov, P. P., Buchta, D. A., Anderson, M. J., Massa, L., Capecelatro, J., Bodony, D. J., and Freund, J. B. "Machine learning-assisted early ignition prediction in a complex flow," *Combustion and Flame* Vol. 206, 2019, pp. 451-466.  
doi: <https://doi.org/10.1016/j.combustflame.2019.05.014>
- [38] Lapeyre, C. J., Misdariis, A., Cazard, N., Veynante, D., and Poinso, T. "Training convolutional neural networks to estimate turbulent sub-grid scale reaction rates," *Combustion and Flame* Vol. 203, 2019, pp. 255-264.  
doi: <https://doi.org/10.1016/j.combustflame.2019.02.019>
- [39] Seltz, A., Domingo, P., Vervisch, L., and Nikolaou, Z. M. "Direct mapping from LES resolved scales to filtered-flame generated manifolds using convolutional neural networks," *Combustion and Flame* Vol. 210, 2019, pp. 71-82.  
doi: <https://doi.org/10.1016/j.combustflame.2019.08.014>
- [40] Akintayo, A., Lore, K. G., Sarkar, S., and Sarkar, S. "Early Detection of Combustion Instabilities using Deep Convolutional Selective Autoencoders on Hi-speed Flame Video," *ArXiv* Vol. abs/1603.07839, 2016.
- [41] Sarkar, S., Lore, K. G., Sarkar, S., Ramanan, V., Chakravarthy, S. R., Phoha, S., and Ray, A. "Early detection of combustion instability from hi-speed flame images via deep learning and symbolic time series analysis," *Proceedings of the Annual Conference of the Prognostics and Health Management Society, PHM*. 2015, pp. 353-362.
- [42] Ghosal, S., Ramanan, V., Sarkar, S., Chakravarthy, S. R., and Sarkar, S. "Detection and Analysis of Combustion Instability From Hi-Speed Flame Images Using Dynamic Mode Decomposition," *ASME 2016 Dynamic Systems and Control Conference*. Vol. 1, 2016.
- [43] Sarkar, S., Chakravarthy, S. R., Ramanan, V., and Ray, A. "Dynamic data-driven prediction of instability in a swirl-stabilized combustor," *International Journal of Spray and Combustion Dynamics* Vol. 8, No. 4, 2016, pp. 235-253.  
doi: 10.1177/1756827716642091
- [44] Janakiraman, V. M., Nguyen, X., and Assanis, D. "Stochastic gradient based extreme learning machines for stable online learning of advanced combustion engines," *Neurocomputing* Vol. 177, 2016, pp. 304-316.  
doi: <https://doi.org/10.1016/j.neucom.2015.11.024>
- [45] Tóth, P., Garami, A., and Csordás, B. "Image-based deep neural network prediction of the heat output of a step-grate biomass boiler," *Applied Energy* Vol. 200, 2017, pp. 155-169.  
doi: <https://doi.org/10.1016/j.apenergy.2017.05.080>

- [46] Michelén Ströfer, C., Wu, J., Xiao, H., and Paterson, E. "Data-Driven, Physics-Based Feature Extraction from Fluid Flow Fields," *arXiv e-prints*, 2018.
- [47] Hasti, V. R., Kumar, G., Liu, S., Lucht, R. P., and Gore, J. P. "Large Eddy Simulation of Pilot Stabilized Turbulent Premixed CH<sub>4</sub>+Air Jet Flames," *2018 AIAA Aerospace Sciences Meeting*, No. AIAA 2018-0675, 2018.  
doi: 10.2514/6.2018-0675
- [48] Hasti, V. R., Liu, S., Kumar, G., and Gore, J. P. "Comparison of Premixed Flamelet Generated Manifold Model and Thickened Flame Model for Bluff Body Stabilized Turbulent Premixed Flame," *2018 AIAA Aerospace Sciences Meeting*, No. AIAA 2018-0150, 2018.  
doi: doi:10.2514/6.2018-0150
- [49] Hasti, V. R., Lucht, R. P., and Gore, J. P. "Large eddy simulation of hydrogen piloted CH<sub>4</sub>/air premixed combustion with CO<sub>2</sub> dilution," *Journal of the Energy Institute*, 2019.  
doi: <https://doi.org/10.1016/j.joei.2019.10.004>
- [50] Convergent Science Inc. *CONVERGE CFD, Version 2.4*,. Madison, WI, 2017.
- [51] Pomraning, E. *Development of Large Eddy Simulation Turbulence Models*. Madison, WI: University of Wisconsin-Madison, 2000.
- [52] Pomraning, E., and Rutland, C. J. "Dynamic One-Equation Nonviscosity Large-Eddy Simulation Model," *AIAA Journal* Vol. 40, No. 4, 2002, pp. 689-701.  
doi: 10.2514/2.1701
- [53] Yeo, W. K. "A Generalized High Pass/Low Pass Averaging Procedure for Deriving and Solving Turbulent Flow Equations." 1987.
- [54] Duwig, C., Nogenmyr, K.-J., Chan, C.-k., and Dunn, M. J. "Large Eddy Simulations of a piloted lean premix jet flame using finite-rate chemistry," *Combustion Theory and Modelling* Vol. 15, No. 4, 2011, pp. 537-568.  
doi: 10.1080/13647830.2010.548531
- [55] Jain, S. K., and Aggarwal, S. K. "Compositional effects on the ignition and combustion of low octane fuels under diesel conditions," *Fuel* Vol. 220, 2018, pp. 654-670.  
doi: <https://doi.org/10.1016/j.fuel.2018.02.015>
- [56] Gholamisheeri, M., Wichman, I. S., and Toulson, E. "A study of the turbulent jet flow field in a methane fueled turbulent jet ignition (TJI) system," *Combustion and Flame* Vol. 183, 2017, pp. 194-206.  
doi: <https://doi.org/10.1016/j.combustflame.2017.05.008>
- [57] Pomraning, E., Richards, K., and Senecal, P. K. "Modeling Turbulent Combustion Using a RANS Model, Detailed Chemistry, and Adaptive Mesh Refinement." SAE International, 2014.
- [58] Rahimi Boldaji, M., Gainey, B., and Lawler, B. "Thermally stratified compression ignition enabled by wet ethanol with a split injection strategy: A CFD simulation study," *Applied Energy* Vol. 235, 2019, pp. 813-826.  
doi: <https://doi.org/10.1016/j.apenergy.2018.11.009>
- [59] Liu, Z., Zhou, L., Liu, B., Zhao, W., and Wei, H. "Effects of equivalence ratio and pilot fuel mass on ignition/extinction and pressure oscillation in a methane/diesel engine with pre-chamber," *Applied Thermal Engineering* Vol. 158, 2019, p. 113777.  
doi: <https://doi.org/10.1016/j.applthermaleng.2019.113777>

- [60] Chen, L., Pan, J., Wei, H., Zhou, L., and Hua, J. "Numerical analysis of knocking characteristics and heat release under different turbulence intensities in a gasoline engine," *Applied Thermal Engineering* Vol. 159, 2019, p. 113879.  
doi: <https://doi.org/10.1016/j.applthermaleng.2019.113879>
- [61] Hafiz, N. M., Mansor, M. R. A., and Wan Mahmood, W. M. F. "Simulation of the combustion process for a CI hydrogen engine in an argon-oxygen atmosphere," *International Journal of Hydrogen Energy* Vol. 43, No. 24, 2018, pp. 11286-11297.  
doi: <https://doi.org/10.1016/j.ijhydene.2018.05.022>
- [62] Edwards, J. R., Boles, J. A., and Baurle, R. A. "Large-eddy/Reynolds-averaged Navier-Stokes simulation of a supersonic reacting wall jet," *Combustion and Flame* Vol. 159, No. 3, 2012, pp. 1127-1138.  
doi: <https://doi.org/10.1016/j.combustflame.2011.10.009>
- [63] Feyz, M. E., Hasti, V. R., Gore, J. P., and Nalim, M. R. "Large eddy simulation of hot jet ignition in moderate and high-reactivity mixtures," *Computers & Fluids* Vol. 183, 2019, pp. 28-37.  
doi: <https://doi.org/10.1016/j.compfluid.2019.03.014>
- [64] Feyz, M. E., Nalim, M. R., Hasti, V. R., and Gore, J. P. "Modeling and Analytical Solution of Near-Field Entrainment in Suddenly Started Turbulent Jets," *AIAA Journal* Vol. 57, No. 5, 2019, pp. 1877-1884.  
doi: 10.2514/1.J057612
- [65] Feyz, M. E., Hasti, V. R., Gore, J. P., Chowdhury, A., and Nalim, M. R. "Scalar predictors of premixed gas ignition by a suddenly-starting hot jet," *International Journal of Hydrogen Energy* Vol. 44, No. 42, 2019, pp. 23793-23806.  
doi: <https://doi.org/10.1016/j.ijhydene.2019.07.066>
- [66] El-asrag, H., and Li, S. "Investigation of Extinction and Reignition Events Using the Flamelet Generated Manifold Model," *ASME Turbo Expo 2018: Turbomachinery Technical Conference and Exposition*. Vol. Volume 4A: Combustion, Fuels, and Emissions, 2018.
- [67] El-Asrag, H. A., Braun, M., and Masri, A. R. "Large eddy simulations of partially premixed ethanol dilute spray flames using the flamelet generated manifold model," *Combustion Theory and Modelling* Vol. 20, No. 4, 2016, pp. 567-591.  
doi: 10.1080/13647830.2016.1159732
- [68] Ihme, M., Cha, C. M., and Pitsch, H. "Prediction of local extinction and re-ignition effects in non-premixed turbulent combustion using a flamelet/progress variable approach," *Proceedings of the Combustion Institute* Vol. 30, No. 1, 2005, pp. 793-800.  
doi: <https://doi.org/10.1016/j.proci.2004.08.260>
- [69] Ihme, M., and Pitsch, H. "Prediction of extinction and reignition in nonpremixed turbulent flames using a flamelet/progress variable model: 1. A priori study and presumed PDF closure," *Combustion and Flame* Vol. 155, No. 1, 2008, pp. 70-89.  
doi: <https://doi.org/10.1016/j.combustflame.2008.04.001>
- [70] Ma, P. C., Wu, H., Labahn, J. W., Jaravel, T., and Ihme, M. "Analysis of transient blow-out dynamics in a swirl-stabilized combustor using large-eddy simulations," *Proceedings of the Combustion Institute* Vol. 37, No. 4, 2019, pp. 5073-5082.  
doi: <https://doi.org/10.1016/j.proci.2018.06.066>
- [71] van Oijen, J. A., Donini, A., Bastiaans, R. J. M., ten Thije Boonkkamp, J. H. M., and de Goey, L. P. H. "State-of-the-art in premixed combustion modeling using flamelet

- generated manifolds," *Progress in Energy and Combustion Science* Vol. 57, 2016, pp. 30-74.  
doi: 10.1016/j.pecs.2016.07.001
- [72] Amsden, A. A. "KIVA-3V: A Block Structured KIVA Program for Engines with Vertical or Canted Valves, Los Alamos National Laboratory Technical Report LA-13313-MS." 1997, pp. Los Alamos National Laboratory Report LA-13313-MS.
- [73] Amsden, A. A., O'Rourke, P. J., and Butler, T. D. "KIVA-II: A Computer Program for Chemically Reactive Flows with Sprays," *Los Alamos National Laboratory Technical Report LA-11560-MS*, 1989.
- [74] Liu, A. B., Mather, D., and Reitz, R. D. "Modeling the Effects of Drop Drag and Breakup on Fuel Sprays," *SAE Transactions* Vol. 102, 1993, pp. 83-95.
- [75] Dooley, S., Won, S. H., Chaos, M., Heyne, J., Ju, Y., Dryer, F. L., Kumar, K., Sung, C.-J., Wang, H., Oehlschlaeger, M. A., Santoro, R. J., and Litzinger, T. A. "A jet fuel surrogate formulated by real fuel properties," *Combustion and Flame* Vol. 157, No. 12, 2010, pp. 2333-2339.  
doi: <https://doi.org/10.1016/j.combustflame.2010.07.001>
- [76] Dooley, S., Won, S. H., Heyne, J., Farouk, T. I., Ju, Y., Dryer, F. L., Kumar, K., Hui, X., Sung, C.-J., Wang, H., Oehlschlaeger, M. A., Iyer, V., Iyer, S., Litzinger, T. A., Santoro, R. J., Malewicki, T., and Brezinsky, K. "The experimental evaluation of a methodology for surrogate fuel formulation to emulate gas phase combustion kinetic phenomena," *Combustion and Flame* Vol. 159, No. 4, 2012, pp. 1444-1466.  
doi: <https://doi.org/10.1016/j.combustflame.2011.11.002>
- [77] Dooley, S., Won, S. H., Jahangirian, S., Ju, Y., Dryer, F. L., Wang, H., and Oehlschlaeger, M. A. "The combustion kinetics of a synthetic paraffinic jet aviation fuel and a fundamentally formulated, experimentally validated surrogate fuel," *Combustion and Flame* Vol. 159, No. 10, 2012, pp. 3014-3020.  
doi: <https://doi.org/10.1016/j.combustflame.2012.04.010>
- [78] Dooley, S., Won, S. H., Haas, F. M., Santner, J., Ju, Y., Dryer, F. L., and Farouk, T. I. "Development of reduced kinetic models for petroleum-derived and alternative jet fuels," *50th AIAA/ASME/SAE/ASEE Joint Propulsion Conference 2014*, No. April 2015, 2014, pp. 1-23.  
doi: 10.2514/6.2014-3661
- [79] Haas, F. M., Won, S. H., and Dryer, F. L. "Detailed and compact combustion kinetic models for iso-dodecane and Gevo alcohol-to-jet (ATJ) alternative fuel," *2016 Spring Technical Meeting of the Eastern States Section of the Combustion Institute, ESSCI 2016*, 2016.
- [80] Senecal, P. K., Richards, K. J., Pomraning, E., Yang, T., Dai, M. Z., McDavid, R. M., Patterson, M. A., Hou, S., and Shethaji, T. "A New Parallel Cut-Cell Cartesian CFD Code for Rapid Grid Generation Applied to In-Cylinder Diesel Engine Simulations." Vol. Technical Paper 2007-01-0159, SAE International, 2007, pp. 776-790.
- [81] Berger, M., and Aftosmis, M. "Progress Towards a Cartesian Cut-Cell Method for Viscous Compressible Flow," *50th AIAA Aerospace Sciences Meeting including the New Horizons Forum and Aerospace Exposition*. American Institute of Aeronautics and Astronautics, 2012.
- [82] Ingram, D. M., Causon, D. M., and Mingham, C. G. "Developments in Cartesian cut cell methods," *Mathematics and Computers in Simulation* Vol. 61, No. 3, 2003, pp. 561-572.

- doi: [https://doi.org/10.1016/S0378-4754\(02\)00107-6](https://doi.org/10.1016/S0378-4754(02)00107-6)
- [83] Park, S., and Shin, H. "Efficient generation of adaptive Cartesian mesh for computational fluid dynamics using GPU," *International Journal for Numerical Methods in Fluids* Vol. 70, No. 11, 2012, pp. 1393-1404.  
doi: 10.1002/fld.2750
- [84] Drennan, S. A., and Kumar, G. "Demonstration of an Automatic Meshing Approach for Simulation of a Liquid Fueled Gas Turbine with Detailed Chemistry," *50th AIAA/ASME/SAE/ASEE Joint Propulsion Conference*, 2014, pp. 1-8.  
doi: 10.2514/6.2014-3628
- [85] Bokhart, A., Shin, D., Rodrigues, N. S., Sojka, P., Gore, J. P., and Lucht, R. P. "Spray Characteristics of a Hybrid Airblast Pressure-Swirl Atomizer at Near Lean Blowout Conditions using Phase Doppler Anemometry," *2018 AIAA Aerospace Sciences Meeting*. American Institute of Aeronautics and Astronautics, 2018.
- [86] Buschhagen, T., Zhang, R. Z., Bokhart, A. J., Gejji, R. M., Naik, S. V., Lucht, R. P., Gore, J. P., Sojka, P. E., Slabaugh, C. D., and Meyer, S. "Effect of Aviation Fuel Type and Fuel Injection Conditions on Non-reacting Spray Characteristics of a Hybrid Airblast Fuel Injector," *54th AIAA Aerospace Sciences Meeting*, No. January, 2016, pp. 1-18.  
doi: 10.2514/6.2016-1154
- [87] Issa, R. I. "Solution of the implicitly discretised fluid flow equations by operator-splitting," *Journal of Computational Physics* Vol. 62, No. 1, 1986, pp. 40-65.  
doi: [https://doi.org/10.1016/0021-9991\(86\)90099-9](https://doi.org/10.1016/0021-9991(86)90099-9)
- [88] Rhie, C. M., and Chow, W. L. "Numerical study of the turbulent flow past an airfoil with trailing edge separation," *AIAA Journal* Vol. 21, No. 11, 1983, pp. 1525-1532.  
doi: 10.2514/3.8284
- [89] Aceves, S. M., Flowers, D. L., Westbrook, C. K., Smith, J. R., Pitz, W., and Dibble, R. "A Multi-Zone Model for Prediction of HCCI Combustion and Emissions Reprinted From : Compression Ignition Combustion Processes," No. 724, 2000.
- [90] Raju, M., Wang, M., Dai, M., Piggott, W., and Flowers, D. "Acceleration of Detailed Chemical Kinetics Using Multi-zone Modeling for CFD in Internal Combustion Engine Simulations," *SAE 2012 World Congress & Exhibition*, No. Technical Paper 2012-01-0135, 2012.  
doi: <https://doi.org/10.4271/2012-01-0135>
- [91] Lucht, R. P. "Effects of Exhaust Gas Recirculation (EGR) on Turbulent Combustion and Emissions in Advanced Gas Turbine Combustors with HighHydrogen-Content (HHC) Fuels " *Project Report Submitted to U. S. Department of Energy, National Energy Technology Laboratory (NETL), University Turbine Systems Research (UTSR) Program, DOE Award Number: DE-FE0011822*, 2017.
- [92] Elkady, A. M., Evulet, A., Brand, A., Ursin, T. P., and Lynghjem, A. "Exhaust Gas Recirculation in DLN F-Class Gas Turbines for Post-Combustion CO<sub>2</sub> Capture," *ASME Turbo Expo 2008: Power for Land, Sea, and Air* Vol. 3, No. GT2008-51152, 2008, pp. 847-854.  
doi: 10.1115/GT2008-51152
- [93] Evulet, A. T., Elkady, A. M., Branda, A. R., and Chinn, D. "On the Performance and Operability of GE's Dry Low NO<sub>x</sub> Combustors utilizing Exhaust Gas Recirculation for PostCombustion Carbon Capture," *Energy Procedia* Vol. 1, No. 1, 2009, pp. 3809-3816.  
doi: <https://doi.org/10.1016/j.egypro.2009.02.182>

- [94] Li, H., ElKady, A., and Evulet, A. "Effect of Exhaust Gas Recirculation on NO<sub>x</sub> Formation in Premixed Combustion System," *47th AIAA Aerospace Sciences Meeting including The New Horizons Forum and Aerospace Exposition*, No. AIAA 2009-226, 2009.  
doi: <https://doi.org/10.2514/6.2009-226>
- [95] Tanaka., Y., Nose., M., Nakao., M., Saitoh., K., Ito., E., and Tsukagoshi., K. "Development of Low NO<sub>x</sub> Combustion System with EGR for 1700 ° C-class Gas Turbine," *Mitsubishi Heavy Industries Technical Review* Vol. 50, No. 1, 2013, pp. 4-9.
- [96] Rokke, P. E., and Hustad, J. E. "Exhaust gas recirculation in gas turbines for reduction of CO<sub>2</sub> emissions; Combustion testing with focus on stability and emissions," *International Journal of Thermodynamics* Vol. 8, No. 4, 2005, pp. 167-173.  
doi: 10.5541/ijot.1034000158
- [97] Reuter, C. B., Won, S. H., and Ju, Y. "Effects of CO<sub>2</sub> Addition on the Turbulent Flame Front Dynamics and Propagation Speeds of Methane/Air Mixtures," *Journal of Engineering for Gas Turbines and Power* Vol. 141, No. 1, 2018, pp. 011503-011503-12.  
doi: 10.1115/1.4040518
- [98] Wang, J., Matsuno, F., Okuyama, M., Ogami, Y., Kobayashi, H., and Huang, Z. "Flame front characteristics of turbulent premixed flames diluted with CO<sub>2</sub> and H<sub>2</sub>O at high pressure and high temperature," *Proceedings of the Combustion Institute* Vol. 34, No. 1, 2013, pp. 1429-1436.  
doi: 10.1016/j.proci.2012.06.154
- [99] Kobayashi, H., Yata, S., Ichikawa, Y., and Ogami, Y. "Dilution effects of superheated water vapor on turbulent premixed flames at high pressure and high temperature," *Proceedings of the Combustion Institute* Vol. 32, No. 2, 2009, pp. 2607-2614.  
doi: <https://doi.org/10.1016/j.proci.2008.05.078>
- [100] Galmiche, B., Halter, F., Foucher, F., and Dagaut, P. "Effects of Dilution on Laminar Burning Velocity of Premixed Methane/Air Flames," *Energy & Fuels* Vol. 25, No. 3, 2011, pp. 948-954.  
doi: 10.1021/ef101482d
- [101] Li, H.-M., Li, G.-X., Sun, Z.-Y., Zhou, Z.-H., Li, Y., and Yuan, Y. "Fundamental Combustion Characteristics of Lean and Stoichiometric Hydrogen Laminar Premixed Flames Diluted With Nitrogen or Carbon Dioxide," *Journal of Engineering for Gas Turbines and Power* Vol. 138, No. 11, 2016, pp. 111501-111501-9.  
doi: 10.1115/1.4032315
- [102] Han, D., Satija, A., Kim, J., Weng, Y., Gore, J. P., and Lucht, R. P. "Dual-pump vibrational CARS measurements of temperature and species concentrations in turbulent premixed flames with CO<sub>2</sub> addition," *Combustion and Flame* Vol. 181, 2017, pp. 239-250.  
doi: <https://doi.org/10.1016/j.combustflame.2017.03.027>
- [103] Han, D., Satija, A., Gore, J. P., and Lucht, R. P. "Experimental study of CO<sub>2</sub> diluted, piloted, turbulent CH<sub>4</sub>/air premixed flames using high-repetition-rate OH PLIF," *Combustion and Flame* Vol. 193, 2018, pp. 145-156.  
doi: <https://doi.org/10.1016/j.combustflame.2018.03.012>
- [104] Kobayashi, H., Hagiwara, H., Kaneko, H., and Ogami, Y. "Effects of CO<sub>2</sub> dilution on turbulent premixed flames at high pressure and high temperature," *Proceedings of the Combustion Institute* Vol. 31 I, 2007, pp. 1451-1458.

- doi: 10.1016/j.proci.2006.07.159
- [105] Kato, S., Fujimori, T., Dowling, A. P., and Kobayashi, H. "Effect of heat release distribution on combustion oscillation," *Proceedings of the Combustion Institute* Vol. 30, No. 2, 2005, pp. 1799-1806.  
doi: <https://doi.org/10.1016/j.proci.2004.08.154>
- [106] Pitsch, H., and Steiner, H. "Large-eddy simulation of a turbulent piloted methane/air diffusion flame (Sandia flame D)," *Physics of Fluids* Vol. 12, No. 10, 2000, pp. 2541-2554.  
doi: 10.1063/1.1288493
- [107] Chen, Y., and Ihme, M. "Large-eddy simulation of a piloted premixed jet burner," *Combustion and Flame* Vol. 160, No. 12, 2013, pp. 2896-2910.  
doi: 10.1016/j.combustflame.2013.07.009
- [108] Gövert, S., Mira, D., Kok, J. B. W., Vazquez, M., and Houzeaux, G. "Turbulent combustion modelling of a confined premixed methane / air jet flame using tabulated chemistry," *Energy Procedia* Vol. 66, 2015, pp. 313-316.  
doi: 10.1016/j.egypro.2015.02.070
- [109] Hawkes, E. R., and Chen, J. H. "Direct numerical simulation of hydrogen-enriched lean premixed methane-air flames," *Combustion and Flame* Vol. 138, No. 3, 2004, pp. 242-258.  
doi: <https://doi.org/10.1016/j.combustflame.2004.04.010>
- [110] Rowinski, D. H., and Pope, S. B. "Computational study of lean premixed turbulent flames using RANSPDF and LESPDF methods," *Combustion Theory and Modelling* Vol. 17, No. 4, 2013, pp. 610-656.  
doi: 10.1080/13647830.2013.789929
- [111] Trisjono, P., and Pitsch, H. "A direct numerical simulation study on NO formation in lean premixed flames," *Proceedings of the Combustion Institute* Vol. 36, No. 2, 2017, pp. 2033-2043.  
doi: <https://doi.org/10.1016/j.proci.2016.06.130>
- [112] Wang, H., and Zhang, P. "A unified view of pilot stabilized turbulent jet flames for model assessment across different combustion regimes," *Proceedings of the Combustion Institute* Vol. 36, No. 2, 2017, pp. 1693-1703.  
doi: 10.1016/j.proci.2016.06.008
- [113] Jeong, J., and Hussain, F. "On the identification of a vortex," *Journal of Fluid Mechanics* Vol. 285, 1995, pp. 69-94.  
doi: 10.1017/S0022112095000462
- [114] Haller, G. "An objective definition of a vortex," *Journal of Fluid Mechanics* Vol. 525, 2005, pp. 1-26.  
doi: 10.1017/S0022112004002526
- [115] Dubief, Y., and Delcayre, F. "On coherent-vortex identification in turbulence," *Journal of Turbulence* Vol. 1, 2000, pp. N11-N11.  
doi: 10.1088/1468-5248/1/1/011
- [116] Bray, K. N. C. "The challenge of turbulent combustion," *Symposium (International) on Combustion* Vol. 26, No. 1, 1996, pp. 1-26.  
doi: [https://doi.org/10.1016/S0082-0784\(96\)80195-0](https://doi.org/10.1016/S0082-0784(96)80195-0)

- [117] Bray, K. N. C., Libby, P. A., Masuya, G., and Moss, J. B. "Turbulence Production in Premixed Turbulent Flames," *Combustion Science and Technology* Vol. 25, No. 3-4, 1981, pp. 127-140.  
doi: 10.1080/00102208108547512
- [118] Bray, K. N. C., Libby, P. A., and Moss, J. B. "Unified modeling approach for premixed turbulent combustion—Part I: General formulation," *Combustion and Flame* Vol. 61, No. 1, 1985, pp. 87-102.  
doi: [https://doi.org/10.1016/0010-2180\(85\)90075-6](https://doi.org/10.1016/0010-2180(85)90075-6)
- [119] Lucht, R. P. "Project 029(A) National Jet Fuels Combustion Program – Area #5: Atomization Test and Models, Purdue University," *ASCENT National Jet Fuel Combustion Program (NJFCP)*, 2019.
- [120] Rida, S., Reynolds, R., Chakravorty, S., and Gupta, K. "Imprinted Effusion Modeling and Dynamic CD Calculation in Gas Turbine Combustors," *ASME Turbo Expo 2012: Turbine Technical Conference and Exposition*. 2012, pp. 1-11.
- [121] Kundu, P., Ameen, M. M., and Som, S. "Importance of turbulence-chemistry interactions at low temperature engine conditions," *Combustion and Flame* Vol. 183, 2017, pp. 283-298.  
doi: <https://doi.org/10.1016/j.combustflame.2017.05.025>
- [122] Skeen, S. A., Manin, J., and Pickett, L. M. "Simultaneous formaldehyde PLIF and high-speed schlieren imaging for ignition visualization in high-pressure spray flames," *Proceedings of the Combustion Institute* Vol. 35, No. 3, 2015, pp. 3167-3174.  
doi: <https://doi.org/10.1016/j.proci.2014.06.040>
- [123] Giusti, A., and Mastorakos, E. "Detailed chemistry LES/CMC simulation of a swirling ethanol spray flame approaching blow-off," *Proceedings of the Combustion Institute* Vol. 36, No. 2, 2017, pp. 2625-2632.  
doi: <https://doi.org/10.1016/j.proci.2016.06.035>
- [124] Mongia, H., Vermeersch, M., and Held, T. "A simple reactor-based approach for correlating lean blowout of turbopropulsion engine combustors," *37th Joint Propulsion Conference and Exhibit*. American Institute of Aeronautics and Astronautics, 2001.
- [125] Muruganandam, T. M., Nair, S., Scarborough, D., Neumeier, Y., Jagoda, J., Lieuwen, T., Seitzman, J., and Zinn, B. "Active Control of Lean Blowout for Turbine Engine Combustors," *Journal of Propulsion and Power* Vol. 21, No. 5, 2005, pp. 807-814.  
doi: 10.2514/1.7254
- [126] Li, H., Zhou, X., Jeffries, J. B., and Hanson, R. K. "Active control of lean blowout in a swirl-stabilized combustor using a tunable diode laser," *Proceedings of the Combustion Institute* Vol. 31, No. 2, 2007, pp. 3215-3223.  
doi: <https://doi.org/10.1016/j.proci.2006.07.006>
- [127] Nair, S., and Lieuwen, T. "Acoustic Detection of Blowout in Premixed Flames," *Journal of Propulsion and Power* Vol. 21, No. 1, 2005, pp. 32-39.  
doi: 10.2514/1.5658
- [128] Yi, T., and Gutmark, E. J. "Real-Time Prediction of Incipient Lean Blowout in Gas Turbine Combustors," *AIAA Journal* Vol. 45, No. 7, 2007, pp. 1734-1739.  
doi: 10.2514/1.25847
- [129] Ehn, A., Zhu, J., Li, X., and Kiefer, J. "Advanced Laser-Based Techniques for Gas-Phase Diagnostics in Combustion and Aerospace Engineering," *Applied Spectroscopy* Vol. 71, No. 3, 2017, pp. 341-366.

- doi: 10.1177/0003702817690161
- [130] Muruganandam, T. M., and Seitzman, J. M. "Fluid Mechanics of Lean Blowout Precursors in Gas Turbine Combustors," *International Journal of Spray and Combustion Dynamics* Vol. 4, No. 1, 2012, pp. 29-60.  
doi: 10.1260/1756-8277.4.1.29
- [131] Massey, J. C., Chen, Z. X., and Swaminathan, N. "Lean Flame Root Dynamics in a Gas Turbine Model Combustor," *Combustion Science and Technology* Vol. 191, No. 5-6, 2019, pp. 1019-1042.  
doi: 10.1080/00102202.2019.1584616
- [132] Sarkar, S., Lore, K. G., Sarkar, S., Ramanan, V. R., Chakravarthy, S. R., Phoha, S., and Ray, A. "Early Detection of Combustion Instability from Hi-speed Flame Images via Deep Learning and Symbolic Time Series Analysis," *Proceedings of the Annual Conference of the Prognostics and Health Management Society, PHM. Annual Conference of The Prognostics and Health Management Society, 2015.*
- [133] Ghosal, S., Ramanan, V., Sarkar, S., Chakravarthy, S. R., and Sarkar, S. "Detection and Analysis of Combustion Instability From Hi-Speed Flame Images Using Dynamic Mode Decomposition," *Proceedings of the ASME 2016 Dynamic Systems and Control Conference* Vol. 1, 2016.  
doi: 10.1115/DSCC2016-9907
- [134] Smola, A. J., and Schölkopf, B. "A tutorial on support vector regression," *Statistics and Computing* Vol. 14, No. 3, 2004, pp. 199-222.  
doi: 10.1023/B:STCO.0000035301.49549.88
- [135] Pedregosa, F., Varoquaux, G., Gramfort, A., Michel, V., Thirion, B., Grisel, O., Blondel, M., Prettenhofer, P., Weiss, R., Dubourg, V., Vanderplas, J., Passos, A., Cournapeau, D., Brucher, M., Perrot, M., and Duchesnay, É. "Scikit-learn: Machine Learning in Python," *J. Mach. Learn. Res.* Vol. 12, 2011, pp. 2825-2830.
- [136] Masci, J., Meier, U., Cireşan, D., and Schmidhuber, J. "Stacked Convolutional Auto-Encoders for Hierarchical Feature Extraction," *Artificial Neural Networks and Machine Learning – ICANN 2011*. Springer Berlin Heidelberg, Berlin, Heidelberg, 2011, pp. 52-59.
- [137] Abadi, M., Agarwal, A., Barham, P., Brevdo, E., Chen, Z., Citro, C., Corrado, G. S., Davis, A., Dean, J., Devin, M., Ghemawat, S., Goodfellow, I. J., Harp, A., Irving, G., Isard, M., Jia, Y., Józefowicz, R., Kaiser, L., Kudlur, M., Levenberg, J., Mané, D., Monga, R., Moore, S., Murray, D. G., Olah, C., Schuster, M., Shlens, J., Steiner, B., Sutskever, I., Talwar, K., Tucker, P. A., Vanhoucke, V., Vasudevan, V., Viégas, F. B., Vinyals, O., Warden, P., Wattenberg, M., Wicke, M., Yu, Y., and Zheng, X. "TensorFlow: Large-Scale Machine Learning on Heterogeneous Distributed Systems," *ArXiv* Vol. abs/1603.04467, 2015.
- [138] Kingma, D. P., and Ba, J. "Adam: A Method for Stochastic Optimization," *CoRR* Vol. abs/1412.6980, 2014.

## **VITA**

Veeraraghava Raju Hasti holds a Bachelor of Technology (B. Tech) degree from Sri Venkateswara University, India and a Master of Science (M.S) degree from Purdue University, USA. He worked as a Scientist / Engineer in Vikram Sarabhai Space Center, Indian Space Research Organization, India from 2003 to 2006 and then as a Technology Specialist in Honeywell from 2006 to 2014. He has received top honors from Honeywell and outstanding recognitions from Indian Space Research Organization.

## PUBLICATIONS

1. Veeraraghava Raju Hasti, Rober P. Lucht, and Jay P. Gore, "Large eddy simulation of hydrogen piloted CH<sub>4</sub>/air premixed combustion with CO<sub>2</sub> dilution", Journal of the Energy Institute, October 2019  
<https://doi.org/10.1016/j.joei.2019.10.004>
2. Mohammad Feyz, Veeraraghava Raju Hasti, Jay Gore, A. Chowdhury, and Razi Nalim, "Scalar Predictors of Premixed Gas Ignition by a Suddenly-starting Hot Jet", International Journal of Hydrogen Energy, Volume 44, Issue 42, pp:23793-23806, 2019,  
<https://doi.org/10.1016/j.ijhydene.2019.07.066>
3. Mohammad Feyz, Veeraraghava Raju Hasti, Jay Gore, Razi Nalim, "Large Eddy Simulation of Hot Jet Ignition in Moderate and High-Reactivity Mixtures", Computers and Fluids, 183, pp:28–37, 2019  
<https://doi.org/10.1016/j.compfluid.2019.03.014>
4. M. E. Feyz, M. R. Nalim, V. R. Hasti, and J. P. Gore., "Modeling and analytical solution of the near-field entrainment in starting turbulent jets", AIAA Journal, pp: 1-8, 2019,  
<https://doi.org/10.2514/1.J057612>
5. Veeraraghava Raju Hasti, Shuaishuai Liu, Gaurav Kumar, and Jay P. Gore. "Comparison of Premixed Flamelet Generated Manifold Model and Thickened Flame Model for Bluff Body Stabilized Turbulent Premixed Flame", 2018 AIAA Aerospace Sciences Meeting, AIAA SciTech Forum, Kissimmee, Florida, USA (AIAA 2018-0150)
6. Veeraraghava Raju Hasti, Gaurav Kumar, Shuaishuai Liu, Robert P. Lucht, and Jay P. Gore. "Large Eddy Simulation of Pilot Stabilized Turbulent Premixed CH<sub>4</sub>+Air Jet Flames", 2018 AIAA Aerospace Sciences Meeting, AIAA SciTech Forum, Kissimmee, Florida, USA (AIAA 2018-0675)
7. Veeraraghava Raju Hasti, Prithwish Kundu, Gaurav Kumar, Scott A. Drennan, Sibendu Som, and Jay P. Gore. "A Numerical Study of Flame Characteristics during Lean Blow-Out in a Gas Turbine Combustor", 2018 Joint Propulsion Conference, AIAA Propulsion and Energy Forum, (AIAA 2018-4955)
8. Veeraraghava Raju Hasti, Prithwish Kundu, Gaurav Kumar, Scott A. Drennan, Sibendu Som, Sang Hee Won, Frederick L. Dryer, and Jay P. Gore. "Lean blow-out (LBO) computations in

- a gas turbine combustor", 2018 Joint Propulsion Conference, AIAA Propulsion and Energy Forum, (AIAA 2018-4958)
9. Veeraraghava Raju Hasti, Prithwish Kundu, Gaurav Kumar, Scott A. Drennan, Sibendu Som, and Jay P. Gore. "Numerical Simulation of Flow Distribution in a Realistic Gas Turbine Combustor", 2018 Joint Propulsion Conference, AIAA Propulsion and Energy Forum, (AIAA 2018-4956).
  10. Veeraraghava Raju Hasti, Gaurav Kumar, Shuaishuai Liu, Robert P Lucht and Jay P Gore "A Computational Study on H2 Piloted Turbulent Methane / Air Premixed Flame with CO2 Dilution", 2018 Spring Technical Meeting, Central States Section of the Combustion Institute, Minneapolis, MN 55455 USA
  11. Vikrant Goyal<sup>1</sup>, Rathziel Roncancio, Jupyong Kim, Abhishek Navarkar, Veeraraghava Raju Hasti, and Jay P. Gore, "Effect of initial fuel temperature on flame spread rate of alternative aviation fuels", 11th US National Combustion Meeting, March 24 -27, 2019, Pasadena, CA 91101 USA
  12. Vikrant Goyal, Yerbatur Tursyn, Veeraraghava Raju Hasti, Jay P. Gore, "Experimental Investigation of Hot Surface Ignition Temperatures for Aviation Fuels", 11th US National Combustion Meeting, March 24 -27, 2019, Pasadena, CA 91101 USA
  13. Rathziel Roncancio, Abhishek Navarkar, Veeraraghava Raju Hasti, Vikrant Goyal, Jay P. Gore, "Effect of carbon nanotubes addition on the Flame Spread Rate over a Jet A pool", 11th US National Combustion Meeting, March 24 -27, 2019, Pasadena, CA 91101 USA
  14. M. E. Feyz, M. R. Nalim, V. R. Hasti, J. P. Gore, Statistical analysis of scalars for ignition via transient hot jet, 11th US National Combustion Meeting, March 24 -27, 2019, Pasadena, CA 91101 USA
  15. Vikrant Goyal, Veeraraghava Raju Hasti, Jay P. Gore, Hukam C. Mongia, "Detached eddy simulation of turbulent swirl-stabilized flame" 9th U.S. National Combustion Meeting, Central States Section of the Combustion Institute, May 17-20, 2015, Cincinnati, Ohio, USA
  16. Dong Han, Veeraraghava Raju Hasti, Jay P. Gore and Robert P Lucht, "An Experimental and Computational Study of Turbulent Lean Premixed Flames", Propellants and Combustion Session, AIAA Propulsion and Energy 2015 Conference, Orlando, Florida, USA (AIAA 2015-4086)